Computational systems biology approaches to investigate cellular senescence

A thesis submitted by

Sharmilla Chandrasegaran

For the Degree of Doctor of Philosophy

Newcastle University

Biosciences Institute

September 2023

Abstract

Cellular senescence is a complex stress response that results in an irreversible cell cycle arrest, accompanied by phenotypic, metabolic, and secretory changes termed as the senescence-associated secretory phenotype (SASP). Senescent cells accumulate with age and are associated with several age-related pathologies, including fibrosis and chronic wounds. However, they also play important functional roles, such as in cancer suppression, embryogenesis, and wound healing. The inherent complexity of cellular senescence requires an approach where multiple levels of complexity can be addressed individually, followed by an investigation of the interactions between these levels, as well as the whole system. For this reason, a computational systems biology approach was adopted, which uses bioinformatics methods and computational/mathematical modelling to address biological processes. A tissue-level agent-based computational model was developed to investigate the dynamics of senescent cells in healthy wound healing. This model was then used to explore how perturbations in the system lead to pathological healing outcomes, such as fibrosis and chronic wounds. The model suggests that an appropriate number of senescent cells be present during the mid to late stages of wound healing to promote healthy healing, whereas higher background levels of senescence promote an inflammatory chronic wound. Furthermore, the model suggests that an abundance of pre-existing senescent cells, as during ageing, also promotes a chronic wound response. In contrast, an insufficient number of senescent cells was shown to promote a fibrotic response due to a lack of fibrolytic factors. Lastly according to the model, the delayed induction of senescent cells also results in fibrotic responses, due to a delay in the necessary fibrolytic activity. Overall, these results suggest that the functional versatility of senescent cells can be attributed to differences in SASP composition, duration of senescence and temporal induction of senescence relative to the healing phase. The range of outcomes demonstrated by the model strongly highlight the dynamic and heterogenous role of senescent cells in wound healing, as well as fibrotic and chronic wounds, and their necessary fine-tuned control. At the intracellular level, a bioinformatic workflow was developed to analyse a recently published multi-omic time-series dataset gathered during replicative senescence (RS). The primary output from the workflow were mechanistic networks driving RS, which confirmed the multi-step and gradual nature of senescence progression. Network analysis also revealed that senescence processes, especially involving cell cycle arrest

and apoptosis evasion, begin early through to intermediate senescence, followed by effectors involved in SASP production during late senescence. Overall, multiple computational methods were used in this thesis to investigate the role of cellular senescence, at the tissue-level both in physiological and pathological settings, as well as to investigate intracellular mechanisms driving senescence. Furthermore, the wound healing model provides an extensible resource that can be used for further investigation with appropriate data. The bioinformatic workflow can be readily used to analyse other multi-omic datasets to generate mechanistic hypotheses.

Acknowledgements

First and foremost, I would like to thank my supervisor Dr. Daryl Shanley for giving me the opportunity to pursue a PhD, and for believing in me. It really has been a dream come true for me. I am beyond grateful for Daryl's invaluable mentorship, guidance, and support over the years. I would also like to thank Dr. Carmen Martin-Ruiz, for her support and for her thorough review of my thesis.

I would like to acknowledge and thank Dr. Krutik Patel, who has been a mentor to me throughout these years – all the way from teaching me good coding practices to providing me with valuable feedback on this thesis. I would also like to thank Dr. James Wordsworth and Dr. Glyn Nelson, for their guidance and help.

I would like to thank Dr. James Sluka for all his help, advice, and the time he spent to have discussions with me. I am very grateful for everything he has done.

I would like to thank the members of my group (past and present), who have been great company throughout the PhD, and have taught me so much: Dr. Ciaran Welsh, Rebekah Scanlan, Dr. Louise Pease and Dr. Peter Clark.

A special thanks to Charalampos Ntigkakis and my friends, without whom I am not sure how I would have survived this. I would also like to thank my brother Logan and my parents: amma and appa, for their love and for everything they have done for me.

Declaration

I declare the work presented within this thesis is based my own research and has not been submitted as part of another degree at any institution. Information derived from published work has been cited in the bibliography.

List of Figures

List of Tables

List of Abbreviations

Abbreviations	Full Description
ABM	Agent-based model
AGE	Advanced glycation end products
AI	Artificial intelligence
αSMA	α-smooth muscle actin
ATP	Adenosine triphosphate
COM	center of mass
CPM	Cellular-Potts Model
CSF1	Colony stimulating Factor 1
DDR	DNA Damage Response
ECM	Extracellular matrix
EGF	epidermal growth factor
EMT	Epithelial-to-mesenchymal transition
EndMT	Endothelial-mesenchymal transition
FN	Fibronectin
GOBP	Gene Ontology Biological Process
GREA	Genomic region enrichment analysis
GSEA	Gene set enrichment analysis
HSC	hepatic stellate cells
IFN-γ	interferon-gamma
KO	Knockout
LDL-C	Low-Density Lipoprotein Cholesterol
MCS	Monte Carlo Step
ML	Machine learning
MMP	matrix metalloproteinase
MOFA	Multi-omic factor analysis
MSEA	Metabolite enrichment analysis
NAC	N-acetyl L-cysteine
NMR	Nuclear magnetic resonance

ODE	Ordinary differential equation
OIS	Oncogene-induced senescence
ORA	Over-representation analysis
PDE	Partial differential equation
PDGF	Platelet-derived growth factor
PDL	Population doubling
PKN	Prior knowledge network
PSO	Particle Swarm Optimisation
RIS	RAS-induced senescence
ROS	Reactive oxygen species
RS	Replicative senescence
SASP	Senescence-associated secretory phenotype
TEC	tubular epithelial cells
TF	Transcription factor
TGF-β	Transforming growth factor-β
TIMP	Tissue inhibitor of metalloproteinases
TNF	Tumour necrosis factor
TRN	Transcriptional regulatory network
TSS	Transcription start site
UTP	Uridine 5'-triphosphate
VSN	Variance stabilising normalisation
WT	Wildtype

Nomenclature

When referring to genes and proteins: *GENE*, PROTEIN

Contents

Chapter 1. Introduction

1.1 The biology of cellular senescence

Cellular senescence is a process whereby cells undergo an irreversible cell cycle arrest in response to a diverse range of stresses. It was first discovered by Hayflick and Moorhead, who demonstrated that cultured human fibroblasts had an exhaustive replicative capacity before entering a state of replicative senescence (RS) (Hayflick and Moorhead, 1961). Cell cycle arrest in senescent cells occurs in the G1 or G2 phase, hence preventing their proliferation (Di Leonardo *et al.*, 1994; Gire and Dulic, 2015). This is in contrast to quiescent cells which experience a reversible cell cycle arrest in the G0 phase in response to nutrition or growth factor scarcity (Sun and Buttitta, 2017). Additionally, the upregulation of survival pathways such as the BCL-2 family of anti-apoptotic proteins, confers resistance to apoptosis in senescent cells (Yosef *et al.*, 2016). This resistance to apoptosis, along with an age-related decline in the efficiency of immune system-mediated clearance of senescent cells, results in their accumulation and persistence in ageing tissues (Gorgoulis *et al.*, 2019).

Senescence is a dynamic multi-step process involving distinct but overlapping molecular mechanisms that play a role at different times from the cell cycle exit to late-stage senescence. Senescence can result from multiple types of stressors including oncogene activation, telomere erosion, DNA damaging agents, chromatin changes and mitochondrial dysfunction (Figure 1.1). Nuclear DNA damage has been reported to be the main cause of senescence (Ovadya *et al.*, 2018; Di Micco *et al.*, 2021). DNA damage leads to the activation of the DNA damage response (DDR) pathway which blocks cell cycle progression, therefore preventing defective genetic information from being passed on (Jackson and Bartek, 2009; Gorgoulis *et al.*, 2019). The DDR cascade results in the stabilisation of the tumour suppressor p53, which stimulates the expression of its transcriptional target cyclin-dependent kinase inhibitor p21 (Jackson and Bartek, 2009). Additionally, another cyclin-dependent kinase inhibitor p16 also plays an important role in many types of senescence by blocking cell cycle progression through inhibition of CDK4 and CDK6-mediated retinoblastoma protein inactivation (Beauséjour *et al.*, 2003). However, p21 is suggested to be primarily activated during the early stages of the senescence process, whereas p16 is activated later to maintain senescence (Dulić *et al.*, 2000).

The irreversible cell cycle arrest in senescence is also accompanied by distinct phenotypic and metabolic features, as well as the senescence-associated secretory phenotype (SASP) (Figure 1.1). SASP is characterised by the transcriptional activation of several factors including growth factors, cytokines, chemokines, extracellular matrix (ECM) components and matrix proteinases (Coppé *et al.*, 2010). Senescent cells can exert effects on its surrounding microenvironment in many ways depending on context. Through SASP, senescent cells can reinforce the senescence phenotype in an autocrine manner, whereby senescent cells produce and secrete SASP factors, followed by binding of those factors to receptors on the same senescent cells, leading to signal transduction that reinforces the cell cycle arrest. Furthermore, SASP can induce secondary senescence in neighbouring cells through paracrine signalling, whereby cytokines secreted by senescent cells diffuse and bind to receptors on neighbouring cells. This phenomenon is also known as the 'bystander effect' (Acosta *et al.*, 2013a; da Silva *et al.*, 2019). In addition to paracrine-mediated secondary senescence induction, senescent cells can also induce secondary senescence in a juxtacrine manner, through cell-to-cell contact, mediated by Notch signalling (Hoare *et al.*, 2016; Teo *et al.*, 2019). The term primary senescence is used for induction by any of the stress in an intrinsic manner, as discussed previously, whereas secondary senescence is used for that caused by neighbouring senescent cells. Finally, SASP can also attract and recruit immune cells to organ sites, leading to chronic inflammation (Lagnado *et al.*, 2021), and even contributes to dysregulated stem cell and progenitor cell function (Ogrodnik *et al.*, 2019).

SASP activation and production are highly dynamic processes, with different types of stress stimuli activating distinct SASP factors (Özcan *et al.*, 2016). For instance, protein secretion is increased in oncogene-induced SASP compared to irradiation-induced or RS (Coppé *et al.*, 2008). However, despite these differences, a common core SASP program has been reported in many types of senescent cells *in vitro* induced. This core SASP includes pro-inflammatory mediators such as, the interleukins IL-6 and IL-8, and the monocyte attractant protein CCL2 (Coppé *et al.*, 2008). In addition to these pro-inflammatory molecules, SASP also includes ECM remodelling enzymes such as matrix metalloproteinases (MMPs), SERPINs and tissue inhibitor of metalloproteinases (TIMPs) (Özcan *et al.*, 2016).

SASP production is regulated by persistent DDR activation, with depletion of key DDR regulators such as ATM, NBS1 and CHK2 resulting in decreased cytokine production in response to stress

(Kumari and Jat, 2021). In contrast to this, p53 inhibition is required for effective regulation of the SASP as it attenuates SASP production (Rodier *et al.*, 2009). However, since DDR signalling happens on a shorter time frame compared to SASP development, other pathways are also involved in its modulation such as the MAPK p38 pathway. Interestingly, MAPK p38 is crucial and necessary to induce growth arrest and SASP production and is able to do so even without DNA damage (Freund, Patil and Campisi, 2011a). Despite being independent, both DDR and MAPK p38 pathways converge to regulate SASP through activation of NF-κB, which is a key transcription factor (TF) for SASP genes (Chien *et al.*, 2011; Freund, Patil and Campisi, 2011a).

The regulation of SASP is extremely complex and requires many TFs and chromatin regulators. TFs including NF-κB, GATA4 and C/EBPβ regulate the transcription of SASP genes (Acosta *et al.*, 2008; Kuilman *et al.*, 2008; Kang *et al.*, 2015; Hoare *et al.*, 2016). Aside from activating several SASP genes individually, the TFs involved also interact with each other to modulate SASP. For example, GATA4, which accumulates following DDR, has been proposed to be the link between the upstream DDR pathway and downstream NF-κB activation for a full SASP production (Kang *et al.*, 2015). On the other hand, chromatin regulators, such as BRD4, which binds to acetylated histones, can also regulate SASP genes; BRD4 is recruited to sites adjacent to SASP genes during oncogene-induced senescence (OIS) (Tasdemir *et al.*, 2016; Kumari and Jat, 2021). Many other pathways and factors are involved in SASP regulation, including JAK2/STAT3, inflammasomes, mTOR, PI3K, HSP90 and non-coding RNAs (Di Micco *et al.*, 2021; Kumari and Jat, 2021).

Senescent cell phenotype and SASP are highly heterogenous, that may in part be due to differing contribution from different TFs (Hernandez-Segura *et al.*, 2017; Wiley *et al.*, 2017; Kirschner *et al.*, 2020). Moreover, the temporal characteristics of SASP may also be governed by other factors, such as NOTCH1 signalling which can regulate the composition of SASP. NOTCH1 increases during the early phases of senescence, where it activates a transforming growth factor-β (TGF-β)-mediated SASP while repressing C/EBPβ, resulting in the decreased production of pro-inflammatory factors. However, during deep senescence where NOTCH1 is decreased, pro-inflammatory SASP production is induced (Hoare *et al.*, 2016; Ito, Hoare and Narita, 2017). Interestingly, differences also exist between primary and secondary senescence as observed by single-cell analysis (Teo *et al.*, 2019). SASP from secondary senescence had decreased levels of inflammatory cytokines and increased levels of collagen production. This was observed with OIS

but would be interesting to study in other types of senescence (Teo *et al.*, 2019; Kirschner *et al.*, 2020). Additionally, transcriptomic studies have identified distinct transcriptomic signatures that are associated with specific stressors or cell types, demonstrating the dynamic nature of the senescence phenotype at different time intervals (Hernandez-Segura *et al.*, 2017).

To summarise, the senescence phenotype is highly diverse depending on the cell type affected, type of stressor, physiological location and process specificity, and signalling pathways involved (Parry *et al.*, 2018; Lee and Schmitt, 2019; Kirschner *et al.*, 2020). Depending on these factors, SASP composition itself is also heterogenous and temporally dynamic (Hoare *et al.*, 2016; Lee and Schmitt, 2019). Moreover, primary and secondary senescence result in distinct types of SASP (Teo *et al.*, 2019). All these variations allow senescent cells to be involved in a wide range of pathways across many physiological processes, disease pathologies and ageing.

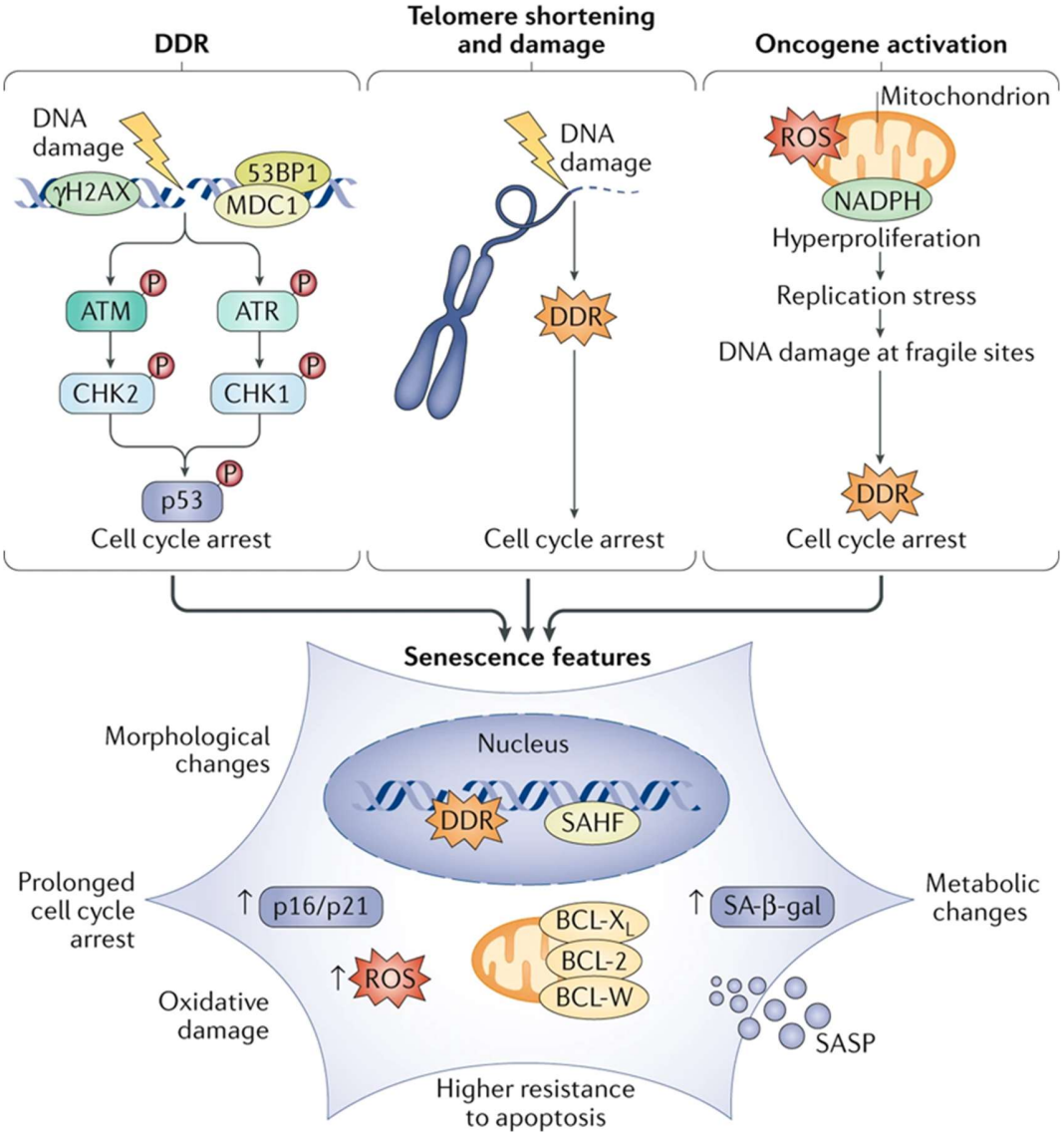

Figure 1.1 **Illustration of the drivers and phenotypic changes in cell senescence.** DNA damage is one of the main causes of cellular senescence. It leads to the activation of the signalling cascade known as DDR, which involves phosphorylation of the core histone protein variant H2AX to form γH2AX, leading to the recruitment of DDR effectors such as 53BP1, MDC1, and ATM. These proteins mediate downstream DDR signal transduction via CHK2 and CHK1, ultimately leading to p53 activation and subsequently, cell cycle arrest. Furthermore, telomere damage and oncogene activation can also result in DNA damage, leading to DDR activation and replicative arrest. Prolonged activation of DDR signalling leads to cell senescence. Aside from prolonged cell cycle arrest, that is mediated by the upregulation of the cell cycle inhibitors p16 and p21, senescence is also characterised by oxidative damage due to high levels of reactive oxygen species (ROS). Additionally, senescent cells experience a high resistance to apoptosis due to the upregulation of anti-apoptotic proteins from the BCL-2 family; metabolic changes like the accumulation of senescence-associated-β-galactosidase; chromatin changes termed senescence-associated heterochromatin foci; and lastly a distinct secretory phenotype known as SASP, which consists of

a plethora of growth factors, cytokines, proteases, chemokines, and other proteins secreted by senescent cells. Image was taken from (Di Micco *et al.*, 2021)

1.1.1 Senescence in ageing, pathology, and physiology

Senescent cells accumulate in tissues and organs with age and, as such, senescence is one of the hallmarks of ageing (López-Otín *et al.*, 2013). Their accumulation and ineffective removal can be attributed to their resistance to apoptosis, ability to induce senescence in neighbouring cells and the age-related decline in the ability of the immune system to successfully remove senescent cells (McHugh and Gil, 2018). Increased p16 activity, which is crucial for senescence, is observed in several organ systems including the islet of Langerhans in the pancreas (Helman *et al.*, 2016), fat tissue (Xu *et al.*, 2015) and the renal cortex (Krishnamurthy *et al.*, 2004; Melk *et al.*, 2004). The causal role of senescent cells in ageing is supported by intervention studies using selective ablation of senescent cells. Baker et al. was the first to show that selectively ablating senescent cells using an inducible suicide gene under the regulation of the p16 promoter in progeroid BubR1 mice, resulted in extended lifespan and healthspan (Baker *et al.*, 2011) and went on to confirm this in chronologically aged mice (Baker *et al.*, 2016). Interestingly, transferring a small number of senescent cells into mouse visceral fat impaired function and decreased lifespan in a dose-dependent manner (Xu *et al.*, 2018). However, these negative effects were rescued by senolytic compounds that can selectively clear senescent cells.

Senescent cells are involved in many age-related pathologies including Parkinson's disease (Chinta *et al.*, 2018), osteoarthritis (Jeon *et al.*, 2017), atherosclerosis (Childs *et al.*, 2016), fibrosis (Ritschka *et al.*, 2020), chronic wounds (Wang and Shi, 2020) and many others (Di Micco *et al.*, 2021). They contribute to ageing and age-related pathologies through several mechanisms. Ageing is accompanied by increased levels of circulating inflammatory factors, a phenomenon known as inflammageing (Franceschi *et al.*, 2000). Indeed, increased levels of inflammation represent a major risk factor for many age-related conditions including cancer, cardiovascular disease, neurodegeneration as well as frailty and early death (Di Micco *et al.*, 2021). Interestingly, genome wide association studies have revealed that the gene loci for key mediators of senescence growth arrest (including p16 and ARF) were highly associated with the risk of age-related diseases such as atherosclerosis, cancer, type 2 diabetes and glaucoma (Jeck, Siebold and

Sharpless, 2012), as well as the risk of developing frailty with increasing age (Melzer *et al.*, 2007). Many SASP components also contribute to age-related pathologies. For instance, increased levels of IL-6, IL-1 receptor antagonist and tumour necrosis factor (TNF) receptor 2 have been identified as predictors of chronic illness in the elderly (Fabbri *et al.*, 2015). Furthermore, ageing is also accompanied by an accumulation of mutations in the mitochondrial DNA, which lead to a dysregulation in several aspects of mitochondrial dynamics; Impaired mitochondrial dynamics is characterised by reduced mitochondrial membrane potential, as well as increased reactive oxygen species accumulation leading to increased oxidative stress (Stout and Birch-Machin, 2019). Indeed, impaired mitochondrial function plays a significant role in senescent cell induction through an accumulation of oxidation damage and stress (Figure 1.1) (Sreedhar, Aguilera-Aguirre and Singh, 2020; Hunt *et al.*, 2023). In addition to increased production of reactive oxygen species, this mitochondrial damage accumulation leads to increased inflammation, downregulation of collagen production and increased collagen degrading enzyme activity leading to increased overall ECM degradation, all of which are characteristic of chronically inflamed wounds (Berneburg and Krutmann, 2000; Oyewole *et al.*, 2014).

Given the role of cellular senescence in ageing and age-related pathologies, targeting senescent cells is a reasonable treatment avenue for many diseases (van Deursen, 2019). The detrimental effects of senescent cells can be targeted through compounds that can selectively eliminate senescent cells, known as senolytics, or through compounds that block the inflammatory secretome of senescent cells, known as senostatics (Kang, 2019). With that said, regulating senescence and its associated inflammatory response through senolytic drugs has been shown to attenuate or ameliorate many diseases, for example: cancer cell metastasis and cancer recurrence (Demaria *et al.*, 2017), liver fibrosis (Krizhanovsky *et al.*, 2008), idiopathic pulmonary fibrosis (Schafer *et al.*, 2017) and kidney fibrosis (Valentijn *et al.*, 2018).

However, senescent cells also play many beneficial roles, primarily in the context of embryonic development, tumour suppression, and wound healing and tissue repair. During mammalian embryonic development, senescent cells appear at multiple locations of the developing embryo, including the limbs, gut endoderm, and nervous system, as well as the placenta, where they mediate growth and tissue patterning (Storer *et al.*, 2013; Gal *et al.*, 2020). Intriguingly, senescent cells also accumulate in the embryonic kidney, where they signal immune cells through the SASP

to mediate kidney development by means of senescent cell phagocytosis by macrophages (Muñoz-Espín *et al.*, 2013). Additionally, mammalian senescent decidual cells (population of cells that appear and play important roles in the mammalian endometrium during pregnancy) produce several factors crucial for successful embryonic implantation (Rawlings *et al.*, 2021). Lastly, knocking down p21 in developing murine embryos leads to developmental abnormalities, highlighting the importance of senescent cells in embryonic development (Storer *et al.*, 2013).

The role of senescent cells in tumour suppression is primarily mediated by their cell cycle arrest feature, with the clearance of these senescent cells by the immune system through SASP-mediated surveillance crucial to limiting tumorigenesis (Xue *et al.*, 2007; Kang *et al.*, 2011; Ruscetti *et al.*, 2018). Contrastingly, through SASP, chronic senescence can lead to enhanced cancer development and metastasis, resistance to treatment and increased recurrence risk (Demaria *et al.*, 2017; Mario Gonzalez-Meljem *et al.*, 2017; Lau *et al.*, 2019). Furthermore, senescence is also involved in tissue repair and wound healing and is therefore associated with pathologies such as fibrosis and chronic wounds (Demaria *et al.*, 2014; Ritschka *et al.*, 2020; Wang and Shi, 2020). This will be reviewed and discussed further in Chapter 2 and Chapter 3.

Senescence during the early stages of life is involved in tissue morphogenesis and development, before shifting to an anti-cancer mechanism and tissue repair regulation (Demaria *et al.*, 2014; Lee and Schmitt, 2019). Although senescent cells play a role in embryogenesis, tissue repair and immunosurveillance mechanisms, their persistent activity leads to chronic inflammation, age-related pathologies, and cancer (De-Carvalho, Jacinto and Saúde, 2021).

1.2 A computational systems biology approach

As discussed, senescence is an inherently complex process that happens progressively, involving multiple domains ranging from intracellular molecular reactions to the tissue level, impacting entire organ systems. Senescence is strongly linked to the ageing process and has been established as one of the hallmarks of ageing (López-Otín *et al.*, 2013). Senescence phenotypes are associated with regulatory signalling changes including the DDR, presence of cyclin-dependent kinase inhibitors and cell cycle arrest, a secretory phenotype, resistance to apoptosis, metabolic changes, endoplasmic reticulum stress as well as other morphological changes, all features of senescence highlighted previously by others (Hernandez-Segura, Nehme and Demaria,

2018). The heterogeneity and dynamic nature of the senescence phenotype, whereby it differs between different cell types, physiological and pathological processes, as well as on the temporal scale, makes it highly complex. Therefore, a full understanding necessitates a hybrid reductionist-integrative strategy, addressing the multiple levels of complexity individually, breaking them down into simpler elements, in order to assess their individual contributions as isolated systems. This would then be followed by investigating the interactions and influence each of these elements have on one another and the system as a whole. This latter approach is the basis of systems biology: it adopts principles and methodologies from computer science, physics, engineering and mathematics together with experimental biology to gain a mechanistic understanding of the biological system in question (Kirkwood, 2011).

The methodology behind computational systems biology primarily includes data mining with bioinformatic analysis and/or using computational and mathematical models for a simulation-based analysis. The former is used to gather knowledge from large biological datasets, resulting in the formulation of a hypothesis, whereas simulation-based analysis allows the testing of a hypothesis using *in silico* models to make predictions, which can aid the design of *in vivo* and *in vitro* experiments (Kitano, 2002). Several approaches are used to model biological systems. Ordinary differential equation (ODE) models are perhaps the most commonly used in systems biology (Glont *et al.*, 2018). In the context of senescence research, Dalle Pezze et al. developed a comprehensive ODE model of cellular senescence that combined existing models of the DDR, energy signalling and mitochondrial function (Dalle Pezze *et al.*, 2014). The model was robust as it was calibrated with biochemical data and was tested with a series of targeted perturbations. Insights from the model led to further experiments, which revealed that mitochondrial fission was dysregulated in cellular senescence.

However, several other multi-scale frameworks have been used as well, such as agent-based models (ABM), which will be discussed further in Chapter 2. While ODE models can give us useful insights about intracellular and intercellular processes, they do not provide spatial configuration, which is crucial to understanding tissue-level behaviour. To summarise, applying a systems biology approach brings together existing data from disparate and individual experiments to provide the details of the underlying complexity without which we could never truly understand

the roles of senescent cells in various contexts, and the mechanisms behind the development of senescence.

1.2.1 Multi-scale modelling in ageing and senescence biology

Ageing is a systemic phenomenon resulting from complex interactions between multiple functional and organisational levels, including interactions between cells, between the cell and its microenvironment, the biomechanical activities of the cell and the dynamics of tissue-level organisation. These processes operate across several different spatiotemporal domains, which makes ageing a multi-scale problem comprising of age-related defects at the cellular level, eventually resulting in whole body frailty and disease (Kirkwood, 2005).

One systems biology approach to addressing a multi-scale system is through the construction of cell-based models. This framework involves representing a system, such as a tissue of interest as an aggregate of individual agents, each with its own set of distinct characteristics and mechanisms. These individual agents can represent cells or subcellular compartments. This type of framework allows us to take an integrative approach to understanding a system by analysing the spatiotemporal dynamics of individual elements and how they collectively result in a particular phenotype. Furthermore, multi-cell models have the capacity to combine different model types of varying resolution, for example an ODE model, to dictate individual cell behaviour through intracellular biochemical activity, may be coupled with an ABM to ascertain tissue level behaviour. In keeping with this, Guimera et al. (Guimera *et al.*, 2017) developed a multi-cell senescence model coupled with an intracellular ODE model of irradiation-induced senescence from (Dalle Pezze *et al.*, 2014). The model showed that just 10% of irradiation-induced senescent cells was sufficient to drive a whole tissue into senescence, therefore highlighting the importance of the bystander effect (Acosta *et al.*, 2013a; da Silva *et al.*, 2019). Additionally, further model simulations showed that senescent cell clearance by immune cells largely determines progression of the model towards a steady state, suggesting that targeted immunotherapy against senescent cells would be a more effective therapeutic approach rather than targeting SASP (Guimera *et al.*, 2017).

Other approaches to multiscale modelling include whole-body modelling, which are particularly useful to study whole-body metabolism as it integrates molecular and physiological data. Mc

Auley et al. developed a whole-body mathematical model of cholesterol metabolism to investigate the age-related rise of Low-Density Lipoprotein Cholesterol (LDL-C) (Mc Auley *et al.*, 2012). The model integrates aspects of cholesterol metabolism from different resolutions, from the molecular to the physiological level, and was used to explore the age-related changes to the rate of clearance of LDL-C by the liver from the plasma, and the rate of cholesterol absorption by the intestine. Interestingly, the model showed that changes to LDL-C levels with age are more significantly impacted by changes to the rate of clearance of LDL-C from the circulation than by changes to cholesterol absorption.

Although multiscale modelling in ageing is still in its infancy, some notable work has been done to explore the evolution of ageing. Nelson and Masel developed a mathematical multi-cell model of somatic selection within an organism that elucidated the imperfectness of somatic conflict suppression within multi-level biological systems (Nelson and Masel, 2017). This is contrary to the general idea that in multicellular organisms, higher level selection, such as at the individual level, supersedes selection at lower levels, such as the cell level, in order to protect the fitness of the organism (Szathmáry and Smith, 1995). The study concluded that the resulting intercellular somatic competition might make ageing inevitable in multi-cellular organisms. Goldsby et al. developed a computational model of experimental evolution consisting of 'digital' multicellular organisms to study the mutagenic effects of metabolism that could promote the evolution of reproductive division of labour (Goldsby *et al.*, 2014). By analysing the lineages of the simulated organisms that were able to successfully differentiate, they demonstrated that organisms could evolve to harbour the potential for cell differentiation, resulting in reproductive or somatic maintenance functions, and that somatic phenotypes could be associated with ageing, while the reproductive cells remain protected. Similarly, Radzvilavicius et al. developed an evolutionary ABM showing that mitochondrial fitness drives the evolution of the germline, and that gamete sequestration reduces mutational load since copying errors in gametes is reduced. They also showed that greater organismal complexity and higher numbers of mitochondria does not contribute to germline sequestration (Radzvilavicius *et al.*, 2016). More recently, Pen and Flatt developed a simple cell-based model to investigate the role of parent-child asymmetry in the evolution of division of labour and cellular senescence. Their model showed that asymmetry and the division of labour was not required for the evolution of senescence, since symmetrically

reproducing cells with equally partitioned damage were still able to develop senescence (Pen and Flatt, 2021). Additionally, Martin et al. used a minimal 2D stochastic model to study the spread of senescent cells, where they reported that juxtacrine-mediated secondary senescence can keep the spread of senescent cells under control, compared to paracrine signalling, and that this effect was positively correlated with the delay in the induction of SASP (Martin, Schumacher and Chandra, 2023). This and the preceding section were published as part of a book chapter (Chandrasegaran *et al.*, 2023).

1.2.2 Multi-omics approaches in ageing and senescence biology

Ageing and cell senescence affect complex molecular pathways involving components from different biological layers that interact with one another. Each of these biological layers pertains to an omic data type such as genomics, transcriptomics, proteomics, and metabolomics, with databases such as the Aging Atlas providing access to curated multi-omic datasets including transcriptomics, single-cell transcriptomics, epigenomics, proteomics, and pharmacogenomics (Liu *et al.*, 2021).

Multi-omic datasets have been used in a number of ways in the realm of ageing biology and senescence. Omic datasets have most widely been used in the development of chronological age predictors or ageing clocks through machine learning (ML) to identify ageing biomarkers. Ageing clocks are ML models that learn patterns in molecular features from a large number of samples which can then be used to estimate the age of the sample source. This estimated age has been hypothesised to measure an individual's biological age, with the difference between chronological and estimated biological age reflecting rate of ageing. Several omic data types have been used in the development of ageing clocks, including genomic, DNA methylation, transcriptomic, proteomic and metabolomic (Rutledge, Oh and Wyss-Coray, 2022; Mavromatis *et al.*, 2023). In the realm of DNA methylation, Hovarth et al. investigated CpG methylation across 8000 samples from 51 human tissues and cell lines to discover widely conserved methylation changes that occur with age (Horvath, 2013). Ageing clocks based on transcriptomic data have higher interpretability and are easier to experimentally validate as they link more directly to the genes involved in ageing. In keeping with this, Meyer et al. developed a transcriptomic ageing clock with flexible performance across multiple ageing treatment conditions, including irradiation, caloric restriction and daf2 mutants, in *C elegans* (Meyer and Schumacher, 2021).

With the loss of proteostasis being a hallmark of ageing and proteins providing direct mechanistic links to processes involved in ageing, proteomics is a particularly good basis for the development of ageing clocks. Lehallier et al. developed a highly predictive plasma protein-based ageing clock that was able to demonstrate links between the proteomic age gap and many ageing characteristics including cognitive and motor function decline (Lehallier *et al.*, 2019). Many studies have used mass spectrometry and nuclear magnetic resonance (NMR) methods to identify plasma metabolites and their interactions with the ageing process. As part of an NMR biobank study, Akker et al. developed a metabolic clock from 56 plasma metabolites and investigated the links between the metabolomic age-gap, cardiovascular phenotypes, and mortality (Van Den Akker *et al.*, 2020).

Making comparisons between different omics ageing clocks is challenging as they are all unique. However, Jansen et al. developed telomere length, epigenetic, transcriptomic, proteomic, and metabolomic clocks using data from one cohort with 3000 subjects and demonstrated mild correlations between epigenetic and transcriptomic clock age gaps, and between proteomic and metabolomic clock age gaps, along with no correlations between epigenetic age gaps and proteomic and metabolic age gaps (Jansen *et al.*, 2021). This is interesting as it highlights the different ageing signals being captured by different technologies at different resolutions. These valuable molecular insights from multi-omic studies can be taken a step further by being used to inform signalling networks involved in ageing and senescence.

1.3 Thesis outline and aims

The general aim of this thesis was to use computational approaches to investigate cellular senescence. More specifically, this thesis was aimed at using computational systems biology methods to investigate cell senescence in physiology and disease at the tissue level, as well as the progression of cellular senescence at an intracellular mechanism level. To this end, a multi-scale computational model of wound healing that included the dynamics of senescent cells was developed, which will be discussed in Chapter 2. The wound healing process was chosen since senescent cells not only play an important role in the healthy tissue repair process but are also associated with debilitating conditions as a result of dysregulated repair. This provided a context to investigate the role of senescent cells in a physiological process (wound healing), along with its pathological counterparts (fibrosis and chronic wounds). With that, senescent cell dynamics

within fibrosis and chronic wounds was investigated using the model developed, which will be discussed in Chapter 3. Lastly, an integrated multi-omic analysis was performed to gain molecular insights into the progression of cellular senescence, which will be detailed in Chapter 4. Lastly, Chapter 5 provides a general discussion and summary of the work presented in this thesis, along with some key limitations and future work.

Chapter 2. Computational modelling of senescent cell dynamics in physiological wound healing

2.1 Background

As discussed in the introduction chapter, cellular senescence is a complex stress response that is accompanied by an irreversible growth arrest, phenotypic, metabolic, and secretory changes including the production of several cytokines, growth factors and MMPs, collectively known as the SASP. Senescent cells accumulate with age and are thought to drive age-related pathology; however, they also play important physiological roles in cancer suppression, embryogenesis and wound healing (Muñoz-Espín and Serrano, 2014).

2.1.1 Wound healing

Wound healing is a crucial process involving several cell types, their interactions, mechanical effects, and chemical components. It is tightly regulated and generally consists of three individual but overlapping phases that occur sequentially: 1. haemostasis and inflammation, 2. proliferation and 3. remodelling (Figure 2.1). These stages represent the principles of tissue repair for most tissue injuries (Singer and Clark, 1999).

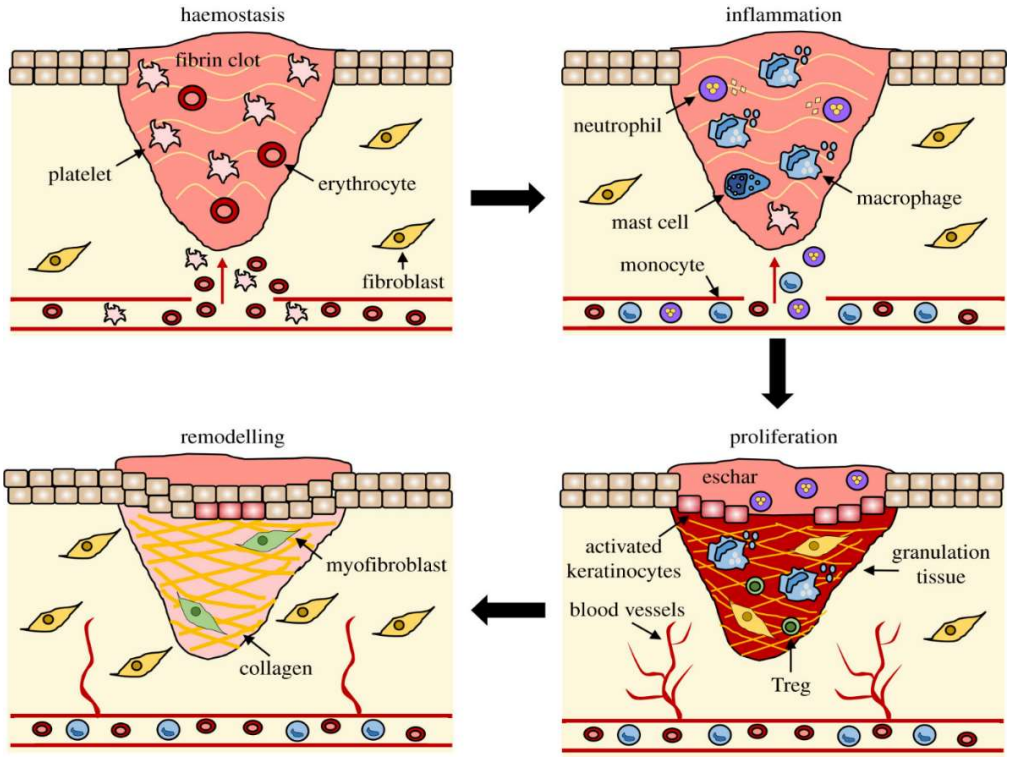

Figure 2.1 **Phases of wound healing.** During the first phase of wound healing, haemostasis, an insoluble fibrin rich clot is formed, along with platelet aggregation at the wound site in response to the coagulation cascade activation. This fibrin rich platelet clot is crucial in preventing further blood loss. This is followed by the second phase, inflammation. During this phase, neutrophils infiltrate the wound site in response to activation of the complement cascade, cytokines released by platelets during haemostasis (e.g., platelet-derived growth factor (PDGF), TGF-β, epidermal growth factor (EGF) and insulin-like growth factor), and histamine from mast cells. Blood monocytes arrive at the wound site later where they differentiate into macrophages. Neutrophils and macrophages play crucial roles in removing wound debris and preventing infections. The third phase is proliferation, where re-epithelialisation takes place through keratinocyte migration and proliferation to close the epidermal wound gap. During this phase, new blood vessels are also formed, a process known an angiogenesis. Additionally, fibroblasts replace the provisional fibrin clot with Type III collagen rich granulation tissue. Alternatively activated pro-healing M2 macrophages are also crucial to this phase. Towards the end of the proliferative phase, fibroblasts begin differentiating into myofibroblasts. The last phase of healing is remodelling, which is primarily mediated by fibroblasts, myofibroblasts and macrophages. During this phase, the granulation ECM is broken down and replaced by Type I collagen. Myofibroblasts also contract the wound, resulting in wound closure. Image was taken from (Wilkinson and Hardman, 2020).

2.1.1.1 Haemostasis and inflammation phase

Immediately following a tissue injury, lesioned blood vessels contract and blood coagulation takes place to prevent further blood loss and maintain tissue integrity. Coagulation is primarily

mediated by platelets, which also secrete cytokines and chemokines to attract immune cells including macrophages and neutrophils to the wound site. In addition to the chemokine attractants, immune cells can also be captured in the insoluble clot composed of fibrin and fibronectin (FN) that is formed during the coagulation process (Golebiewska and Poole, 2015; Rodrigues *et al.*, 2019). The fibrin clot further serves as a barrier against pathogen invasion as well as a temporary matrix for cell migration to the wound site.

The influx of immune cells results in the production of pro-inflammatory mediators that stimulate vasodilation (i.e., widening of blood vessels), further promoting the adhesion and influx of immune cells, such as neutrophils, monocytes, T cells and mast cells. Neutrophils are recruited to the wound site in response to damage-associated molecular patterns (released by damaged and necrotic cells), platelet degranulation and activation of the complement system (De Oliveira, Rosowski and Huttenlocher, 2016). At the wound site, neutrophils produce their own pro-inflammatory secretome mediated by the activation of inflammatory signalling pathways including NF-κB (Kolaczkowska and Kubes, 2013). Additionally, neutrophils help to remove wound debris through phagocytosis of necrotic tissue and pathogens (Kolaczkowska and Kubes, 2013). In the absence of an infection, wound neutrophil levels decline soon after the beginning of the inflammatory phase through apoptosis, necrosis, phagocytosis, or by returning to circulation (Kim *et al.*, 2008).

Around this time, circulating monocytes recruited to the wound site differentiate into macrophages, which are one of the master regulators of tissue repair. Macrophages engulf wound debris and pathogens within the wound through phagocytosis. Importantly, they also respond to various external stimuli and signals with specific transcriptional pathways that can result in a wide range of macrophage phenotypes (Ginhoux *et al.*, 2015). Macrophage activation states should be viewed as a spectrum dependent on tissue conditions and cell milieu (Xue *et al.*, 2014) which confers them functional versatility within the wound microenvironment (Das *et al.*, 2015). Nevertheless, for the sake of simplicity and for the purpose of this work, the more canonical assumption that wound macrophages shift between classically activated pro-inflammatory (M1) and alternatively activated anti-inflammatory (M2) phenotypes will be considered hereafter.

Pro-inflammatory stimuli, including interferon-gamma (IFN-γ), TNF-α and bacterial endotoxins such as lipopolysaccharide, skew macrophages towards a classically activated M1 phenotype, which promotes inflammation through the production of ROS, inflammatory cytokines, such as IL-1, IL-6 and TNF-α, and growth factors (Ginhoux *et al.*, 2015). They also produce MMP-2 and MMP-9 which contribute to immune cell infiltration by breaking down the matrix (Murray and Wynn, 2011). However, as the inflammatory phase progresses, macrophages begin to shift to a "pro-healing" anti-inflammatory M2 phenotype in response to changes in the cytokine profile in the wound site (Krzyszczyk *et al.*, 2018). Depending on the stimuli, M2 macrophages exhibit distinct functional and phenotypic properties, and this plasticity is crucial for the wound healing process. They promote healing through the production of growth factors that are crucial for cell proliferation, ECM production and angiogenesis, such as PDGF, IGF-1, VEGF and TGF-β. Additionally, they produce anti-inflammatory cytokines, such as IL-4, IL-13 or IL-10, and TIMP to counteract MMPs (Murray and Wynn, 2011).

The importance of macrophages in wound healing is evident from conditional knockdown studies in mouse models where macrophage depletion results in impaired wound healing due to delayed re-epithelialisation, reduced collagen deposition, impaired angiogenesis, increased inflammation, and decreased cell proliferation (Mirza, DiPietro and Koh, 2009). Furthermore, macrophage depletion during the early phases of healing (i.e., the inflammatory phase) diminishes granulation tissue formation, angiogenesis, and epithelialisation, whilst knockdown during the mid-proliferative phase results in impaired ECM production and scar formation, leading to haemorrhage in the wound tissue (Lucas *et al.*, 2010). Towards the end of the inflammatory phase, apoptotic immune cells such as neutrophils are cleared from the wound site through macrophage phagocytosis, with this process also contributing to macrophages becoming M2 polarised (Filardy *et al.*, 2010; Krzyszczyk *et al.*, 2018).

2.1.1.2 Proliferation phase

The proliferative phase begins with the recruitment and activation of fibroblasts, keratinocytes, macrophages and endothelial cells to orchestrate tissue re-growth. Keratinocyte activation at the wound edge is induced by mechanical and electrical changes, and exposure to growth factors and cytokines, leading to a migratory and proliferative phenotype. As a result, keratinocytes form

pseudopod-like projections to migrate laterally across the wound where they proliferate leading to re-epithelisation (Li, Chen and Kirsner, 2007).

Fibroblasts are the primary source of Type III collagen-rich granulation ECM, which replaces the fibrin/FN clot that was acting as a provisional matrix. They respond to several stimuli including cytokines, such as PDGF and TGF-β derived from platelets, macrophages, and endothelial cells, as well as mechanical cues from the wound microenvironment (D'Urso and Kurniawan, 2020). Depending on the stimulus, fibroblast activation results in ECM production, proliferation, or differentiation into myofibroblasts. PDGF for instance is a primary mediator of fibroblast migration, proliferation, and ECM production within the wound (Beer, Longaker and Werner, 1997; Juhl et al., 2020).

Myofibroblasts are key players in ECM synthesis and remodelling, as well as wound contraction. They are characterised by highly contractile microfilament bundles known as stress fibres, often containing the actin isoform α-smooth muscle actin (αSMA) (Skalli *et al.*, 1986). Moreover, myofibroblasts have highly developed focal adhesions that allow them to transmit cytoskeletal force onto the ECM and are also able to produce large amounts of collagen namely, Types I, III, IV, V and VI (B. Hinz, 2016).

The differentiation of fibroblasts into myofibroblasts requires a cytokine stimulus, such as PDGF or TGF-β, coupled with changes in the mechanical microenvironment (Tomasek *et al.*, 2002). TGF-β, which induces αSMA expression in fibroblasts through transcriptional regulation mediated by SMAD3, is known to be a crucial factor in myofibroblast differentiation (Hu, Wu and Phan, 2003). However, SMAD3 knockout (KO) mice presented increased αSMA expression and an increased number of αSMA-positive cells in experimentally induced liver (Schnabl *et al.*, 2001) and cardiac (Dobaczewski *et al.*, 2010) fibrosis respectively. Furthermore, adenovirus-mediated inhibition of SMAD3 in hepatic stellate cells (HSC) attenuated αSMA production compared to wildtype (WT) controls at day 1 but by day 7, expression levels were similar (Uemura *et al.*, 2005). This may reflect that HSC cells are able to adjust by compensating with alternative non-canonical pathways involved in the induction of myofibroblast differentiation. These other important signalling pathways involve MAPK (including ERK, p38 MAPK and JNK) (Dolivo, Larson and Dominko, 2019),

Wnt/B-catenin (Hamburg-Shields *et al.*, 2015), mTOR (Woodcock *et al.*, 2019), PI3K/AKT (Conte *et al.*, 2011), JAK-STAT (Liu *et al.*, 2013), EGFR (Midgley *et al.*, 2013) and Rho/Rock (Ji *et al.*, 2014).

PDGF also plays a crucial role in the expansion of myofibroblasts by stimulating their differentiation, proliferation, and migration (Juhl *et al.*, 2020). Myofibroblasts themselves express PDGF in an autocrine manner forming a positive feedback loop (Trojanowska, 2008). The mechanism by which PDGF induces myofibroblast differentiation is not fully understood. However, inhibition of the PDGF pathway has been shown to be a potent anti-fibrotic strategy, with blocking of the PDGF receptors inhibiting myofibroblast differentiation in experimentally induced lung (Atanelishvili *et al.*, 2019) and kidney (Lebleu and Kalluri, 2011) fibrosis. Furthermore, inhibition of PDGF activity prevents myofibroblast differentiation in mouse corneal cells (Singh *et al.*, 2011).

As for the mechanical effectors on myofibroblast differentiation, mechanosensitive TFs, including MRTF/MLK1 and SRF, play key roles. They positively regulate myofibroblast gene expression, such as that of cytoskeletal stress fibre proteins, under the influence of mechanical stress, since the nuclear translocation of these TFs is dependent on the state of actin polymerisation in the cytoskeleton (X. Huang *et al.*, 2012). Following nuclear localisation, MRTF and SRF bind to CArG boxes in the αSMA promoter region, directly influencing stress fibre formation in myofibroblasts, which is one of their most important characteristics (Varney *et al.*, 2016). The mechanosensitive YAP/TAZ TFs also positively regulate myofibroblast differentiation by providing a positive feedback link between mechanical cues and transcriptional activity (Dupont et al., 2011; Liu et al., 2015; Muppala et al., 2019; Tschumperlin et al., 2018).

During the proliferative phase, M2-polarised macrophages continue to play an important role in angiogenesis and the production of growth factors required for adequate fibroblast and myofibroblast function such as PDGF. They also produce MMPs, initially aiding in the breakdown of the fibrin-rich clot, and subsequently helping to break down the granulation tissue towards the end of the proliferative phase, to be replaced by ECM composed of Type I collagen (Krzyszczyk *et al.*, 2018).

2.1.1.3 Remodelling phase

In the final stage of the healing process, Type III collagen-rich granulation tissue is replaced with the more tensile Type I collagen-rich scar tissue by the fibrolytic action of macrophage-derived MMPs and fibrogenic action of myofibroblasts. Fibrolytic factors are those that hinder and attenuate ECM production/deposition, whereas fibrogenic factors are those that enhance and promote ECM production/deposition. It has been suggested that MMP production by macrophages during this phase could be the result of a shift towards a pro-inflammatory phenotype induced by the cytokine milieu of the wound microenvironment at this point (Vannella and Wynn, 2017). Interestingly, MMP production can also be stimulated by macrophage contact with matrix proteins, which has been shown to have a significant augmenting effect. For instance, MMP-1 production by macrophages is increased following contact with Type I and III collagens (Shapiro, Kobayashi and Ley, 1993).

The replacement with Type I collagen directly enhances the tensile strength of the scar tissue (Witte and Barbul, 1997). Collagen is the most abundant protein in the ECM and in the human body. There are 28 collagen subtypes with distinct features with Type I collagen being the most abundant protein in all vertebrates. Collagens play a role in providing structure and tensile strength to tissues. They also regulate chemotaxis, migration, tissue development and cell adhesion (Kadler, Hill and Canty-Laird, 2008).

Myofibroblasts also produce TIMPs to counteract the MMP production by macrophages and exert contractile forces on the surrounding ECM to remodel collagen (Boris Hinz, 2016). Despite the resulting mature matrix organisation and tensile strength, the scar tissue never returns to its pre-damaged state. This is because collagen fibrils in scar tissue are arranged in a parallel pattern as opposed to normal tissue where a basket weave orientation is prevalent (Witte and Barbul, 1997). Generally, a successful wound remodelling phase requires a balance between ECM production and breakdown.

Towards the end of the remodelling phase, fibroblasts and myofibroblasts undergo apoptosis (Desmoulière *et al.*, 1997), exit the wound site or in the case of myofibroblasts, revert to a fibroblast phenotype (Hinz and Lagares, 2019). The two major apoptosis pathways comprise the extrinsic pathway via the so-called cell surface “death receptors”, and the mitochondria-mediated

intrinsic pathway, with both resulting in the activation of apoptotic caspases. In the wound, both pathways are involved in the apoptosis of myofibroblasts. For instance, the pro-apoptotic cytokine FGF1 induces extrinsic apoptosis mediated by caspase-3 in scar tissue dermal myofibroblasts, but not in normal fibroblasts (Ishiguro *et al.*, 2009).

Apoptosis through the intrinsic pathway is dependent on mitochondrial priming. This term refers to the relative proximity of a cell to mitochondrial outer membrane permeabilisation when the complex interactions between pro- and anti-apoptotic BCL-2 proteins become imbalanced; a cell will undergo apoptosis if it passes the mitochondrial priming threshold (King *et al.*, 2022). Interestingly, in the case of myofibroblasts the trigger for such imbalance can be the release of mechanical tension: in rat studies the release of tension in splinted wounds promotes myofibroblast apoptosis and wound closure (Hinz *et al.*, 2001). A possible mechanism is the disruption of integrin and focal adhesion kinase signalling, resulting in apoptosis induced by the accumulation of pro-apoptotic BCL-2 proteins, a process known as anoikis (Horowitz *et al.*, 2007; Kulkarni *et al.*, 2011).

Macrophages and other immune cells phagocytose apoptotic and senescent cells, after which they undergo apoptosis themselves or return to circulation, marking the end of the wound healing process (Vannella and Wynn, 2017).

2.1.2 The role of senescent cells in physiological wound healing

Senescent cells transiently appear during the mid to late stages of tissue repair and are removed by the immune system during the remodelling phase. Several SASP factors, including PDGF and MMPs, have been shown to play important roles in maintaining tissue homeostasis during the repair process, when their effect is temporary (Muñoz-Espín and Serrano, 2014).

Induction of senescent cells has been shown to mitigate fibrosis during tissue repair following damage in the liver (Krizhanovsky *et al.*, 2008), skin (Jun and Lau, 2010), heart (Meyer *et al.*, 2016) and kidney (Wolstein *et al.*, 2010a). For instance, Krizhanovsky et al. reported that the attenuated fibrotic response following experimentally induced liver damage was the result of senescence-mediated fibrolytic enzyme activity and SASP-mediated recruitment of immune cells, which regulated the removal of cells involved in the fibrogenic processes (Krizhanovsky *et al.*, 2008). Similarly, Meyer et al. confirmed that senescence mitigated fibrosis in a cardiac injury model,

whereas genetic ablation of p16 and p53 aggravated the fibrotic response and impaired cardiac function (Meyer *et al.*, 2016). Furthermore, they reported that fibrosis was also significantly decreased by ectopic CCN1 expression which increased the number of senescent cells. According to Jun et al., the matricellular protein CCN1 induces senescence by binding to α6β1 integrin, which triggers the DDR through oxidative stress via NOX1, activating the p16 and p53 pathways. Moreover, they reported that mice with defective CCN1 developed excessive fibrosis following cutaneous injury (Jun and Lau, 2010). The same team also showed that another protein belonging to the CCN family, CCN2, was able to reduce fibrosis in cutaneous mouse wounds by inducing senescence through a similar mechanism to CCN1 (Jun and Lau, 2017). In the kidney, Wolstein et al. demonstrated that p16 KO mice subjected to experimentally induced kidney injury showed an exacerbated fibrotic response compared to WT mice (Wolstein *et al.*, 2010a). All these studies show the beneficial effects of senescent cells in mitigating fibrotic responses.

Transient senescence activity during cutaneous wound repair was first observed by Jun et al., followed by Demaria et al. in murine wound models where ablation of p16 and p21-expressing cells resulted in impaired ECM production and rate of wound closure (Jun and Lau, 2010; Demaria *et al.*, 2014). Interestingly however, the wounds became excessively fibrotic later in the repair process. In both studies, transient senescence was observed in cells with myofibroblast-like characteristics and was accompanied by a PDGF-rich SASP (Jun and Lau, 2010; Demaria *et al.*, 2014). This could imply that senescent cells participate in the fibrogenic as well as fibrolytic wound processes. Additionally, Hiebert et al. also demonstrated the significance of transient senescence in wound healing in a study reporting increased fibroblast senescence due to NRF2 overexpression, which resulted in enhanced re-epithelialisation and ECM deposition (Hiebert *et al.*, 2018). Furthermore, another study reported an upregulation of stemness markers and increased skin regenerative capacity following transient SASP exposure in keratinocytes; contrarily, prolonged senescence led to impaired healing (Ritschka *et al.*, 2017). The key studies discussed here clearly demonstrate that transient, rather than persistent, senescence is crucial for effective and successful tissue repair.

In summary, senescent cells produce SASP containing PDGF that is beneficial for wound healing, following which they drive their own clearance through immune surveillance. This suggests a temporally regulated shift from a pro-healing phenotype to an inflammatory phenotype that is

required to recruit immune cells or induce inflammatory polarisation in macrophages, and participate in ECM remodelling (Lujambio *et al.*, 2013; Ito, Hoare and Narita, 2017). Indeed, studies have suggested NOTCH-mediated temporal regulation of SASP composition and senescence-associated chromatin structure with at least two distinct SASP types, including a NOTCH-induced or TGF-β dominant SASP, and a RAS-induced or inflammatory SASP (Figure 2.2) (Hoare *et al.*, 2016; Parry *et al.*, 2018). Using pharmacologic and genetic methods to manipulate the Notch pathway in the context of primary Ras-induced senescence (RIS), Hoare et al. showed that NOTCH mediates a TGF-β rich SASP that is fibrogenic in nature. This was reported to be achieved through the repression of the TF C/EBPβ which along with NF-κB is responsible for the transcriptional regulation of SASP factors. This fibrogenic SASP, rich in growth factors such as PDGF and collagens, was reportedly accompanied by the ability to laterally induce non-autonomous senescence in neighbouring cells through cell-cell contact, i.e., juxtacrine-mediated secondary senescence. This juxtacrine mechanism to induce senescence was found to be mediated directly by NOTCH and its ligand JAG. Contrastingly, as senescence progressed, NOTCH activity was downregulated, renewing the ability of C/EBPβ to transcriptionally regulate the production of a pro-inflammatory fibrolytic SASP consisting of inflammatory cytokines and MMPs, along with its ability to induce secondary senescence in neighbouring cells in a paracrine manner (Acosta *et al.*, 2013b; Hoare *et al.*, 2016; Rattanavirotkul, Kirschner and Chandra, 2021). Furthermore, a study by Teo et al. using single-cell RNA sequencing to investigate primary OIS and secondary senescence cell populations, reported that secondary senescence was not only driven by paracrine mechanisms but also significantly through NOTCH-mediated juxtacrine mechanisms following which they produced SASP rich in collagen and growth factors (Teo *et al.*, 2019). Notably, a study by Shi et al. showed that Wnt and Notch pathway activation is required for healthy wound healing, where they mediate epidermal stem cell proliferation, differentiation and migration of keratinocytes, and follicle regeneration (Shi *et al.*, 2015). The crucial role of the Notch pathway potentially highlights the prevalence of juxtacrine secondary senescence, and thereby the fibrogenic SASP, in the healthy healing process.

It is evident from the studies discussed above that the dynamic nature of SASP as well as the accompanying mechanisms for secondary senescence makes senescent cell activity complementary and essential to the wound healing process. A possible explanation for this is that

fibrogenic SASP could initially enhance the proliferative phase by inducing myofibroblast differentiation and collagen deposition, followed by a shift towards a pro-inflammatory fibrolytic SASP which helps breakdown excess ECM and triggers immune surveillance to remove effector cells, concluding the healing process Figure 2.2.

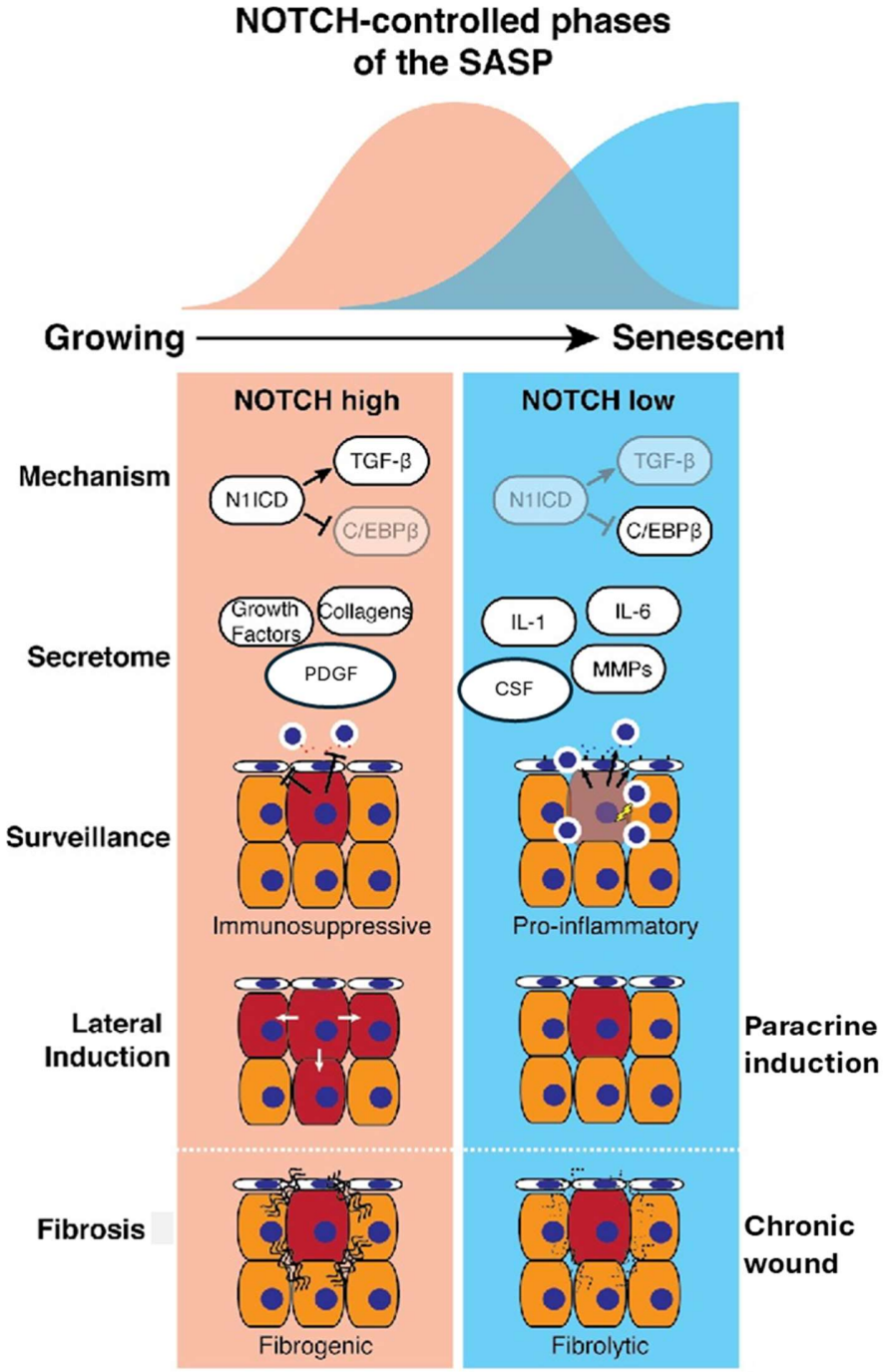

Figure 2.2 **SASP regulation by NOTCH signalling.** NOTCH mediates a TGF-β rich SASP that is fibrogenic in nature, through the repression of the TF C/EBPβ which along with NF-κB is

responsible for the transcriptional regulation of SASP factors. The duration of this fibrogenic SASP is approximately three days and it is rich in growth factors such as PDGF and collagens, is accompanied by the ability to laterally induce non-autonomous senescence in neighbouring cells through cell-cell contact, i.e., juxtacrine-mediated secondary senescence. As senescence progressed, NOTCH activity was downregulated, renewing the ability of C/EBPβ to transcriptionally regulate the production of a pro-inflammatory fibrolytic SASP consisting of inflammatory cytokines and MMPs, along with its ability to induce secondary senescence in neighbouring cells in a paracrine manner. Fibrogenic SASP could play an important role in promoting fibrosis, whereas fibrolytic SASP could promote chronic inflammation in non-healing wounds. Image was taken and modified from (Hoare and Narita, 2017)

To summarise, the functional, phenotypic, and biochemical heterogeneity across the senescence process, due to the dynamic regulation of SASP, highlights the possibility of a crucial role for its spatiotemporal shifts in the wound healing process. Studying this role is important to better understand heterogeneity in healing and repair outcomes, as well as treatment avenues, especially with the increasing use of senolytic compounds. Fully understanding the role of senescent cells in tissue repair and associated disorders first requires individually addressing the multiple levels of complexity, pertaining to the various cell behaviours. This should then be followed by investigating the interactions and influence each of these elements have on one another, and the whole system. Therefore, a systems biology approach was adopted whereby a multi-scale tissue-level cellular-potts model (CPM) of wound healing was developed to investigate the dynamics of senescent cells in wound healing, including key cell types, factors, and mechanisms. The CPM framework is described in more detail in section 2.1.4.

2.1.3 Overview of ABMs

ABMs are discrete models where the basic unit is the cell, with the state of each cell characterised by a state vector that holds information on the cell's position, velocity, and biological state. ABM frameworks are useful to model multicellular and tissue-level systems, which has led to the development of several approaches including fixed-lattice methods such as cellular automata and the CPM, as well as the lattice-free vertex models and centre-based models (Pleyer and Fleck, 2023).

In a cellular automata model, each cell is represented by an individual site or pixel in a fixed lattice, therefore lacking in any shape characteristics. Cell dynamics such as motility, growth, death, and

differentiation evolve simultaneously for all lattice sites with a fixed time step or event-driven approach. The new cell state is determined by rules, as well as the previous state of the system (Ermentrout and Edelstein-Keshet, 1993).

In vertex models, the cell membrane is represented as a connection of nodes/vertices in a lattice-free space, where cell movement is controlled by shifts in the nodes. Cell interfaces and volumes are defined by the positions of the nodes that form an enclosed space (Alt, Ganguly and Salbreux, 2017). The nodes can experience viscoelastic or spring-like forces, or other constraints that can be described through potential energy equations (Honda, Tanemura and Nagai, 2004). Therefore, the model evolves by minimising these energy or cost functions, or by moving the vertices towards the direction of the total force (Fletcher *et al.*, 2013).

Centre-based models are another lattice-free approach whereby a cell is represented as a point in space. The cell shape dynamics are determined by the surrounding points that are closer to the centre of the cell than that of other cells, a method known as the Voronoi approach. The cell's compressibility limit is also defined by a radius around the centre (Honda, 1978).

In contrast to lattice-free approaches, lattice-based approaches, like the CPM which is also known as the Glazier-Graner-Hogeweg model, consist of generalised cells represented by collections of pixels on a simulation lattice. Because of this, the CPM can provide greater spatial resolution at the cost of being more computationally expensive. Pixels are assigned to individual cells in a stochastic manner that depends on probabilities determined by an energy cost function that describes cell properties. The model's time unit, known as a Monte Carlo Step (MCS), refers to the number of model update attempts, which is determined by the total number of pixels (Graner and Glazier, 1992; Glazier and Graner, 1993).

Centre-based models and simpler versions of cellular automata assume cells are functionally symmetric. This symmetry can be broken by associating a vector to each cell in order to bias their properties. However, Vertex and CPM models are able to represent cell shapes explicitly. Furthermore, being able to apply oriented bias in the cost equations is valuable as it allows cell characteristic anisotropies, which is, biologically, more meaningful. Therefore, Vertex and CPM modelling approaches are usually favoured over centre-based and cellular automata models for

modelling biological systems. The wound healing model in this chapter was therefore developed using a CPM framework, which is described in more detail in the following section.

2.1.4 The Cellular Potts Model (CPM)

The CPM represents space as a regular lattice of pixels, also known as, voxels. In this lattice, biological cells and/or compartments are represented as generalised 'cells' that occupy sets of pixels in the lattice (Graner and Glazier, 1992). The generalised 'cell' may represent a biological cell, an extracellular domain, a subcellular compartment, a cluster of cells, non-cellular material, fluid or medium. Each pixel in the lattice has a position $\vec{\imath}$ and an index σ that specifies the generalised 'cell' occupying the pixel; generalised 'cells' σ are assigned a cell type $\tau(\sigma)$ which represents distinct biological phenotypes. While each pixel has a unique identifier $\sigma_{\vec{\imath}}$, many pixels may share the same cell type $\tau(\sigma)$. Cell motility, in the absence of an external stimuli, occurs through cytoskeletal membrane fluctuations and is dependent on differential matrix adhesion properties. This random walk pattern to mimic biological cell movement through pseudopod extensions and retractions is achieved by means of stochastic exchanges of pixels occupied by each generalised 'cell'. This is done using a dynamic Monte Carlo simulation algorithm to minimise free energy dictated by an effective energy equation, or Hamiltonian equation, that includes terms describing generalised 'cell' properties including volume and surface constraints, mechanical interactions, chemotaxis etc. An example of such Hamiltonian equation would be:

$$\boldsymbol{H} = \sum_{\vec{\imath},\vec{\jmath}} \boldsymbol{J}(\boldsymbol{\tau}(\boldsymbol{\sigma}_{\vec{\imath}}), \boldsymbol{\tau}(\boldsymbol{\sigma}_{\vec{\jmath}})))(\mathbf{1} - \boldsymbol{\delta}(\boldsymbol{\sigma}_{\vec{\imath}}, \boldsymbol{\sigma}_{\vec{\jmath}})) + \sum_{\boldsymbol{\sigma}} \boldsymbol{\lambda_{vol}}(\boldsymbol{\sigma})\big(\boldsymbol{v}(\boldsymbol{\sigma}) - \boldsymbol{V_t}(\boldsymbol{\sigma})\big)^2 \qquad 2.1$$

The first term in the Hamiltonian equation describes intercellular adhesion, where $J(\tau(\sigma_{\vec{\imath}}), \tau(\sigma_{\vec{\jmath}})))$ is the effective contact energy between 'cells' at *i* and *j*, whilst δ is the Kronecker delta function in the term $1 - \delta(\sigma_{\vec{\imath}}, \sigma_{\vec{\jmath}})$, which ensures that only contact energies between pixels from different 'cells' are included in the energy calculation, so as to capture the interactions between the different 'cells'. The second term describes the volume of 'cells', where $v(\sigma)$ is the number of pixels within a 'cell', $V_t(\sigma)$ is the target volume and $\lambda_{vol}(\sigma)$ is the strength of the volume constraint. Similarly, various generalised 'cell' properties can be described within the

Hamiltonian equation using such constraints, which can also be specifically assigned to different 'cell' or biological cell groups.

For the lattice configuration to evolve, the algorithm begins by randomly selecting a source pixel lattice site and attempts to copy its index to a neighbouring target site, also chosen at random. If the target site belongs to a different generalised cell and has a different index, the algorithm calculates the energy cost of making this move. Index copying occurs stochastically with a Boltzmann acceptance function with the aim of minimising the effective energy of the system (described in more detail in section 2.2.2). As previously stated, the intrinsic simulation time unit is an MCS, which corresponds to the number of model update attempts. Figure 2.3 shows the lattice configuration evolution to minimise effective energy of the system.

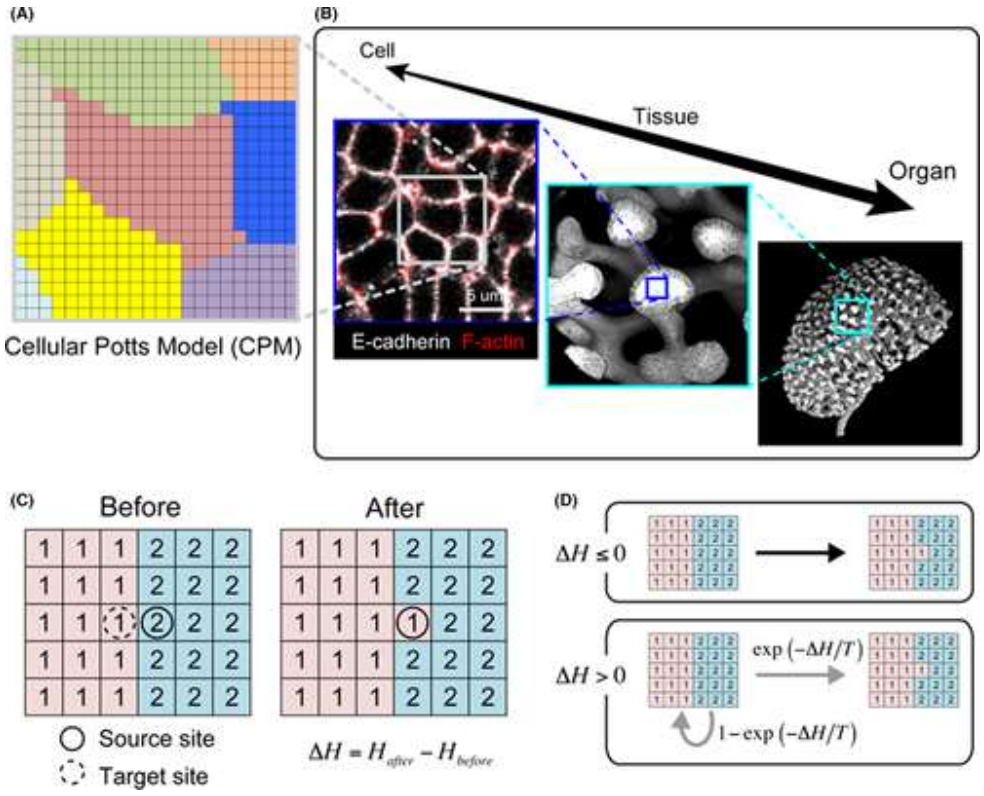

Figure 2.3 **The CPM**. **A:** Schematic representation of the CPM lattice. Every colour represents an individual cell. **B:** CPM can be used to model mechanisms at multiple scales, for instance, cells in the model can represent biological cells for tissue-level modelling. **C:** The CPM lattice configuration evolves by first randomly selecting a source and target site, followed by attempting to copy the source index (unique identifier of the source) to the target site. **D:** Successful index copying can only occur if the effective energy *(ΔH)* ≤ 0. Otherwise, index copying occurs with a new probability that is calculated with the amplitude of fluctuation parameter *T*. Image was taken from (Hirashima, Rens and Merks, 2017).

2.1.5 Computational and mathematical models of wound healing

Computational models have the potential to further our understanding of wound healing mechanisms, disease context-dependent healing progression and treatment avenues, by highlighting the interactions between key mechanisms of tissue repair and providing a flexible and versatile system for hypothesis testing. Tissue-level models are particularly valuable as they allow the exploration of interactions between and within cells that lead to complex tissue patterning in various biological contexts. As mentioned previously, this is especially valuable for wound healing. The two main approaches to tissue-level modelling include continuum models and ABMs. Briefly, continuum models consist of cell-density fields and partial differential equations (PDE) that represent cell interactions without explicitly modelling individual cells. On the other hand, ABMs represent cells and interactions explicitly, providing spatial resolution which is highly beneficial for modelling the wound healing process.

Mathematical and computational models of wound healing have advanced as productive means to understanding the complex multiscale processes involved in wound healing. One of the first wound healing models was a continuum model, specifically a cell-level reaction-diffusion model, that was used to investigate epidermal cell migration and its regulation mediated by growth factors (Sherratt and Murray, 1990). The experimentally validated model showed that biochemical regulation of epidermal cell replication and migration was crucial to successful healing. This model was expanded to incorporate more cell types including fibroblasts and myofibroblasts, as well as ECM forces, which provided valuable insights into tissue biomechanics during wound healing and related disorders (Tranquillo and Murray, 1992; Olsen, Sherratt and Maini, 1995). For instance, with the addition of fibroblasts, ECM and cell traction forces, Tranquillo and Murray's model showed how fibroblast traction forces drive wound contraction as they are able to induce different spatial behaviours of cells (Tranquillo and Murray, 1992). On the other hand, with the addition of fibroblasts, myofibroblasts, ECM and a growth factor stimulus, Sherratt and Maini showed that dysregulated wound contraction, primarily mediated by myofibroblasts and collagen kinetics, drive fibro-contractive diseases (Olsen, Sherratt and Maini, 1995). Most studies focus on specific phases of the healing process, primarily on the inflammatory and proliferative phases, although there are a few that investigate the remodelling phase as well.

During wound healing, keratinocytes at the wound edge crawl laterally and proliferate across the wound to restore the epidermal barrier, constituting the process known as re-epithelialisation, as discussed previously. Aside from intercell crosstalk, signalling through growth factors, such as TGF-β1 and EGF, also dictates the behaviour of the wound leading-edge keratinocytes. Many models have focussed on the re-epithelialisation process of healing and have reported interesting insights into growth factor-mediated keratinocyte proliferation (Sun *et al.*, 2009) and migration (Andasari *et al.*, 2018), epidermal stem cell cluster regulation (Savill and Sherratt, 2003) and biomechanics of epidermal wound closure (Bai and Zeng, 2023).

In keeping with epidermal healing, an ABM used to investigate the role of TGF-β1 during epidermal wound healing revealed a specific spatiotemporal order of events in physiological and pathological wound healing (Sun *et al.*, 2009). This model demonstrated that normal re-epithelisation involved an initially attenuated proliferative response coupled with a high level of motility at the leading edge of the wound, which is then followed by a proliferative population of keratinocytes. The model also showed that disrupting TGF-β1 balance resulted in either a chronic wound or a fibrotic wound. Additionally, a CPM of re-epithelialisation was used to investigate the relationship between keratinocyte migration and EGF activity, since EGF governs integrin expression through differences in its diffusion, secretion, and integrin-ligand binding affinity. The experimentally validated model showed that epidermal healing could be accelerated or decelerated depending on EGF diffusion and secretion rates; a deceleration in the process could result in delayed re-epithelialisation, which could progress to a chronic wound (Andasari *et al.*, 2018).

The formation of new blood vessels, known as angiogenesis, is crucial to the healing process. For that reason, angiogenesis is another aspect of wound healing that has received a lot of attention in modelling. Although continuum models have provided valuable insights, cell-based models have allowed for the overlap of biological features necessary to predict vascular network structure during healing (Guerra, Belinha and Jorge, 2018). For instance, a discrete dynamic model of angiogenic morphogenesis revealed that vascular endothelial cell interactions can lead to cell-mixing, elongation, and bifurcation during the early stages of angiogenesis (Matsuya *et al.*, 2016). Additionally, the cellular automata framework has been used to elegantly model microvascular network patterning, with the ability to predict angiogenic remodelling in response to epigenetic

stimuli and molecular signals (Peirce, Van Gieson and Skalak, 2004). Some studies have combined ABM frameworks, such as CPM, with PDEs to model chemical signalling. For instance, a CPM consisting of endothelial cells along with PDEs to describe chemoattractant behaviour was used for the investigation of intercellular adhesion dynamics and cell morphology (Merks, Newman and Glazier, 2004). The model revealed that endothelial cell adhesion was crucial for stable blood vessel formation. Similarly, another CPM of angiogenesis, that also included the subsequent reoxygenation process of hypoxic tissue, using reaction-diffusion equations to describe VEGF and oxygen dynamics, revealed that vessel pattern is heavily influenced by ECM topological properties (Scianna, Bassino and Munaron, 2015).

Collagen deposition and wound contraction during healing have also been studied through modelling, with an important feature of these models being that they include fibroblast and myofibroblast dynamics along with mechanical and mechanosensing processes. Most studies in this area have adopted a hybrid discrete-continuous framework where the ECM is represented as a continuous field and cells as discrete entities. For example, a hybrid mathematical model of fibroblast response to macrophage-derived TGF-β, where the ECM was modelled using a vector-based representation and cells as discrete entities, showed that TGF-β kinetics have significant impacts on the healing process. The model showed that the fibroblasts cluster around chemoattractant rich areas where they replace the provisional fibrin matrix with collagen, and that the subsequent decrease in TGF-β diffusion results in improper clustering, reduced collagen deposition and impaired healing (Cumming, McElwain and Upton, 2010). Similarly, a hybrid model based on CPM coupled with a continuous field for the ECM revealed that healing is significantly impacted by cell speed during fibroblast influx from surrounding tissue to the wound site (Maini, Olsen and Sherratt, 2002). The ECM is highly structured and complex, making it challenging to model. In order to develop more realistic 3-dimensional wound geometries, some studies have used finite element modelling. The finite element method involves breaking down a system into smaller elements, with equations to describe the behaviour of each element. This results in a system of equations which are solved to determine the behaviour of the overall system. In this regard, a finite element model of skin expansion was used to investigate the effect of increased mechanical stretch on collagen production and fibroblast mitosis (Socci *et al.*, 2007). Overall,

models like these could be used as predictive methods to develop and optimise personalised clinical treatments.

Other models have focussed on specific processes in wound healing such as mesenchymal cell migration (Fortuna *et al.*, 2020), myofibroblast and macrophage population dynamics (Adler *et al.*, 2020), factors affecting cell invasion in wound healing assays (Scianna, 2015) and functional and phenotypic fibroblast dynamics mediated by ECM during wound maturation (Rognoni *et al.*, 2018). This brief review was aimed at demonstrating the richness of the role of computational and mathematical modelling methods to investigate wound healing. However, dynamic models that include senescent cell function in wound healing and tissue repair are lacking. Given the significance of senescent cells in tissue repair and tissue repair-related disorders (Chapter 3), modelling the spatiotemporal dynamics of senescent cells and SASP could provide valuable mechanistic insights, and inform treatment and diagnostic avenues.

2.2 Model and Methods

The wound healing model was built using the software CompuCell3D, which is an open-source modelling environment, implementing the lattice-based CPM framework as previously described, combined with PDE solvers, reaction-kinetics solvers and other tools (Swat *et al.*, 2012). The CPM framework was summarised in section 2.1.4, but briefly, every simulation lattice is divided into a collection of pixels representing generalised 'cells', each with an assigned 'cell' type. 'Cells' interact with each other and their environment based on parameters that can approximate biological constraints. These parameters can be based on their *in vitro* or *in vivo* biological counterparts and steer the simulation through the effective energy or Hamiltonian (H), that is calculated at each simulation time step (or MCS). Terms of the effective energy equation for the wound healing model will be described in the next sections.

2.2.1 Model conceptualisation: Overview and Assumptions

The first step taken to develop a mechanism-based computational model was to gather biological experimental observations within the system to formulate a conceptual model to help clarify a hypothesis and identify questions of interest. Once completed, a qualitative model with a formal structure was built including the essential model elements that capture the observed biology, along with abstractions and assumptions. The model underwent several rounds of optimisation

to fine tune representations of biological phenomena such as dynamics of ECM composition, cell migration, proliferation, and cell state transitions. The importance of these components was detailed in section 2.1.

This iterative process resulted in the conceptual model summarised in Figure 2.4: Fibroblasts proliferate and become activated in response to PDGF. Primarily three types of PDGF (-A and -B dimeric isoforms: PDGF-AA, -AB and -BB) have been shown to play important roles in myofibroblast differentiation, chemotaxis and proliferation, as well as stimulation of collagen production in fibroblasts and myofibroblasts (Bonner, 2004; Adler *et al.*, 2020). Since PDGF was modelled as a single entity for the sake of computational feasibility, the three isoforms discussed will collectively be referred to as PDGF. Activated fibroblasts produce ECM and colony stimulating factor 1 (CSF1), hereafter referred to as CSF. In response to PDGF and mechanical stimuli, activated fibroblasts differentiate into myofibroblasts, which produce large amounts of ECM, PDGF and CSF. Myofibroblasts are highly proliferative cells that replicate in response to PDGF. Myofibroblasts become senescent through CCN1-induced primary senescence, and paracrine- and juxtacrine-induced secondary senescence. Macrophages on the other hand proliferate in response to CSF and are the primary source of several growth factors within the wound environment. The mathematical description, evidence and justification for these interactions are described in the following sections.

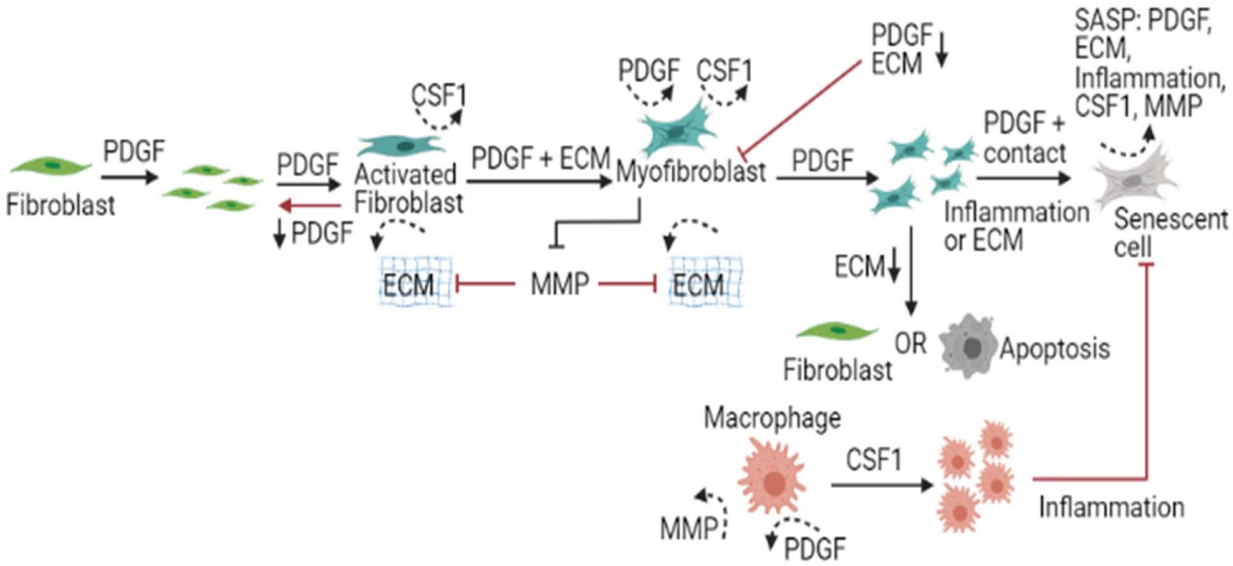

Figure 2.4 **Conceptual illustration of the wound healing model.** This is a schematic representation of the qualitative model which was developed before being applied to a computational framework. The model consists of explicitly described generalised cell types including fibroblasts, myofibroblasts, senescent myofibroblasts, macrophages and ECM. Chemical fields within the model include PDGF, CSF, MMP and Inflammation.

The multiscale model of wound healing represents a two-dimensional wounded dermal section that is of size 200×200×1 pixel (600 μm × 600 μm). Pixel units and corresponding cell lengths and volumes are provided in Table 2.1. All cells are chemically homogeneous as no chemical diffusion is modelled within the intracellular space; this was to keep the focus on tissue-level and intercell behaviours, rather than intracellular processes. Growth factors and cytokines are modelled using reaction diffusion equations, described in more detail in later sections. The primary focus of the model is to investigate the dynamics of senescent cells in the healing process, hence the model simulation begins at the end of the inflammatory phase, since the proliferative phase is when senescent cells are most prevalent in healthy healing (Muñoz-Espín and Serrano, 2014). Furthermore, the papillary and reticular dermis are assumed to be combined within the model, similar to previous work from Rognoni et al. where papillary and reticular fibroblast populations were represented by a single cell type for the purpose of modelling simplification (Rognoni *et al.*, 2018).

2.2.2 Cell dynamics and motility

Cell motility driven by the cytoskeleton is modelled within the CPM using a modified Metropolis algorithm which consists of a series of stochastic pixel-copy attempts (Swat *et al.*, 2012; Cipra, 2018). Before every attempt, a source pixel $\vec{\imath}$ and a target pixel $\vec{\imath}\,'$ are chosen. If $\sigma_{\vec{\imath}}$ and $\sigma_{\vec{\imath}'}$ belong to different generalised 'cells', then the difference in energy (ΔH) to copy the index (unique ID of a pixel) from the source to the target site is calculated. With that, the probability of accepting a new model configuration is given by:

$$P(\sigma_{\vec{\imath}} \to \sigma_{\vec{\imath}'}) = \begin{cases} 1, & for\ \Delta H \leq 0 \\ f(\Delta H), for\ \Delta H > 0 \end{cases} \qquad 2.2$$

Where,

$$f(\Delta H) = e^{\frac{-\Delta H}{T_m}} \quad 2.3$$

Where the parameter T_m represents the amplitude of cell membrane fluctuations in the model. This means that the new configuration (from $\sigma_{\vec{i}}$ to $\sigma_{\vec{i}'}$) is accepted if the difference in effective energy calculated between the two configurations is less than or equal to zero. Otherwise, a new probability for the change in model configuration from $\sigma_{\vec{i}}$ to $\sigma_{\vec{i}'}$ is calculated using equation 2.3. The overall aim of this algorithm is to minimise the effective energy of the system's configuration, while obeying the biological mechanisms described within the terms in the effective energy equation (full equation as shown in 2.20).

One pixel in the simulation was taken to be equal to 3µm, as this seemed biologically appropriate to represent cells in terms of pixels. Cells in the simulation were found to have an average speed of ~0.1 pixel/MCS, which equated to 0.2 microns/MCS. This speed was determined by running multiple simulations of a cell without any hindrance and taking an average of the difference between the current and previous center of mass (COM) values. In order to calculate the real time equivalent of one MCS, maximum fibroblast migration speed during wound healing was considered as a reference, which peaks towards the end of the healing process with a speed of 40 µm/h (Shabestani Monfared, Ertl and Rothbauer, 2020). Therefore, one MCS was calculated to be 27 secs (0.3*3600/40).

2.2.3 ***Cell types, volume, and surface***

The model consists of fibroblasts, myofibroblasts, macrophages, senescent myofibroblasts and ECM defined as individual cell types with distinct properties, as shown in Figure 2.4. The dermal layer is composed of ECM and resident fibroblasts, whereas the wound is populated by M2-polarised macrophages. Fibroblasts differentiate into myofibroblasts through mechanisms described in later sections. Myofibroblasts can either undergo apoptosis or become senescent myofibroblasts.

Each cell has a defined volume and surface area (Table 2.1), which contribute to the effective energy equation as:

$$H = \sum_{\sigma} \lambda_{vol}(\sigma)\big(v(\sigma) - V_t(\sigma)\big)^2 + \sum_{\sigma} \lambda_{surf}(\sigma)\big(s(\sigma) - S_t(\sigma)\big)^2 \quad 2.4$$

Where $v(\sigma)$ and s(σ) represent a cell's instantaneous volume and surface, and $V_t(\sigma)$ and $S_t(\sigma)$ represent the target volume and target surface, respectively. In addition, $\lambda_{vol}(\sigma)$ and $\lambda_{surf}(\sigma)$ represent the volume and surface constraints of the cell and can be correlated to Young's modulus (i.e., modulus of elasticity); a higher λ value would result in an increased energy cost for any deviations from the target volume or surface values. The λ values used in the model are provided in Table 2.1 and are assumed to be the same for every cell type, similar to previous work by (Swat *et al.*, 2015).

2.2.4 ***Cell growth and proliferation***

Within the model, cell growth is limited to fibroblasts, myofibroblasts and macrophages. As discussed previously, PDGF is a primary mediator of fibroblast and myofibroblast migration, proliferation, and ECM production within the wound (Beer, Longaker and Werner, 1997; Juhl et al., 2020). Hence, fibroblast and myofibroblast growth were modelled by increasing cell target volume according to PDGF concentration using the Monod growth equation given as,

$$\frac{dV_t(Fibroblast,Myofibroblast)}{dt} = \frac{G_{\max(F,MF)} \times PDGF(\vec{x}_{COM})}{PDGF(\vec{x}_{COM}) + PDGF_0} \quad 2.5$$

Where $PDGF(\vec{x}_{COM})$ is PDGF concentration at the cell's COM, $PDGF_0$ is the concentration at which cell growth is half its maximum, and $G_{\max(F,MF)}$ is the maximum cell cycle time for fibroblasts and myofibroblasts. Similarly, CSF-dependent macrophage growth is given as,

$$\frac{dV_t(Macrophage)}{dt} = \frac{G_{\max(M)} \times CSF(\vec{x}_{COM})}{CSF(\vec{x}_{COM}) + CSF_0} \quad 2.6$$

Where $CSF(\vec{x}_{COM})$ is CSF concentration at the cell's COM, CSF_0 is the concentration at which growth is half its maximum, and $G_{max(M)}$ is the maximum cell cycle time for macrophages. The Monod equation relates cell growth to the concentration of a limiting factor, which in this case is PDGF for fibroblasts and myofibroblasts, and CSF for macrophages (Charlebois and Balázsi, 2019).

Cell growth and proliferation are limited by contact inhibition, which can occur through two ways: mechanical stress and contact-dependent growth inhibition (Heit *et al.*, 2001; Gumbiner and Kim, 2014). Mechanical stress-dependent inhibition was modelled by imposing a volume constraint for mitosis whereby cells undergo mitosis only when they reach their doubling volume by dividing along a randomly chosen axis. Cell doubling volume was taken as twice the original target volume of that particular cell type (fibroblasts, myofibroblasts or macrophages), with the daughter cells acquiring the target volume of the parent cells.

Contact-dependent growth inhibition was modelled by allowing an increase in cell volume only if the surface of the cell in contact with neighbouring cells, R_s, is below a specified threshold T_{CI} (Li and Lowengrub, 2014). R_s is given by:

$$R_s = \frac{\mathrm{s}(\sigma)_{medium}}{\mathrm{s}(\sigma)} \qquad 2.7$$

Where $\mathrm{s}(\sigma)_{medium}$ is the cell surface area in contact with the medium and $\mathrm{s}(\sigma)$ is the cell surface area. The ratio R_s measures how much of a cell's surface area is not in contact with other neighbouring cells. If R_s is below the threshold, T_{CI} then cell growth is arrested at the current cell volume $v(\sigma)$ along with the initial lambda value $\lambda_{vol}(\sigma)$, and if R_s is above T_{CI}, cell volume is determined by equations 2.5 and 2.6. An illustration of the cell-state transition rules in the form of a flowchart for these processes is shown in Figure 2.5.

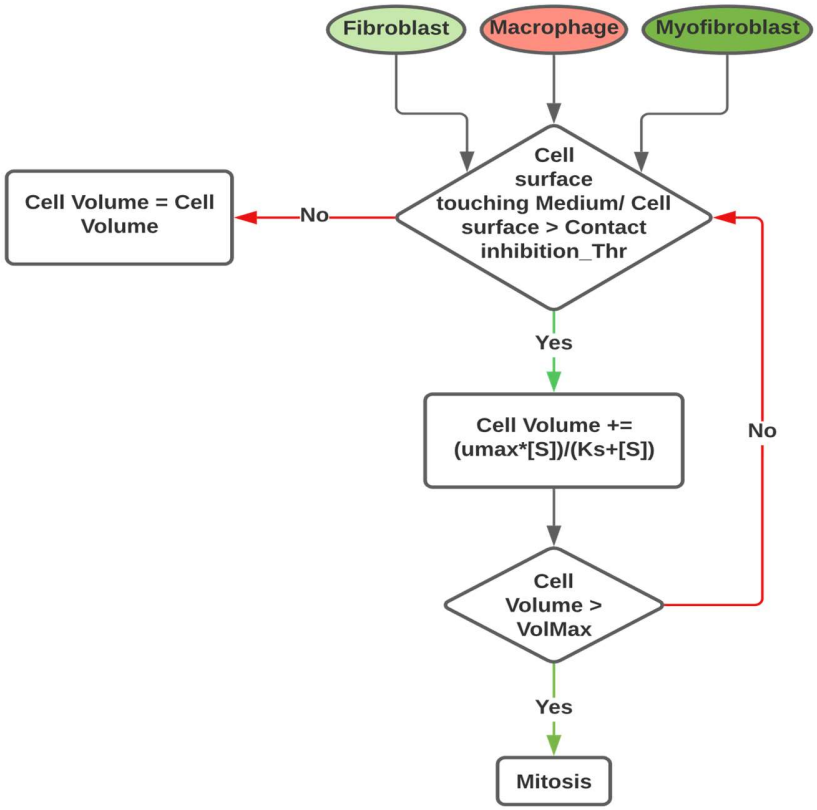

Figure 2.5 **Model cell-state transition flowchart for cell growth and proliferation.** Fibroblast, macrophage and myofibroblast growth is limited by contact inhibition. If the percentage of a cell's surface area that is in contact with the medium (i.e., not in contact with other cells) is greater than a threshold (inhibition_Thr), then cell growth takes place based on the Monod equation. Cells replicate once a volume threshold is reached (VolMax).

*2.2.5 **Cell adhesion***

Adhesion and repulsion between neighbouring cells are represented in the effective energy equation by the function:

$$H = \sum_{\vec{i},\vec{j}} J(\tau(\sigma_{\vec{i}}), \tau(\sigma_{\vec{j}}))(1 - \delta(\sigma_{\vec{i}}, \sigma_{\vec{j}})) \qquad 2.8$$

Where $\sigma_{\vec{i}}, \sigma_{\vec{j}}$ are the IDs of the cells to which pixels *i* and *j* belong, $\tau(\sigma)$ is the type of cell σ, J is the contact energy between cells at *i* and *j*, and δ is the Kroenecker delta function given as,

$$\delta(\sigma_{\vec{i}}, \sigma_{\vec{j}}) = \begin{cases} 0, & \sigma_{\vec{i}} \neq \sigma_{\vec{j}} \\ 1, & \sigma_{\vec{i}} = \sigma_{\vec{j}} \end{cases} \quad 2.9$$

The term $(1 - \delta(\sigma_{\vec{i}}, \sigma_{\vec{j}}))$ will ensure that only pixels belonging to different cells will be considered in the sum of contact energies between neighbouring pixels (Swat *et al.*, 2012). The contact energies between different cell types are given in Table 2.1. Generally, a higher contact energy results in repulsion, whereas a lower contact energy leads to adhesion between cells.

2.2.6 ***Cell state transitions, growth factors and cytokines***

Fibroblasts, myofibroblasts and macrophages interact by exchanging growth factors. As stated previously, macrophages respond to various external stimuli that can result in a wide range of activation phenotypes. Macrophages within the model shift between classically (M1) and alternatively (M2) activated phenotypes depending on contact with the inflammation field, which represents inflammatory SASP (Lujambio *et al.*, 2013). The inflammatory component of SASP, as previously discussed, is highly complex and consists of many key factors (Hoare *et al.*, 2016). However, for the sake of computational feasibility, inflammatory SASP was considered as one chemical field.

If the concentration of the inflammation field at the COM of a macrophage is greater than the threshold parameter INF_{thr}, then the macrophage secretes MMPs (also referred to as proteinase), characteristic of the M1 phenotype. However, if the inflammation field concentration is less than INF_{thr}, the macrophage secretes PDGF (Murray and Wynn, 2011). MMPs can also be produced by macrophages following contact with ECM, that is, if ECM is surrounding the cell periphery (macrophage target surface) (Shapiro, Kobayashi and Ley, 1993). Since the model begins at the end of the inflammation phase, macrophages are M2 activated and secrete PDGF for fibroblasts and myofibroblasts (Krzyszczyk *et al.*, 2018). For the sake of simplicity, and to focus on senescent cell activity during the proliferative phase of healing, inflammatory SASP is the only form of inflammation considered in this model.

Quiescent fibroblasts become activated in response to PDGF, stimulating the production of CSF (Falkenburg *et al.*, 1990; Abboud and Pinzani, 1991). Myofibroblasts also produce CSF for macrophages, as well as PDGF, forming an autocrine loop (Adler *et al.*, 2020). In the model, if PDGF concentration at a fibroblast's COM is above the threshold parameter $PDGF_f$, then the

fibroblast is activated from a quiescent state. Growth factors, especially CSF, exchange occurs in a cell-cell contact-dependent manner (Zhou *et al.*, 2018). Therefore, CSF secretion by activated fibroblasts and myofibroblasts only occur in cells sharing common surface area with macrophages. Activated fibroblasts and macrophages in the model were removed at a rate of μ (Zhou *et al.*, 2018). Macrophages also undergo apoptosis following growth factor withdrawal (Xaus *et al.*, 2001; Hundal *et al.*, 2003), which was modelled by removing macrophages with CSF concentration less than a threshold parameter CSF_{thr} at the cell's COM.

Myofibroblast differentiation typically requires growth factor stimulation, along with mechanical stimulation (Tomasek *et al.*, 2002). PDGF is one such growth factor that is known to play an important role in granulation tissue formation and myofibroblast differentiation during tissue repair (Boström *et al.*, 1996; Lindahl *et al.*, 1997; Lindahl and Betsholtz, 1998). On the other hand, mechanical stimulation is crucial for the formation of the contractile features characteristic of myofibroblasts (Grotendorst, Rahmanie and Duncan, 2004; Avivi-Green, Singal and Vogel, 2006; Bansal *et al.*, 2017). In the model, myofibroblast differentiation occurs if the value of PDGF at a fibroblast's COM is greater than $PDGF_f$ and common surface area with ECM is greater than ECM_{thr}. Every activated fibroblast within the wound region in the model has a chance of differentiation that is calculated by drawing a random integer from a binomial distribution with probability $P_{MF.}$ Since myofibroblasts are known to produce TIMPs, a simple mechanism to inhibit proteases was included, whereby MMP concentration at a myofibroblast's COM was reduced by the MMP threshold MMP_{thr} (Iredale *et al.*, 1996). An important feature of fibroblasts and myofibroblasts is their ability to produce large amounts of ECM. Fibroblasts and myofibroblasts produce ECM if PDGF concentration at the cell's COM is above the threshold parameter $PDGF_f$. The amount of ECM produced by myofibroblasts (ECM_{Myof}) is assumed to be double that produced by fibroblasts (ECM_{Fib}). This value was selected to be most appropriate after running multiple preliminary model simulations with different parameter values. ECM degradation by MMP occurs by removing ECM 'cells' which have a MMP concentration at their COM greater than MMP_{thr}.

Myofibroblast activity can resolve in many ways. Myofibroblasts can undergo apoptosis due to release of mechanical tension or exposure to pro-apoptotic inflammatory cytokines, de-differentiate to a fibroblast phenotype or become senescent (Hinz and Lagares, 2019). To model apoptosis due to release of mechanical tension, myofibroblasts that shared common surface area

with ECM below a threshold represented by the parameter ECM_{thr}, were removed (Grinnell *et al.*, 1999). Apoptosis by exposure to inflammation was modelled by removing a cell if concentration of the inflammatory SASP field at the COM of the cell was greater than the threshold parameter INF_{thr} (Zhang and Phan, 1999). The chance of a myofibroblast becoming senescent was calculated by drawing a random integer from a binomial distribution with probability P_{SNC}. Senescence can be induced in myofibroblasts through the matricellular protein CCN1 during the mid to late stages of healing (Jun and Lau, 2010; Demaria *et al.*, 2014; Muñoz-Espín and Serrano, 2014). Therefore, a time constraint T_{SEN} was set for the induction of senescence to limit it to the mid to late stages of the repair process. In keeping with this, if time is less than T_{SEN}, a myofibroblast in the model with common surface area with ECM that is greater than the parameter ECM_{thr} will become a senescent myofibroblast. Senescent myofibroblasts produce two distinct types of SASP: a fibrogenic SASP consisting of PDGF and ECM lasting for about three days (T_{NIS}), followed by a fibrolytic SASP consisting of CSF, Inflammation and MMP. This value for T_{NIS} was chosen because preliminary work suggests that NOTCH-mediated fibrogenic SASP and juxtacrine secondary senescence is prevalent up to approximately three days after senescence activation (Hoare *et al.*, 2016; Teo *et al.*, 2019).

With that said, in addition to CCN1-induced senescence, mechanisms of secondary senescence include juxtacrine and paracrine senescence, which are more prevalent during the fibrogenic and fibrolytic phases of the senescence program respectively (Hoare *et al.*, 2016). Therefore, within the model, the juxtacrine mechanism involves induction of senescence if a myofibroblast is in contact with a senescent cell in its fibrogenic SASP phase, and if PDGF concentration at the myofibroblast's COM was greater than the threshold parameter SNC_{thr}. For paracrine senescence, if a myofibroblast is neighbouring a senescent cell in its fibrolytic SASP phase and had an inflammatory SASP field concentration greater than $INF_{thr,}$ then the cell would become senescent. Senescent cells during wound healing are removed by immune cells, e.g., phagocytosis by macrophages (Kale *et al.*, 2020). Hence, senescent cells within the model are removed on contact with macrophages to model phagocytosis. They also have an equal chance of getting removed if the concentration of the inflammation field at the senescent cell's COM is greater than $INF_{thr,}$ to account for other immune-surveillance mechanisms. An illustration of the cell-state transition

rules in the form of flowcharts for these processes are shown in Figure 2.6, Figure 2.7 and Figure 2.8.

The governing reaction-diffusion equations for the four chemical fields in the model are given as below:

$$\frac{\partial[PDGF](\vec{x},t)}{\partial t} = D_{PDGF}\nabla^2[PDGF](\vec{x},t) - \delta_{PDGF}[PDGF](\vec{x},t) + S_{PDGF} \quad 2.10$$

$$\frac{\partial[CSF](\vec{x},t)}{\partial t} = D_{CSF}\nabla^2[CSF](\vec{x},t) - \delta_{CSF}[CSF](\vec{x},t) + S_{CSF} \quad 2.11$$

$$\frac{\partial[MMP](\vec{x},t)}{\partial t} = D_{MMP}\nabla^2[MMP](\vec{x},t) - \delta_{MMP}[MMP](\vec{x},t) + S_{MMP} \quad 2.12$$

$$\frac{\partial[INF](\vec{x},t)}{\partial t} = D_{INF}\nabla^2[INF](\vec{x},t) - \delta_{INF}[INF](\vec{x},t) + S_{INF} \quad 2.13$$

Where $[PDGF](\vec{x},t)$, $[CSF](\vec{x},t)$, $[MMP](\vec{x},t)$, $[INF](\vec{x},t)$ represent the concentrations of the chemical fields at pixel $\vec{x}$ at time t, *D* represents the diffusion coefficients, δ represents the decay constant and S represents the rate of secretion for the fields PDGF, CSF, INF and MMP. All chemical fields were set to no flux in the x and y axes. The solver 'DiffusionSolverFE' within CompuCell3D was used to solve the PDEs by implementing the Forward Euler method.

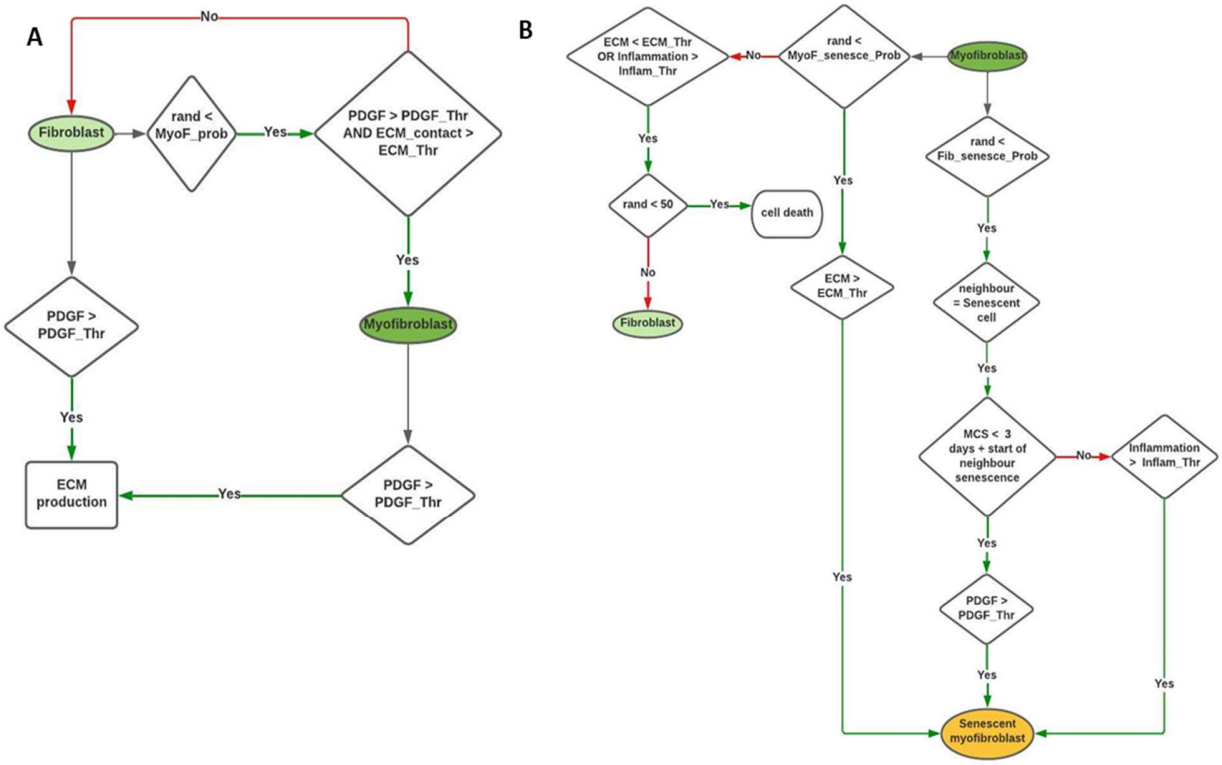

Figure 2.6 **Model cell-state transition flowcharts for fibroblast and myofibroblast behaviours**. **A:** This flowchart shows the dynamics of ECM production by fibroblasts and myofibroblasts, as well as myofibroblast differentiation. Fibroblasts and myofibroblasts produce ECM if PDGF concentration within the cell is greater than a threshold (PDGF_Thr). Fibroblast differentiation into myofibroblasts occurs with a probability (MyoF_prob), in addition to a PDGF concentration threshold constraint (PDGF_Thr) and a mechanical stimulation threshold constraint (ECM_Thr). **B:** This flowchart shows the dynamics of myofibroblast senescence, death, and de-differentiation back to a fibroblast. CCN1-induced primary myofibroblast senescence occurs with a probability (MyoF_senesce_Prob) and an ECM threshold constraint (ECM_Thr). Secondary myofibroblast senescence occurs with a probability (Fib_senesce_Prob) and if the cell neighbouring the myofibroblast is senescent. This occurs via two mechanisms: Juxtacrine secondary senescence occurs if the neighbouring senescent cell is in its fibrogenic SASP phase (first 3 days of senescence) and the concentration of PDGF affecting the myofibroblast is past a threshold (PDGF_Thr); paracrine secondary senescence occurs if the neighbouring senescent cell is in its fibrolytic SASP phase (after three days post senescence) and the inflammatory SASP concentration affecting the myofibroblast is past a threshold (Inflam_Thr). Alternatively, myofibroblasts can apoptose or de-differentiate back to a fibroblast with an equal chance, in response to release of mechanical tension controlled by a cell contact with ECM threshold (ECM_Thr) or exposure to inflammatory SASP controlled using a threshold constraint (Inflam_Thr).

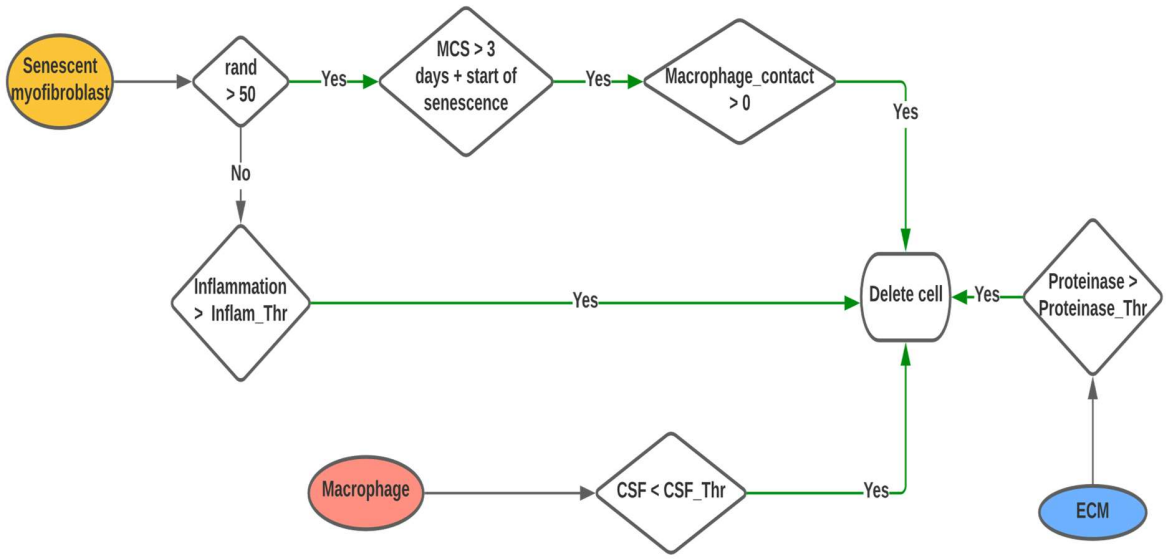

Figure 2.7 **Model cell-state transition flowchart for cell clearance mechanisms.** Senescent myofibroblasts which are in their fibrolytic SASP phase (three days post senescence induction) and in contact with macrophages are removed. Additionally, they have an equal chance of getting removed if they have an inflammatory SASP concentration greater than a threshold (Inflam_Thr). Macrophages are cleared when they experience growth factor depletion; therefore, macrophages with a CSF concentration below a threshold (CSF_Thr) are removed. ECM is removed upon exposure to a concentration of proteinase greater than a threshold (proteinase_Thr).

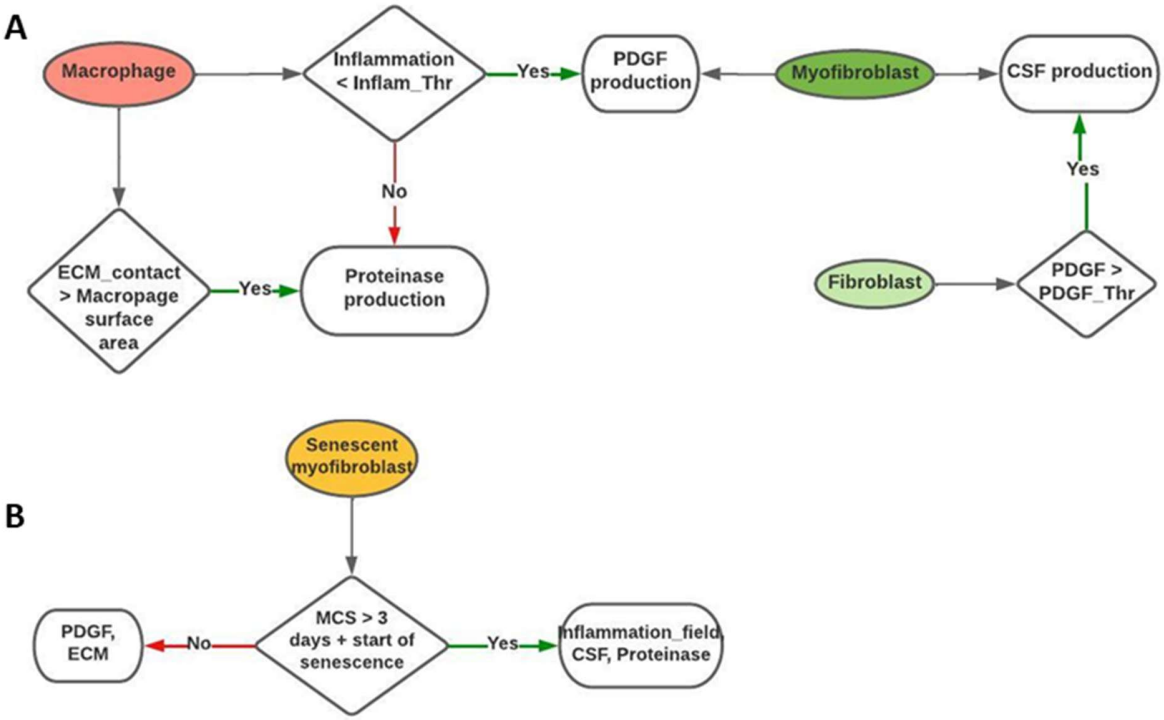

Figure 2.8 **Model cell-state transition flowcharts for chemical field production. A:** This flowchart shows the dynamics for macrophage, myofibroblast and fibroblast chemical field production. Macrophages produce PDGF, due to an M2 anti-inflammatory phenotype, if the concentration of inflammatory SASP within them is below a threshold (Inflam_Thr). On the contrary, if the concentration of inflammatory SASP within a macrophage is above the threshold, then the macrophage produces proteinase. On the other hand, myofibroblasts produce PDGF and CSF. Fibroblasts also produce CSF but only after PDGF-mediated activation controlled by a threshold (PDGF_Thr). **B:** Senescent myofibroblasts produce a fibrogenic SASP consisting of PDGF and ECM during the first three days following induction of senescence, followed by a fibrolytic SASP consisting of inflammatory SASP, CSF and proteinase after three days.

2.2.7 ***Chemotaxis***

Chemotaxis refers to cell migration directed towards a chemical stimulus and is an important element in wound healing as it is one of the main mechanisms by which cells are recruited to the wound site. Within the model, chemical field gradients of PDGF and inflammation cause cells to chemotax towards them. Both fibroblast and myofibroblast chemotaxis towards PDGF (Seppa *et al.*, 1982) is represented in the effective energy equation as,

$$\Delta E_{PDGF} = -\lambda_{PDGF}([PDGF](\vec{x}) - [PDGF](\vec{x}')) \quad 2.14$$

Where λ_{PDGF} is the chemotaxis strength coefficient, $[PDGF](\vec{x})$ is the concentration of PDGF at the source site and $[PDGF](\vec{x}')$ is the concentration at the target site. Fibroblast migration is directed by orientation of ECM fibres and they travel along the ECM through integrin-collagen adhesions (McDougall *et al.*, 2006). To model this effect of ECM fibres on cell migration, the chemotaxis strength coefficient was increased to $\lambda_{PDGF(ECM)}$ for fibroblasts and myofibroblasts in contact with ECM.

Macrophages, which are involved in immune surveillance for senescent cells, chemotax towards the inflammation field produced by senescent cells (Vannella and Wynn, 2017). Similar to PDGF, chemotaxis is represented as,

$$\Delta E_{INF} = -\lambda_{INF}([INF](\vec{x}) - [INF](\vec{x}')) \quad 2.15$$

2.2.8 ***Model parameter estimation***

One of the most important constructs when modelling are the parameters – values which alter the model behaviour as presented in the equations describing model mechanics, as well as the various threshold parameters described thus far. Model parameters were obtained from literature where possible. However, direct experimental measurements or accurate estimates were not always available (Table 2.2). Therefore, where experimental evidence was available, parameter values were obtained from qualitative sources from literature. Where this was not possible, parameter values were simulated from theoretically sound estimates to produce a biologically reasonable representation of the tissue repair process based on the information gathered from literature. For parameters for which even an estimate is challenging, Particle Swarm Optimisation (PSO) was used by fitting the model behaviour to data gathered from literature shown in Figure 2.10 for fibroblasts, macrophages, myofibroblasts, senescent myofibroblasts and the rate of wound closure.

2.2.8.1 PSO algorithm

PSO is an algorithm commonly used in computational modelling to identify likely values for parameters. The PSO algorithm solves for parameters by using populations of candidate solutions,

called swarms, and a measure of the quality of candidate solutions (Figure 2.9) (Bonyadi and Michalewicz, 2017). PSO was chosen because it is suitable for large parameter spaces as it makes very few assumptions about the system being optimised. Particles move around the search space following a protocol that updates its position and velocity based on the fitness measure. The fitness measure in this case was taken as the quality of fit in the form of relative error between the experimental data points (Figure 2.10) and model simulation output. A particle's movement depends on its own previous best-known position as well as the best-known position across the swarm. This moves the swarm towards the best-known solution. The stepwise movement of each particle is independent of the others, which allows for parallelisation. The direction from a particular particle's current position to the best solution the particle has found so far, $pbest$, is given as,

$$pbest(i,t) = \underset{\substack{k=1,\dots,t \\ i=1,\dots,N_p}}{\arg min}\left[f\left(Pi(k)\right)\right], \tag{2.16}$$

Similarly, $gbest$ is the direction to the best candidate solution across the swarm given and is given as,

$$gbest(t) = \underset{\substack{k=1,\dots,t \\ i=1,\dots,N_p}}{\arg \min}\left[f\left(Pi(k)\right)\right] \tag{2.17}$$

Where i is the particle's index, N_p is the total number of particles, t is the current iteration number and f is the fitness function which rewards candidate solutions with a good quality of fit. P is the position and V is velocity given by,

$$V_i(t+1) = \omega V_i(t) + c_1 r_1\left(pbest(i,t) - P_i(t)\right) + c_2 r_2\left(gbest(t) - P_i(t)\right) \tag{2.18}$$

$$P_i(t+1) = P_i(t) + V_i(t+1) \tag{2.19}$$

Where ω is the inertia weight used to balance the particle's momentum, i.e., the speed and direction of the search; c_1 and c_2 are acceleration coefficients, both positive constant parameters that control the weight to be given between refining the search result locally and exploring the search result of the swarm. Lastly, r_1 and r_2 are uniformly distributed random variables within the rage [0,1] (Zhang, Wang and Ji, 2015). Values for the parameters used for PSO include: ω =

0.73, c_1 = 1.50 and c_2 = 1.50. The total number of swarms was 2, with 16 particles each and 2 duplicate runs (since CC3D simulations are stochastic) which were run for 60 iterations. Model parameter ranges for optimisation were determined by running the initial model several times with various parameter sets. The final set of ranges is summarised in Table 2.2. Parameter estimation using PSO for this model was run on a Linux cluster hosted by Indiana University.

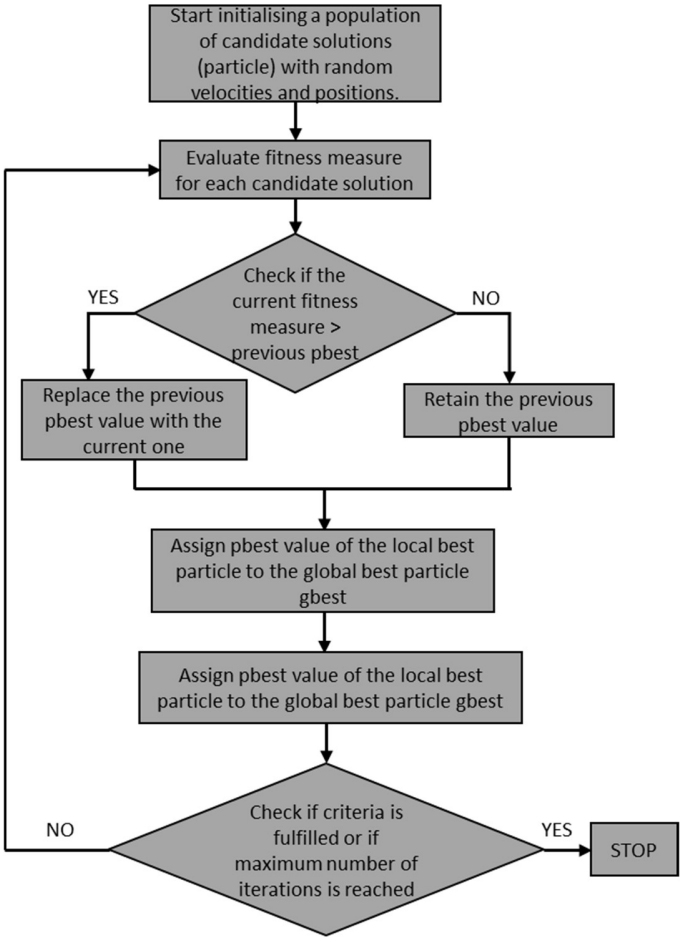

Figure 2.9 **The principle behind the PSO algorithm for parameter estimation**. Adapted from (Bonyadi and Michalewicz, 2017).

2.2.8.2 Data used for PSO

Quality of fit for candidate solutions was determined using relative error between simulation output and data from literature where possible, as mentioned previously. This includes cell population profiles for fibroblasts, myofibroblasts, macrophages and senescent myofibroblasts, ECM production and rate of wound closure, which are shown in Figure 2.10.

Fibroblast and macrophage curves were informed using a study by Zhou et al., where an *in vitro* system of murine fibroblasts and macrophages, interacting via growth factor exchange (PDGF for fibroblasts and CSF for macrophages), was used to investigate the stability of the two-cell circuit (Zhou *et al.*, 2018). The results from this study, which showed that fibroblasts and macrophages form a stable cell circuit, was also used in another study by Adler et al. to investigate the myofibroblast and macrophage cell circuit in tissue repair and fibrosis (Adler *et al.*, 2020). Hence, this data was used, along with the curves depicting the timeline of cellular activity from Witte et al., to inform the fibroblast and macrophage curves (Witte and Barbul, 1997).

The curve for senescent myofibroblasts was informed using the data from Jun et al., where a mouse model of cutaneous wound healing was used to investigate CCN1-induced senescence in wound healing and fibrosis (Jun and Lau, 2010). The study reported that senescent cells, which constituted 15% of all cells, accumulated in wounds between 7-9 days post-wounding; these senescent cells were identified as myofibroblasts through biomarkers. The curve for myofibroblasts was obtained from McAndrews et al. where a murine wound healing model was used to investigate myofibroblast function in wound healing (McAndrews *et al.*, 2022). This study was used since the murine wound experimental work provided time-course data of αSMA-positive cells and wound area, with the time points investigated being comparable to the wound healing model's time scale (~18 days).

The rate of wound closure curve for human wounds was obtained from Bain et al. (Bain *et al.*, 2019). Acquiring ECM data was particularly challenging since most studies investigate particular types of collagen or other components of the ECM, which have crucial functions in the wound healing process. For the sake of simplicity and computational feasibility, ECM in this model was considered as a single entity, instead of modelling each component explicitly. Because of this, the curve for ECM was informed by Adler et al. (Adler *et al.*, 2020), where a computational model of tissue repair included ECM modelled as a single entity, and Urciuolo et al. (Urciuolo *et al.*, 2022) which provides a schematic of ECM components across the wound healing process. The data was calibrated and converted to numerical data using the online tool WebPlotDigitizer (Ankit Rohatgi, 2022).

Model parameter ranges for PSO were selected with the aim of minimising the time and iterations required by the PSO algorithm to converge to an appropriate parameter set with minimal error. With that in mind, multiple preliminary PSO runs (10 prior runs of 2 swarms, with 16 particles each with 2 replicates and 60 iterations) led to the identification of optimal approximate parameter ranges as shown in Table 2.2.

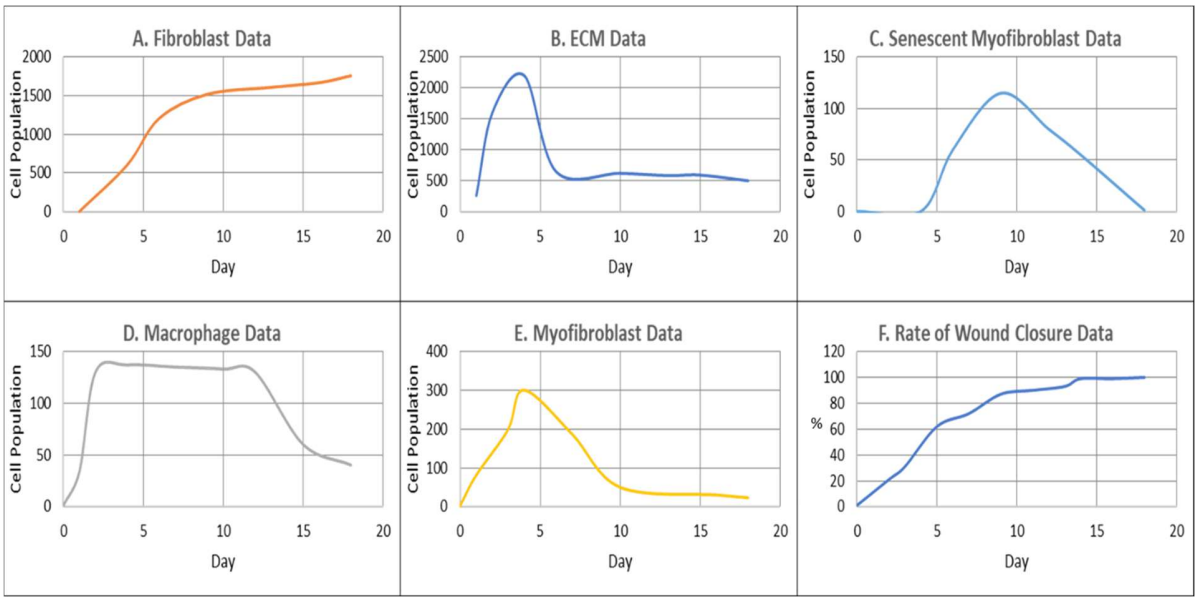

Figure 2.10 **Data used for PSO.** Curves show the timeline for cellular and ECM levels across the duration of wound healing, calibrated to the model. These curves were informed using existing studies, and are shown for **A:** Fibroblasts, **B:** ECM, **C:** Senescent myofibroblasts, **D:** Macrophages, **E:** Myofibroblasts, **F:** Rate of wound closure. Days are shown on the x axis and cell population and percentage of wound closure are shown on the y axis.

2.2.9 Simulation specifications

A baseline parameter set was established for all CPM parameters and model mechanisms described in the above sections. These are provided in Table 2.1 and Table 2.2. Simulation data was collected at a frequency of 500 MCS for each model run. Three replicate runs were performed.

Table 2.1 **Baseline parameter values and conversion factors for the wound healing model.**

Conversion Factors	Value	Reference/Rationale
Simulation time step Δt (MCS)	27 seconds	Cells in the simulation have an average speed of ~0.1 pixel/MCS (0.2 microns/MCS). This was determined by running multiple simulations of a cell without any hindrance

		and taking an average of the difference between the current and previous COM values (Fortuna *et al.*, 2020). As a reference, fibroblast migration speed during wound healing was considered, which peaks towards the end of the healing process with a speed of 40 µm/h (Shabestani Monfared, Ertl and Rothbauer, 2020). Therefore, 1 MCS was calculated to be 27 secs (0.3x3600/40).
1 voxel or pixel	3 µm	Selected based on diameters of cells.
Simulation lattice size	200 x 200 pixels	Varied and selected based on the appropriate size of the wound and computational feasibility.
Simulation Parameters	**Value**	**Reference/Rationale**
PDGF diffusion coefficient D_{PDGF}	0.01mm^2/h	Value selected was for diffusion through normal tissue (Haugh, 2006), but diffusion could be slower in dense ECM (Kihara, Ito and Miyake, 2013). Therefore, diffusion coefficient was taken to be 50% slower.
PDGF decay constant δ_{PDGF}	2/day	(Adler *et al.*, 2020)
MMP diffusion coefficient D_{CSF}	0.6x10^{8}cm^2 /s	Diffusion coefficient for MMP 9 on collagen fibrils (Collier *et al.*, 2011)
MMP decay constant δ_{MMP}	2x10^{-3}/s	(Saitou *et al.*, 2012), (Uekita *et al.*, 2001)
Inflammatory cytokine diffusion coefficient D_{INF}	0.01mm^2/h	Used the same value as the diffusion coefficient of PDGF since some inflammatory interleukins and PDGF have similar molecular weights (Li *et al.*, 2009; Kihara, Ito and Miyake, 2013)
Inflammatory cytokine decay constant δ_{INF}	2/day	Used the same value as the decay constant of PDGF since some inflammatory interleukins and PDGF have similar molecular weights
CSF diffusion coefficient D_{CSF}	3.33x10^{-3} mm^2/h	Molecular weight of CSF is 60 kDa, therefore diffusion coefficient was assumed to be 1/3rd that of PDGF (Li *et al.*, 2009; Kihara, Ito and Miyake, 2013)
CSF decay constant δ_{CSF}	2/day	(Adler *et al.*, 2020)

PDGF secretion rate S_{PDGF}	1	Estimated
MMP secretion rate S_{MMP}	1	Estimated
Inflammatory cytokine secretion rate S_{INF}	1	Estimated
CSF secretion rate S_{CSF}	1	Estimated
PDGF molecular weight	30 kDa	(Cochran, 1985)
CSF molecular weight	60 kDa	(Hornbeck *et al.*, 2015)
Inflammatory cytokine molecular weight	23 kDa	Estimated to be the molecular weight of interleukins (Hornbeck *et al.*, 2015)
MMP molecular weight	80 kDa	Estimated to be the molecular weight of MMP9 (Hornbeck *et al.*, 2015)
Fibroblast target volume	196 μm^2	Unit for 2D simulation (Freitas Robert A, 1999)
Fibroblast target surface	56 µm	Unit for 2D simulation (Freitas Robert A, 1999)
Macrophage target volume	324 μm^2	Unit for 2D simulation (BNID103565)
Macrophage target surface	72 µm	Unit for 2D simulation (BNID103565)
Senescent fibroblast target volume	196 μm^2	Unit for 2D simulation (BNID108244)
Senescent fibroblast target surface	56 µm	Unit for 2D simulation (BNID108244)
Myofibroblast target volume	324 μm^2	Unit for 2D simulation. (Estimate)
Myofibroblast target surface	72 µm	Unit for 2D simulation. (Estimate)
Lambda volume λ_{vol}	2	Same lambda volume value was used for all cells for appropriate cell volume deformation (Estimate)
Lambda surface λ_{surf}	2	Same lambda surface value was used for all cells for appropriate cell surface deformation (Estimate)
Probability of myofibroblast senescence	0.15	Previous work has shown that the percentage of senescent myofibroblasts in healthy wound healing was ~15-18% (Jun

P_{SNC}		and Lau, 2010)
Probability of myofibroblast differentiation P_{MF}	0.2	Percentage of myofibroblast cells in wound healing has previously been shown to be approximately ~20-25% (Volk *et al.*, 2011)
PDGF concentration at half maximum fibroblast growth $PDGF_0$	49.8 pg/ml	(Cochran, 1985)
CSF concentration at half maximum macrophage growth CSF_0	141.15 pg/ml	(Adler *et al.*, 2020)
Fibroblast max growth rate $G_{\max(F,MF)}$	0.9/day	(Adler *et al.*, 2020)
Macrophage max growth rate $G_{max(M)}$	0.8/day	(Adler *et al.*, 2020)
Fibroblast activation PDGF threshold $PDGF_f$	0.5	Estimated
Myofibroblast juxtacrine senescence PDGF threshold SNC_{thr}	Varied.	Estimated using PSO
Proteinase threshold for ECM breakdown MMP_{thr}	Varied	Estimated using PSO
Myofibroblast deactivation ECM threshold ECM_{thr}	Varied	Estimated using PSO
Inflammatory SASP threshold INF_{thr}	Varied	Estimated using PSO
CSF threshold for macrophage depletion CSF_{thr}	Varied	Estimated using PSO
Contact inhibition threshold T_{CI}	0.05	(Li and Lowengrub, 2014)

Base macrophage and fibroblast removal rate (apart from cell death due to growth factor depletion) μ	1 cell/3.3 days	(Adler *et al.*, 2020)
Probability of senescent cell clearance through immune surveillance by macrophages; removal by other immune cells not explicitly modelled	50%; 50%	Estimated
Duration of notch induced senescence T_{NIS}	3 days	Preliminary work suggests that NOTCH-mediated juxtacrine secondary senescence induction and fibrogenic SASP are prevalent up to approximately 3 days (Hoare *et al.*, 2016; Teo *et al.*, 2019)
Senescence induction time constraint T_{SEN}	12 days	Estimated
Rate of ECM production by myofibroblasts ECM_{Myof}	2 cells	Selected to be most appropriate after running multiple preliminary model simulations with different parameter values.
Rate of ECM production by fibroblasts ECM_{Fib}	1 cell	Selected to be most appropriate after running multiple preliminary model simulations with different parameter values.
Probability of Myofibroblast de-differentiation; myofibroblast apoptosis	50%; 50%	Approximated from (Kato *et al.*, 2020)
Cell membrane fluctuation amplitude T_m	30	Estimated

Adhesion energies J						
Cell Type	Medium	Fibroblast	Myofibroblast	Macrophage	Senescent fibroblast	ECM

Medium	0	1	-1	-2	-1	-1
Fibroblast	--	2	1	-1	2	1
Myofibroblast	--	--	-1	-1	-1	1
Macrophage	--	--	--	2	-1	1
Senescent fibroblast	--	--	--	--	5	1
ECM	--	--	--	--	--	-2

2.3 Results

2.3.1 A multiscale model of healthy wound healing including senescent cell dynamics

This chapter presents the development of a computational model of healthy wound healing that includes the dynamics of senescent cells and their interactions with the different components of the wound healing process. A multiscale model was built using CompuCell3D, which is a modelling environment based on the lattice-based CPM framework (Swat *et al.*, 2012). The model includes cells, growth factors and cytokines crucial for the wound healing process. Furthermore, in contrast to existing computational models of wound healing, this model includes the dynamics of senescent cells and key SASP components involved in the healing process.

Briefly, cell types within the model were represented by collections of pixels with unique identifiers. Cells interact with each other based on parameters that were obtained from literature or estimated. The parameters steer model behaviour through the effective energy or Hamiltonian equation given as:

$$H = \sum_{\vec{i},\vec{j}} J(\tau(\sigma_{\vec{i}}),\tau(\sigma_{\vec{j}}))(1-\delta(\sigma_{\vec{i}},\sigma_{\vec{j}})) + \sum_{\sigma} \lambda_{vol}(\sigma)\big(v(\sigma)-V_t(\sigma)\big)^2 + \sum_{\sigma} \lambda_{surf}(\sigma)\big(s(\sigma)-S_t(\sigma)\big)^2 + \Delta E_{PDGF} + \Delta E_{INF} \qquad 2.20$$

Where each cell σ possesses a cell type $\tau(\sigma)$ and is represented by pixels *i* and *j*. The first term in the Hamiltonian equation represents intercellular adhesion, where J is the contact energy between cells at *i* and *j*, and δ is the Kronecker delta function which ensures that only contact energies between pixels from different cells are included in the energy calculation. The second and third terms describe the volume and surface area of cells, where $v(\sigma)$ and s(σ) are the number of pixels within a cell and comprising the cell perimeter, respectively. $V_t(\sigma)$ and $S_t(\sigma)$ are the target volume and target surface, respectively, whereas $\lambda_{vol}(\sigma)$ and $\lambda_{surf}(\sigma)$ are volume and surface constraints, respectively. The last two terms in the equation represent cell chemotaxis towards the PDGF and inflammation chemical fields.

The simulation evolves stochastically through a Monte Carlo method by minimising the effective energy at individual sites. At each time step, the algorithm randomly selects a source site $\vec{\imath}$ and a

target site $\vec{\imath}\,'$. The change in the effective energy ΔH required to copy the index from the source to the target site is then calculated, which in turn determines the probability of accepting a new model configuration. Growth factors and cytokines within the model were defined using reaction diffusion PDEs as described in section 2.2.6.

2.3.2 Parameter estimation using PSO

The wound healing model had a large number of parameters, some of which were obtained from literature, summarised in Table 2.1, whereas others were estimated using PSO. The protocol for this is described in the methods section 2.2.8 and in Figure 2.9. Briefly, PSO requires a measure of quality for candidate solutions, known as particles. Quality of fit of candidate solutions for the model was determined using relative error between simulation data and data from existing studies, shown in Figure 2.10. The aim of PSO here was to minimise the error between simulation data points and experimental data. Particles move around the search space following a protocol that updates its position and velocity based on the fitness measure. A particle's movement depends on its own previous best-known position as well as the best-known position across the swarm.

The best parameter sets identified by PSO are given in Table 2.2. Summary of the output from running PSO is given in Table A.1 in Appendix A. PSO was run for a total of 60 iterations, and the best parameter set was found at the 46th iteration. Parameters initially start with random values resulting in poor quality of fit, which appeared to be associated with a high amount of run-to-run variability as shown in Figure 2.11. Eventually, parameter sets with better quality of fit were found following iteration 15, which show low run-to-run variability. Parameter values from swarm 1 were used for the final model as it had a slightly better fitness measure (relative error of 27.84). Plots of the resulting simulation data, plotted against data used for calibration for fibroblasts, senescent fibroblasts, myofibroblasts, ECM, macrophages and wound closure rate are shown in Figure 2.13A-F, along with the simulation cell field in Figure 2.12 showing a successfully healed wound. Despite the effort put into making the model parameters as physiologically and biologically relevant as possible, it was not possible to match or find appropriate data for some parameters. For these, parameter values were simulated from theoretically sound estimates to produce a biologically reasonable representation of the wound healing process based on information gathered from literature, as previously stated and provided in Table 2.1.

Table 2.2 **Summary of PSO output for individual swarms.** PSO was run with 2 swarms, 16 particles each, for 60 iterations. The best particle (i.e., parameter set) was identified at iteration 46, and is shown in the table. Swarm 1, which has a slightly lower relative error, was chosen to be used with the baseline parameter set.

Parameter	**Swarm 1**	**Swarm 2**	**Relative standard deviation (%)**	**Min**	**Max**
Fibroblast activation PDGF threshold ($PDGF_f$)	8.1044e-02	5.7022e-02	17.4%	0.05	2.0
PDGF concentration threshold for myofibroblast juxtacrine senescence (SNC_{thr})	4.2876e+00	4.7675e+00	5.3%	1.0	5.0
Proteinase threshold for ECM breakdown (MMP_{thr})	2.0926e-02	2.1085e-02	0.4%	0.02	2.0
Myofibroblast deactivation ECM threshold (ECM_{thr})	8.0205e+00	8.7545e+00	4.4%	5.0	11.0
Inflammation threshold (INF_{thr})	2.3734e+00	2.8003e+00	8.3%	1.0	3.0
CSF threshold for macrophage depletion (CSF_{thr})	3.2847e+00	3.3808e+00	1.4%	2.0	5.0
Relative error value	27.84	27.92	--	--	--

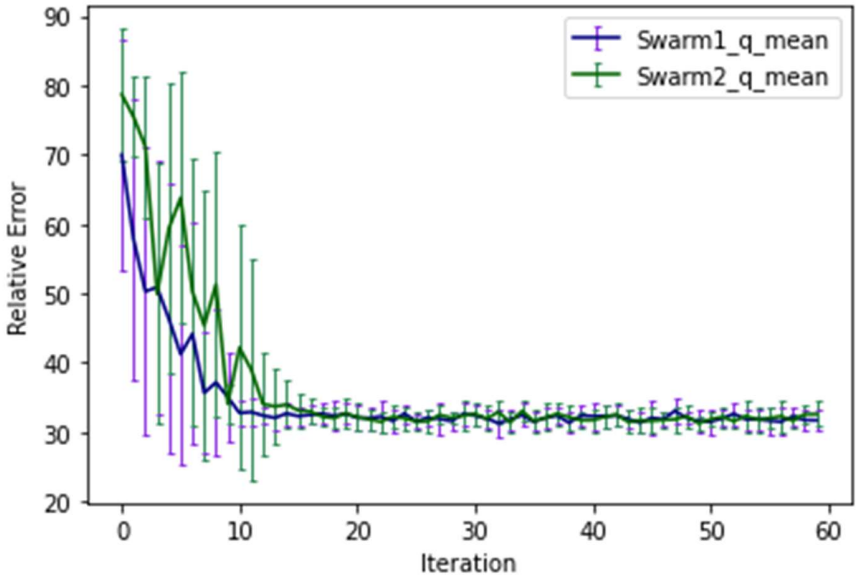

Figure 2.11 Plot of relative error for the best particle (parameter set) for each swarm across the iterations. PSO was run with 2 swarms, 16 particles each for 60 iterations. Each point in the plot represents the average fitness measure across all particles in swarms 1 and 2 for each iteration. Error bars represent standard deviation for the simulations performed for every iteration across the two swarms.

2.3.3 Healthy wound healing is accompanied by tightly controlled transient senescent cell activity

The model begins with a dermal layer consisting of fibroblasts and ECM along with a wound populated by anti-inflammatory M2 macrophages, representative of the end stages of the inflammatory phase of wound healing (Figure 2.12A). Anti-inflammatory M2 polarised macrophages are prevalent during the proliferative phase and are an important source of PDGF for fibroblasts. As a result, PDGF levels begin to rise steadily until approximately ~day 4 (Figure 2.14C), setting off a cascade of events that will eventually result in myofibroblast differentiation, which will be described hereafter. As the simulation progresses, fibroblasts proliferate in response to rising PDGF levels resulting in a steady increase in fibroblast numbers at around ~day 1 to day 5 after which it rises at a slower pace, corresponding to PDGF levels. which begin to subside at near ~day 4 (Figure 2.13A and Figure 2.14C).

PDGF also induces fibroblast activation, which leads to the production of CSF and ECM. This leads to rising CSF levels (Figure 2.14A), which results in macrophage proliferation and an increase in macrophage numbers by 2-fold, before reaching a plateau at ~day 3.5 (Figure 2.13E). Macrophage

numbers correspond to CSF levels, which begin to drop briefly around the same time (Figure 2.14A). Levels of ECM rise sharply at day 1, which is a simple representation of Type III collagen and FN-rich granulation tissue (Figure 2.13D). The production of ECM at this point, during the transition from inflammatory to proliferative phase, is an important source of mechanical stimulation which is necessary for myofibroblast differentiation of fibroblasts.

Appropriate PDGF levels and mechanical stimuli promote full myofibroblast differentiation of the activated fibroblasts. Myofibroblast numbers begin to rise at day 1, peaking at day 4 (Figure 2.13C). Myofibroblasts also produce large amounts of ECM, along with PDGF, in an autocrine manner, as well as CSF for macrophages. However, ECM levels plateau after a 0.7-fold drop at ~day 3 during this rise in myofibroblast levels, due to macrophage-derived MMP, which breaks down excess ECM (Figure 2.13D and Figure 2.14B). MMP levels also experience a decline due to its enzymatic activity on ECM and inhibition by myofibroblasts through TIMP activity. The plateau in ECM levels demonstrates a balance between ECM production by myofibroblasts and fibroblasts, and breakdown by MMPs. Myofibroblast numbers eventually begin to decline around day 4 by 0.5-fold, mediated by either apoptosis (due to release of mechanical tension), de-differentiation to a fibroblast phenotype or cellular senescence (Figure 2.13C).

Around the same time as the drop in myofibroblast numbers, the number of senescent myofibroblasts begins to rise at ~day 4, reaching a peak at ~day 7 (Figure 2.13B). Senescence is induced in myofibroblasts through the matricellular protein CCN1. During the first three days after becoming senescent, myofibroblasts produce a fibrogenic SASP consisting of PDGF and ECM. Due to this SASP regulation, ECM plateau is still maintained between ~day 4 to 7, as shown in Figure 2.13D, despite the drop in myofibroblast numbers. This fibrogenic SASP is also accompanied by juxtacrine-mediated induction of secondary senescence in neighbouring cells, which rises at ~day 4.5 and begins to drop at ~day 7.5 (Figure 2.13G). The model shows that this fibrogenic SASP phase of senescent myofibroblasts helps to maintain the existing fibrogenic state of the proliferative phase while controlling myofibroblast population through the induction of secondary senescence.

Senescent myofibroblasts then shift to the production of a fibrolytic SASP consisting of CSF, inflammatory SASP and MMP as shown by the sharp rises in these chemical fields at ~day 7 (Figure

2.14A, B, D). The significance of the prior short-lived fibrogenic phase is evident, since with the onset of the fibrolytic phase at ~day 7, PDGF levels begin to drop 0.6-fold, along with a 0.5-fold drop in ECM levels (Figure 2.13D, Figure 2.14C). The fibrolytic activity of senescent myofibroblasts following ~day 8 is crucial for wound remodelling, where ECM is produced and broken down eventually coming to an equilibrium as seen with the second plateau in ECM levels (Figure 2.13D). Inflammatory SASP field also promotes M1 polarisation of wound macrophages, further increasing MMP production to break down scar tissue. This phase is also accompanied by paracrine-mediated induction of senescence, which rises at ~day 9 just as levels of juxtacrine-induced senescent cell levels begin to decrease. Interestingly, compared to the almost 40-fold increase in juxtacrine-induced senescent cells, paracrine-induced cell number remained rather low with just less than 10-fold increase.

Most senescent cells are eventually removed by immune surveillance mechanisms such as macrophage phagocytosis. Nevertheless, some senescent cells continue to persist long after the wound has healed, where they continue to participate in wound remodelling (Figure 2.13B). Because of this, MMP levels also remain high to break down excess ECM (Figure 2.14B), along with inflammatory SASP levels which attract immune cells to further clear senescent cells (Figure 2.14D). Macrophages eventually undergo apoptosis at the time CSF levels drop due to growth factor depletion at ~day 18, when the wound is sufficiently clear of senescent cells (Figure 2.13E and Figure 2.14A).

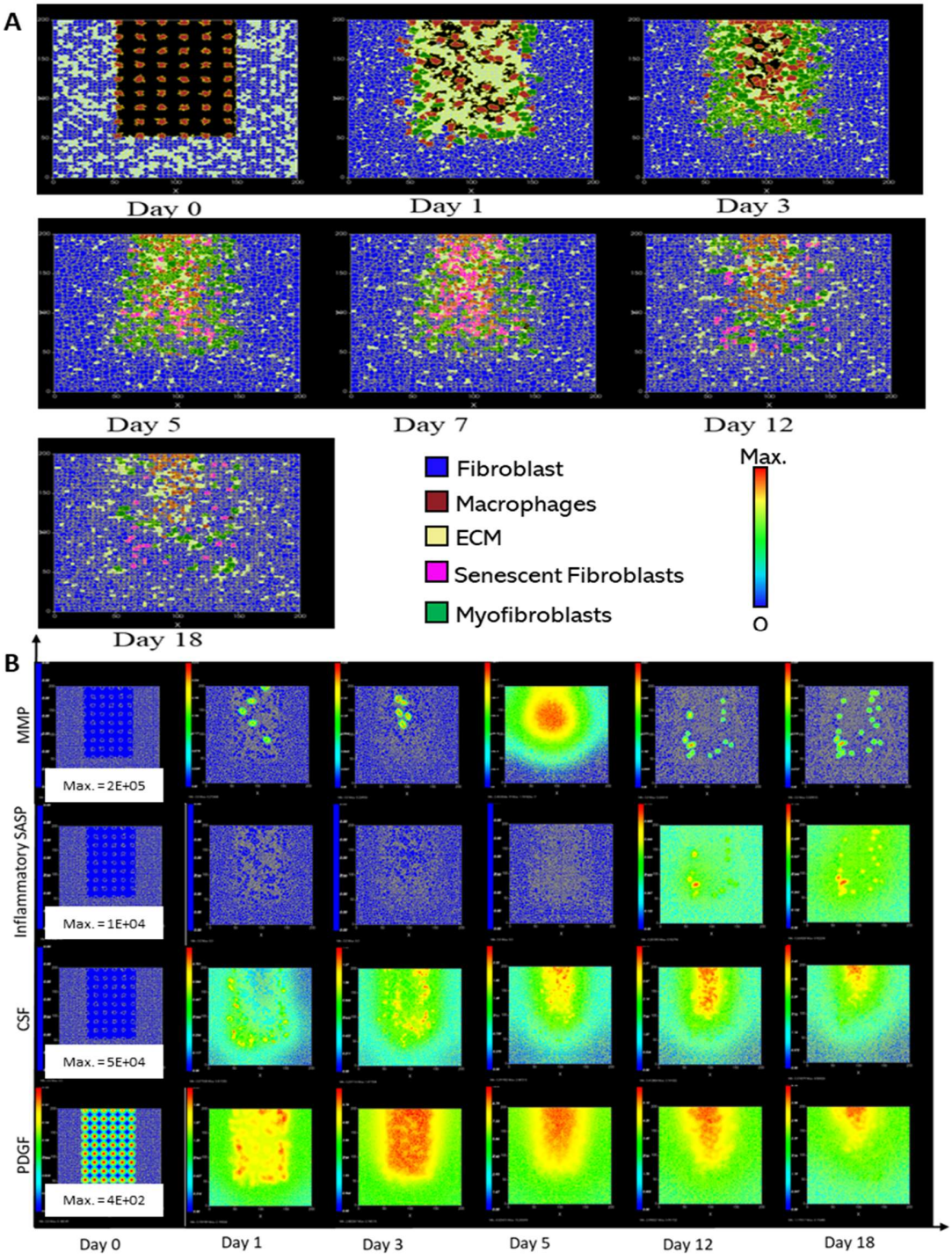

Figure 2.12 **Simulation of healthy physiological wound healing in a dermal patch of size 600 µm x 600 µm using the baseline parameters presented in Table 2.1.** This figure shows snapshots of spatial configuration *vs* time for the progression of a simulated wound healing process. The simulation represents healthy wound healing from the end of the inflammatory phase to the remodelling phase, including fibroblasts, myofibroblasts, macrophages, ECM and senescent myofibroblasts, as well as, chemical species including MMP, inflammatory SASP, CSF and PDGF.

A: Snapshots of the simulation cell field at different time points, representing a wounded dermal layer consisting of fibroblasts (blue), myofibroblasts (green), macrophages (brown), ECM (yellow) and senescent myofibroblasts (pink). Snapshots are shown for the time points day 0, 1, 3, 5, 7, 12 and 18. **B:** Snapshots of simulation chemical fields shown for the levels of MMP (top row), inflammatory SASP (second row), CSF (third row) and PDGF (last row), at time points, left to right: day 0, 1, 3, 5, 12 and 18. Fields are shaded where red corresponds to the maximum value specified in the first snapshot panel for each field, and blue corresponds to zero (shown in the colour bar).

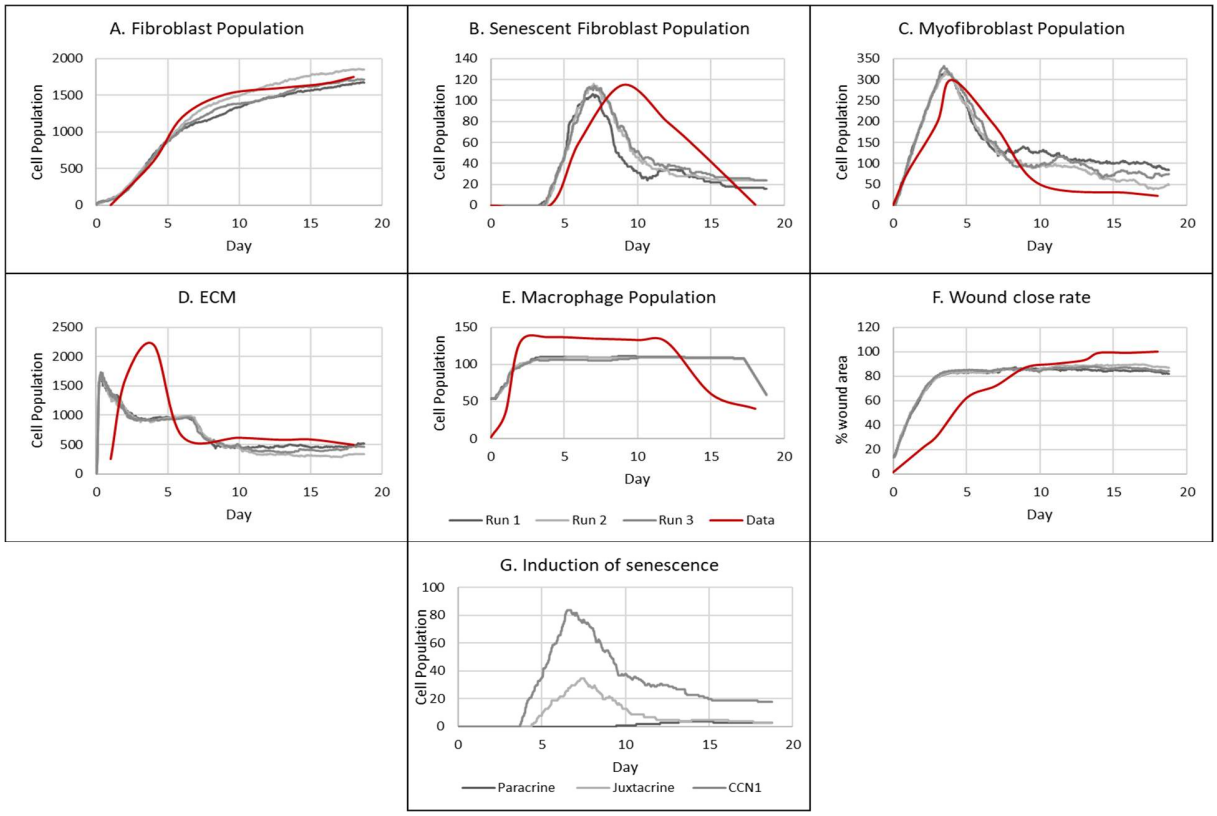

Figure 2.13 **Simulation time series for the model of healthy physiological wound healing in a dermal patch of size 600 µm x 600 µm using the baseline parameters presented in Table 2.1, shown for model cell types and rate of wound closure.** This figure shows the simulation time series for the progression of a simulated wound healing process, with number of cells or rate of wound closure on the y axis and time (day) on the x axis, shown for **A:** Fibroblasts, **B:** Senescent myofibroblasts, **C:** Myofibroblasts, **D:** ECM, **E:** Macrophages, **F:** Wound closure rate and **G:** Mechanism of senescence induction. For the time series plots A-F, the three shades of grey represent the different replicate runs as indicated below plot E (since the model is stochastic); the red line represents data used for parameter estimation using PSO informed by existing studies, as shown in Figure 2.10. For the plot G, different shades of grey represent the different mechanisms of senescence induction, as indicated below the plot; dark grey: paracrine secondary senescence; light grey: juxtacrine secondary senescence; and medium grey: CCN1-induced primary senescence. Replicate runs are not shown for the different mechanisms for ease of

readability, but total senescent cell numbers for the three replicate runs are shown in plot B, as explained.

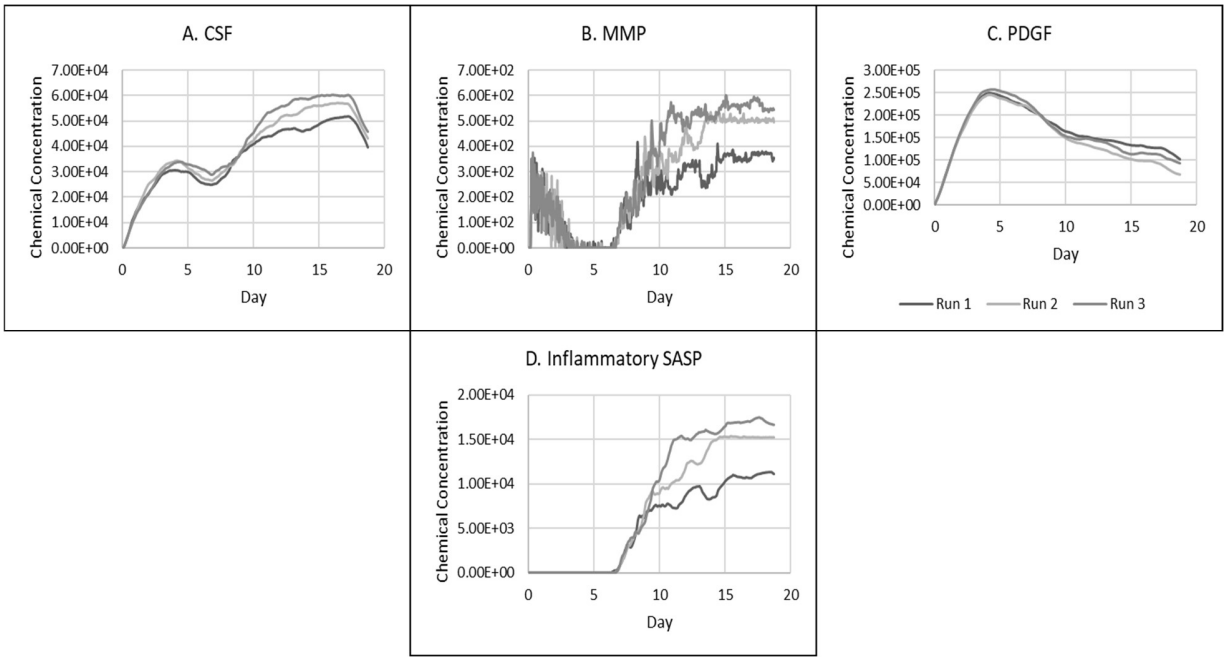

Figure 2.14 **Simulation time series for the model of healthy physiological wound healing in a dermal patch of size 600 µm x 600 µm using the baseline parameters presented in Table 2.1, shown for model chemical fields.** This figure shows the simulation time series for the progression of a simulated wound healing process, with total chemical field on the y axis and time (day) on the x axis, shown for **A:** CSF, **B:** MMP, **C:** PDGF and **D:** Inflammatory SASP. The three shades of grey represent the different replicate runs as indicated below plot C, since the model is stochastic.

2.4 Discussion

Cellular senescence is a complex stress response that is accompanied by irreversible growth arrest, phenotypic, metabolic, and secretory changes including the production of several cytokines, growth factors and MMPs, collectively known as SASP. Senescent cells accumulate with age and are thought to drive age-related pathology through the SASP (Gorgoulis *et al.*, 2019). However, they also play important physiological roles such as cancer suppression, embryogenesis, and tissue repair and wound healing (Muñoz-Espín and Serrano, 2014). On the other hand, wound healing is also a complex and tightly regulated process that generally consists of four discrete but overlapping phases that occur sequentially (Singer and Clark, 1999). Briefly, the first two phases, haemostasis and inflammation, involve coagulation mediated by platelets, which also secrete cytokines and chemokines to attract macrophages and neutrophils to the wound site. The inflammation phase ends with the recruitment of fibroblasts and revascularisation of the wound. This is followed by the proliferation phase which begins with the formation of granulation tissue. During this phase, re-epithelialisation takes place and fibroblasts differentiate into myofibroblasts, which are highly contractile cells responsible for wound contraction and ECM deposition. Lastly, ECM remodelling takes place whereby ECM is produced, and excess is broken down, resulting in tissue with mature matrix organisation and tensile strength (Witte and Barbul, 1997; Rodrigues *et al.*, 2019; Wilkinson and Hardman, 2020).

Senescent cells transiently appear during the mid to late stages of wound healing and are removed by the immune system during the remodelling phase. Several SASP factors, including PDGF and MMPs, play important roles in maintaining tissue homeostasis during the repair process (Muñoz-Espín and Serrano, 2014). Senescent cells have been shown to mitigate fibrosis during tissue repair in the skin, liver, heart and kidney (Krizhanovsky *et al.*, 2008; Jun and Lau, 2010; Wolstein *et al.*, 2010a; Meyer *et al.*, 2016). Aside from being an anti-fibrotic mechanism, they also promote myofibroblast differentiation through SASP, which is crucial for ECM production and dermal wound closure (Demaria *et al.*, 2014). With that said, the aim of this work was to investigate the spatiotemporal dynamics of senescent cells and SASP within the wound healing process. To that end, a CPM including key aspects of wound healing and senescent cell dynamics was developed.

Since the primary focus of the model was on senescent cell dynamics, while capturing key events in dermal wound healing, it was assumed reasonable to restrict the model to the final stages of the inflammatory phase to the remodelling phase. This was done to make the model more computationally feasible. The model starts with a dermal layer consisting of fibroblasts and ECM along with a wound populated by anti-inflammatory M2 macrophages (Figure 2.12). This is representative of the end stages of the inflammatory phase of wound healing, where M2 macrophages (specifically M2b) have been found to be prevalent (Filardy *et al.*, 2010). M2 macrophages are crucial during the proliferative phase and are an important source of growth factors, especially PDGF for fibroblasts (Krzyszczyk *et al.*, 2018; Adler *et al.*, 2020). In the model, macrophage-derived PDGF levels begin to rise rapidly until ~day 4 (Figure 2.14C), setting off a cascade of processes that will eventually result in myofibroblast differentiation. Fibroblasts proliferate in response to rising PDGF levels resulting in a steady increase in fibroblast numbers at ~day 1, after which it rises at a slower pace following a drop in PDGF levels at ~day 4 (Figure 2.13A and Figure 2.14C). Previous studies have shown that PDGF is a key mediator of fibroblast migration and proliferation (Beer, Longaker and Werner, 1997; Juhl et al., 2020).

Aside from proliferation, PDGF induces fibroblast activation from quiescence in the model, which leads to the production of CSF and ECM. PDGF has been reported to induce CSF production in murine stromal and fibroblast cells (Falkenburg *et al.*, 1990; Abboud and Pinzani, 1991). Rising CSF levels (Figure 2.14A) result in macrophage proliferation with an increase in macrophage numbers by 2-fold before reaching a plateau at ~day 3.5 (Figure 2.13E). This corresponds to CSF levels which begin to drop briefly around the same time. Levels of ECM rise sharply at day 1, as a simple representation of Type III collagen and FN-rich granulation tissue. Indeed, PDGF can induce Type III collagen expression in fibroblasts, a crucial component of granulation tissue (Juhl *et al.*, 2020). The production of ECM at this point is an important source of the mechanical stimulation necessary for full differentiation into myofibroblast (Tomasek *et al.*, 2002).

Myofibroblast numbers begin to rise due to PDGF and mechanical stimulation. They produce large amounts of ECM along with PDGF and CSF. However, ECM levels plateau after a drop at ~day 3 despite the rise in myofibroblast levels, likely due to M1-polarised macrophage derived MMP, which breaks down excess ECM (Figure 2.13D and Figure 2.14B). Levels of MMP also drop due to its enzymatic activity. This demonstrates that macrophage plasticity in response to different

stimuli is crucial in creating a balance between fibrogenic and fibrolytic processes during wound healing. The plateau in ECM levels indicates an equilibrium between ECM production by myofibroblasts and fibroblasts, and its break down by macrophage-derived MMPs. Macrophages here are stimulated to produce MMP through contact with ECM; indeed, macrophages are induced to secrete MMPs through matrix protein stimulation (Shapiro, Kobayashi and Ley, 1993). Myofibroblast numbers drop around day 4 through three mechanisms which have been previously reported: apoptosis (as a consequence of the release of mechanical tension), de-differentiation to a fibroblast phenotype or cellular senescence (Figure 2.13C) (Hinz and Lagares, 2019).

Senescent myofibroblasts begin to emerge at ~day 4 and peak at ~day 7 through CCN1 stimulation (Figure 2.13B) (Jun and Lau, 2010). During the first three days after the induction of senescence, senescent myofibroblasts produce a fibrogenic SASP consisting of PDGF and ECM. As previously explained in section 2.2, preliminary work suggests that NOTCH-mediated juxtacrine secondary senescence induction and fibrogenic SASP are prevalent up to approximately three days following induction (Hoare *et al.*, 2016; Teo *et al.*, 2019). Due to this fibrogenic SASP, ECM plateau is still maintained between ~day 4 to 7 despite a drop in myofibroblast numbers, demonstrating that senescent cells here may assist in maintaining tissue integrity while controlling the myofibroblast population, however, this needs to be experimentally validated. The fibrogenic SASP at this point is also accompanied by juxtacrine secondary senescence in neighbouring cells, which rises at ~day 4.7 and begins to drop at ~day 7.5 (Figure 2.13G).

Subsequently, senescent myofibroblasts shift to the production of a fibrolytic SASP consisting of CSF, Inflammation and MMP around ~day 7 (Figure 2.14A, B, D). As expected, the onset of the fibrolytic phase was accompanied by a decrease in ECM and PDGF levels at ~day 7 (Figure 2.13D, Figure 2.14C). This demonstrates how the fibrogenic SASP is able to augment the existing fibrogenic activity of the proliferative phase. The fibrolytic activity of senescent myofibroblasts following ~day 8 is crucial for wound remodelling, which involves breaking down and producing ECM, as seen with the second plateau in ECM levels (Figure 2.13D). Inflammatory SASP also promotes M1 polarisation of wound macrophages, further increasing MMP production to break down scar tissue. This phase is also accompanied by paracrine-mediated induction of senescence,

which begins to increase just as levels of juxtacrine-induced senescent cell levels begin to decrease.

Interestingly, compared to the increase in juxtacrine-induced senescent cells, paracrine-induced senescent cell number remained rather low, according to the model. Higher levels of juxtacrine-induced senescence, compared to paracrine, in this healthy healing model was unsurprising since most deleterious effects of senescent cells, including dysregulated repair and regeneration, age-related pathology and enhanced tumorigenesis, are mediated by the paracrine-induced spread of senescence (Campisi, 2005; Ferreira-Gonzalez *et al.*, 2018; Gonzalez-Meljem *et al.*, 2018; De-Carvalho, Jacinto and Saúde, 2021). Moreover, the prevalence of juxtacrine senescence, which can only be laterally induced through NOTCH action, could explain the local containment of senescent cells in wound healing, which can then easily be removed by immune cells as the wound resolves. Indeed, the ability of juxtacrine-induced secondary senescence to contain the spread of senescence, compared to paracrine-induced senescence, was recently demonstrated using computational modelling (Martin, Schumacher and Chandra, 2023).

Although most senescent cells are eventually removed by immune cells including macrophages, some senescent cells persist long after the wound has healed, where they continue to participate in wound remodelling (Figure 2.13B) (Hinz and Lagares, 2019). Because of this, MMP levels also remain high to break down excess ECM (Figure 2.14B), along with inflammatory SASP levels, which attract immune cells to clear senescent cells (Figure 2.14D). Macrophages eventually undergo apoptosis at the time CSF levels drop due to growth factor depletion when the wound is sufficiently clear of senescent cells (Figure 2.13E and Figure 2.14A). Overall, these results demonstrate the mechanisms behind the tightly controlled and transient nature of senescent cells in healthy wound healing, and the model output is in agreement with literature as discussed here. However, these results need to be experimentally validated, but can be used as a base for further development or to inform experimental work.

The wound healing process is so tightly controlled that dysregulation in any of the phases can result in conditions such as fibrosis and chronic wounds. Fibrosis can occur in multiple organ types and is a result of more ECM being produced than degraded during the late proliferative, and remodelling phases of repair (Wynn, 2008). On the contrary, chronic wounds are those that

persist in the inflammatory phase unable to proceed to the proliferative phase, with insufficient proliferation and ECM deposition (Zhao *et al.*, 2016).

Aside from their role in physiological wound healing, senescent cells have been implicated in the pathophysiology of fibrotic conditions across several organ systems including lung, heart and liver fibrosis (Zhu *et al.*, 2013; Ogrodnik *et al.*, 2017; Schafer *et al.*, 2017). Interestingly, the accumulation of senescent cells has also been linked to the development of chronic wounds (Mendez et al., 1998; Stanley and Osler, 2001; vande Berg et al., 2005). Furthermore, the risk of both fibrosis and chronic wounds increases with age, which is accompanied by an accumulation of senescent cells (Kapetanaki, Mora and Rojas, 2013). On the one hand, the absence of senescent cells impairs wound healing, promotes pro-fibrotic activity and tumorigenesis, and on the other hand, an excess results in unresolved inflammation. This is further complicated by the temporal regulation of SASP by Notch signalling where the initial portion of the senescence programme involves a fibrogenic SASP, followed by a shift to a fibrolytic SASP (Hoare *et al.*, 2016). The different spatiotemporal dynamics of senescent cells during repair could steer the process towards different outcomes, including healthy repair or a tendency towards fibrosis or chronic inflammation. This aspect of the role of senescent cells in dysregulated tissue repair will be explored further in the next chapter using the model developed here.

Chapter 3. Investigating the spatiotemporal dynamics of senescent cells in fibrosis and chronic wounds

3.1 Background

In this chapter, the effects of senescent cell dynamics in the context of tissue repair complications, including fibrosis and chronic wounds, will be explored using the wound healing model developed in Chapter 2. Briefly, the model includes the dynamics of senescent cell behaviour and corresponding SASP composition within the wound microenvironment, alongside other key components of the healing process, such as fibroblasts, ECM and macrophages.

3.1.1 Wound healing and tissue repair dysregulation

The repair process is tightly regulated and generally consists of four distinct but overlapping phases that occur sequentially (Singer and Clark, 1999). The first two phases, haemostasis, and inflammation, involve coagulation mediated by platelets, which will also secrete cytokines and chemokines to attract macrophages and neutrophils to the wound site. The inflammation phase ends with the recruitment of fibroblasts, and re-vascularisation of the wound. This is followed by the proliferation phase which begins with the formation of granulation tissue. During this phase, re-epithelialisation takes place and fibroblasts differentiate into myofibroblasts, which are highly contractile cells responsible for wound contraction and ECM deposition. Lastly, ECM remodelling takes place whereby ECM is produced, and excess is broken down, resulting in tissue with mature matrix organisation and tensile strength (Witte and Barbul, 1997).

Tissue repair is crucial to life, evidenced by various redundant and compensatory mechanisms that ensure that minor deviations from the tightly controlled processes involved are insufficient to result in major complications. For instance, removal of certain MMPs (Hartenstein *et al.*, 2006), specific stem cell subsets (Driskell *et al.*, 2015) or growth factors (Luetteke *et al.*, 1993; Guo, Degenstein and Fuchs, 1996) fails to substantially disrupt the repair process. However, sufficient, and appropriate perturbation to the system will lead to dysregulation which typically results in fibrotic scarring or chronic wound inflammation. Fibrosis can occur in multiple organ systems and appears when more ECM is produced than degraded during the late proliferative and remodelling phases of repair (Wynn, 2008). On the contrary, chronic wounds are those that persist in the

inflammatory phase, with insufficient ECM deposition (Zhao *et al.*, 2016). Simply put, fibrosis and chronic wounds can be viewed as “over-healed” and “under-healed” wounds respectively.

3.1.1.1 Fibrosis

As opposed to normal tissue repair, where myofibroblasts are cleared from the wound site following successful repair, fibrotic processes involve persisting myofibroblasts that are continually activated due to the cytokine, growth factor and mechanical milieu (Hinz and Lagares, 2019). This results in excessive ECM deposition, which not only increases tissue stiffness but also decreases oxygen diffusion, hence leading to further tissue damage (Beyer *et al.*, 2009). But in addition to excessive ECM, the fibrotic process is also accompanied by other dysfunctions. For instance, fibrosis due to repetitive injury results in epithelial cell apoptosis, leading to disrupted re-epithelialisation, and pathogenic fibroblast activation (Parimon *et al.*, 2020). Epithelial cells in fibrotic conditions also undergo epithelial-to-mesenchymal transition (EMT) more readily. EMT, which is an important source of myofibroblasts, not only reduces the number of normally functioning epithelial cells, but also promotes the production of ECM (Yao *et al.*, 2019).

Due to the increased proliferation and activation of fibroblasts in fibrotic processes, there is a higher demand for blood nutrients resulting in abnormal angiogenesis. For instance, amongst the endothelial cells that primarily constitute the blood vessels, there are subtypes specific to fibrotic conditions that have been identified in the liver where they promote leukocyte infiltration (Ramachandran *et al.*, 2019) and, in the lung, where they produce collagen alongside fibroblasts and myofibroblasts (Adams *et al.*, 2020). Aside from abnormal angiogenesis, aberrant immune system behaviour is also prevalent in fibrosis as an early event. Many immune cell types are involved in the pathogenesis of fibrosis, including macrophages, T-lymphocytes, granulocytes, and dendritic cells, which promote the progression of fibrosis by producing factors that lead to the activation of fibroblasts and their differentiation into myofibroblasts (Serezani *et al.*, 2022; Xue *et al.*, 2022). For example, in a pulmonary fibrosis mouse model, a subset of macrophages was identified adjacent to fibroblasts, promoting fibrosis through the production of PDGF as a mediator of fibroblast proliferation and activation (Aran *et al.*, 2019). Furthermore, another subset of macrophages identified in liver fibrosis promoted increased collagen production by HSCs (Ramachandran *et al.*, 2019).

The differentiation of fibroblasts into myofibroblasts is a key driver of fibrotic conditions. Specific myofibroblast function, including their secretome, the ability to produce large amounts of ECM, and contractile nature, plays an important role in the development and progression of fibrosis (Hinz and Lagares, 2019). Myofibroblasts are induced by factors produced by immune cells, the tissue mechanical environment, EMT, and endothelial-mesenchymal transition (EndMT) (Yuan, Tan and Liu, 2019). Intriguingly, myofibroblasts have been found to possess transcriptomic plasticity with dynamic changes in fibrotic processes across different organs (Farbehi *et al.*, 2019). For instance, lung fibroblasts in fibrotic pathological states use alternative differentiation pathways than those in normal tissue (Xie *et al.*, 2018). Furthermore, myofibroblasts in the fibrotic process have the capacity to evade apoptosis, which disrupts programmed cell death mechanisms and limits treatment efficacy (Maher *et al.*, 2010; Hinz and Lagares, 2019).

Equally, MMPs play important but diverse and complex functions in fibrosis, with both attenuating and augmenting effects on the fibrotic phenotype, depending on the type of MMP and organ system (Giannandrea and Parks, 2014). For instance, significantly decreased levels of MMP-1 collagenase have been found in skin biopsies from systemic sclerosis patients (Takeda *et al.*, 1994; Frost *et al.*, 2012; Zhou *et al.*, 2017). A possible mechanism for this could be pro-fibrotic microRNAs, such as microRNA-202-3p, which have been found to inhibit MMP-1 in skin from fibrosis patients (Zhou *et al.*, 2017). Likewise, genetically induced membrane type-1 matrix metalloproteinase-deficient mice develop skin fibrosis due to decreased Type I Collagen cleaving activity. Interestingly, tissue rigidity and external stiffness have been found to promote the downregulation of MMP-9, possibly through mechanosensitive TFs (Lachowski *et al.*, 2019). This not only perpetuates fibrosis but also results in a reinforcement of the fibrotic processes. The gelatinase MMP-2 is also anti-fibrotic, as shown by MMP-2 KO mice displaying increased fibrosis following experimentally induced liver fibrosis, compared to healthy mice (Onozuka *et al.*, 2011). On the contrary, some MMPs have pro-fibrotic effects. For instance, liver fibrosis is reduced in MMP-19 KO mice compared to WT mice (Jirouskova *et al.*, 2012), whilst MMP-3 KO mice display significantly decreased pulmonary fibrosis following bleomycin-induced fibrosis (Yamashita *et al.*, 2011).

Many growth factors, cytokines and signalling pathways come into play during fibrotic processes by influencing myofibroblast differentiation and functioning, ECM crosslinking, EMT and EndMT

(Zhao *et al.*, 2022). For instance, myofibroblasts in fibrosis are chronically activated through the upregulation of growth factors by activated immune cells and this is accompanied by increased EMT resulting in higher myofibroblast numbers. In turn, these myofibroblasts produce ECM unhindered and also exert contractile forces, further enhancing ECM production (Distler *et al.*, 2019; Kuehlmann *et al.*, 2020). The main growth factors involved in such fibrotic processes include include TGF-βs, PDGFs, FGFs and CTGF, with downstream effector pathways including PI3K/AKT, JAK/STAT and WNT/β-catenin (Zhao *et al.*, 2022).

3.1.1.2 Chronic wound inflammation

Chronic wounds are those that fail to heal appropriately and are a major cause for concern in the older population and the diabetic (Moura *et al.*, 2019). They are mainly driven by excessive inflammation, resulting in insufficient matrix production and matrix destruction. Chronic wounds typically contain elevated numbers of immune cells including pro-inflammatory macrophages (Loots *et al.*, 1998) and neutrophils (Diegelmann, 2003), and proteolytic enzymes (Wysocki, Staiano-Coico and Grinnell, 1993). Dysregulated immune cell function and pathological levels of immune cell subsets are typically involved in chronic wound inflammation. For instance, chronic wound macrophages are inefficient in efferocytosis and phagocytosis, which is necessary for the clearing out of pathogens, other immune cells and wound debris (Khanna *et al.*, 2010), and are ineffective in polarising to an anti-inflammatory M2 phenotype (Bannon *et al.*, 2013). Additionally, T cell diversity and numbers are greatly reduced in chronic wounds (Moura *et al.*, 2017). Overall, chronic wounds not only fail to progress past the inflammatory phase due to immune cell dysfunction but are also more susceptible to infections due to the chronic wound microenvironment. Pro-inflammatory factors are also upregulated in chronic wounds, for instance, GM-CSF has been found to be elevated in chronic wound fluid compared to acute wounds, where its pro-inflammatory abilities are amplified compared to healthy healing (Lacey *et al.*, 2012; Stacey *et al.*, 2019; Pulido, Velarde and Alimirah, 2021).

Aside from dysregulated inflammatory phase processes, chronic wounds also display aberrant tissue remodelling and re-epithelialisation. For instance, chronic wound edges are typically hyperproliferative with decreased migratory capability, resulting in incomplete keratinocyte differentiation and the presence of nuclei in a thick cornified layer, a condition known as hyper- and parakeratosis (Stojadinovic *et al.*, 2005). The attenuation of keratinocyte migration is driven

by abnormally high levels of nuclear β-catenin and increased c-myc, which leads to improper healing (Waikel *et al.*, 2001). Additionally chronic wound epidermis also displays deregulated differentiation and cell cycle markers (Stojadinovic *et al.*, 2008), depleted stem cell niche (Stojadinovic *et al.*, 2014) and attenuated fibrogenic signalling pathways such as TGF-β (Pastar *et al.*, 2010). Altogether, these factors lead to improper re-epithelialisation.

In addition to this, chronic wounds contain high levels of proteolytic enzymes which not only inhibit matrix reconstitution (Wysocki, Staiano-Coico and Grinnell, 1993), but also lead to signalling dysregulation by degrading growth factors such as TGF-β and VEGF (Yager *et al.*, 1997; Lauer *et al.*, 2000), and cytokines including TNF-α (Wallace and Stacey, 1998). Furthermore, chronic wounds experience a decreased production of fibrogenic growth factors such as PDGF (Pierce *et al.*, 1995). Additionally, genetic ablation of myofibroblasts was shown to result in impaired healing, including lack of re-epithelialisation and granulation tissue formation, dysregulated angiogenesis, and increased hypoxia, all of which are hallmarks of chronic wounds (McAndrews *et al.*, 2022). Altogether, imbalances between levels of proteolytic activity and matrix production prevent the wound from progressing.

Chronic wounds are especially relevant in the context of (age-related) diabetes. Hyperglycaemia contributes to dysregulated healing through impaired immune cell function (Stegenga *et al.*, 2008), inducing senescence in cells crucial for healing (Prattichizzo *et al.*, 2018), depletion of stem cell populations involved in vascularisation (Januszyk *et al.*, 2014), and causing the accumulation of advanced glycation end products (AGEs) (Gkogkolou and Böhm, 2012). AGEs trigger inflammation and ROS, subsequently promoting impaired neovascularisation (Gkogkolou and Böhm, 2012).

3.1.2 Role of cellular senescence in dysregulated tissue repair

The role of senescent cells in physiological wound healing and tissue repair was reviewed in Chapter 2. Briefly, senescent cells transiently appear during the mid to late stages of tissue repair and are removed by the immune system during the later stages. Several SASP factors, including PDGF and MMPs, play important roles in maintaining tissue homeostasis during the repair process (Muñoz-Espín and Serrano, 2014). Senescent cells have been shown to mitigate fibrosis during tissue repair in the skin, cornea, liver, heart and pancreas (Krizhanovsky *et al.*, 2008; Jun and Lau,

2010; Fitzner *et al.*, 2012; Meyer *et al.*, 2016; Wang *et al.*, 2019). Aside from being an anti-fibrotic mechanism, they also promote myofibroblast differentiation through SASP, which is crucial for ECM production and dermal wound closure (Demaria *et al.*, 2014). However, senescence has also been implicated in the pathophysiology of fibrotic conditions across several organ systems, as well as in the development of chronic wounds, which will be discussed further in the following sections.

3.1.2.1 Cellular senescence in fibrosis

In the skin, senescent fibroblasts and endothelial cells produce PDGF and TGF-β which promote myofibroblast differentiation and are important factors in wound healing, as discussed in Chapter 2. Consistently, genetic ablation of senescent cells delays cutaneous healing due to persisting necrotic cells and wound debris, delayed angiogenesis, and insufficient ECM deposition (Demaria *et al.*, 2014; Razdan, Vasilopoulos and Herbig, 2018). A mechanism for senescence in dermal wound healing has previously been identified; following cutaneous injury, the matricellular protein CCN1 is upregulated, which induces senescence in myofibroblasts (Jun and Lau, 2010). Through the expression of anti-fibrotic factors, these senescent myofibroblasts can mitigate fibrosis. Indeed, CCN1 KO mice exhibit reduced numbers of senescent cells and increased fibrosis, which responds positively to topical CCN1 treatment (Jun and Lau, 2010). In keeping with this, NRF2 overexpression was also found to induce fibroblast senescence, which resulted in improved epidermal wound healing, but also promoted skin tumorigenesis (Hiebert *et al.*, 2018). In contrast to these beneficial effects of senescent cells in skin fibrosis, patients with systemic sclerosis exhibit a high number of oxidative stress-induced senescent fibroblasts, promoting a pro-fibrotic and pro-inflammatory response (Kizilay Mancini *et al.*, 2022).

Senescent cells are also prevalent during cardiac repair, where they also play beneficial and detrimental roles. The downregulation of p53 and p16INK4a led to decreased senescent cell numbers in adult and neonatal mice, subsequently increasing fibroblast numbers, which in turn resulted in increased ECM deposition, fibrosis, and impaired cardiac function (Zhu *et al.*, 2013; Meyer *et al.*, 2016; Xie *et al.*, 2017; Feng *et al.*, 2019; Shibamoto *et al.*, 2019). Similarly, CCN1 overexpression following cardiac injury in adult and neonatal mice is able to mitigate fibrosis, improving cardiac function (Cui *et al.*, 2018; Feng *et al.*, 2019). These studies highlight the beneficial effects of senescent cells in cardiac fibrosis. However, clearance of senescent cells in

adult mice using navitoclax results in decreased expression of pro-fibrotic, pro-inflammatory and anti-angiogenic factors leading to attenuated fibrosis and improved cardiac function, highlighting the detrimental effects of senescence in cardiac fibrosis (Walaszczyk *et al.*, 2019).

In the liver, senescent cell number is directly proportional to disease severity and degree of impaired regeneration, as seen in acute liver disease in humans and liver injury mouse models (Bird *et al.*, 2018). Here, senescence has been found to spread to uninjured hepatocytes with the help of macrophage-derived TGF-β, disrupting the repair process. Reducing the number of senescent cells through the downregulation of p21 or inhibiting TGF-β signalling results in increased cell proliferation, improved repair processes and liver function (Bird *et al.*, 2018; Ferreira-Gonzalez *et al.*, 2018). Furthermore, the accumulation of senescent cells with age has also been associated to declining liver function. In keeping with this, downregulation of p21 following liver injury as well as senolytic treatment before injury, are both able to improve regenerative capacity and liver function in aged mice (Ritschka *et al.*, 2020). Again, these studies highlight the detrimental effects of senescent cells on liver repair and function. In contrast, senescent HSCs promote the resolution of fibrosis and tissue scarring by limiting ECM secretion and improving immunosurveillance within the repair site, highlighting beneficial effects of senescence in liver fibrosis (Krizhanovsky *et al.*, 2008).

Increased senescent cell activity has also been observed in many renal diseases. Following acute kidney injury, many cell types become senescent; this acute injury can progress to chronic kidney disease depending on the repair process, with senescent cells playing an important role in this transition (Naesens, 2011). The most prominent cell type to become senescent in the kidney are tubular epithelial cells (TECs). The presence of senescent TECs attenuates cell proliferation overall and promotes myofibroblast differentiation, promoting fibrotic activity and ECM deposition (Jin *et al.*, 2019). However, reducing the number of senescent TECs attenuates fibrosis and inflammation (Jin *et al.*, 2019; Li *et al.*, 2021). In aged mice, impaired regenerative capacity following kidney injury can be improved with senolytic treatment with navitoclax prior to injury (Kim *et al.*, 2019). Senolytic treatment promoted TEC proliferation and decreased kidney fibrosis and damage markers, with these effects being controlled in part by senescent cell-derived TGF-β1 (Mylonas *et al.*, 2021). These studies indicate the detrimental effects of senescent cells in renal disease. However, although kidney injury leads to renal fibrosis that is associated with high levels

of senescence markers, p16 KO mice (which have reduced senescent cells) also exhibit an aggravated fibrotic response (Wolstein *et al.*, 2010b). Within this p16 KO model, the fibrotic response, mediated by increased cell proliferation, ECM deposition and myofibroblast differentiation, was observed under normal conditions as well as following kidney injury. Similarly, in a model of ischemia-induced kidney injury, inhibition of cyclin-dependent kinases, which leads to cell cycle arrest, resulted in decreased renal damage (Dirocco *et al.*, 2014). Therefore, these studies show the beneficial effects of senescence in renal disease. In summary, cell senescence plays beneficial and detrimental roles in fibrotic conditions, within and across several organ systems.

3.1.2.2 Cellular senescence in chronic wounds

As mentioned previously, chronic wounds are mostly prevalent in elderly and/or diabetic individuals (Moura *et al.*, 2019). Since the ageing process and pathophysiology of diabetes involves senescent cells (Palmer *et al.*, 2019), it is unsurprising that chronic wound pathology is also linked to senescence cell activity (Mendez *et al.*, 1998; Harding, Moore and Phillips, 2005; Wang and Shi, 2020). Senescent cells in chronic wounds exacerbate impaired healing, with chronic ulcers containing more than 15% senescent cells exhibiting difficulty in healing appropriately (Stanley and Osler, 2001). Chronic wounds contain increased p21 expression and elevated senescent cell numbers compared to acute wounds as shown recently in an oxidative stress-induced chronic wound mouse model (Wyles *et al.*, 2023). In this model, increased senescent cell activity resulted in impaired healing mediated by SASP factors including MMPs, MCP and TGF-β. Similarly, increased senescent cell numbers in young mouse skin also leads to impaired healing, resembling healing dynamics of aged mice, through the activity of several SASP factors, namely IL-6, MCP-1, MMP-3, MMP-9, and TGF-β (Samdavid Thanapaul *et al.*, 2022).

Immune cell accumulation is a hallmark of chronic wound biology as it results in increased local inflammation, leading to impaired healing; many factors can contribute to this, including local factors such as iron, which promotes pro-inflammatory macrophage polarisation as well as fibroblast senescence (Sindrilaru *et al.*, 2011). Many SASP factors, such as MCP-1, recruit pro-inflammatory polarised macrophages (Lujambio *et al.*, 2013; Prattichizzo *et al.*, 2018). Ageing is another factor which, aside from senescent cell accumulation, is also associated with impaired macrophage function; this leads to disrupted senescent cell clearance mechanisms and to the

prolonged presence of senescent cells that can be seen in pathological wound healing (Swift *et al.*, 2001).

The chronic wound microenvironment is generally rich in pro-inflammatory factors that promotes senescence. This coupled with impaired age-related immunosurveillance mechanisms and systemic accumulation of (inflammatory) senescent cells leads to dysregulation of the tightly controlled wound healing process. Interestingly, wound fluid obtained from venous leg ulcers is able to induce senescence in neonatal fibroblasts (Mendez *et al.*, 1999). Aside from fibroblasts, other cell types are known to become senescent in pathological wound healing. For instance, senescent keratinocytes are prevalent in aged skin where they are suggested to contribute to impaired epidermal repair processes (Zouboulis *et al.*, 2008). In summary, senescent cells, with their pro-inflammatory function, contribute to chronic wound pathology by exacerbating the inflammatory response.

3.1.3 Senescence heterogeneity in tissue repair and related disorders

Cell senescence plays beneficial and detrimental roles in wound healing and fibrosis: as discussed above, senescence has been implicated in the pathophysiology of fibrotic conditions across several organ systems (Zhu *et al.*, 2013; Ogrodnik *et al.*, 2017; Schafer *et al.*, 2017), and at the same time, the accumulation of senescent cells has been linked to the development of chronic wounds (Mendez et al., 1998; Stanley and Osler, 2001; vande Berg et al., 2005). This in itself is interesting since fibrosis and chronic wounds represent two extreme situations equivalent to 'over-healed' and 'under-healed' wounds respectively.

Beneficial effects of senescent cells are evident from their transient role in tissue repair, with the absence of senescent cells impairing the repair process, promoting pro-fibrotic activity and tumorigenesis (Krizhanovsky *et al.*, 2008; Jun and Lau, 2010; Fitzner *et al.*, 2012; Muñoz-Espín and Serrano, 2014; Meyer *et al.*, 2016; Wang *et al.*, 2019). In contrast, an excess of senescent cells results in unresolved inflammation (Stanley and Osler, 2001; Samdavid Thanapaul *et al.*, 2022; Wyles *et al.*, 2023).

Persistent senescent cells, despite cell cycle arrest, remain metabolically active within the wound microenvironment and can communicate with surrounding cells through paracrine signalling. This is further complicated by the composition and functionality of SASP produced within the repair

system which has been shown to be temporally regulated by Notch signalling; the beginning of the senescence programme involves a fibrogenic SASP, followed by a fibrolytic SASP (Hoare *et al.*, 2016; Lee and Schmitt, 2019; Huang *et al.*, 2022). Keeping in mind that tissue repair is an inherently complex process, with several other factors at play, the timing of induction of senescent cells and variations in SASP composition during wound repair could steer the process towards different outcomes, either healthy repair or a tendency towards fibrosis or chronic inflammation. Interplay between varying senescent cell activity and their surroundings could lead to a wide range of qualitatively distinct spatiotemporal dynamics, that could result in these different repair outcomes. To investigate this, the model developed in Chapter 2 was used here to demonstrate and investigate the range of senescent cell functional heterogeneity within dysregulated repair, namely, fibrotic, and chronic wounds.

3.2 Methods

3.2.1 Model classifications

The wound healing model developed, as described in Chapter 2, was used to investigate the spatiotemporal dynamics of senescent cells during tissue repair. This was done by introducing perturbations to senescent cell dynamics within the model. Additionally, another model state including pre-existing inflammatory senescent cells was created to represent both age-related changes, and the early induction of senescent cells during the inflammatory phase of healing. These inflammatory senescent cells produce inflammatory SASP, CSF and proteinase within the model, with all other properties (such as size and contact energies) the same as for senescent myofibroblasts.

To study the changes induced by differences in senescent cell activity alone, no other factors or parameters were changed in this investigation. Two parameters related to senescent cell dynamics from the model were changed to produce the different outcome classifications: The probability of senescence in myofibroblasts, which is dictated by the parameter P_{SNC} and the time of induction of senescent cells in the model, determined by the time constraint parameter T_{SEN}. Simply put, the parameter P_{SNC} controls the population size of senescent cells, and the parameter T_{SEN} controls when senescent cells are induced at the wound site. Original model values are 0.15 for P_{SNC} and 12 for T_{SEN} (see Table 2.1).

To investigate changes in wound healing in response to a lack of senescent cells, P_{SNC} was set to zero, with no changes to T_{SEN}. On the other hand, to investigate the effects of increased number of senescent cells within the wound, $P_{SNC,}$ was set to 0.75, with no changes to T_{SEN}. A value of 0.75 was chosen for the parameter P_{SNC} after running preliminary simulations with higher P_{SNC} values, as it represented an aberrantly high percentage of senescent cells. Therefore, this value was used because the aim here was to explore an extreme scenario of senescent cell population in wound healing.

To explore the temporal aspects of senescence, two scenarios were considered. The first scenario was the early induction of senescence during the beginning of the inflammatory phase (representing age-related accumulation of senescent cells), for which the model with pre-existing inflammatory senescent cells was used with no other changes. The second scenario was the late induction of senescent cells during the later phases of healing; in this case, for the model, P_{SNC} was not altered, but T_{SEN} was set to 15 days. A three-day delay was chosen as it represents senescence induction during the later remodelling phase of the wound healing process, as opposed to the proliferative phase which is seen in healthy healing, as previously discussed in section 2.1.2. Additionally, preliminary work suggests that NOTCH-mediated juxtacrine secondary senescence induction and fibrogenic SASP production are prevalent up to approximately three days (Hoare *et al.*, 2016; Teo *et al.*, 2019). Therefore, a three-day delay was chosen in order to simulate delayed fibrogenic activity during the healing process. Three replicate runs were performed for each classification.

3.2.2 Multidimensional sensitivity analysis

To investigate the trade-offs between the two parameters, probability of senescence in myofibroblasts P_{SNC} and time of senescence induction T_{SEN}, a multidimensional sensitivity analysis was performed using the parameter sweep feature within CompuCell3D. Parameter value ranges were chosen as evenly spaced values, taking into consideration computational feasibility. Simulation time series data was collected every 500 MCS (model time step; equal to 3.75 hours) for each parameter set considered. A total of 25 simulations were run.

3.3 Results

3.3.1 Classification of wound healing outcomes based on spatiotemporal dynamics of senescent cells

To demonstrate the full range of senescent cell function within wound healing, a model of healthy wound healing with baseline parameters was first developed (Chapter 2). This model was used to explore the spatiotemporal dynamics of senescent cells within healthy wound healing. Successful wound healing with appropriate levels of ECM, cell composition, and cytokine and growth factor concentrations depends on multiple model parameters. Senescent cell dynamics within the model were primarily controlled by two parameters. These are the probability of senescence in myofibroblasts, which is dictated by the parameter P_{SNC} and the time of induction of senescent cells in the model, determined by the time constraint parameter T_{SEN}. Varying these two parameters around their healthy healing simulation baseline values (see Table 2.1) revealed four different scenarios of dysregulated tissue repair ranging from chronic wound to fibrosis. These classifications were based on transient model dynamics and the final simulation state at 18 days.

3.3.1.1 Chronic wound inflammation resulting from an increased percentage of senescent cells

The probability of myofibroblast senescence P_{SNC} was increased from 0.15 to 0.75 to examine the model's response to a high percentage of senescent cells, with no changes made to the time of senescence induction parameter T_{SEN}. The increased number of senescent cells, as shown in Figure 3.2C, resulted in a chronic wound outcome as shown in Figure 3.1. Although, chronic wounds involve several other dysregulated mechanisms, no other parameters were changed here with the aim of exclusively investigating the effects of the senescent cell population size and dynamics on the repair process. This chronic wound model classification is characterised by insufficient ECM production (Figure 3.2A), and an accumulation of inflammatory and fibrolytic factors namely, CSF (Figure 3.2I), inflammatory SASP (Figure 3.2G) and MMP (Figure 3.2H), compared to its healthy wound healing model counterpart. The corresponding spatial configurations of these characteristics are shown in Figure 3.1: Senescent cells and macrophages accumulate at the chronic wound site as a result of inefficient immunosurveillance, because the wound macrophages are unable to appropriately handle the high senescent cell load in this simulation; the simulation snapshots also show insufficient ECM deposition; additionally, MMP,

inflammatory SASP and CSF accumulate at the wound site, whereas total PDGF levels are reduced especially at day 18.

ECM production during the late healing stages, which is when most matrix remodelling occurs, is significantly lower compared to its healthy counterpart by day 18 (Figure 3.2A). The decreased amount of ECM can be attributed to increased production of MMP (Figure 3.2H) by inflammatory M1-polarised macrophages, and senescent cells as shown by the rise in paracrine senescence compared to the healthy healing model (Figure 3.2J); as discussed previously, paracrine senescence is prevalent during the inflammatory/fibrolytic SASP phase of senescence. This is coupled with attenuated ECM production from fibroblasts and myofibroblasts due to the drop in PDGF around this time (Figure 3.2F), in line with the decreased PDGF production as a result of M2 inflammatory macrophage polarisation.

The decreased production of PDGF also leads to reduced myofibroblast proliferation following day ~11 compared to healthy healing (Figure 3.2B). However, initial myofibroblast numbers are maintained close to its healthy counterpart since Notch phase (fibrogenic SASP phase) senescent cells promote myofibroblast differentiation through the production of PDGF and matrix components (Demaria *et al.*, 2014; Muñoz-Espín and Serrano, 2014). The following decline occurs as senescent cells shift towards an inflammatory fibrolytic phenotype. Furthermore, macrophage numbers remain elevated, compared to the drop in healthy healing at day ~ 17.5 (Figure 3.2E). This is the consequence of elevated CSF levels from SASP, which along with the inflammation and MMP fields, begins to rise around day ~6 (Figure 3.2G, H, I).

Inflammatory SASP has been shown to induce paracrine senescence in surrounding cells (Hoare *et al.*, 2016). Consistently, paracrine senescence is more prevalent in this scenario compared to healthy healing cells (Figure 3.2J). Interestingly, the number of fibroblasts within the wound region is slightly increased in this classification (Figure 3.2D).

The inflammatory and proteolytic activity of senescent cells is usually strongly controlled by macrophage immunosurveillance. However, in this classification, the senescent cell burden is too large for macrophage-mediated clearance resulting in impaired healing.

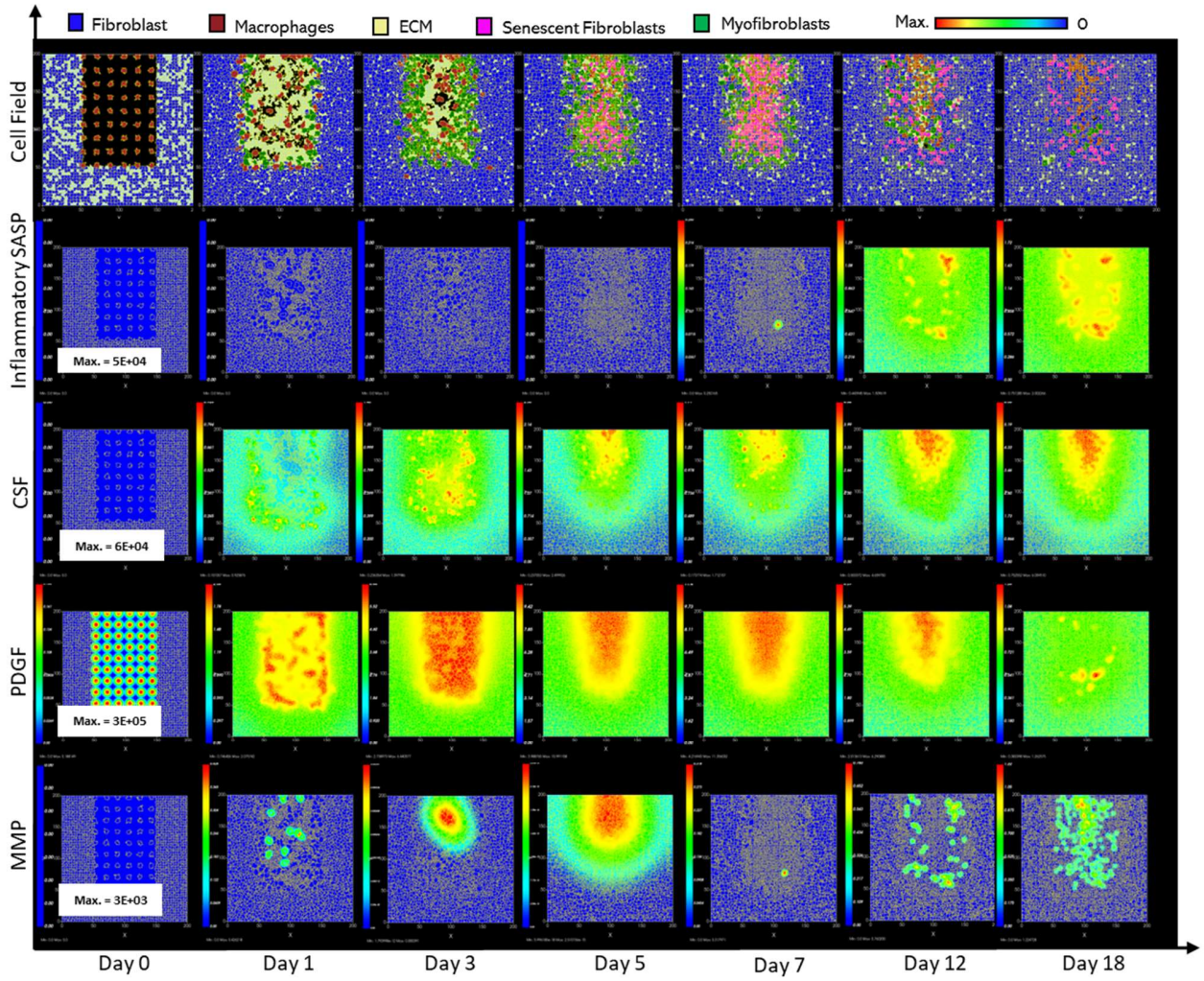

Figure 3.1 **Simulation of chronic wound dynamics in a dermal patch of size 600 µm x 600 µm due to a high percentage of senescent cells.** This figure shows snapshots of spatial configuration *vs* time for the progression of a simulated chronic wound due to an excessive number of senescent cells, which results in a chronic wound. The model includes fibroblasts, myofibroblasts, macrophages, ECM and senescent myofibroblasts, and chemical species including inflammatory SASP, CSF, PDGF and MMP. **Top row:** Snapshots of the simulation cell field at different time points with fibroblasts (blue), myofibroblasts (green), macrophages (brown), ECM (yellow) and senescent myofibroblasts (pink). Snapshots of simulation chemical fields are shown from the second to the last row; **Second row:** Inflammatory SASP, **Third row:** CSF, **Fourth row:** PDGF, **Fifth row:** MMP. Fields are shaded where, red corresponds to the maximum value specified in the first snapshot panel for each field, and blue corresponds to zero (shown in the colour bar at the top). Snapshots are shown for the time points, left to right, day 0, 1, 3, 5, 7, 12 and 18.

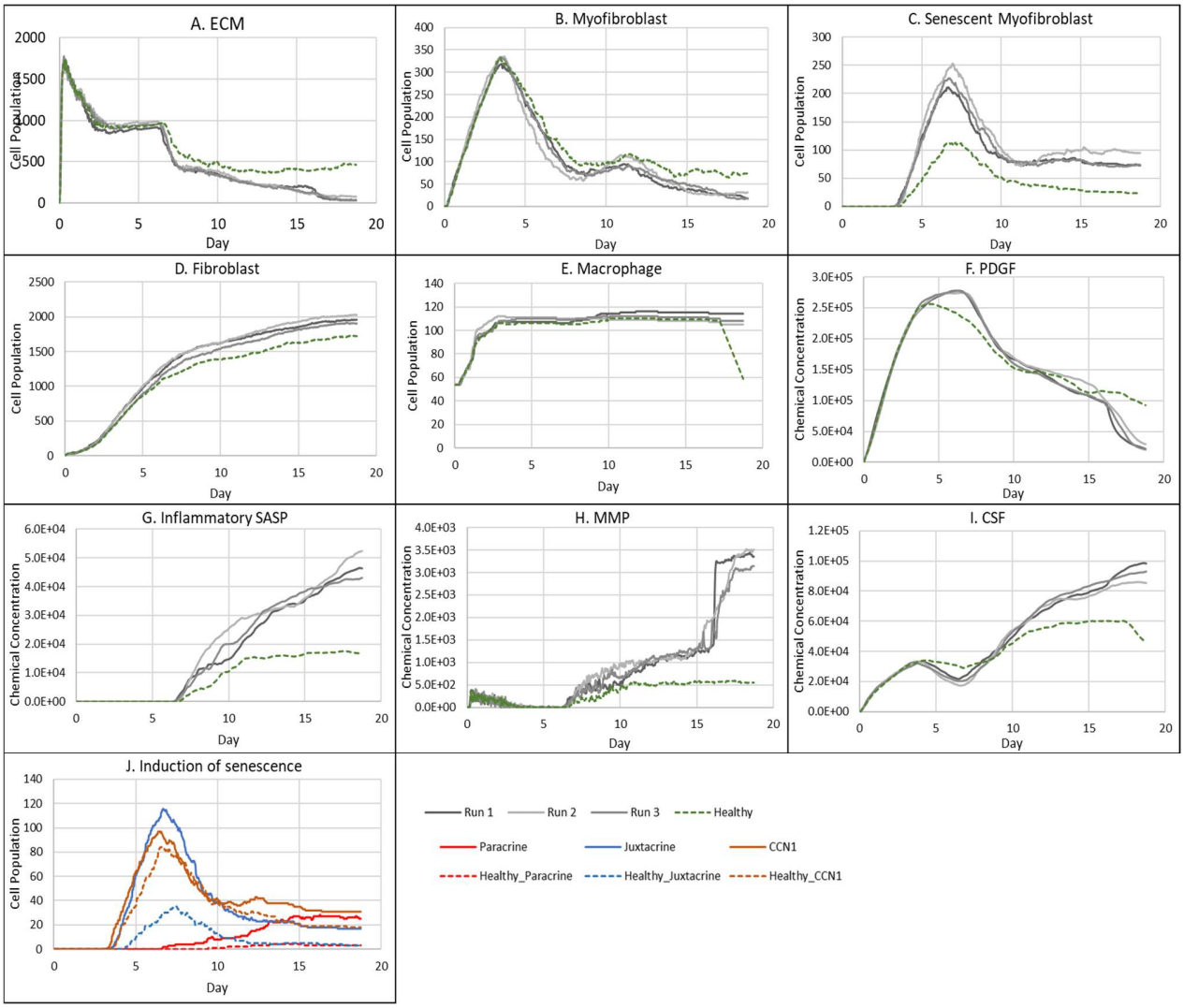

Figure 3.2 **Simulation time series for chronic wound dynamics in a dermal patch of size 600 µm x 600 µm due to a high percentage of senescent cells, shown for model cell types, rate of wound closure and model chemical fields.** This figure shows the simulation time series for the progression of a simulated chronic wound due to an excessive number of senescent cells, which results in a chronic wound. Number of cells and total chemical field are shown on the y axis and time (day) is shown on the x axis. Solid lines represent simulation time series for the chronic wound scenario, and the dotted lines in all plots represent simulation time series from the healthy physiological wound healing model from Chapter 2 (Figure 2.13 and Figure 2.14), included for comparison. Plot are shown for **A:** ECM, **B:** Myofibroblasts, **C:** Senescent myofibroblasts, **D:** Fibroblast, **E:** Macrophages, **F:** PDGF, **G:** Inflammatory SASP, **H:** MMP, **I:** CSF and **J:** Induction of senescence. For the time series plots A-I, the three shades of grey represent the different replicate runs as indicated in the legend (since the model is stochastic). For the plot J, different colours represent the different mechanisms of senescence induction, as indicated in the legend; red: paracrine secondary senescence, blue: juxtacrine secondary senescence and orange: CCN1-induced primary senescence. Replicate runs are not shown for the different mechanisms for ease of readability, but total senescent cell numbers for the three replicate runs are shown in plot C.

3.3.1.2 Fibrotic wound response in the absence of senescent cells

To investigate repair mechanisms in response to a complete removal of senescent cells, probability of myofibroblast senescence P_{SNC} was set to zero. The lack of senescent cells (Figure 3.4C) resulted in a fibrotic response with excessive ECM deposition (Figure 3.3). The spatial configuration for this response is shown in Figure 3.3, characterised by: scar tissue formation due to a high level of ECM deposition as shown in the cell field panel; lack of inflammatory SASP due to the absence of senescent cells; high and persistent levels of PDGF; and decreased total MMP levels.

As stated, this classification shows significantly increased ECM levels compared to healthy healing (Figure 3.4A). This can be explained in part by elevated PDGF concentration (Figure 3.4F) and myofibroblast numbers (Figure 3.4B). Additionally, an important factor contributing to this is the significant decrease in MMP levels compared to healthy healing (Figure 3.4G). Overall, the simulation shows increased myofibroblast presence and PDGF levels coupled with decreased MMP production to counteract excessive ECM production, all leading to scar tissue production. This can be attributed to insufficient pro-inflammatory polarisation of macrophages by senescent cell factors in the wound, which is necessary for fibrolytic mechanisms during the late stages of healing. This is illustrated by attenuated CSF levels (Figure 3.4H) and a lack of pro-inflammatory SASP (Figure 3.3), which control macrophage proliferation and pro-inflammatory M1 polarisation, respectively. Furthermore, for this classification, the lack of MMP production by senescent cells contributes to the observed impaired ECM breakdown in the scar tissue.

Therefore, the removal of senescent cells disrupts the balance between fibrogenic and fibrolytic mechanisms within the wound, both necessary for a healthy and controlled matrix reconstitution.

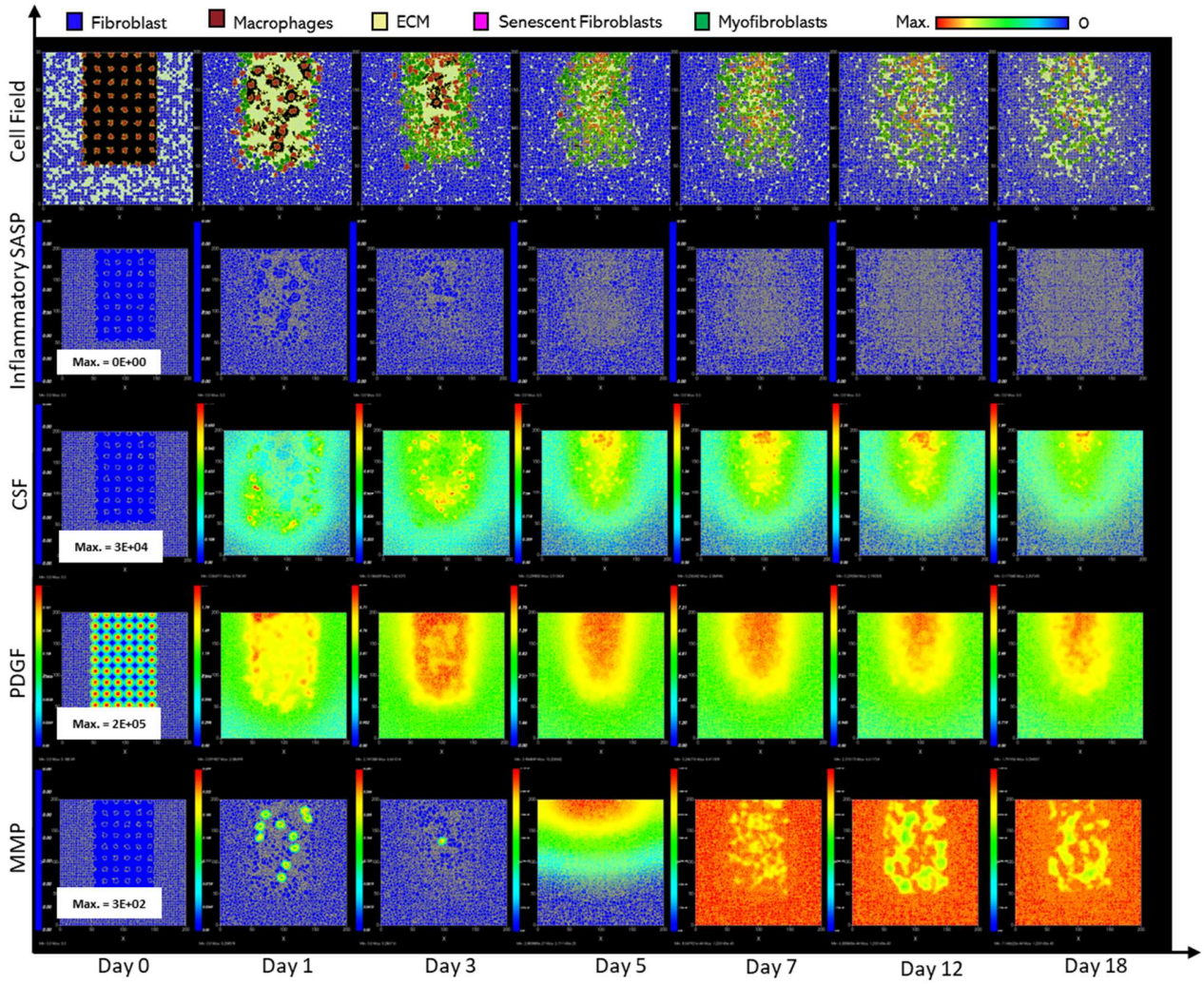

Figure 3.3 **Simulation of fibrotic wound dynamics in a dermal patch of size 600 µm x 600 µm due to the absence of senescent cells.** This figure shows snapshots of spatial configuration *vs* time for the progression of a simulated fibrotic wound due to the absence of senescent cells, which results in a fibrotic response. The model includes fibroblasts, myofibroblasts, macrophages and ECM, as well as chemical species including CSF, PDGF and MMP. **Top row:** Snapshots of the simulation cell field at different time points with fibroblasts (blue), myofibroblasts (green), macrophages (brown) and ECM (yellow). Snapshots of simulation chemical fields are shown from the second to the last row; **Second row:** Inflammatory SASP (which is at zero due to the absence of senescent cells; other types of inflammation were not included in this model), **Third row:** CSF, **Fourth row:** PDGF, **Fifth row:** MMP. Fields are shaded, where red corresponds to the maximum value specified in the first snapshot panel for each field, and blue corresponds to zero (shown in the colour bar at the top). Snapshots are shown for the time points, left to right, day 0, 1, 3, 5, 7, 12 and 18.

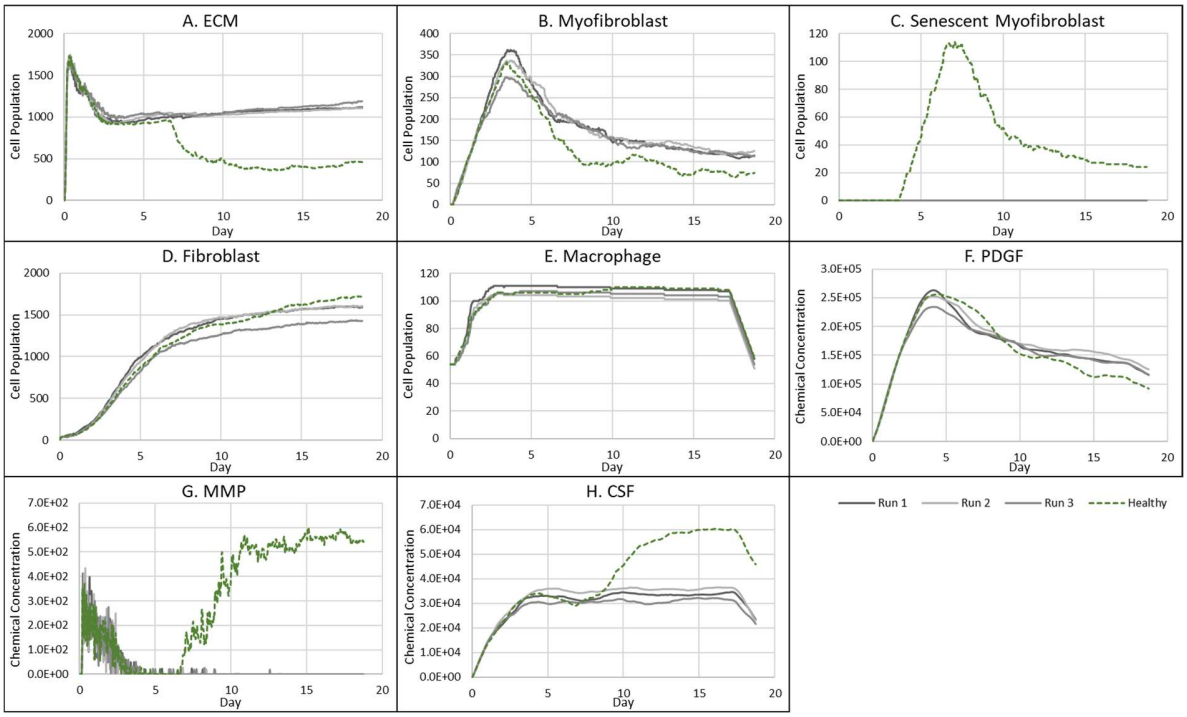

Figure 3.4 **Simulation time series for fibrotic wound dynamics in a dermal patch of size 600 µm x 600 µm due to the absence of senescent cells.** This figure shows the simulation time series for the progression of a simulated fibrotic wound due to the absence of senescent cells, which results in a fibrotic response in the wound. Number of cells and total chemical field are shown on the y axis and time (day) is shown on the x axis. Solid lines represent simulation time series for the fibrotic wound scenario, and the dotted lines in all plots represent simulation time series from the healthy physiological wound healing model from Chapter 2 (Figure 2.13 and Figure 2.14), included for comparison. Plot are shown for **A:** ECM, **B:** Myofibroblasts, **C:** Senescent myofibroblasts, **D:** Fibroblast, **E:** Macrophages, **F:** PDGF, **G:** MMP and **H:** CSF. For all the time series plots, the three shades of grey represent the different replicate runs as indicated in the legend (since the model is stochastic).

3.3.1.3 Fibrotic wound response as a result of delayed induction of senescence

To investigate the effect of a delay in the induction of senescence on wound healing, T_{SEN} was set to 15 days instead of 12 in the healthy healing model. This means that senescent cells will only appear at the wound site during the later stages of repair. Interestingly, this temporal change resulted in a fibrotic response as shown in Figure 3.5: This fibrotic response is characterised by an accumulation of ECM as well as senescent cells, as shown in the cell field; the delay in senescent cell induction results in delayed inflammatory SASP production, shown to appear in the day 18 panel.

As expected, senescent cells in this model classification rise around day ~15.5 (Figure 3.6C). The resulting fibrotic response is accompanied by elevated ECM levels compared to the healthy healing simulation (Figure 3.6A). A small drop in ECM is observed, coinciding with an increase in MMP levels at around ~day 18 (Figure 3.6H), which otherwise remained significantly low throughout the simulation. This response, along with small increases in inflammatory SASP and CSF (Figure 3.6G-H and inflammatory SASP panel shown in Figure 3.5) implies the shift of senescent cells to an inflammatory phenotype at this time point. MMP levels peak at day 18 as they are produced by senescent cells in their inflammatory phase and M1 polarised macrophages, which is triggered by this short increase in inflammatory SASP (Figure 3.6G). However, this fibrolytic activity is too late to attenuate the fibrotic response by breaking down the scar tissue. Furthermore, due to the delay in MMP activity, ECM levels remain elevated despite a drop in myofibroblast levels due to senescence induction (Figure 3.6B). ECM production here is supported by PDGF levels which remain elevated compared to its healthy counterpart as it is produced by fibrogenic phase senescent cells (Figure 3.6F). CSF levels also remain low (Figure 3.6I) but do not have a major impact of macrophage numbers (Figure 3.6E). Aside from CCN1-induced senescent cells, juxtacrine secondary senescence is prevalent (Figure 3.6J). As discussed, this is in accordance with previous work showing that juxtacrine senescence is accompanied by NOTCH-induced fibrogenic SASP rich in PDGF and ECM components (Kirschner *et al.*, 2020). The lack of paracrine secondary senescent cells here is congruent with the lack of fibrolytic activity in the wound model.

In this scenario, due to the timing of senescence induction in the wound, the existing fibrogenic activity of the repair process is augmented by senescent cells which are still in their NOTCH-induced fibrogenic SASP phase, rich in PDGF and ECM in the model (Hoare *et al.*, 2016). This overlap of fibrogenic activity, coupled with a lack of fibrolytic activity leads to a fibrotic response altogether. This lack of fibrolytic activity is due to a delay in the shift to an inflammatory senescence phenotype and insufficient macrophage M1 polarisation during late-stage healing, both of which are required to assist in ECM remodelling.

These results show that aside from SASP composition and secondary senescence mechanisms, the temporal aspect of senescence induction is also a crucial factor in repair outcomes. To summarise, the existing fibrogenic wound activity in this scenario was strengthened by senescent

cells, which eventually shift to a fibrolytic phenotype. However, the shift is too late to repair the scar tissue due to a disruption in the sequence of repair mechanisms.

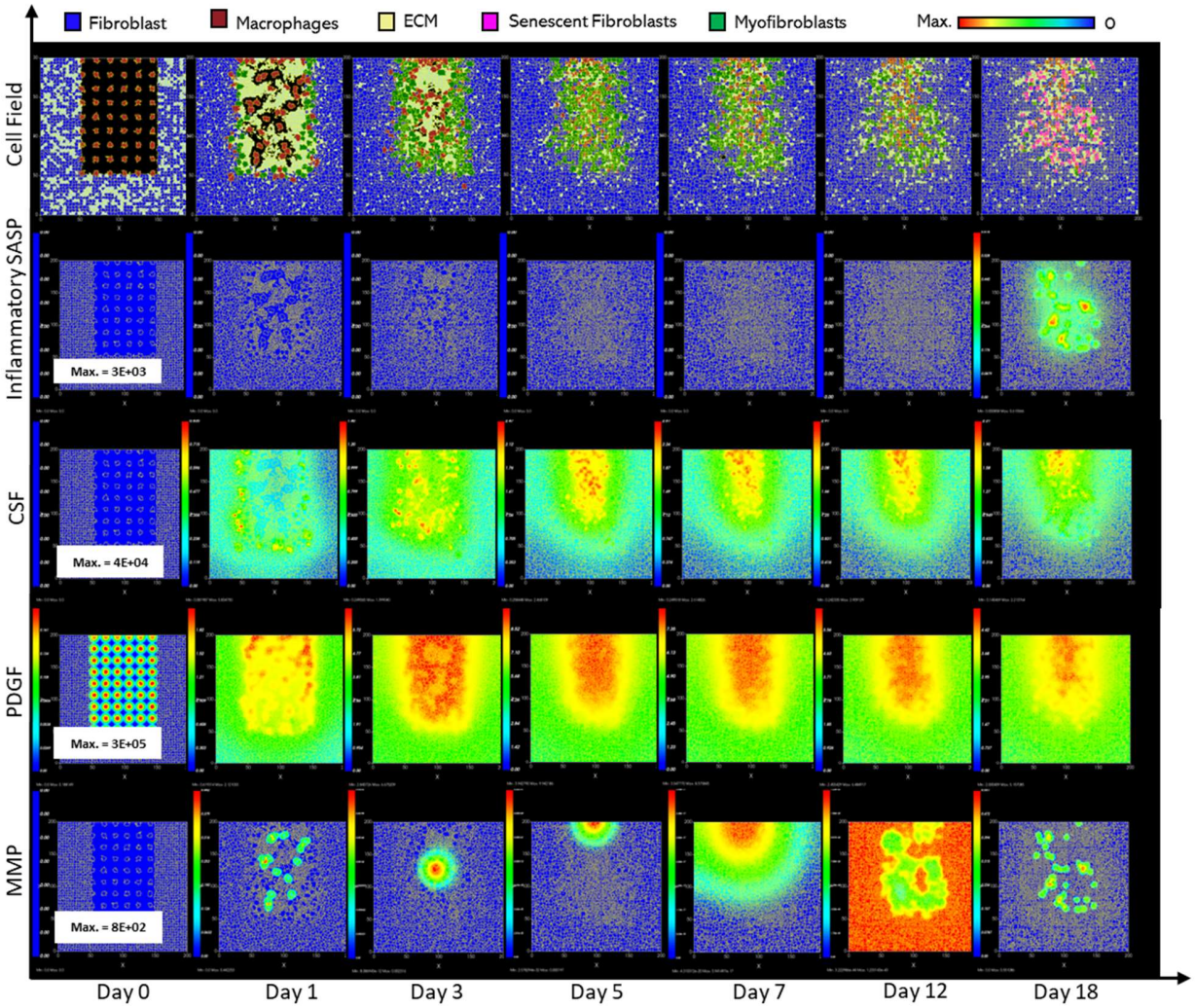

Figure 3.5 **Simulation of fibrotic wound dynamics in a dermal patch of size 600 µm x 600 µm when senescent cell induction is delayed.** This figure shows snapshots of spatial configuration *vs* time for the progression of a simulated fibrotic wound due to the delayed induction of senescent cells during the later stages of healing, which results in a fibrotic response. The model includes fibroblasts, myofibroblasts, macrophages, ECM and senescent myofibroblasts, and chemical species including inflammatory SASP, CSF, PDGF and MMP. **Top row:** Snapshots of the simulation cell field at different time points with fibroblasts (blue), myofibroblasts (green), macrophages (brown), ECM (yellow) and senescent myofibroblasts (pink). Snapshots of simulation chemical fields are shown from the second to the last row; **Second row:** Inflammatory SASP, **Third row:** CSF, **Fourth row:** PDGF, **Fifth row:** MMP. Fields are shaded, where red corresponds to the maximum value specified in the first snapshot panel for each field, and blue corresponds to zero (shown in the colour bar at the top). Snapshots are shown for the time points, left to right, day 0, 1, 3, 5, 7, 12 and 18.

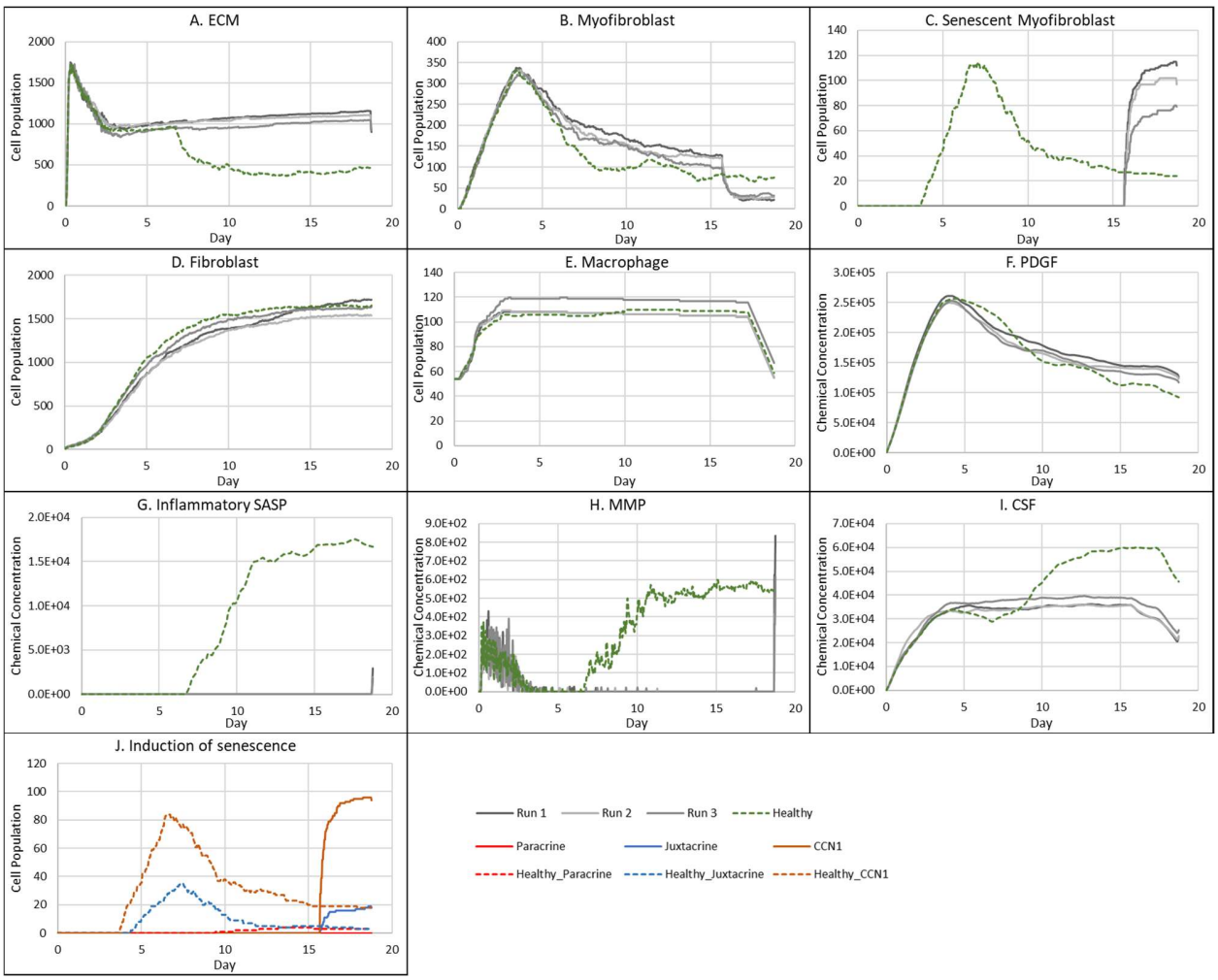

Figure 3.6 **Simulation time series for fibrotic wound dynamics in a dermal patch of size 600 µm x 600 µm when senescent cell induction is delayed.** This figure shows the simulation time series for the progression of a simulated fibrotic wound due to the delayed temporal induction of senescent cells during the later stages of healing, which results in a fibrotic response. Number of cells and total chemical field are shown on the y axis and time (day) is shown on the x axis. Solid lines represent simulation time series for this fibrotic wound scenario, and the dotted lines in all plots represent simulation time series from the healthy physiological wound healing model from Chapter 2 (Figure 2.13 and Figure 2.14), included for comparison. Plot are shown for **A:** ECM, **B:** Myofibroblasts, **C:** Senescent myofibroblasts, **D:** Fibroblasts, **E:** Macrophages, **F:** PDGF, **G:** Inflammatory SASP, **H:** MMP, **I:** CSF and **J:** Induction of senescence. For the time series plots A-I, the three shades of grey represent the different replicate runs as indicated in the legend (since the model is stochastic). For the plot J, different colours represent the different mechanisms of senescence induction, as indicated in the legend; red: paracrine secondary senescence, blue: juxtacrine secondary senescence and orange: CCN1-induced primary senescence. Replicate runs are not shown for the different mechanisms for ease of readability, but total senescent cell numbers for the three replicate runs are shown in plot C.

3.3.1.4 Inflammatory SASP from pre-existing senescent cells leads to chronic wound inflammation

Next, the added effect of inflammatory SASP from pre-existing senescent cells in wound healing was investigated. This scenario represents senescence induction during the early inflammatory phase of the wound healing process, as well as pre-existing senescent cells as seen with age-related accumulation of senescence. To this end, inflammatory senescent cells were introduced at the start of the model simulation with no other parameter changes (Figure 3.7). This classification simplistically represents an ageing or a diabetic wound, both of which are accompanied by an accumulation of inflammatory senescent cells, which is shown at the first simulation cell field snapshot at day 0 in Figure 3.7. High levels of inflammatory SASP are also prevalent at day 0, representing increased systemic inflammation, as seen with age. Similarly, MMP and CSF levels are also high throughout, whereas PDGF levels are significantly reduced (Figure 3.7).

Senescent cell numbers remained steadily elevated throughout the model simulation after an initial drop in numbers at around ~day 2, due to macrophage-mediated clearance (Figure 3.8C). Macrophage immunosurveillance here is mediated by inflammatory SASP produced by the pre-existing senescent cells, which attracts macrophages towards senescent cells in the model. Inflammatory SASP rises sharply at around ~day 1 followed by a decrease at ~day 2.5 and then continues at steady levels, with levels much higher compared to the healthy healing simulation (Figure 3.8G).

The same pattern is observed with other factors produced by senescent cells including MMPs (Figure 3.8H) and CSF (Figure 3.8I), coinciding with the senescent cell levels. MMP levels remain chronically elevated resulting in excessive breakdown of ECM (Figure 3.8A). Rising CSF levels result in uncontrolled macrophage proliferation (Figure 3.8E-I). Aside from triggering macrophage immunosurveillance, pro-inflammatory SASP also induces pro-inflammatory macrophage polarisation (Figure 3.8G). Rising number of inflammatory macrophages also contributes to increased MMP production alongside that of senescent cells.

Pro-inflammatory M1 polarisation of macrophages also means decreased PDGF production, as shown in Figure 3.8F. This results in decreased fibroblast proliferation (Figure 3.8D) and overall

ECM production by fibroblasts and myofibroblasts (Figure 3.8A). Myofibroblast population was significantly reduced compared to healthy healing as shown during the first 7 days of the mid healing stage (Figure 3.8B). This is due to decreased PDGF production by M1 polarised macrophages and inflammatory SASP-producing senescent cells, resulting in decreased myofibroblast differentiation. However, myofibroblast numbers during the later time points match that of healthy healing during which time myofibroblasts usually begin to be cleared out from the wound site.

Insufficient PDGF production leads to attenuated fibroblast levels, as stated previously (Figure 3.8D). Interestingly, in this classification, the number of fibroblasts was decreased compared to the chronic wound in section 3.3.1.1, which could imply decreased fibroblast activation from quiescence. Furthermore, the more prevalent mechanism for secondary senescence in this classification is paracrine, with minimal juxtacrine induction (Figure 3.8J). This makes sense since paracrine senescence is more associated with an inflammatory SASP compared to juxtacrine senescence, as discussed previously. Lastly, this model classification was also accompanied by greater run-to-run variability (Figure 3.8).

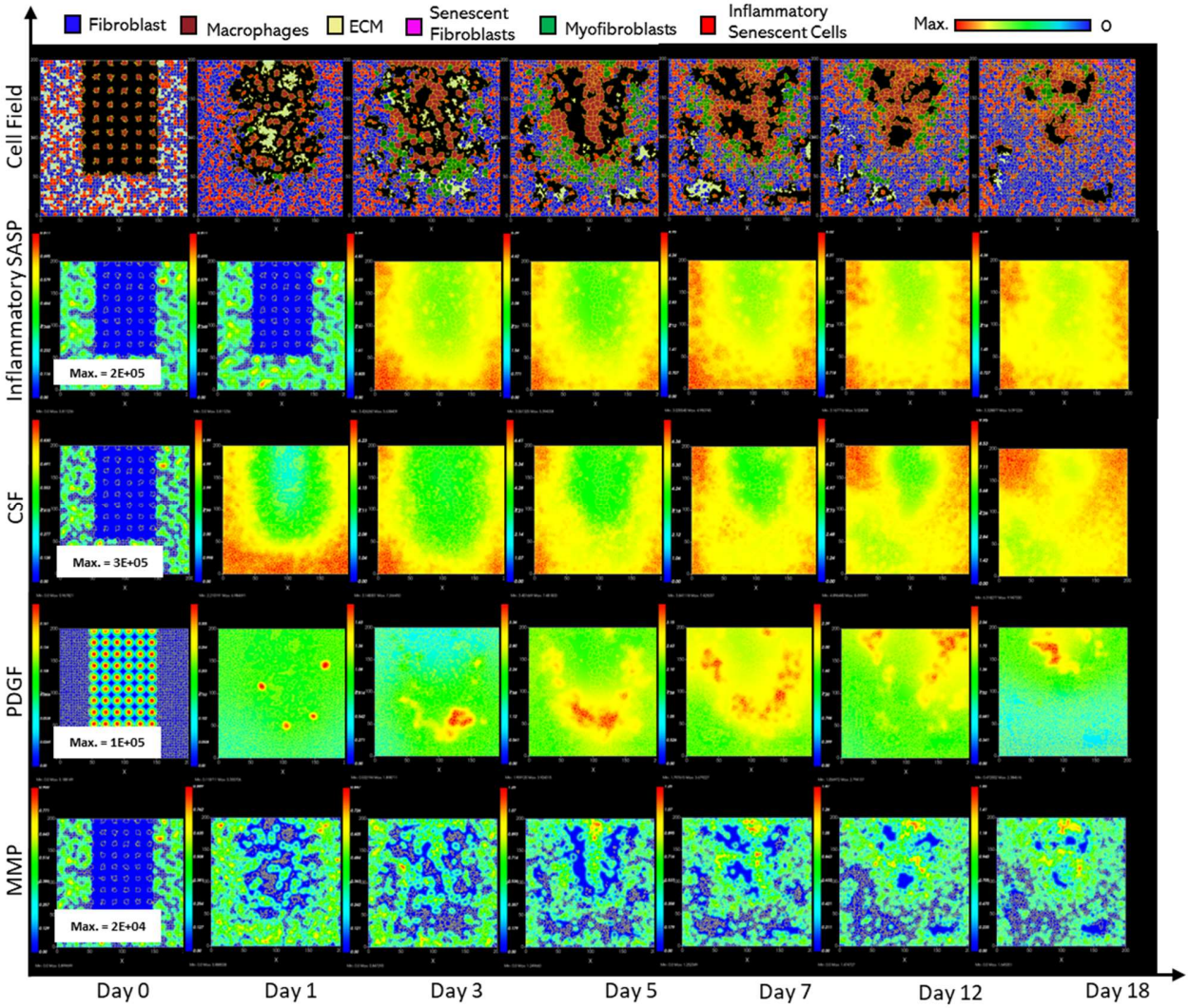

Figure 3.7 **Simulation of chronic wound dynamics in a dermal patch of size 600 µm x 600 µm due to pre-existing (inflammatory) senescent cells.** This figure shows snapshots of spatial configuration *vs* time for the progression of a simulated chronic wound due to pre-existing senescent cells which produce inflammatory SASP; this represents wound healing during ageing, which is accompanied by an accumulation of senescent cells, as well as senescence induced during the inflammatory phase of the wound healing process, resulting in a chronic wound. The model includes fibroblasts, myofibroblasts, macrophages, ECM, pre-existing (inflammatory) senescent cells and senescent myofibroblasts, and chemical species including PDGF, MMP, inflammatory SASP and CSF. **Top row:** Snapshots of the simulation cell field at different time points with fibroblasts (blue), myofibroblasts (green), macrophages (brown), ECM (yellow), pre-existing inflammatory senescent cells (red) and senescent myofibroblasts (pink). Snapshots of simulation chemical fields are shown from the second to the last row; **Second row:** Inflammatory SASP, **Third row:** CSF, **Fourth row:** PDGF, **Fifth row:** MMP. Fields are shaded, where red corresponds to the maximum value specified in the first snapshot panel for each field, and blue corresponds to zero (shown in the colour bar at the top). Snapshots are shown for the time points, left to right, day 0, 1, 3, 5, 7, 12 and 18.

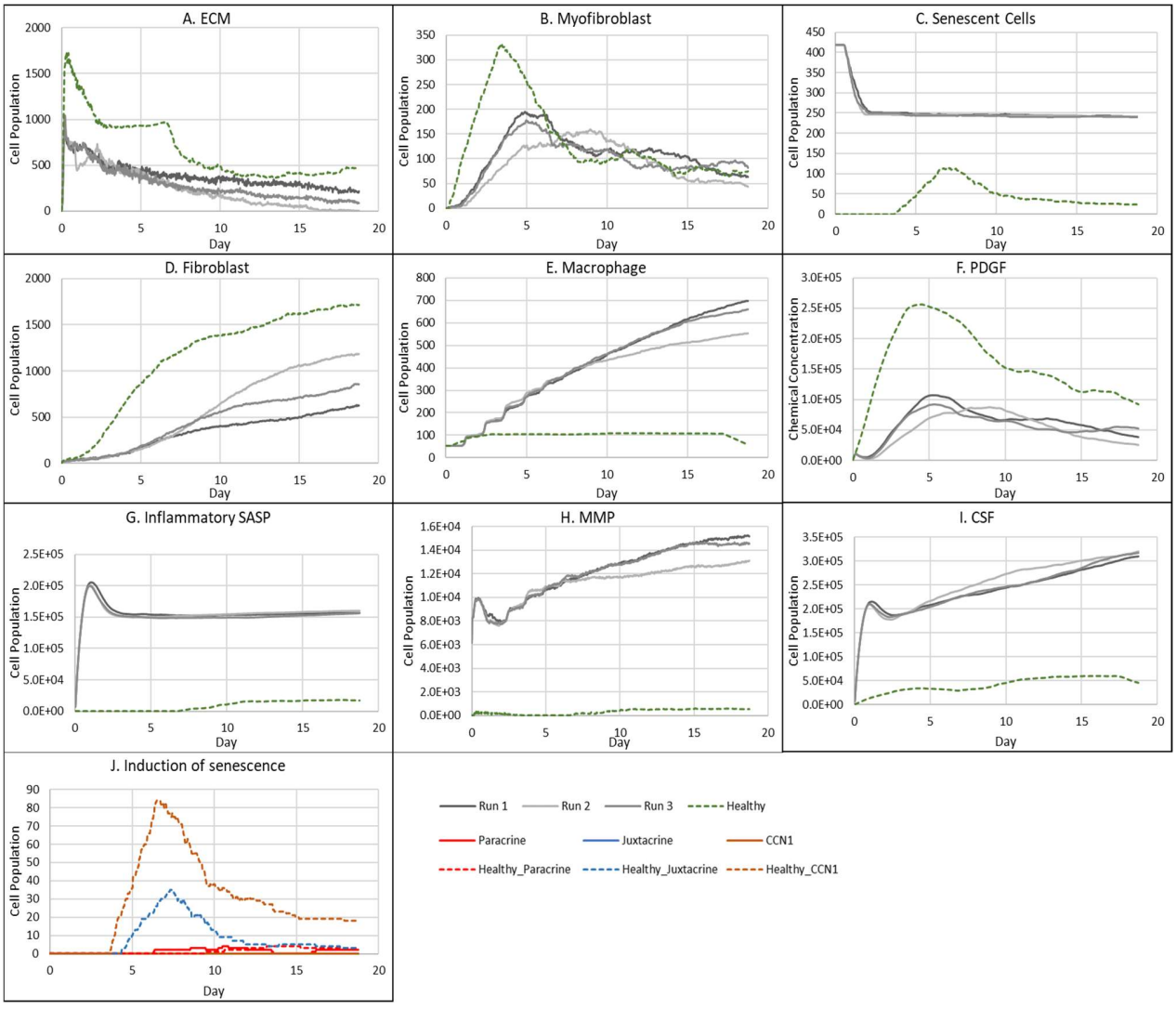

Figure 3.8 **Simulation time series for chronic wound dynamics in a dermal patch of size 600 µm x 600 µm due to pre-existing (inflammatory) senescent cells.** This figure shows the simulation time series for the progression of a simulated chronic wound due to pre-existing senescent cells; this represents wound healing during ageing, which is accompanied by an accumulation of senescent cells, as well as senescence induced during the inflammatory phase of the wound healing process, resulting in a chronic wound. Number of cells and total chemical field are shown on the y axis and time (day) is shown on the x axis. Solid lines represent simulation time series for this chronic wound scenario, and the dotted lines in all plots represent simulation time series from the healthy physiological wound healing model from Chapter 2 (Figure 2.13 and Figure 2.14), included for comparison. Plot are shown for **A:** ECM, **B:** Myofibroblasts, **C:** Total senescent cells, **D:** Fibroblasts, **E:** Macrophages, **F:** PDGF, **G:** Inflammatory SASP, **H:** MMP, **I:** CSF and **J:** Induction of senescence. For the time series plots A-I, the three shades of grey represent the different replicate runs as indicated in the legend (since the model is stochastic). For the plot J, different colours represent the different mechanisms of senescence induction, as indicated in the legend;

red: paracrine secondary senescence, blue: juxtacrine secondary senescence and orange: CCN1-induced primary senescence. Replicate runs are not shown for the different mechanisms for ease of readability, but total senescent cell numbers for the three replicate runs are shown in plot C.

3.3.2 Deviation from the tightly controlled senescence program during wound healing leads to dysregulated repair mechanisms

To explore any trade-offs between the population size of senescent cells and the time of senescence induction during wound healing, a multidimensional parameter sweep of probability of myofibroblast senescence P_{SNC} and senescence induction time constraint T_{SEN} was performed, as described in section 3.2.2. Simulations were run for each parameter set by increasing and decreasing parameter values around their baseline values. For each simulation, the number of myofibroblasts (Figure 3.10), macrophages (Figure 3.11), ECM (Figure 3.12) and senescent cells (Figure 3.13), as well as concentration of PDGF (Figure 3.14), CSF (Figure 3.15), Inflammatory SASP (Figure 3.16) and MMP (Figure 3.17) were examined. Three regions of the parameter space were identified as shown by the final simulation states at day 18 of the parameter sweep in Figure 3.9, where blue indicates fibrotic wound, red indicates chronic inflammation and green indicates healthy healing.

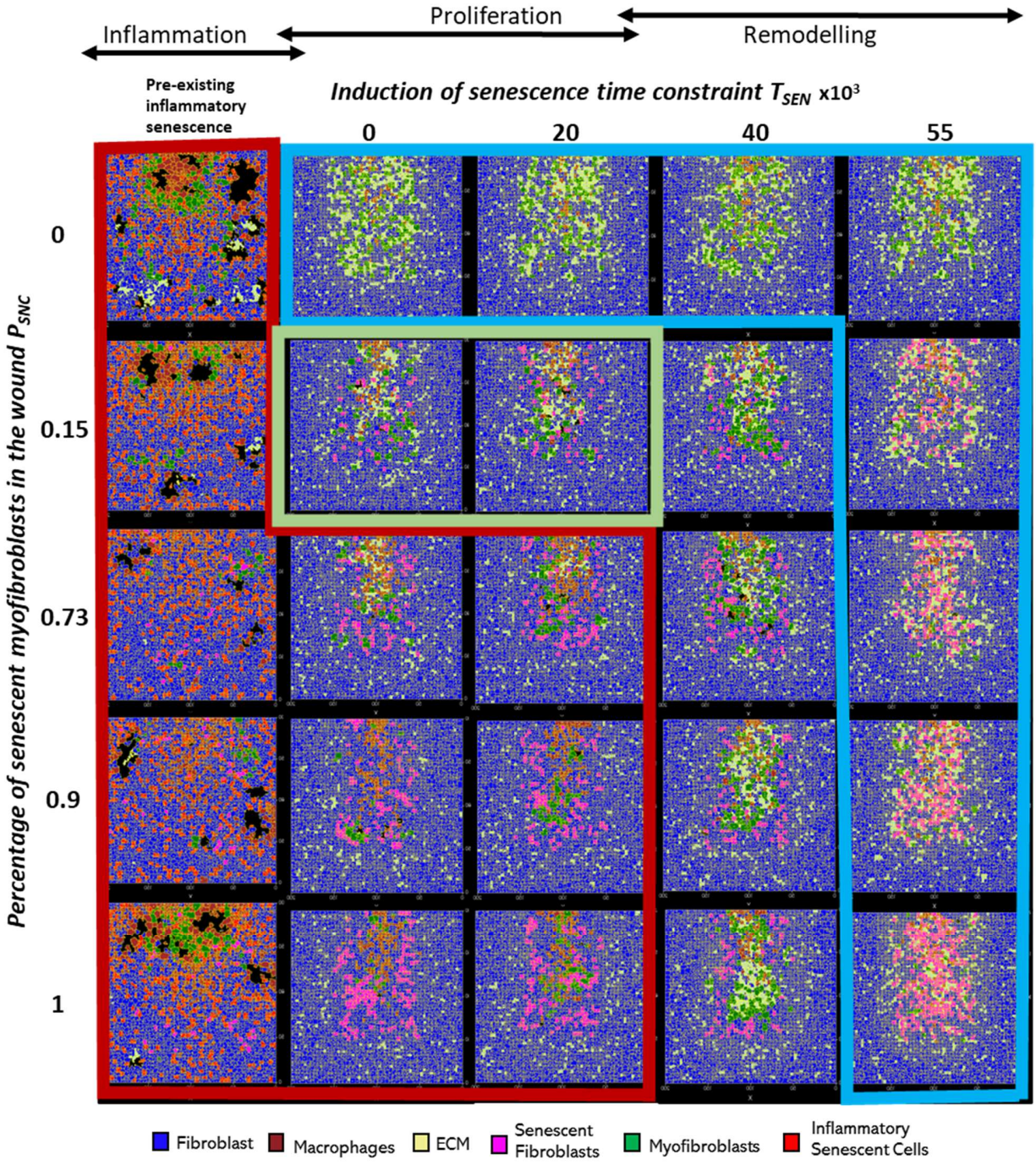

Figure 3.9 **Wound healing model simulation snapshots of the last time point from multidimensional parameter sensitivity analysis for variations in the parameters probability of myofibroblast senescence (P_{SNC}) and senescence induction time constraint (T_{SEN}) showing regions with distinct repair dynamics.** This plot shows the model simulation snapshots of the final time point ~day 18 from a pairwise parameter sweep of the parameters: percentage of myofibroblast senescence P_{SNC} (shown vertically on the left) and senescence induction time constraint T_{SEN} (shown horizontally at the top), around their baseline values (provided in Table

2.1). Along with the different values included in the parameter sweep for the senescence induction time constraint T_{SEN} parameter, pre-existing inflammatory senescent cells are also shown to represent senescence induced during the inflammatory phase of the wound healing process (i.e., before $T_{SEN} = 0$) which was not explicitly included in this model. Arrows above the T_{SEN} parameter sweep values show the wound healing phases (inflammation, proliferation and remodelling phases) represented by the T_{SEN} parameter values. The cell types in the snapshots are fibroblasts (blue), myofibroblasts (green), macrophages (brown), ECM (yellow), pre-existing (inflammatory) senescent cells (red) and senescent myofibroblasts (pink). The boxes highlight regions with distinct repair dynamics for chronic wound inflammation (red border box), healthy healing (green border box) and fibrotic wound response (blue border box).

For all values considered for the probability of myofibroblast senescence P_{SNC}, the presence of pre-existing senescent cells in the wound site (or the induction of senescence during the inflammatory phase of healing) leads to chronic inflammation and an inability for the wound to resolve (red shaded subplots in Figure 3.9 - Figure 3.17). As shown in the plots, the chronic wound formation is due to insufficient ECM production, myofibroblast differentiation and PDGF levels, along with high levels of macrophages, MMP, CSF and inflammatory SASP. Most cellular and chemical components are similar except for the mechanism of secondary senescence, where higher P_{SNC} values are accompanied by higher numbers of paracrine-mediated secondary senescence. Overall, pre-existing inflammatory senescence is accompanied by increased paracrine senescence compared to juxtacrine. This may be expected since SASP in chronic wound is rich in inflammatory and proteolytic factors but deficient in growth factors and matrix proteins (Ito, Hoare and Narita, 2017; Pulido, Velarde and Alimirah, 2021; Wyles *et al.*, 2023).

When P_{SNC} was set to zero (blue shaded subplots top row in Figure 3.9 - Figure 3.17), the simulation resulted in a fibrotic response characterised by excessive ECM deposition and lack of the fibrolytic activity that would usually be mediated by senescent cells and inflammatory M1 polarised macrophages. On the other hand, simulations run with low P_{SNC} and low T_{SEN} values result in healthy healing (green shaded subplots in Figure 3.9 - Figure 3.17). The cell populations and chemical concentrations in these simulations are consistent with their healthy healing counterparts. However, ECM levels remain elevated for a longer duration, until day ~9, for the simulation with a low to moderate T_{SEN} value compared to a low T_{SEN} value. This is because the short delay in senescence induction leads to overall ECM production in the wound being

augmented by senescent cell-derived ECM and PDGF. This does not lead to a fibrotic state since senescent cell and macrophage derived MMP is able to attenuate ECM levels sufficiently and on time.

Contrastingly, for high P_{SNC} and high T_{SEN} values (blue shaded subplots bottom right in Figure 3.9 - Figure 3.17), simulations result in fibrotic states, due to an increased number of senescent myofibroblasts that are induced during the late stages of healing. Myofibroblast numbers in these simulations remain significantly elevated compared to healthy healing, as do ECM levels. This is because the fibrogenic SASP phase of senescent cells is augmenting the intrinsic fibrogenic activity of the wound. This happens through sustained anti-inflammatory macrophage activity whereby they continue to produce PDGF, which are also elevated, for fibroblasts and myofibroblasts. A lack of macrophage pro-inflammatory polarisation leads to insufficient MMP production. Myofibroblasts and fibroblasts continue to produce excessive amounts of ECM in an uncontrolled manner resulting in the scar tissue as shown. This behaviour is consistently observed regardless of the myofibroblast senescence probability parameter P_{SNC} (blue shaded subplots top right in Figure 3.9 - Figure 3.17). That is, simulations with low P_{SNC} and high T_{SEN} values also result in a fibrotic wound state. This highlights the importance of time of induction of senescent cells during the repair process. In all these simulations, juxtacrine induction is the dominant mode of secondary senescence, which is to be expected given that fibrogenic SASP is associated with juxtacrine senescence, as discussed several times.

On the other hand, for the moderate to high T_{SEN} value and low P_{SNC} value (topmost white subplots in Figure 3.9 - Figure 3.17), the fibrotic response is elevated until day ~15, after which it is rescued by the switch to a fibrolytic SASP in the senescent cells, which is indicated by the sharp rise in inflammatory SASP, MMP and CSF, and a drop in PDGF levels. This is also accompanied by macrophages switching to a pro-inflammatory phenotype, contributing to the drop in PDGF and rise in MMP. However, for the same T_{SEN} value but high P_{SNC} values (second to last white subplots in Figure 3.9 - Figure 3.17), simulations are slightly more fibrotic. These are accompanied by sustained myofibroblast activity and higher inflammatory SASP compared to healthy healing. However, they are also able to resolve eventually.

Lastly, simulations run with high P_{SNC} and low T_{SEN} values consistently result in a chronic wound state (red shaded subplots in Figure 3.9 - Figure 3.17). The end of these simulations is accompanied by decreased ECM production and myofibroblast numbers overall. Macrophage numbers remain elevated towards the end of the simulations, when they usually decrease in healthy healing. This is due to increased CSF production by inflammatory senescent cells. Increased inflammation mediated by senescent cells is also characterised by higher inflammatory SASP levels, increased MMP and decreased PDGF levels. Moreover, paracrine secondary senescence is also more prevalent compared to healthy healing. Altogether, increased ECM breakdown and accumulation of inflammatory factors result in an improper wound microenvironment and tissue composition. This is because of a high senescent cell burden that is unable to be resolved by macrophage-mediated immunosurveillance despite their pro-inflammatory polarisation.

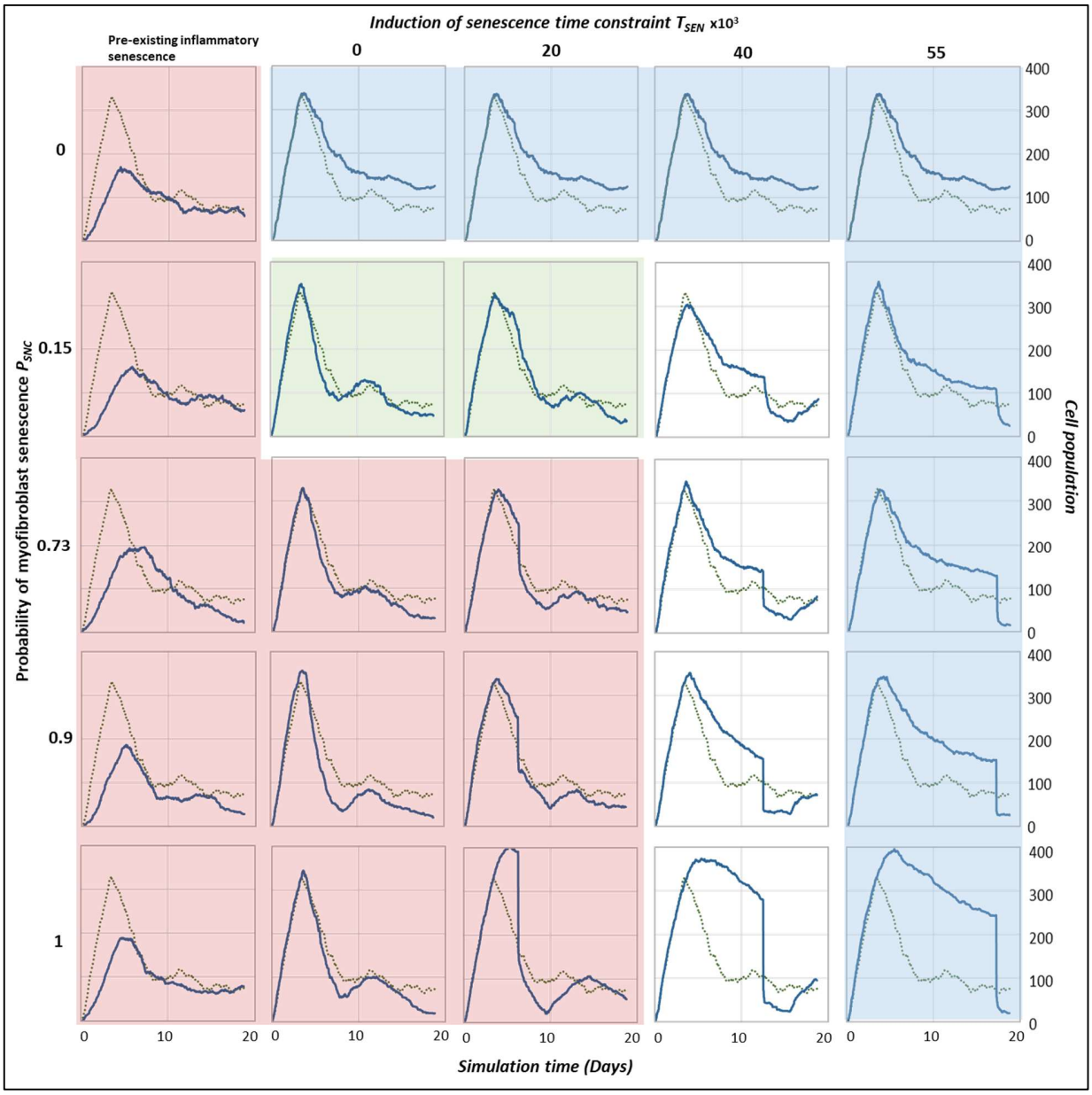

Figure 3.10 **Wound healing model multidimensional sensitivity analysis of the number of myofibroblast vs time for variations in the parameters probability of myofibroblast senescence (P_{SNC}) and senescence induction time constraint (T_{SEN}) showing regions with distinct repair dynamics.** The subplots show the model simulation time series for myofibroblasts in the wound from a pairwise parameter sweep of the parameters: probability of myofibroblast senescence P_{SNC} (shown vertically on the left) and senescence induction time constraint T_{SEN} (shown horizontally at the top), around their baseline values (provided in Table 2.1). Along with the different values included in the parameter sweep for the senescence induction time constraint T_{SEN} parameter, pre-existing inflammatory senescent cells are also shown to represent senescence induced during the inflammatory phase of the wound healing process (i.e., before $T_{SEN} = 0$) which was not explicitly included in the model. Simulation time in days is shown on the x axis and cell population numbers are shown on the y axis. The boxes highlight regions with

distinct repair dynamics: chronic wound inflammation (red shaded box), healthy healing (green shaded box) and fibrotic wound response (blue shaded box). The solid blue line represents simulation time series from the pairwise parameter sweep. The dotted lines in all the plots represent simulation time series from the healthy physiological wound healing model from Chapter 2 (Figure 2.13), included for comparison.

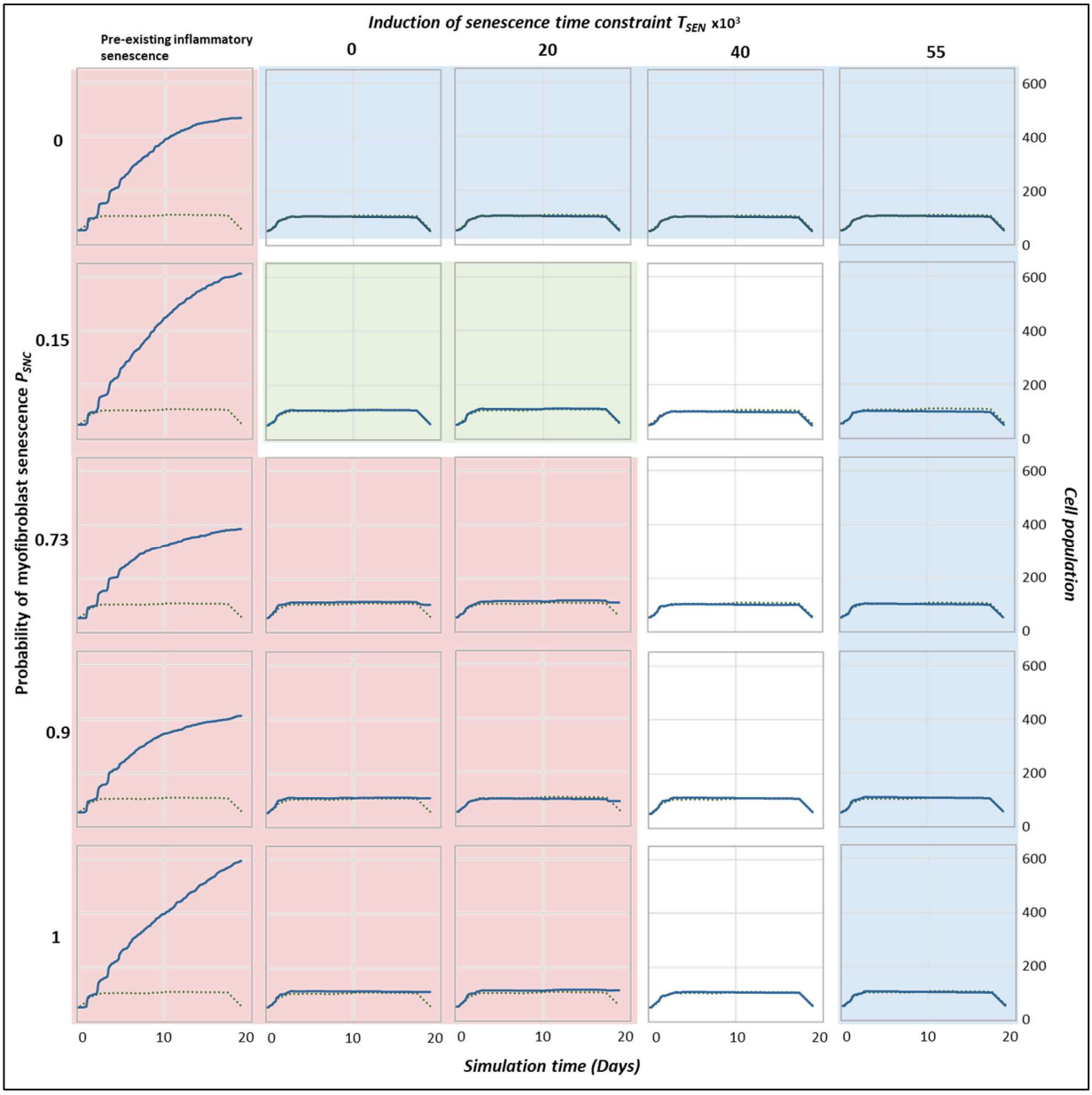

Figure 3.11 **Wound healing model multidimensional sensitivity analysis of the number of macrophages vs time for variations in the parameters probability of myofibroblast senescence (P_{SNC}) and senescence induction time constraint (T_{SEN}) showing regions with distinct repair dynamics.** The subplots show the model simulation time series for macrophages in the wound

from a pairwise parameter sweep of the parameters: probability of myofibroblast senescence P_{SNC} (shown vertically on the left) and senescence induction time constraint T_{SEN} (shown horizontally at the top), around their baseline values (provided in Table 2.1). Along with the different values included in the parameter sweep for the senescence induction time constraint T_{SEN} parameter, pre-existing inflammatory senescent cells are also shown to represent senescence induced during the inflammatory phase of the wound healing process (i.e., before $T_{SEN} = 0$) which was not explicitly included in the model. Simulation time in days is shown on the x axis and cell population numbers are shown on the y axis. The boxes highlight regions with distinct repair dynamics: chronic wound inflammation (red shaded box), healthy healing (green shaded box) and fibrotic wound response (blue shaded box). The solid blue line represents simulation time series from the pairwise parameter sweep. The dotted lines in all the plots represent simulation time series from the healthy physiological wound healing model from Chapter 2 (Figure 2.13), included for comparison.

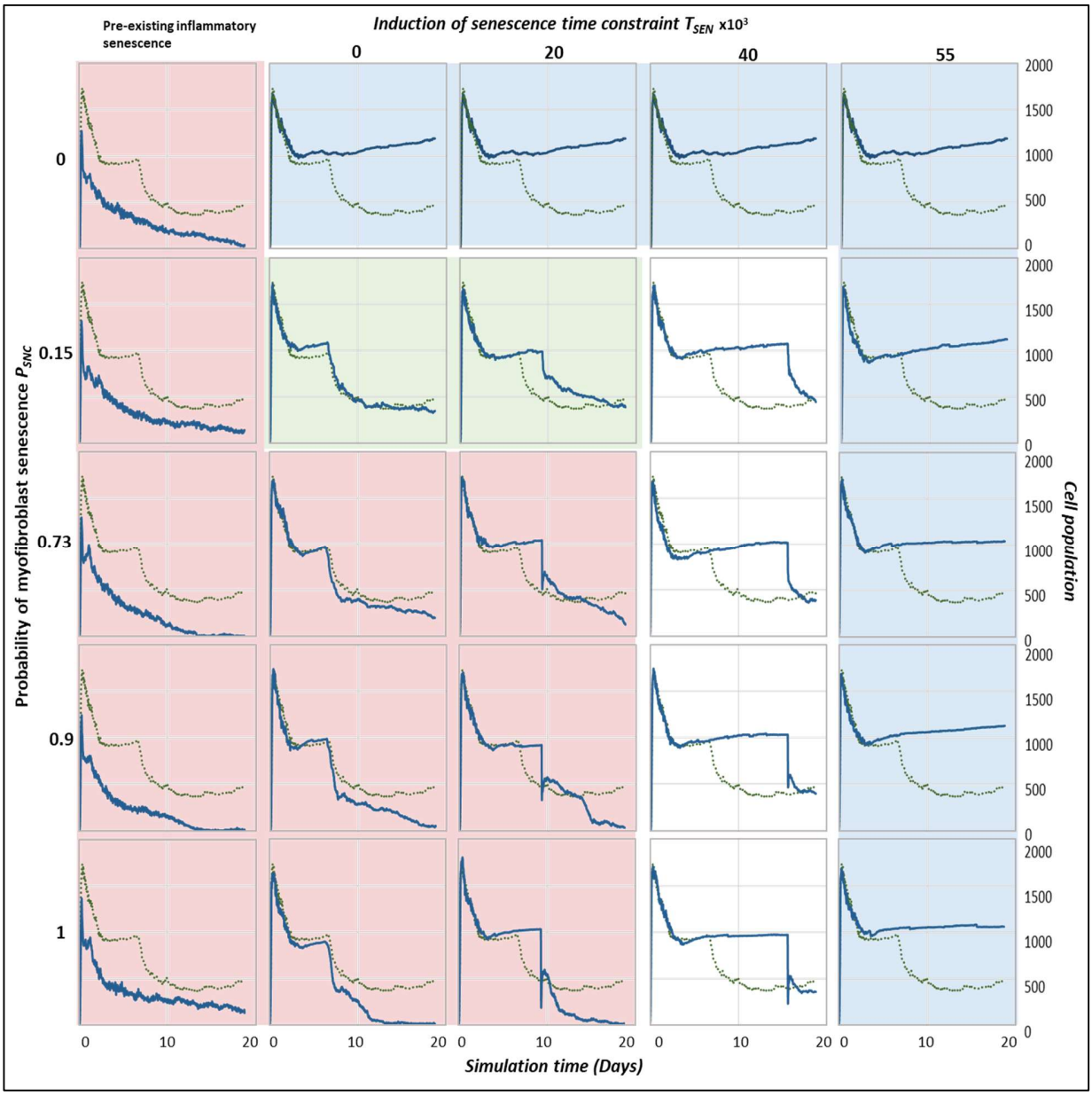

Figure 3.12 **Wound healing model multidimensional sensitivity analysis of the amount of ECM vs time for variations in the parameters probability of myofibroblast senescence (P_{SNC}) and senescence induction time constraint (T_{SEN}) showing regions with distinct repair dynamics.** The subplots show the model simulation time series for ECM levels in the wound from a pairwise parameter sweep of the parameters: probability of myofibroblast senescence P_{SNC} (shown vertically on the left) and senescence induction time constraint T_{SEN} (shown horizontally at the top), around their baseline values (provided in Table 2.1). Along with the different values included in the parameter sweep for the senescence induction time constraint T_{SEN} parameter, pre-existing inflammatory senescent cells are also shown to represent senescence induced during the inflammatory phase of the wound healing process (i.e., before $T_{SEN} = 0$) which was not explicitly included in the model. Simulation time in days is shown on the x axis and cell population numbers are shown on the y axis. The boxes highlight regions with distinct repair dynamics: chronic wound

inflammation (red shaded box), healthy healing (green shaded box) and fibrotic wound response (blue shaded box). The solid blue line represents simulation time series from the pairwise parameter sweep. The dotted lines in all the plots represent simulation time series from the healthy physiological wound healing model from Chapter 2 (Figure 2.13) were included for comparison.

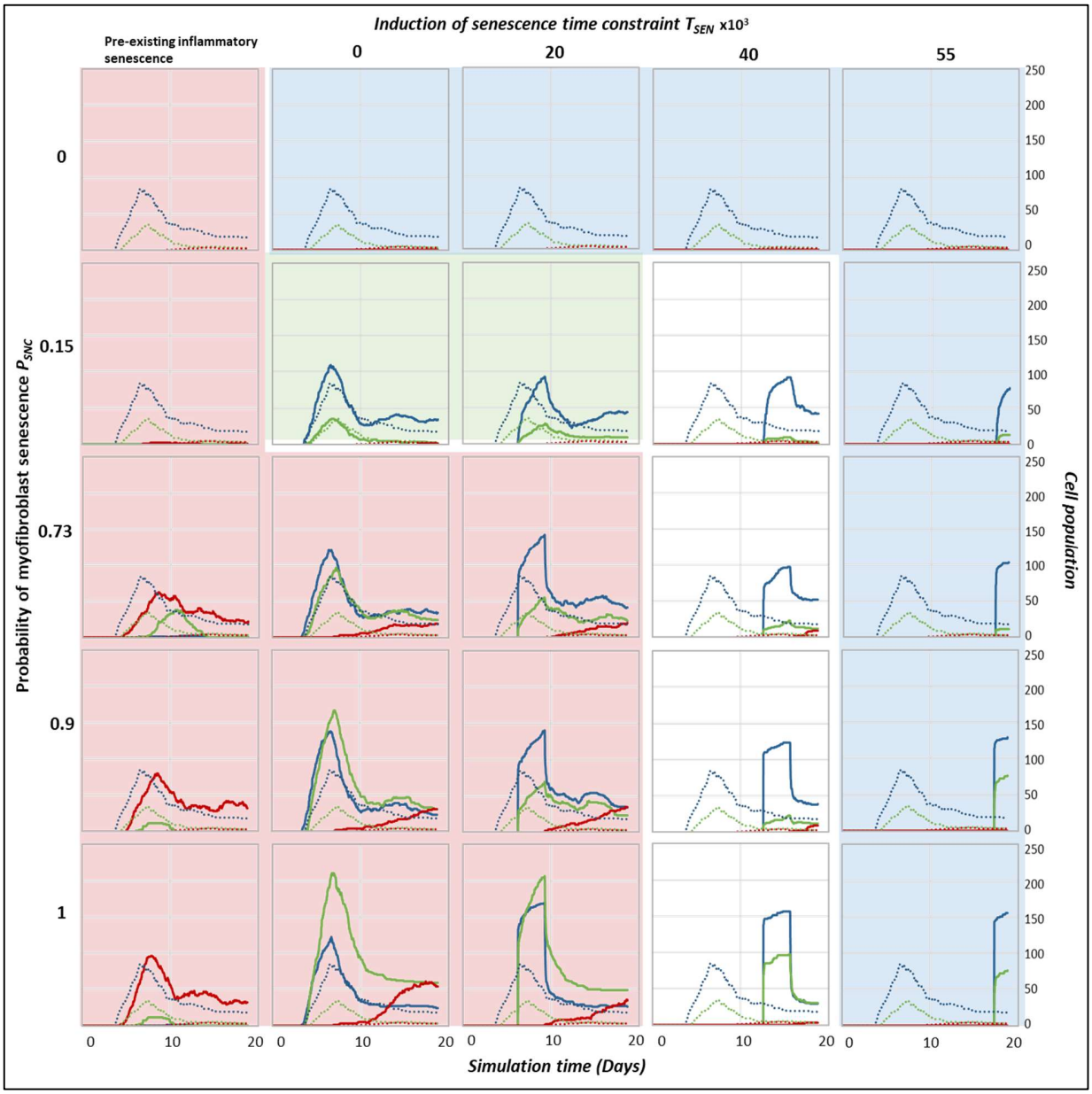

Figure 3.13 **Wound healing model multidimensional sensitivity analysis of the number of senescent cells including senescence induction mechanism vs time for variations in the parameters probability of myofibroblast senescence (P_{SNC}) and senescence induction time constraint (T_{SEN}) showing regions with distinct repair dynamics.** The subplots show the model

simulation time series for senescent cell numbers in the wound from a pairwise parameter sweep of the parameters: probability of myofibroblast senescence P_{SNC} (shown vertically on the left) and senescence induction time constraint T_{SEN} (shown horizontally at the top), around their baseline values (provided in Table 2.1). Along with the different values included in the parameter sweep for the senescence induction time constraint T_{SEN} parameter, pre-existing inflammatory senescent cells are also shown to represent senescence induced during the inflammatory phase of the wound healing process (i.e., before T_{SEN} = 0) which was not explicitly included in the model. Simulation time in days is shown on the x axis and cell population numbers are shown on the y axis. The boxes highlight regions with distinct repair dynamics: chronic wound inflammation (red shaded box), healthy healing (green shaded box) and fibrotic wound response (blue shaded box). The plot colours represent different modes of senescence induction; red: paracrine secondary senescence, blue: juxtacrine secondary senescence and green: CCN1-induced primary senescence. The solid lines represent simulation time series from the pairwise parameter sweep. The dotted lines represent simulation time series from the healthy physiological wound healing model from Chapter 2 (Figure 2.13) were included for comparison.

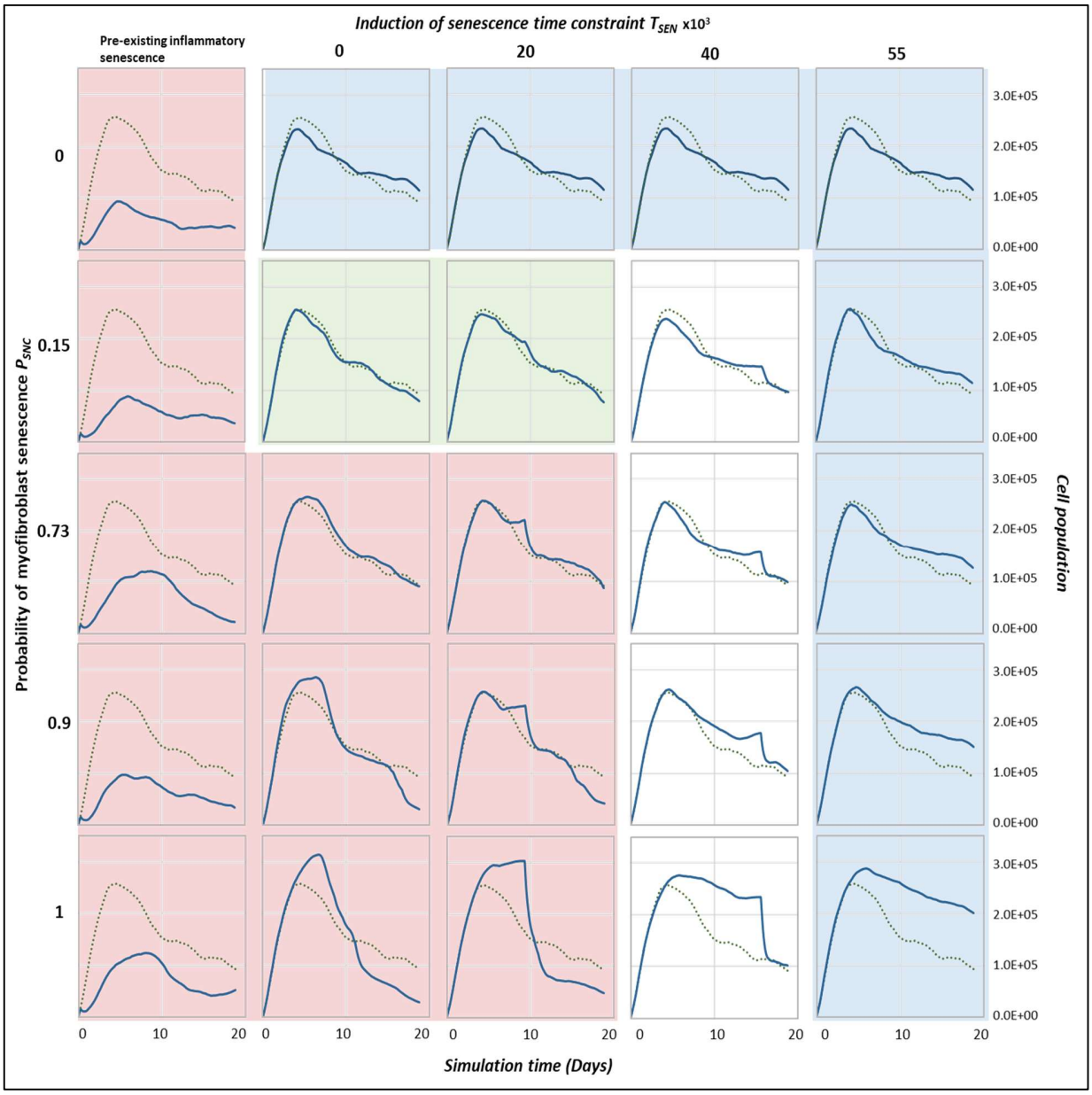

Figure 3.14 **Wound healing model multidimensional sensitivity analysis of total PDGF vs time for variations in the parameters probability of myofibroblast senescence (P_{SNC}) and senescence induction time constraint (T_{SEN}) showing regions with distinct repair dynamics.** The subplots show the model simulation time series for PDGF levels in the wound from a pairwise parameter sweep of the parameters: probability of myofibroblast senescence P_{SNC} (shown vertically on the left) and senescence induction time constraint T_{SEN} (shown horizontally at the top), around their baseline values (provided in Table 2.1). Along with the different values included in the parameter sweep for the senescence induction time constraint T_{SEN} parameter, pre-existing inflammatory senescent cells are also shown to represent senescence induced during the inflammatory phase of the wound healing process (i.e., before $T_{SEN} = 0$) which was not explicitly included in the model. Simulation time in days is shown on the x axis and chemical concentration levels are shown on the y axis. The boxes highlight regions with distinct repair dynamics: chronic wound inflammation

(red shaded box), healthy healing (green shaded box) and fibrotic wound response (blue shaded box). The solid blue line represents simulation time series from the pairwise parameter sweep. The dotted lines in all the plots represent simulation time series from the healthy physiological wound healing model from Chapter 2 (Figure 2.14) were included for comparison.

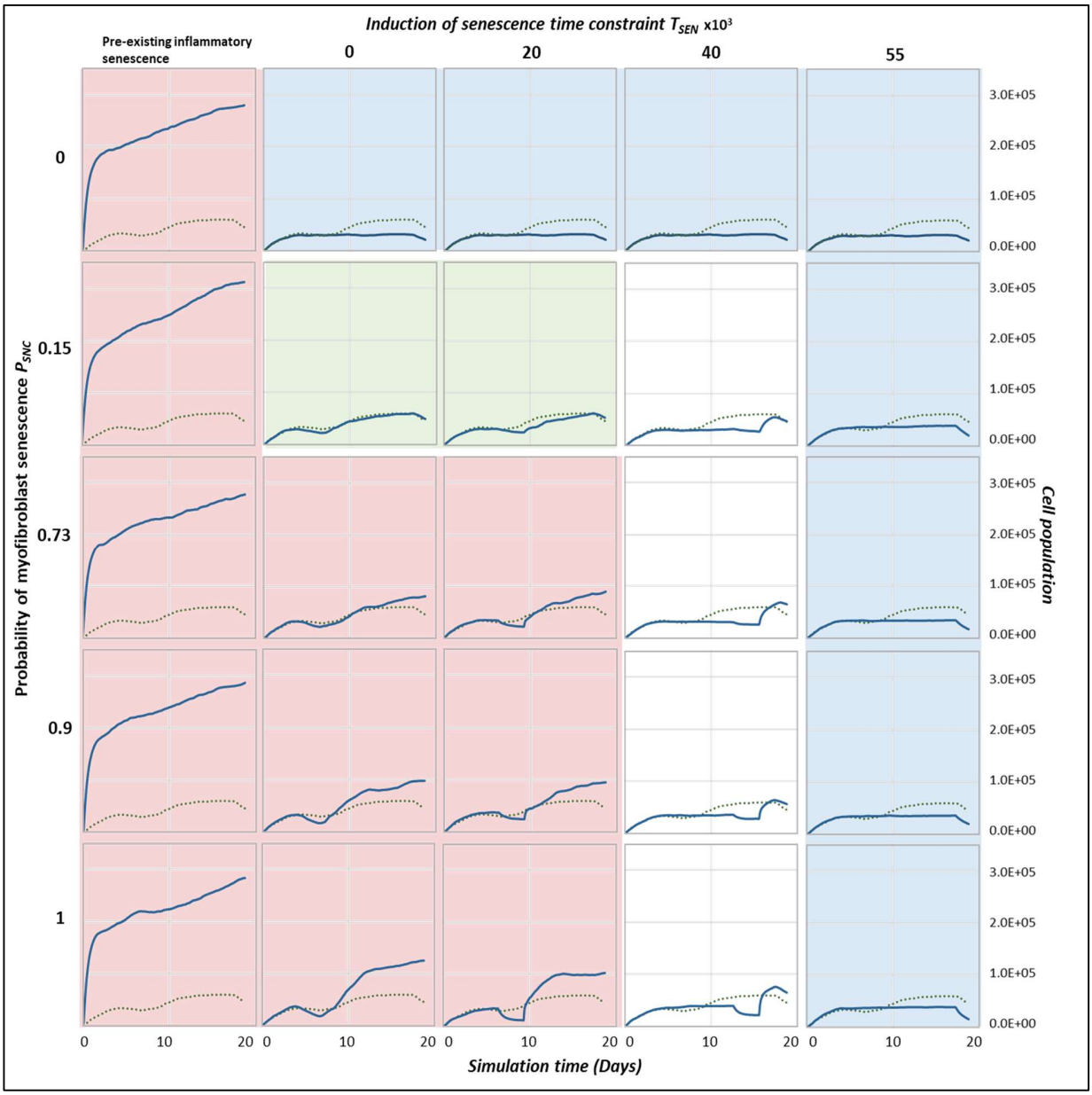

Figure 3.15 **Wound healing model multidimensional sensitivity analysis of total CSF vs time for variations in the parameters probability of myofibroblast senescence (P_{SNC}) and senescence induction time constraint (T_{SEN}) showing regions with distinct repair dynamics.** The subplots show the model simulation time series for CSF levels in the wound from a pairwise parameter sweep of the parameters: probability of myofibroblast senescence P_{SNC} (shown vertically on the

left) and senescence induction time constraint T_{SEN} (shown horizontally at the top), around their baseline values (provided in Table 2.1). Along with the different values included in the parameter sweep for the senescence induction time constraint T_{SEN} parameter, pre-existing inflammatory senescent cells are also shown to represent senescence induced during the inflammatory phase of the wound healing process (i.e., before $T_{SEN} = 0$) which was not explicitly included in the model. Simulation time in days is shown on the x axis and chemical concentration levels are shown on the y axis. The boxes highlight regions with distinct repair dynamics: chronic wound inflammation (red shaded box), healthy healing (green shaded box) and fibrotic wound response (blue shaded box). The solid blue line represents simulation time series from the pairwise parameter sweep. The dotted lines in all the plots represent simulation time series from the healthy physiological wound healing model from Chapter 2 (Figure 2.14) were included for comparison.

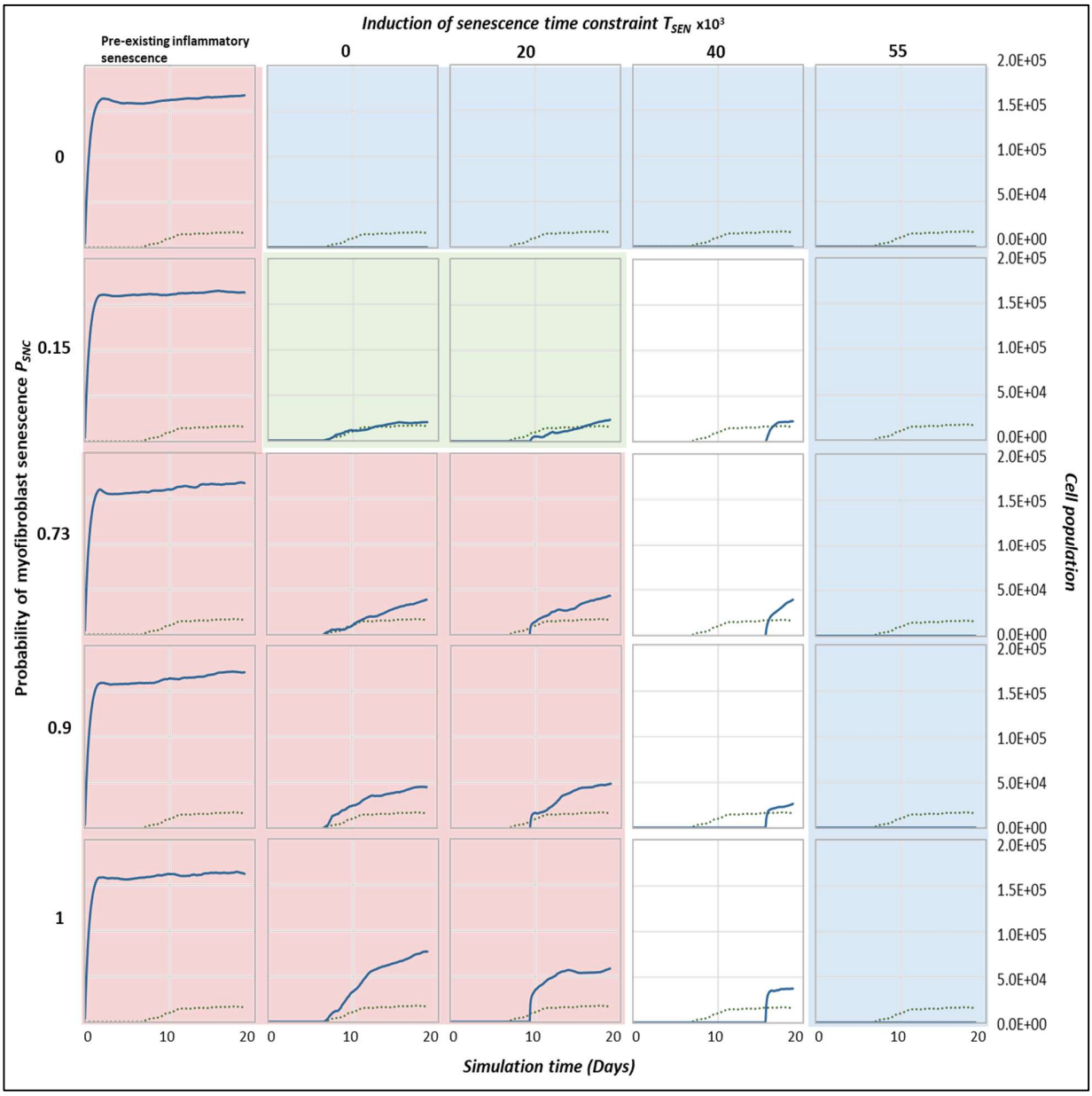

Figure 3.16 **Wound healing model multidimensional sensitivity analysis of total inflammatory SASP vs time for variations in the parameters probability of myofibroblast senescence (P_{SNC}) and senescence induction time constraint (T_{SEN}) showing regions with distinct repair dynamics.** The subplots show the model simulation time series for inflammatory SASP levels in the wound from a pairwise parameter sweep of the parameters: probability of myofibroblast senescence P_{SNC} (shown vertically on the left) and senescence induction time constraint T_{SEN} (shown horizontally at the top), around their baseline values (provided in Table 2.1). Along with the different values included in the parameter sweep for the senescence induction time constraint T_{SEN} parameter, pre-existing inflammatory senescent cells are also shown to represent senescence induced during the inflammatory phase of the wound healing process (i.e., before $T_{SEN} = 0$) which was not explicitly included in the model. Simulation time in days is shown on the x axis and chemical concentration levels are shown on the y axis. The boxes highlight regions with

distinct repair dynamics: chronic wound inflammation (red shaded box), healthy healing (green shaded box) and fibrotic wound response (blue shaded box). The solid blue line represents simulation time series from the pairwise parameter sweep. The dotted lines in all the plots represent simulation time series from the healthy physiological wound healing model from Chapter 2 (Figure 2.14) were included for comparison.

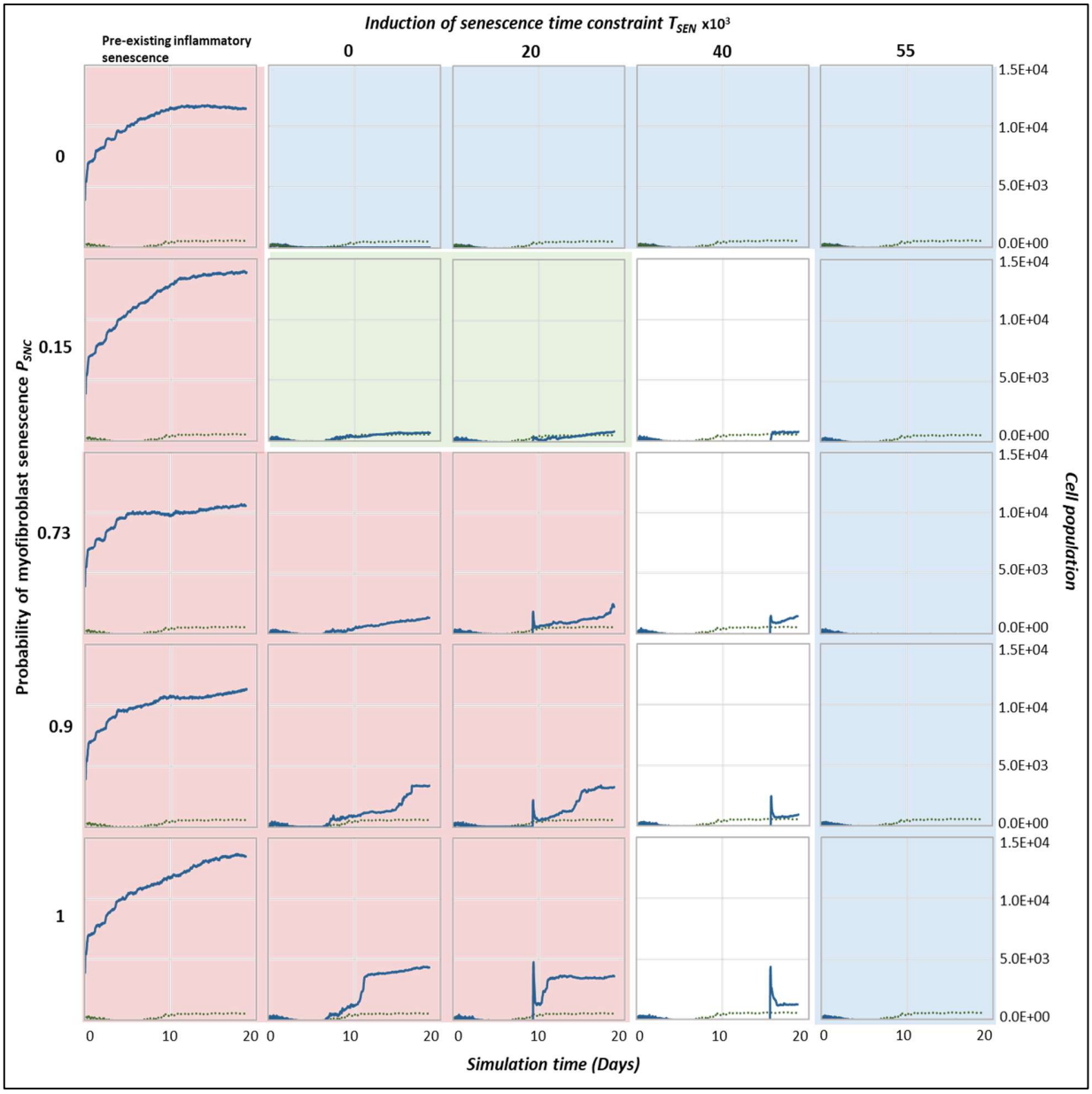

Figure 3.17 **Wound healing model multidimensional sensitivity analysis of total MMP vs time for variations in the parameters probability of myofibroblast senescence (P_{SNC}) and senescence induction time constraint (T_{SEN}) showing regions with distinct repair dynamics.** The subplots show the model simulation time series for MMP levels in the wound from a pairwise parameter sweep of the parameters: probability of myofibroblast senescence P_{SNC} (shown vertically on the

left) and senescence induction time constraint T_{SEN} (shown horizontally at the top), around their baseline values (provided in Table 2.1). Along with the different values included in the parameter sweep for the senescence induction time constraint T_{SEN} parameter, pre-existing inflammatory senescent cells are also shown to represent senescence induced during the inflammatory phase of the wound healing process (i.e., before $T_{SEN} = 0$) which was not explicitly included in the model. Simulation time in days is shown on the x axis and chemical concentration levels are shown on the y axis. The boxes highlight regions with distinct repair dynamics: chronic wound inflammation (red shaded box), healthy healing (green shaded box) and fibrotic wound response (blue shaded box). The solid blue line represents simulation time series from the pairwise parameter sweep. The dotted lines in all the plots represent simulation time series from the healthy physiological wound healing model from Chapter 2 (Figure 2.14) were included for comparison.

3.4 Discussion

Despite their crucial role in physiological tissue repair and in mitigating fibrotic disorders, senescent cells are also involved in the pathogenesis of fibrotic diseases (Zhu *et al.*, 2013; Ogrodnik *et al.*, 2017; Schafer *et al.*, 2017) and chronic wounds (Mendez et al., 1998; Stanley and Osler, 2001; vande Berg et al., 2005). As discussed in Section 3.1, senescent cells play a heterogenous and sometimes paradoxical role in tissue repair. This could be due to the different effects of the duration of the senescence program; transient senescence is beneficial, conferring pro-healing factors, whereas prolonged senescence is detrimental, leading to dysregulated immunosurveillance mechanisms and disrupted tissue repair (De-Carvalho, Jacinto and Saúde, 2021). The wound healing model developed in Chapter 2 was used here to show that aside from this duration of senescence, other factors including dynamic SASP composition and timing of senescence induction, relative to the repair phase, are also important to consider as they steer healing dynamics towards different outcomes.

To demonstrate the full range of senescent cell functions within dysregulated tissue repair, variations in senescent cell spatiotemporal dynamics were investigated. Senescent cell dynamics within the model are primarily controlled by two parameters. These are the probability of senescence in myofibroblasts, which is dictated by the parameter P_{SNC} and the time of induction of senescent cells in the model, determined by the time constraint parameter T_{SEN}. Varying these two parameters around their healthy healing simulation baseline values revealed four distinct classifications of dysregulated tissue repair due to senescent cell spatiotemporal dynamics ranging from chronic wound to fibrosis. To summarise, an increased percentage of background

senescent cells in the wound microenvironment results in a chronic wound, whereas the absence of senescent cells results in a fibrotic wound. Interestingly, the delayed induction of senescent cells during the late stages of healing also results in a fibrotic wound. Lastly, the early induction of senescent cells during the inflammation phase or the presence of systemic pre-existing inflammatory senescence, which represents prolonged senescence in an aged tissue for instance, results in a chronic wound.

A multidimensional parameter sensitivity analysis showed how the interaction between the probability of myofibroblast senescence and time of senescence induction can lead to different outcomes. Simulations with pre-existing pro-inflammatory senescence for all values of probability of myofibroblast senescence (P_{SNC}) resulted in chronic inflammation (Figure 3.9 - Figure 3.17 red shaded subplots). The features of chronic wound dynamics in these simulations confirmed decreased fibrogenic activity, characterised by insufficient ECM production, myofibroblast differentiation and PDGF levels, as previously reported in chronic wounds (Pierce *et al.*, 1995; McAndrews *et al.*, 2022). Additionally, increased proteolytic and inflammatory activity was apparent in these simulations, namely, increased number of macrophages, and high wound concentrations of MMP, CSF and inflammatory SASP, in line with previous observations in clinical studies of chronic wounds (Wysocki, Staiano-Coico and Grinnell, 1993; Loots *et al.*, 1998; Stacey *et al.*, 2019). Intriguingly, pre-existing inflammatory senescence is accompanied by increased paracrine secondary senescence compared to juxtacrine senescence, with the difference augmented with increasing numbers of senescent cells. This result within the model simulations may be expected since paracrine senescence is associated with SASP rich in inflammatory and proteolytic components (Acosta *et al.*, 2013b; Ito, Hoare and Narita, 2017; Pulido, Velarde and Alimirah, 2021; Wyles *et al.*, 2023).

Similarly, simulations with high numbers of senescent cells induced during the mid stages of healing (high P_{SNC} and low T_{SEN} values) also consistently result in a chronic wound state, which has been observed in chronic wound mouse models (Wyles *et al.*, 2023) (Figure 3.9 - Figure 3.17 red shaded subplots). These scenarios were characterised by decreased ECM production and myofibroblast numbers, and elevated inflammatory and proteolytic factors. These simulations were also accompanied by increased paracrine secondary senescence, compared to healthy healing. With increasing P_{SNC} values, paracrine senescence dominated over juxtacrine secondary

senescence. The senescent cell burden in these simulations was too overpowering to be resolved by macrophage-mediated immunosurveillance. Chronic wound inflammation due to a higher percentage of senescent cells, interestingly, exhibited enhanced fibroblast proliferation, compared to the chronic wound resulting from pre-existing inflammatory senescent cells which represents an aged tissue.

Contrastingly, the outcome of simulations with no senescent myofibroblasts (P_{SNC} is set to zero, excluding pre-existing inflammatory senescent cells) was a fibrotic response characterised by excessive ECM deposition and lack of fibrolytic activity, which is typically observed in fibrosis (Takeda *et al.*, 1994; Frost *et al.*, 2012; Zhou *et al.*, 2017; Hinz and Lagares, 2019) (Figure 3.9 - Figure 3.17 blue shaded subplots). This is in agreement with the fact that, aside from being a source of proteolytic enzymes during repair, senescent cells also produce factors that promote pro-inflammatory macrophage polarisation (Lujambio *et al.*, 2013). The polarisation of macrophages to a M1 phenotype is important during the remodelling stages since it selectively upregulates several MMPs involved in breaking down excessive scar tissue during healing (W. C. Huang *et al.*, 2012).

A similar fibrotic response is observed in simulations with a high number of senescent cells induced during the late stages of repair (high P_{SNC} and high T_{SEN} values) (Figure 3.9 - Figure 3.17 blue shaded subplots bottom right). This response is also characterised by typical fibrosis features including elevated myofibroblast numbers and ECM levels. In these simulations the fibrogenic SASP phase of senescent cells is adding to the fibrogenic activity of the repair process. This takes place through sustained anti-inflammatory macrophage activity, whereby they continue to produce PDGF, which is also elevated, for fibroblasts and myofibroblasts. A lack of macrophage pro-inflammatory polarisation leads to insufficient MMP production. myofibroblasts and fibroblasts continue to produce excessive amounts of ECM in an uncontrolled manner resulting in the scar tissue formation. Interestingly, this behaviour is seen consistently regardless of the myofibroblast senescence probability parameter P_{SNC}. This is shown in simulations with the appropriate amount of senescent cells but time of senescence induction is during the late repair stage (low P_{SNC} with high T_{SEN} values) (Figure 3.9 - Figure 3.17 blue shaded subplots top right). This highlights the importance of timing in the induction of senescent cells during the repair process relative to the repair stage, aside from SASP composition itself and the total duration of

senescence. In all these simulations, juxtacrine induction is the dominant mode of secondary senescence, which is to be expected given that fibrogenic SASP is associated with juxtacrine senescence.

Lastly, simulations run with a small number of senescent cells during the mid stages of repair (low P_{SNC} and low T_{SEN} values) result in healthy wound healing (Figure 3.9 - Figure 3.17 green shaded subplots). In these simulations, the presence of transient senescence during the mid stages of healing represented by low T_{SEN} values, promotes healing as shown by the simulation time series data. Senescent cells initially promote myofibroblast differentiation and ECM production, but then shift to promote excess ECM degradation, upregulation of immune surveillance through pro-inflammatory SASP and M1 macrophage polarisation (Lujambio *et al.*, 2013; Hoare *et al.*, 2016; Lee and Schmitt, 2019; Huang *et al.*, 2022). These processes take place in a timely manner with respect to the repair process in place, resulting in healthy healing. Even a slight deviation is shown to result in some scarring, as observed with the simulation with the higher T_{SEN} value. This is because ECM production in the wound is augmented by senescent cell-derived ECM and PDGF. This is evident from the prolonged Notch-mediated juxtacrine senescence compared to healthy healing, which means increased production of fibrogenic factors in an untimely manner and delayed transition to an inflammatory SASP. However, this does not lead to a fibrotic state since senescent cell and macrophage derived MMP is able to eventually attenuate ECM levels sufficiently before further progression.

The model simulations presented in this chapter clearly show that the differences in the spatiotemporal dynamics of senescent cells lead to a number of highly distinct repair outcomes. The difference in senescent cell dynamics can be attributed to differences in SASP composition, duration of senescence and temporal induction of senescence relative to the healing stage. The range of outcomes demonstrated here strongly highlight the dynamic and heterogenous role of senescent cells in wound healing, fibrosis and chronic wounds, and their fine-tuned control. This model serves as a baseline for further investigation into senescent cell dynamics in wound healing and can be explored further; for example, exploring a more comprehensive range of parameter values for sensitivity analysis could provide further insight into senescent cell dynamics.

In summary, the interplay between varying senescent cell activity and their surroundings lead to a wide range of qualitatively distinct spatiotemporal dynamics, summarised in Figure 3.18: An appropriate number of senescent cells present during the mid to late stages of wound healing promotes healthy healing. However, the presence of a large number of senescent cells promotes a non-healing chronic wound. Pre-mature induction of senescence or a large number of pre-existing senescent cells, such as during ageing, also promotes a chronic wound. Insufficient number of senescent cells could result in fibrosis due to lack of ECM breakdown. Lastly, delayed induction of senescent cells could result in fibrosis with delayed fibrolytic activity.

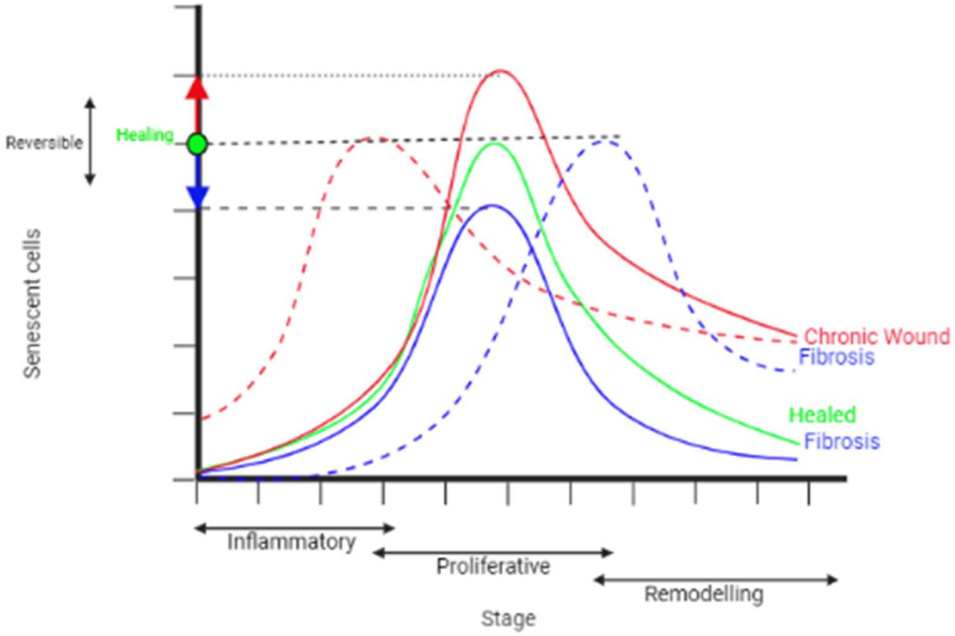

Figure 3.18 **Illustration of the hypothesis for the heterogeneity in senescent cell spatiotemporal dynamics in tissue repair and related pathologies.** The wound healing stage is shown on the horizontal axis and senescent cell percentage is shown on the vertical axis. Green solid line: An appropriate number of senescent cells induced during the mid to late stages of wound healing promotes healthy healing. Blue solid line: An insufficient number of senescent cells leads to a fibrotic response. Red solid line: Excessive senescent cells lead to a chronic wound. Red dotted line: pre-mature induction of senescent cells leads to a chronic wound response despite the total percentage of senescent cells being appropriate. Blue dotted line: Delayed induction of senescent cells leads to a fibrotic response, also despite the total percentage of senescent cells being appropriate. Senescent cell dynamics, for example, cell population, could be manipulated to reverse unfavourable pathological outcomes, within a treatment window of reversibility.

Chapter 4. Integrated time series multi-omics approach to identify networks involved in cellular senescence

4.1 Background

4.1.1 Multi-omic approaches to study cellular senescence

Cellular senescence is driven by complex molecular mechanisms involving components from different biomolecular layers that interact with one another. Each of these layers pertains to an information category and are commonly referred to as different omic types, such as genomics, transcriptomics, proteomics and metabolomics. While analysing individual omic data types can provide valuable insights, an integrated approach yields a better understanding of the system. Although the complementary information from multi-omic studies can help us better understand senescence, and the ageing process and phenotype, it has its challenges. Namely, multi-omic studies produce data that vary in type, scale, and distribution, making integration a complex task. However, several tools and techniques have been developed for the integration of multi-omic data. Integration tools can be broadly divided based on the biological question being addressed including disease subtyping, biomarker prediction and insights into disease biology. Some of the most common methods used by these tools include Bayesian fusion, similarity-based, correlation-based, and other multivariate methods (Subramanian *et al.*, 2020). Multi-omic data integration approaches can also be divided based on the level of integration including post-analysis integration, integrated analysis and systems modelling methods (Pinu *et al.*, 2019). Post-analysis integration involves first analysing the different omics in isolation followed by integrating key features from the individual omics into an overall model pathway. This approach is widely used in precision medicine to produce individual-specific interventions and interpretations (Zhao, Feng and Wei, 2022). Contrastingly, integrated analysis of omic data involves data integration prior to any downstream analysis. Specialised tools have been developed for this type of integration, allowing for multi-omic data visualisation and interpretation at a higher level, which could inform downstream analysis and be used to derive actionable insights into disease biology (Liu *et al.*, 2022). Lastly, the systems modelling method involves using multi-omic datasets to inform and predict mechanistic networks describing complex biological systems. The valuable molecular insights from multi-omic studies can be used to inform networks, using tools such as COSMOS, which integrates omic data to generate causal networks (Dugourd *et al.*, 2021), or TimiRGeN,

which can integrate longitudinal time series mRNA-miRNA datasets to generate networks and perform functional analysis (Patel *et al.*, 2021). These networks can then be combined with dynamic or steady state models to gain further insights (Pinu *et al.*, 2019).

The development of cellular senescence has been proposed to be a dynamic multi-step process (van Deursen, 2014). Senescent cell properties evolve gradually through the duration of senescence, which represents distinct transcriptional, epigenetic, proteomic and metabolomic changes. These changes are involved in the persistent cell cycle arrest as well as SASP regulation, for instance through p53 and MAPKs respectively, both of which are characteristic of senescent cells (Freund, Patil and Campisi, 2011b). Individual omic studies have contributed greatly to further our understanding of senescence biology through SASP characterisation, biomarker identification as well as mechanistic insights (Basisty *et al.*, 2020; Uyar *et al.*, 2020; Wu *et al.*, 2022). An integrated multi-omic approach has also been adopted in studying senescence. For instance, RNA-seq, ATAC-seq and ChIP-seq were used together to investigate regulatory elements of both irradiation-induced senescence and OIS, where the authors reported a robust loss of chromatin accessibility accompanying senescence, along with marked differences in nuclear architecture accessibility between RIS and OIS cells, and novel senescence biomarker genes including NAT1, PBX1 and RRM2 (Song *et al.*, 2022). Another study used RNA-seq, small RNA-seq, qCLASH (linking mRNAs to their attached miRNAs) and kinome profiling to investigate the mechanism whereby cancer cells evade therapy-induced senescence (Gureghian *et al.*, 2023). The study reported insulin signalling to be associated with persisting senescence, as well as a mechanism for escaping senescence through IFNg-mediated induction of EMT and ERK5 signalling activation. Additionally, single-cell RNA-seq and proteomics were used to investigate immune system modulation by mesenchymal stem cells (Gao *et al.*, 2023). Through integrated omic analysis, the study found that mesenchymal stem cell senescence leads to impaired immunomodulation associated with decreased production of the immunosuppressive molecule PD-L1. Lastly, one study used RNA-seq, single-cell RNA-seq, proteomics, metabolomics, and ATAC-seq to investigate the biology of RS; this study is particularly valuable as it provides a time series dataset ranging from cell proliferation to deep senescence (Chan *et al.*, 2022). In addition to the robust multi-omic time series data produced, the study also investigated irradiation-induced senescence and cell density-induced senescence using RNA-seq to disentangle the differences

between the various senescence induction mechanisms. The study pointed out that RS follows a pattern similar to EMT regulated by YAP1/TEAD1 and TGF-β2, a feature of RS that was not shared with RIS and cell density-induced senescence. They also reported a global increase in DNA accessibility throughout the senescence process and that the initiation of RS is potentially regulated by nicotinamide N-methyltransferase.

These multi-omic datasets have not only provided meaningful insights into senescence biology but are valuable resources for further analysis and investigation and can be used to inform mechanistic networks which can potentially provide a targeted approach to computational modelling and therapeutic interventions (Pinu *et al.*, 2019). However, this integrated multi-omic approach to identify causal pathways and networks involved in the cell senescence process for hypothesis generation is still lacking.

With that said, the project in this chapter uses the multi-omic time series data produced by (Chan *et al.*, 2022) to investigate the multi-step evolution of RS. As previously stated, the study by (Chan *et al.*, 2022) used bulk RNA-seq, single-cell RNA-seq, proteomics, metabolomics, and ATAC-seq to investigate the biology of RS, where they pre-processed and analysed each omic data type individually: differential analysis, hierarchical clustering and enrichment analysis for bulk RNA-seq data; differential analysis, clustering and pseudo-time analysis for single-cell RNA-seq data; peak calling, differential and chromatin state analysis, and motif enrichment for ATAC-seq data; and differential analyses for metabolomic and proteomic data. In addition to this, they also performed transcriptional regulator analysis to predict TFs from bulk and single-cell RNA-seq data.

However, the focus of this project was to implement an alternative approach to investigating the multi-omic dataset from (Chan *et al.*, 2022), through an integrated analysis to identify temporal patterns of variation across the progression of senescence, as well as mechanistic networks across the senescence time series, with a workflow developed using existing integration tools, as discussed in the next section.

4.2 Methods

4.2.1 Summary of data

The data was obtained from (Chan *et al.*, 2022), which includes details on study design, data generation and processing. Briefly, samples of WT and hTERT immortalised WI-38 lung fibroblasts

were obtained at time points of 20, 25, 33, 37, 46 and 50 population doublings (PDL) to capture RS. WT RS samples were also obtained at PDL29, but this time point was not available for the hTERT group. Samples were analysed using RNA-seq, ATAC-seq (which is an assay for chromatin accessibility), proteomics and metabolomics. Only paired sample collections that were available for both sample groups (RS and control) and all omic types were used for this analysis since this dataset was chosen particularly because of the multiple omic assays performed across the same time points. WT RS group will be referred to as WI and the control group as hTERT hereafter.

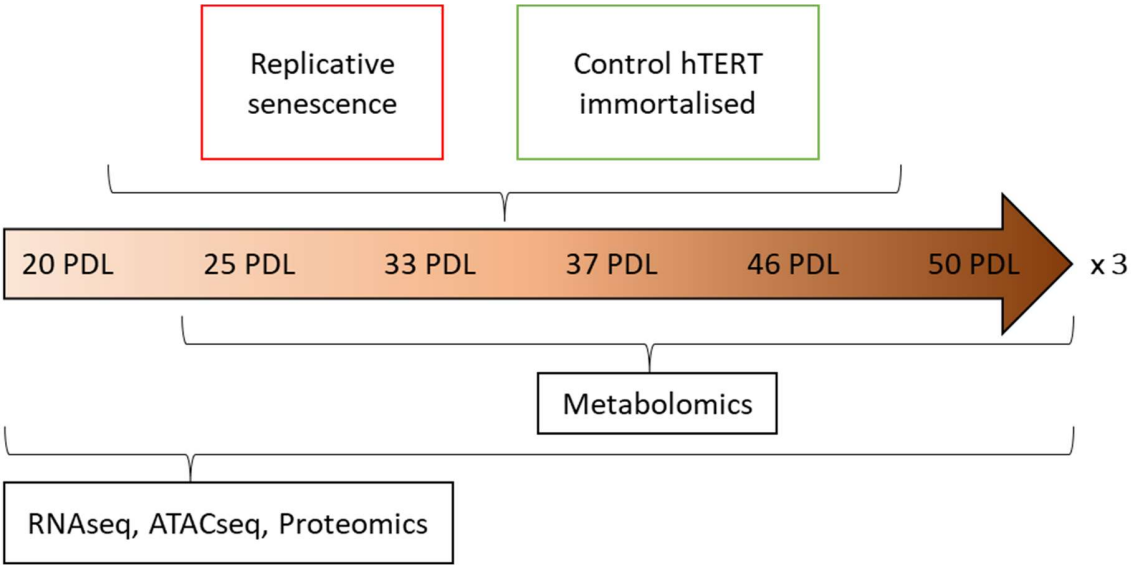

Figure 4.1 **Summary of the multi-omic dataset used in this project**. RNA-seq, ATAC-seq, metabolomic and proteomic data were obtained from (Chan *et al.*, 2022). WT and hTERT immortalised WI-38 lung fibroblasts were obtained at PDL time points 20, 25, 33, 37, 46 and 50. Three replicate samples were obtained. All time point samples were analysed using RNA-seq, ATAC-seq and proteomic analysis. PDL time point samples 25, 33, 37, 46 and 50 were also analysed using metabolomics.

4.2.2 Data pre-processing

RNA-seq data was downloaded from GSE175533 using the *fastq-dump* function from SRA-toolkit (Leinonen *et al.*, 2010). Sequencing quality control was performed using FastQC (Andrews, 2010), and the results were compiled using MultiQC (Ewels *et al.*, 2016). Adapter sequences were identified, which were trimmed using Cutadapt (Martin, 2011), followed by performing quality control steps once more to ensure successful read trimming. Reads were mapped to the transcriptome using Salmon software (Patro *et al.*, 2017) to obtain transcript abundance

estimates. Salmon was used in the quasi-mapping mode. This requires an index of the reference transcriptome, which contains information pertaining to the orientation and position of the fragment origin. The Salmon index was constructed using the reference transcriptome for Homo Sapiens (GRCh38) from Ensembl (release v.109) (Cunningham *et al.*, 2022). Salmon was then implemented on the paired end FASTQ files, along with the indexed transcriptome. Salmon quantification files were then processed and analysed using R. Transcript-level abundance estimates from Salmon were summarised to the gene-level using tximport Bioconductor package (version 1.28.0) (Soneson, Love and Robinson, 2016). Tximport was used with the gene annotation file for Homo Sapiens (GRCh38) from Ensembl, along with AnnotationDbi Bioconductor package (version 1.62.2) to associate transcript level IDs to their gene-level IDs. Ensembl gene IDs were coupled with HGNC gene names using BiomaRt Bioconductor package (version 2.56.1) (Durinck *et al.*, 2005) with the aim of retaining all data for downstream analysis.

Raw ATAC-seq peak counts, metabolomic and proteomic abundance data were obtained from the author's GitHub repository. The authors had carried out sufficient pre-processing of their raw data, as previously described, which facilitated the focus here on downstream analysis and data integration (Chan *et al.*, 2022).

4.2.3 Factor analysis for unsupervised integration of time series omics data

Next, multi-omic factor analysis (MOFA) was used to identify latent factors which represent major sources of variation that can explain the underlying heterogeneity in the data. MOFA, which is a Bayesian ML method, was performed using the MOFA2 Bioconductor package (version 1.10.0) (Argelaguet *et al.*, 2018). In order to deal with the time series nature of this dataset, MEFISTO implemented within MOFA, was used to perform unsupervised multi-omic data integration, to identify major sources of variation (factors) shared between and across the different omics (Argelaguet *et al.*, 2018; Velten *et al.*, 2022).

The input for MOFA can be one or multiple omic datasets known as "views" (in this case it is RNA-seq, ATAC-seq, proteomic and metabolomic), consisting of "features" which refers to the constituents of each omic data type (such as individual genes, proteins, chromosome regions and metabolites). MOFA can also be used with different sets of samples that represent different treatment criteria or conditions, which is referred to as "group" (in this case WI and hTERT). In

addition to this, the MEFISTO framework used with MOFA allows for time series as well as spatial multi-omic data integration. For this reason, MOFA with MEFISTO was used to investigate this time-series multi-omic dataset.

4.2.3.1 Data processing

Before MEFISTO can be implemented, the data needs to be normalised and filtered to obtain highly variable features for each view. RNA-seq and ATAC-seq data with zero and low counts were pre-filtered prior to further analysis. RNA-seq and ATAC-seq counts were normalised using *estimateSizeFactors* and *varianceStabilizingTransformation* functions from DEseq2 (version 1.40.2) (Love, Huber and Anders, 2014), as per the suggestion of MOFA2 developers. Metabolomic data was filtered to remove lowly expressed metabolites and was log transformed to remove heteroscedasticity using base R functions (van den Berg *et al.*, 2006). Proteomic data was also filtered to remove low abundance proteins, followed by variance stabilising normalisation (VSN) using the *performVSNNormalization* function from the R package NormalyzerDE (Willforss, Chawade and Levander, 2019). Highly variable features were selected from each view and all data was mean centred. The top 6000 most highly variable features for RNA-seq, ATAC-seq and proteomic, and top 200 for metabolomic data were chosen for further analysis. The total number of metabolites was quite low compared to the other omic datsets.

4.2.3.2 Model training and selection

MEFISTO model was trained using the processed data with a variance threshold (i.e., threshold for the minimum variance explained by each factor) of 1.5% and default options as per the authors suggestions. PDL time point was used as a covariate and multi-group framework was implemented for WI and hTERT groups. MEFISTO identified outliers and mismatched samples; Outlier samples were disregarded from further analysis in order to avoid skewing downstream results, whereas mismatched samples were rectified by relabelling. Data processing steps were repeated and MEFISTO model was retrained on the clean data.

4.2.3.3 Enrichment analysis

Enrichment analysis was performed on the feature members of the factors of interest to gain further insight into the sources of variation identified by MEFISTO. Gene set enrichment analysis (GSEA) was performed within the MOFA2 R package based on gene sets obtained from MSigDB

(v2023.1. Hs), including the Hallmark gene sets and Gene Ontology Biological Process (GOBP) gene sets (Subramanian *et al.*, 2005). Metabolite enrichment analysis (MSEA) was performed based on KEGG pathways using the web-based tool MetaboAnalyst (version 5.0) (Pang *et al.*, 2021). Genomic region enrichment analysis (GREA) was performed based on MSigDB GOBP gene sets with rGREAT Bioconductor package using hg38 transcription start site (TSS) annotation (Gu and Hübschmann, 2023). Significant enrichment was considered at the standard adjusted p-value threshold of 0.05.

4.2.4 Identification of multi-omic causal networks across the senescence time series

Next, the data was analysed to identify signalling pathways that could explain the multi-step senescence process at each time point available. This was done using CARNIVAL (Liu *et al.*, 2019) and COSMOS (Dugourd *et al.*, 2021). CARNIVAL is a tool that can identify upstream mechanistic signalling processes that drive downstream expression data using prior knowledge networks (PKN) and an optimisation program called linear integer programming to integrate information. COSMOS is a wrapper that utilises CARNIVAL's optimisation method to identify deregulated upstream pathways from downstream multi-omic expression data including transcriptomics, phosphoproteomics, and metabolomics.

4.2.4.1 Differential analysis

Differential features must be used in order for CARNIVAL and COSMOS to identify significantly dysregulated pathways. Hence, differential analysis was performed to identify features that responded differently at each time point after the first, by comparing the WI and hTERT groups while controlling for the first time point (PDL20 for RNA-seq and ATAC-seq, and PDL25 for metabolomic data). Analysis was performed on the data, following MOFA where extreme outliers and zero counts were removed and mismatched samples were rectified as previously described. DESeq2 (version 1.40.2) (Love, Huber and Anders, 2014) was used for gene and peak differential analysis of RNA-seq and ATAC-seq data respectively. Un-normalised counts for both data types were used, as this is required by DESeq2. Pairwise Wald tests were performed between the first time point (PDL20 for RNA-seq and ATAC-seq data) and every subsequent time point to identify differential genes and peaks for each time point in the WI group relative to the hTERT group.

Limma (version 3.56.2) (Ritchie *et al.*, 2015) was used for metabolomic data, which was filtered to remove lowly expressed metabolites and was log transformed using base R functions. Differential analysis was performed for metabolites using the standard functions: *lmFit*, *contrasts.fit* and *eBayes*. Pairwise comparisons were made again between the first time point (PDL25 for metabolomic data) and every subsequent time point to identify differential metabolites for each time point in the WI group relative to the hTERT group.

An adjusted p-value threshold of 0.05 was used for all differential analyses. The t-statistic value was used for downstream network analysis along with the significant features, as per the suggestion of CARNIVAL/COSMOS developers. Time point PDL29 was excluded since hTERT samples for this time point were missing from the data, as stated previously.

4.2.4.2 Identifying transcriptional regulatory networks

Aside from differential features, CARNIVAL and COSMOS also requires TF activity data in the form of transcriptional regulatory networks (TRN) along with a measure for mode of regulation. TRNs refer to a collection of TFs and their target genes (Babu *et al.*, 2004). TRNs were generated for each time point from differentially expressed genes and differentially accessible chromosome regions (or peaks). Differential peak regions for each time point were scanned for TF binding motifs using the command line tool MEME Suite (version 5.5.3) (Bailey *et al.*, 2015). Differential peak regions were first converted to GRanges objects and then to BED files using the Bioconductor packages GenomicRanges (version 1.52.0) and rtracklayer (version 1.60.1) respectively (Lawrence, Gentleman and Carey, 2009; Lawrence *et al.*, 2013). FASTA files were obtained from the BED files using BED2FASTA tool from MEME Suite. FIMO from MEME Suite was then used to scan the sequences for motif occurrences based on the TF binding models from HOCOMOCO (v11 core) (Kulakovskiy *et al.*, 2018). Results from FIMO were then imported into R using the memes Bioconductor package (version 1.8.0). HOCOMOCO motif IDs were converted to their corresponding TF gene names using the annotation file obtained from HOCOMOCO (HOCOMOCOv11_core_annotation_HUMAN_mono). In order to associate source TFs to their target genes, peak motif sequences from FIMO were annotated using ChIPseeker Bioconductor package (Wang *et al.*, 2022). The *annotatePeak* function from ChIPseeker was used with the TxDb object TxDb.Hsapiens.UCSC.hg38.knownGene, org.Hs.eg.db annotation from the org.Hs.eg.db Bioconductor package (version 3.17.0) and default TSS region range of –3000 to 3000. This

resulted in a list of source TFs and their proximal target genes for each time point. A Pearson correlation was performed using the *cor.test* function from the *stats* R package between VST normalised ATAC-seq count data for source TFs and RNA-seq count data for gene targets with replicates averaged. This was done similar to a study on cancer by (Sanghi *et al.*, 2021) where ATAC-seq peak and gene linkage was quantified by performing a Pearson correlation between RNA-seq count values and peak values for peaks proximal to the gene's TSS. Furthermore, another study on T cell regulation of rheumatoid arthritis by (J. Yang *et al.*, 2020) linked ATAC-seq and RNA-seq time course data by performing a paired Pearson correlation between peaks and associated genes.

A p-value threshold of 0.05 was used to obtain significantly correlated TF-target gene sets, which were used for downstream analysis as TRNs. The resulting TRNs and their correlation estimate measure, along with normalised RNA-seq data was used to calculate a normalised enrichment score (NES) using the Weighted Mean method, as suggested by the developers of CARNIVAL/COSMOS. This was done using the *wmean* function from the *decoupleR* Bioconductor package using default options (version 2.6.0) (Badia-I-Mompel *et al.*, 2022).

4.2.4.3 Inferring signalling networks across the senescence process

Once the TRNs, and differential genes and metabolites were processed and prepared, they were used to identify networks involved at each PDL time point. For the first time point, PDL25, the CARNIVAL Bioconductor package (version 2.10.0) (Liu *et al.*, 2019) was used since metabolomic data was not available for this time point. In addition to the analysis performed in the previous sections, CARNIVAL also requires pathway activity scores which were inferred from pathway responsive genes from RNA-seq data. Pathway activity scores were obtained through the PROGENy Bioconductor package (version 1.22.0) as per CARNIVAL developers' suggestions (Schubert *et al.*, 2018). CARNIVAL was then used with the TRNs, differentially expressed genes with t-statistic values and their normalised count data, pathway activity scores from PROGENy and a PKN from Omnipath (Türei, Korcsmáros and Saez-Rodriguez, 2016) which was obtained from CARNIVAL developers' GitHub repository.

For the subsequent time points, COSMOS was used with the TRNs, differentially expressed genes with t-statistic values and their normalised count data, differential metabolites with t-statistic

values and the most up-to-date PKN obtained from the author's GitHub repository containing protein-protein interactions from Omnipath (Türei, Korcsmáros and Saez-Rodriguez, 2016), allosteric regulations from STITCHbd (Szklarczyk *et al.*, 2016) and metabolic reaction networks from redHUMAN (Masid, Ataman and Hatzimanikatis, 2020). Metabolite names were converted to HMDB IDs using MetaboAnalyst prior to being used with COSMOS (Pang *et al.*, 2021). The Cbc-COIN solver was used for both CARNIVAL and COSMOS (Forrest *et al.*, 2023). Network solutions were filtered to discard nodes with zero activity across all solutions from CARNIVAL and COSMOS.

Over-representation analysis (ORA) was performed on the resulting network nodes for each time point based on MSigDB (v2023.1. Hs) Hallmark gene sets and GOBP gene sets using piano Bioconductor package (version 2.16.0) (Subramanian *et al.*, 2005; Väremo, Nielsen and Nookaew, 2013). Networks of interest from significantly represented pathways for each time point were analysed and visualised using igraph (version 1.5.1) and visNetwork (version 2.1.2) R packages.

4.3 Results and discussion

4.3.1 Analysis of senescence dynamics through integrated time series MOFA

To explore the dynamic nature of senescence over time, the first step taken was to identify the major sources of variation in the data, with factor analysis using the methods detailed in section 4.2.3. A MEFISTO model was trained using the time series RNA-seq, ATAC-seq, metabolomic and proteomic data with a minimum explained variance threshold of 1.5%, which identified 6 latent factors (Figure 4.2B) that explain sources of variation within the data as summarised in Figure 4.2A. The unsupervised nature of MEFISTO was able to capture biological as well as technical variability in the data. Factors 1 and 4 are particularly interesting as they explain variance shared across RNA-seq, ATAC-seq and metabolomic data in the WI group specifically (i.e., three out of the four omic types included in this analysis). Contrastingly, factor 2 explains variance in the hTERT group. The proteomic data does not contribute to much variance in any of the factors, especially for the WI group (Figure 4.2D).

Most variance is explained by RNA-seq and ATAC-seq data in the WI group and some by metabolomic data as shown in Figure 4.2D, which is understandable due to the difference in the number of total features per omic type as shown in Figure 4.2A. This is because a higher feature number generally results in more explained variation in the data. However, this could not be

avoided due to the differences in the dataset dimensions. The correlation matrix shown in Figure 4.2C shows that none of the factors are strongly correlated to one another and therefore represent unique sources of variation, indicating good model fit.

Individual factor values were then investigated to identify the specific sources of variation, at the sample level, explained by each factor. The factors identified capture global sources of variation in the data. Each factor value is centred at zero along a one-dimensional axis. The factor value alone cannot be interpreted. However, only the relative positioning of samples is important. Regarding the value signs, samples with different signs display opposite characteristics, with higher absolute values indicating stronger effects.

Factor 1 values captured gradual changes across the PDL time points for the WI group, with little variation explained for the hTERT group (Figure 4.3A and B). This strongly indicates biological variation since the variation is not shared with the control group and also because the factor values fall sequentially according to the different time points with minimal replicate-derived variation. On the other hand, factor 2 primarily captures variation in the hTERT group, whereas factor 3 captures variation derived from replicates (Figure 4.3A and B). Notably, factor 4 captures variation driven by the time point PDL46 within the WI group, and not much in the hTERT group. This is interesting as the time point PDL46 represents the transition from intermediate to late senescence at PDL50. Likewise, factor 5 also captures variation in the WT group, however source of variation appears to be from replicates rather than biological factors as shown in Figure 4.3B. Factor 6 did not represent much variation in either group.

Since factors 1 and 4 were the most biologically interesting to the WI group, as explained in the previous paragraph, these factors were investigated further, as shown in Figure 4.3C. Both factors explain sources of variation strongly present in the WI group and not much in the hTERT group. Moreover, these factors do not explain much inter-replicate variability. In summary, factor 1 explains changes across all the PDL time points, but factor 4 explains differences between the last 2 time points PDL46 and PDL50.

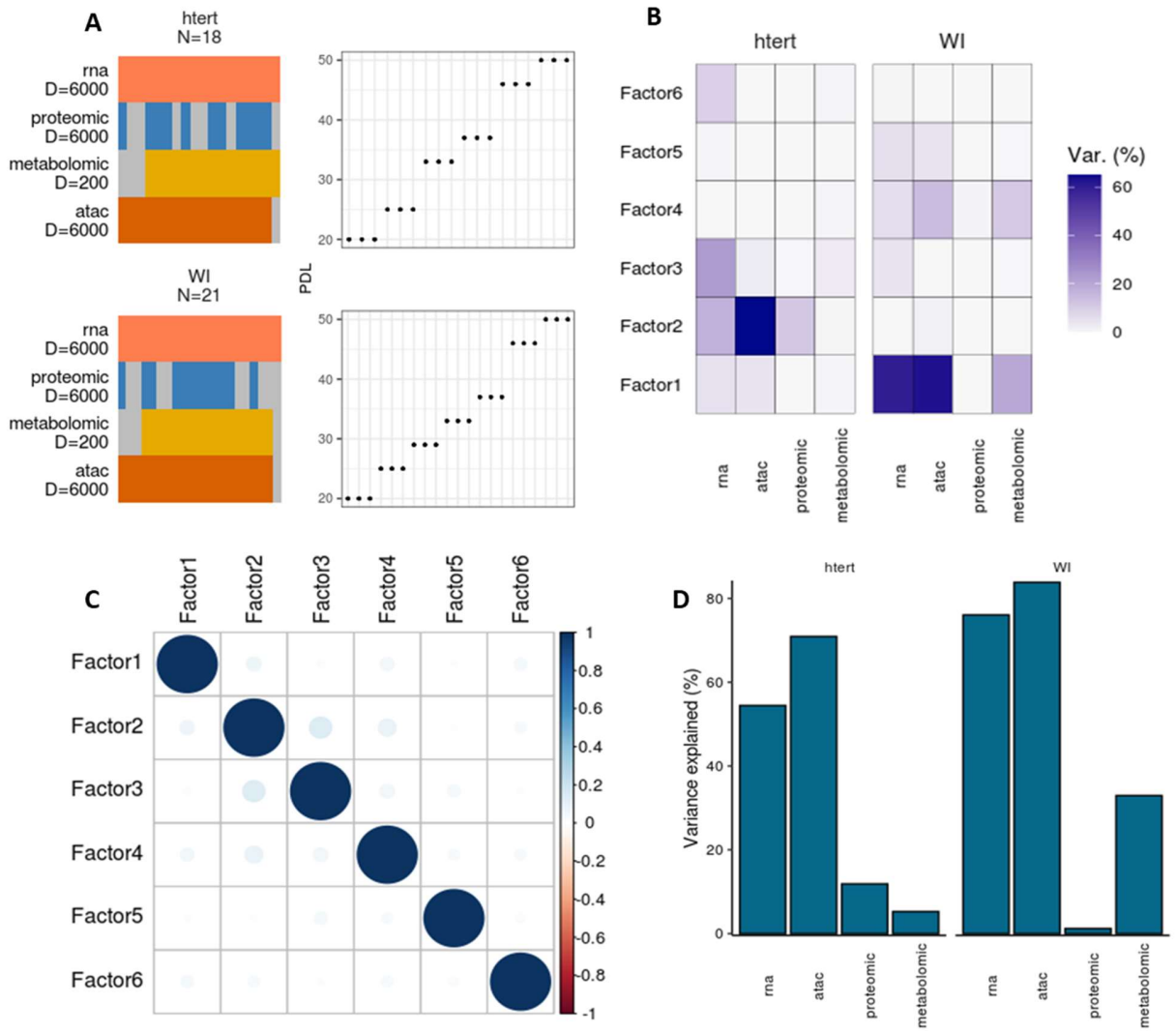

Figure 4.2 **Overview of results from MOFA using MEFISTO. A:** Overview of the input data. The plot shows the two groups (htert (top) and WI (bottom)), with total number of samples N. Right top and bottom plots show the different data modalities presented in each row, along with size of the data (D = number of features). Missing samples are shown by the grey blocks. Left top and bottom plots show the time values for each sample. **B:** Variance decomposition plot. Proportion of total variance explained (variance explained > 1.5%) by each factor for every omic type (view) for the two groups htert (left) and WI (right). **C:** Correlation matrix for the factors. **D:** Cumulative proportion of total variance explained by each omic type (known as view) across all the factors shown for both groups, htert and WI.

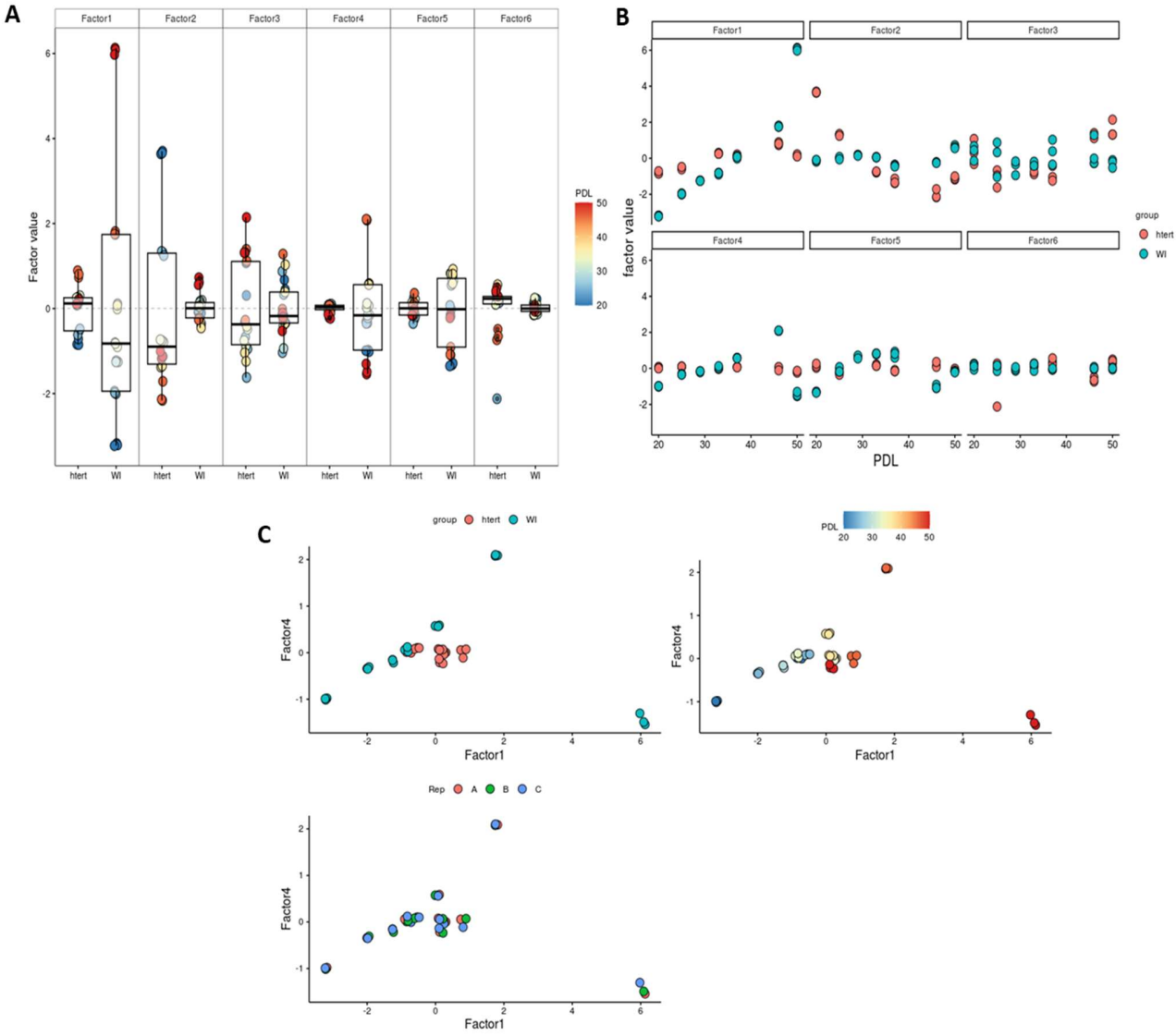

Figure 4.3 **Members of the individual factors identified by MEFISTO.** These plots show inferred factor value annotation based on PDL time points, group and replicate. **A:** Beeswarm plots with individual factor values for each sample, i.e., each dot represents a sample and its inferred factor value. Each subplot is for a factor, consisting of sample factor values for each group (htert and WI), which are coloured based on PDL time points, as indicated in the colour bar to the right. Boxplots show distribution of the factor values. Samples with higher absolute values indicate stronger effects, and different signs display opposite characteristics. **B:** Plot of inferred factor values (y axis) as a function of PDL time points (x axis). Each dot represents a sample and its inferred factor value, coloured by group; htert (pink), WI (blue). **C:** Scatterplot for the combination of factor 1 versus factor 4, with colours denoting group (top left), time point (top right) and replicate (bottom left).

To further investigate the sources of variation in factors 1 and 4 at the feature level for each omic data type, the top 15 features for RNA-seq, ATAC-seq and metabolomic data were plotted as shown in Figure 4.4 and Figure 4.5 for factor 1 and factor 4 respectively. Proteomic data features were not investigated as it did not contribute to any meaningful biological variance in these factors that were investigated, as shown in Figure 4.2B and D under WI group, where as shown, proteomic data does not contribute to any significant variance. The weights presented in these plots indicate how strongly each feature is related to the corresponding factor, with values closer to zero indicating no association. Moreover, features with positive weights are enriched in positive factor values, whereas features with negative weights are enriched in negative factor values. For the sake of ease of interpretation, positive and negative weights were plotted separately.

For factor 1, which as stated before was associated with the gradual time evolution of senescence, positive factor values indicate the last 2 PDL time points (PDL46 and PDL50), whereas negative factor values represent early time points (PDL20 and PDL 25). The positive factor 1 values (Figure 4.4A above the dashed line), associated with later senescent time points PDL46 and PDL50, were driven by genes including *IGFBP7, FOXE1, TXNIP, MASP1* and *TGFB1* (Figure 4.4B). These genes are known to play important roles in senescence. For instance, *IGFBP7* is known to promote G1 phase cell cycle arrest inhibiting cell proliferation and is a prominent SASP member (Wajapeyee *et al.*, 2008; Severino *et al.*, 2013). *FOXE1* has been reported to be a candidate biomarker for senescence, although its specific function remains unknown (Medeiros Tavares Marques *et al.*, 2017; Psaroudis *et al.*, 2022). On the other hand, *TXNIP* has been reported to regulate cell senescence by inhibiting AKT pathways mediated by glucose-derived metabolic stress (Huy *et al.*, 2018; Choi and Park, 2023). *MASP1* is known to be upregulated in senescence, although its specific role is unknown (Avelar *et al.*, 2020; Limbad *et al.*, 2020; Boulet *et al.*, 2023). The role of *MASP1* requires further investigation: it encodes Mannan-binding lectin serine protease 1, involved in the lectin pathway of the complement system, and therefore it could potentially be involved in SASP regulation. Lastly, *TGFB1* is another established regulator and inducer of cell senescence (Tominaga and Suzuki, 2019; Matsuda *et al.*, 2023). In addition to these genes, metabolites such as o-phosphoethanolamine and CDP-ethanolamine, and some chromosome regions (which will be investigated further in later sections) were also associated with the later

time points (Figure 4.4C and D). The metabolites o-phosphoethanolamine and CDP-ethanolamine are involved in phospholipid biosynthesis, a pathway essential for cell membrane formation and the synthesis of lipid-derived signalling molecules (Gibellini and Smith, 2010). Interestingly, although not unexpectedly, phospholipid metabolism has been linked to several regulators of senescence and SASP (Hamsanathan and Gurkar, 2022). For instance, phospholipids mediate eicosanoid synthesis, which contributes to the inflammatory nature of SASP (Narzt *et al.*, 2021).

On the other hand, negative factor 1 values (Figure 4.4A below the dashed line) associated with early time points PDL20 and PDL25 were driven by genes including *MKI67, HAS2, RRM2, TOP2A* and *CDC20* (Figure 4.4E). As expected, all these genes play crucial roles in cell proliferation and DNA replication. For instance, *MKI67* is an established marker of proliferation (Uxa *et al.*, 2021), *HAS2* is involved in cell proliferation as well as cell migration (Itano *et al.*, 2002), *RRM2* and *TOP2A* are crucial for DNA replication (Li *et al.*, 2018; Bossaert *et al.*, 2021), and *CDC20* is an important cell-cycle regulator (Yu, 2007). Although, none of the metabolites were significant, some chromosome regions were associated with the early time points (Figure 4.4F and G).

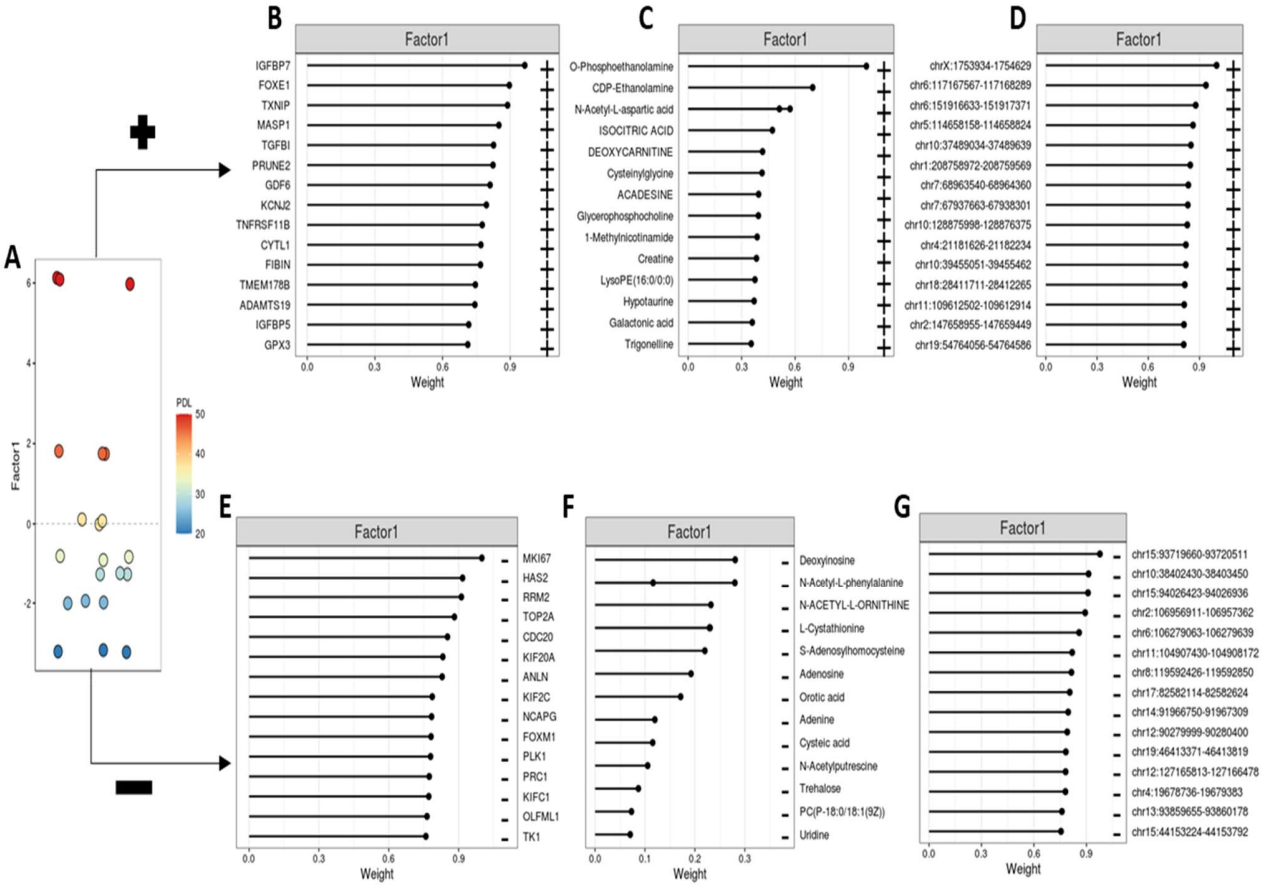

Figure 4.4 **Inferred factor 1 weights for the top 15 features across the omic data types associated with early and late PDL time points. A:** Beeswarm plot with individual factor values for each sample for factor 1, WI group. Samples are coloured based on PDL time points, as indicated in the colour bar to the right. Samples with higher absolute values indicate stronger effects, and different signs display opposite characteristics. **B, C** and **D** show the top 15 genes (**B**), metabolites (**C**) and chromosome regions (**D**) associated with positive factor 1 values (as indicated by the + sign). **E, F** and **G** show the top 15 genes (**E**), metabolites (**F**) and chromosome regions (**G**) associated with negative factor 1 values (as indicated by the - sign). Weight values indicate how strongly each feature (gene, metabolite, or chromosome region) is related to the corresponding factor; values closer to zero indicate no association. Weights were scaled from -1 to 1.

For factor 4, which represents variation derived from the intermediate senescence time point PDL46, positive factor values indicate PDL46, whereas negative factor values represent the time point PDL50. The positive factor 4 values (Figure 4.5A above the dashed line) associated with the time point PDL46 were driven by genes including *FOXE1, CRHBP, HBE1, IGFBP5* and *GRPR* (Figure 4.5B). *FOXE1,* as stated previously, has been reported to be a candidate biomarker for

senescence. *CRHBP* is involved in the stress response, although its specific role in cell senescence requires further investigation (Curley *et al.*, 2021). *HBE1* codes for the protein haemoglobin subunit epsilon involved in oxygen transport. Its role in cell senescence is unknown, however, it has been reported to be overexpressed in cancer cells resistant to radiotherapy-induced apoptosis and could potentially play a role in the ability of senescent cells to evade apoptosis (Busuttil *et al.*, 2003; Park *et al.*, 2019). However, this also requires further investigation. *IGFBP5* on the other hand is a known inducer of senescence (Kwang *et al.*, 2007; Sanada *et al.*, 2018). Interestingly, *GRPR*, as well as other genes with positive weights including SEMA6A and HAS2 are known to attenuate senescence (Avelar *et al.*, 2020; Mastrantonio, You and Tamagnone, 2021). This could highlight the intermediary nature of this time point before reaching full senescence. Besides, metabolites including methylcysteine, L-cysthathionine and thymidine, and some chromosome regions were also associated with PDL46 (Figure 4.5C and D). Methylcysteine is a derivative of cysteine and L-cysthathionine is an intermediate in the synthesis of cysteine. Cysteine has been reported to impair mitochondrial function, which plays an important role in regulating senescence (Hughes *et al.*, 2020; Miwa *et al.*, 2022). Thymidine on the other hand is involved in DNA synthesis and repair (Bitter *et al.*, 2020). This again highlights the intermediary nature of this time point in the multi-step senescence process.

On the other hand, negative factor 4 values (Figure 4.5A below dashed line) associated with late senescence time point PDL50, although weakly, were driven by as *CTSK, MMP3, SLC16A6* and *THBD* (Figure 4.5E). *CTSK* and *MMP3* are involved in tissue destructive responses and code for proteins that are found in SASP (Farr *et al.*, 2017; De-Carvalho, Jacinto and Saúde, 2021; Yue *et al.*, 2022). *SLC16A6* codes for a membrane transport protein that exports ketone bodies. This gene has been reported to be upregulated with senescence although its exact role is unknown and requires further investigation (Wagner *et al.*, 2008). Lastly, *THBD,* which codes for an anticoagulant transmembrane protein has been reported to play a role in the pro-survival pathways that are crucial for senescence (Pan *et al.*, 2023). None of the metabolites were significant in these factor values, although, several chromosome regions were significant (Figure 4.5F and G). Chromosome regions will be analysed further in the following sections.

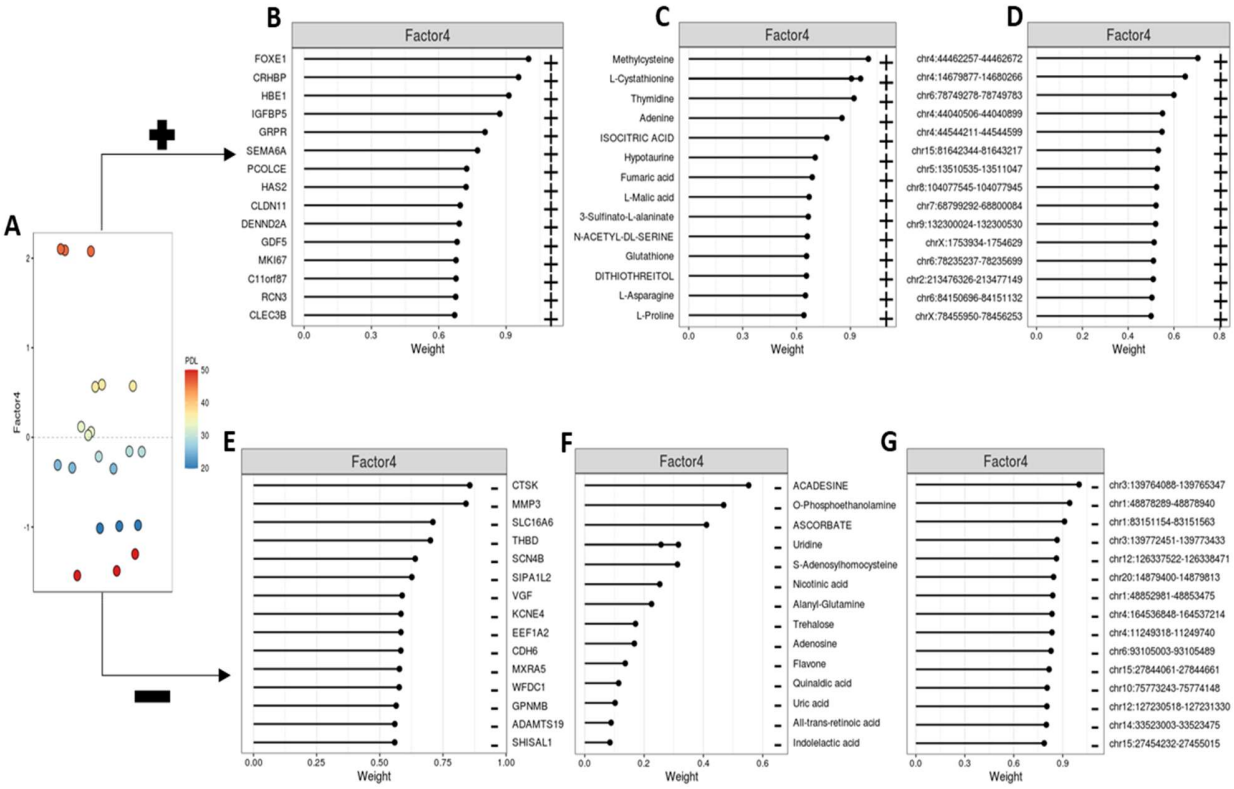

Figure 4.5 **Inferred factor 4 weights for the top 15 features across the omic data types associated with intermediate and late PDL time points. A:** Beeswarm plot with individual factor values for each sample for factor 4, WI group. Samples are coloured based on PDL time points, as indicated in the colour bar to the right. Samples with higher absolute values indicate stronger effects, and different signs display opposite characteristics. **B, C** and **D** show the top 15 genes (**B**), metabolites (**C**) and chromosome regions (**D**) associated with positive factor 4 values (as indicated by the + sign). **E, F** and **G** show the top 15 genes (**E**), metabolites (**F**) and chromosome regions (**G**) associated with negative factor 4 values (as indicated by the - sign). Weight values indicate how strongly each feature (gene, metabolite, or chromosome region) is related to the corresponding factor; values closer to zero indicate no association. Weights were scaled from -1 to 1.

To summarise, factor 1 elucidated the gradual time evolution of senescence and was driven by cell proliferation markers for the early time points and typical senescent cell regulators and markers for the later time points, which is to be expected. On the other hand, factor 4 highlighted the shift from intermediate senescence, driven by factors potentially involved in establishing a durable cell cycle arrest, to late senescence, driven by factors regulating SASP.

Lastly, since factor 1 explained the most amount of gradual time-dependent variation across senescence, the z-scores of the top 30 features were visualised using heatmaps for each omic

type to observe how the samples cluster (Figure 4.6). Late and early senescence time points cluster together for the WI group in the RNA-seq, ATAC-seq and metabolomic data but not for the proteomic data (Figure 4.6). This along with the fact that the proteomic data did not contribute to significant time-dependent variation led to the decision to not include the proteomic dataset for further analyses at this point of time.

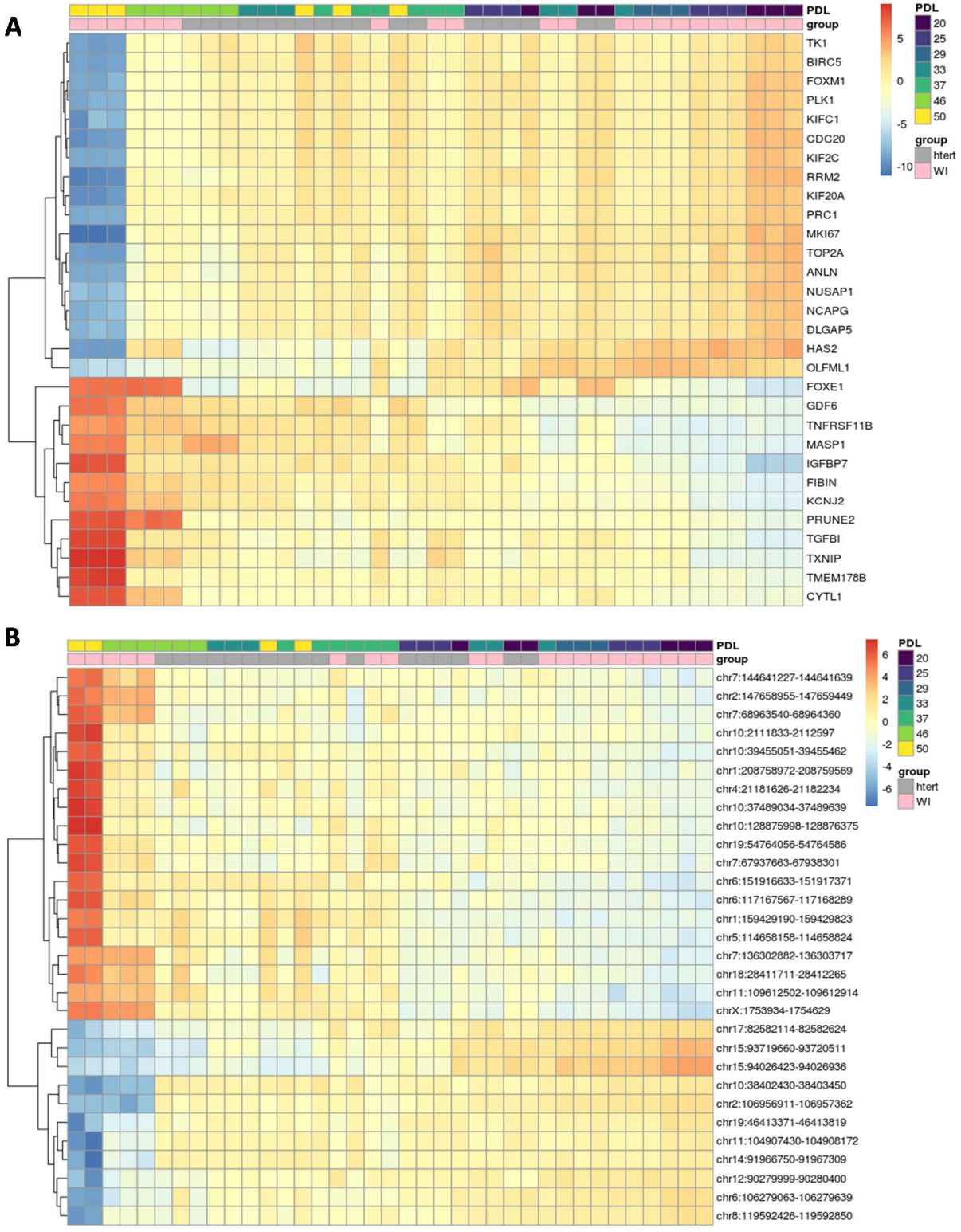
A
PDL
group
TK1
BIRC5
FOXM1
PLK1
KIFC1
CDC20
KIF2C
RRM2
KIF20A
PRC1
MKI67
TOP2A
ANLN
NUSAP1
NCAPG
DLGAP5
HAS2
OLFML1
FOXE1
GDF6
TNFRSF11B
MASP1
IGFBP7
FIBIN
KCNJ2
PRUNE2
TGFBI
TXNIP
TMEM178B
CYTL1
5
0
-5
-10
PDL
20
25
29
33
37
46
50
group
htert
WI
B
PDL
group
chr7:144641227-144641639
chr2:147658955-147659449
chr7:68963540-68964360
chr10:2111833-2112597
chr10:39455051-39455462
chr1:208758972-208759569
chr4:21181626-21182234
chr10:37489034-37489639
chr10:128875998-128876375
chr19:54764056-54764586
chr7:67937663-67938301
chr6:151916633-151917371
chr6:117167567-117168289
chr1:159429190-159429823
chr5:114658158-114658824
chr7:136302882-136303717
chr18:28411711-28412265
chr11:109612502-109612914
chrX:1753934-1754629
chr17:82582114-82582624
chr15:93719660-93720511
chr15:94026423-94026936
chr10:38402430-38403450
chr2:106956911-106957362
chr19:46413371-46413819
chr11:104907430-104908172
chr14:91966750-91967309
chr12:90279999-90280400
chr6:106279063-106279639
chr8:119592426-119592850
6
4
2
0
-2
-4
-6
PDL
20
25
29
33
37
46
50
group
htert
WI

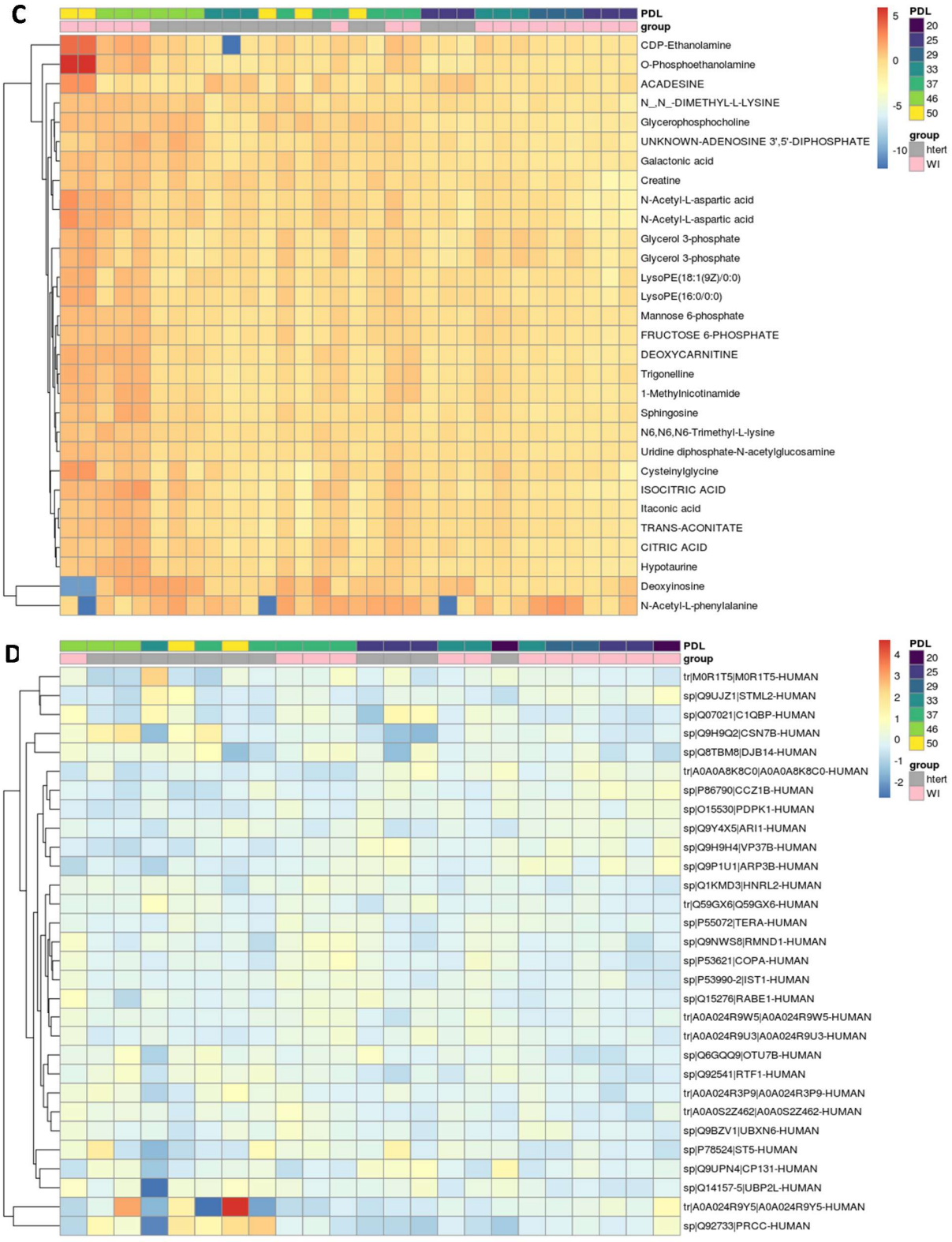

Figure 4.6 **Expression heatmap of the top 30 features in factor 1 across the omic data types.** The heatmaps show z-scores of the top 30 genes (**A**), chromosome regions (**B**), metabolites (**C**) and

proteins (**D**) with the largest weights in factor 1. Sample grouping is shown above the heatmaps in colour blocks, individually for PDL time points and groups. Samples are grouped based on their corresponding factor value (Figure 4.4A) and are coloured based on PDL time points and groups as shown the legends.

4.3.2 Enrichment analysis

Next, enrichment analysis was performed on the features driving factors 1 and 4 to identify sources of variation at a functional and pathway level. The analysis was divided for positive and negative weights in order to detect pathways that were most enriched in the early proliferative, and intermediate and late senescence stages specifically. Significant enrichment across all omic data was considered at a p-value threshold of 0.05. Methods for this analysis are detailed in section 4.2.3.3.

GSEA using the gene members of the positive factor 1 values (representing PDL46 and PDL50) revealed significant enrichment for many gene sets consistent with the original study including the EMT, p53 pathway, myogenesis, coagulation and apoptosis hallmark gene sets (Figure 4.7A). On the other hand, gene members of the negative factor 1 values (representing PDL20 and PDL25) were enriched for E2F targets, G2M checkpoint and mitotic spindle hallmark gene sets as expected (Figure 4.7B).

MSEA using metabolite members of the positive factor 1 values revealed significant enrichment for taurine and hypotaurine metabolism, arginine biosynthesis, vitamin B6 metabolism and pyrimidine metabolism KEGG pathways (Figure 4.8A). On the other hand, negative factor 1 values were enriched for taurine and hypotaurine metabolism, phosphonate and phosphinate metabolism, and cysteine and methionine metabolism KEGG pathways (Figure 4.8B). Taurine metabolism has previously been linked to cell senescence, with high levels having a protective effect against senescence, and taurine levels decreasing with age (Singh *et al.*, 2023). On the other hand, arginine has been reported to accelerate cell senescence (Xiong *et al.*, 2014), whereas pyrimidine deficiency triggers mitochondrial DNA-mediated inflammatory response which is also linked to senescence (Sprenger *et al.*, 2021; Miwa *et al.*, 2022).

Lastly, GREA using the chromosome region members of the positive factor 1 values revealed significant enrichment for positive regulation of histone H4 acetylation, regulation of histone

H4K16 acetylation, positive regulation of RAC protein signal transduction and positive regulation of histone H3K4 methylation GOBP gene sets (Figure 4.9A). Conversely, chromosome region members of the negative factor 1 values were enriched for sialytion and nuclear localization signal bearing protein import into nucleus GOBP gene sets (Figure 4.9B). Indeed, histone acetylation and methylation are known to be associated with ageing and senescence: histone H4 methylation decreases the transcription of some pro-apoptotic genes, whereas increased H4K16 acetylation regulates a pro-survival locus (Dang *et al.*, 2009; Paluvai, Di Giorgio and Brancolini, 2020). Cellular senescence is accompanied by decreased H4K16 acetylation, which may be mediated by SIRT1, subsequently resulting in defective DNA repair mechanisms (Sanders *et al.*, 2013).

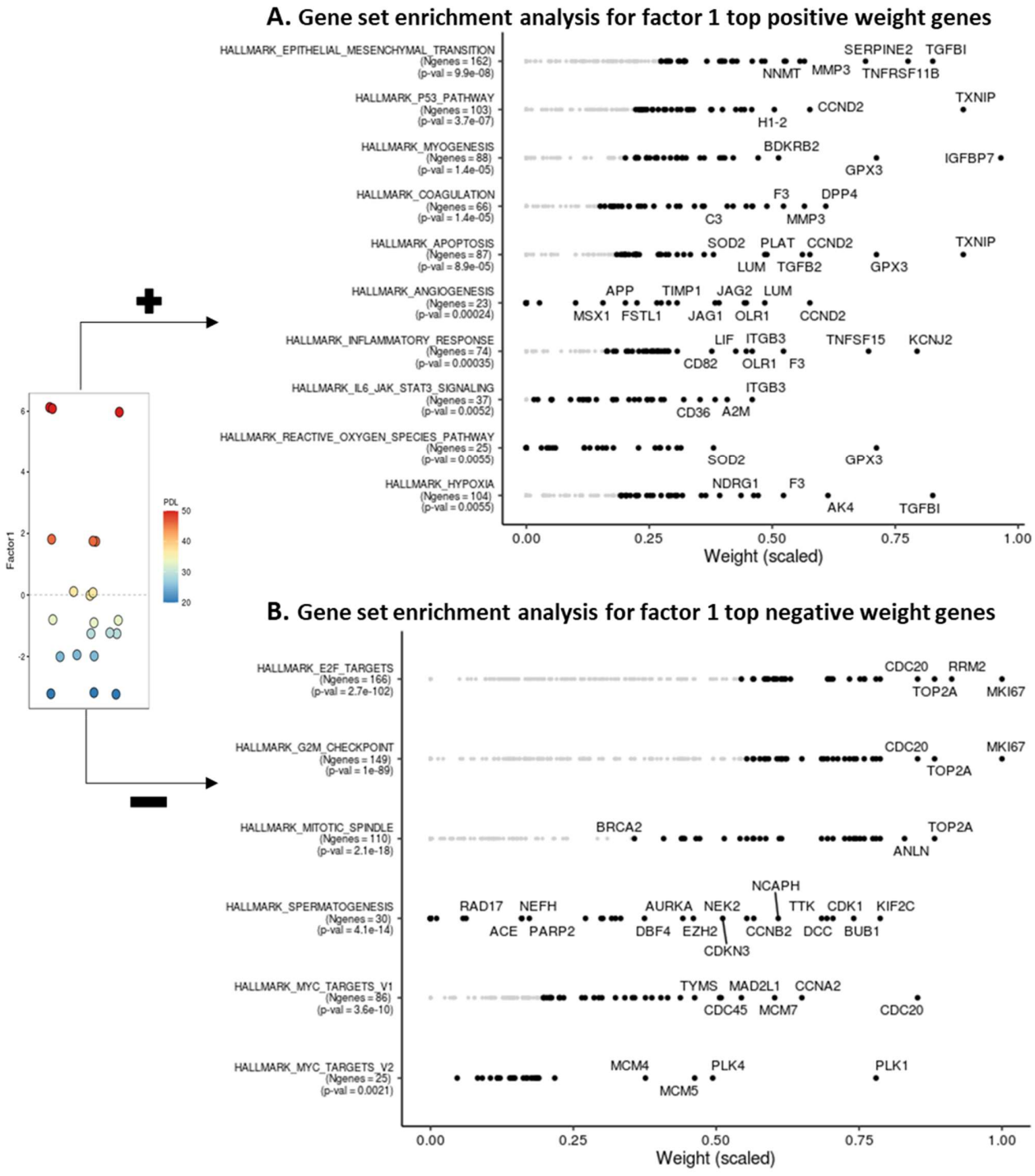

Figure 4.7 **GSEA for the top MSigDB hallmark gene sets in the RNA-seq data with the largest weights from factor 1.** Most significant hallmark gene sets (adjusted p-value < 0.05) in the top weighted RNA-seq data from factor 1 are shown for positive factor 1 values (**A**) and negative factor 1 values (**B**) individually. Top gene sets are shown along the vertical axis and constituent gene weights are shown along the horizontal axis. Each row corresponds to a significant hallmark gene set, arranged by their p-value shown in the brackets. Each dot corresponds to a constituent

gene of the significant gene set. For each gene set, top constituent genes are sorted by the corresponding absolute weight value of the gene. The top genes with the highest absolute weight value are named/displayed and labelled in black, and the remaining genes are displayed as grey dots. Positive and negative factor 1 values represent the last two time points (PDL46 and PDL50) and first two time points (PDL20 and PDL25) respectively, as shown in the colour bar next to the scatterplot of factor 1 values.

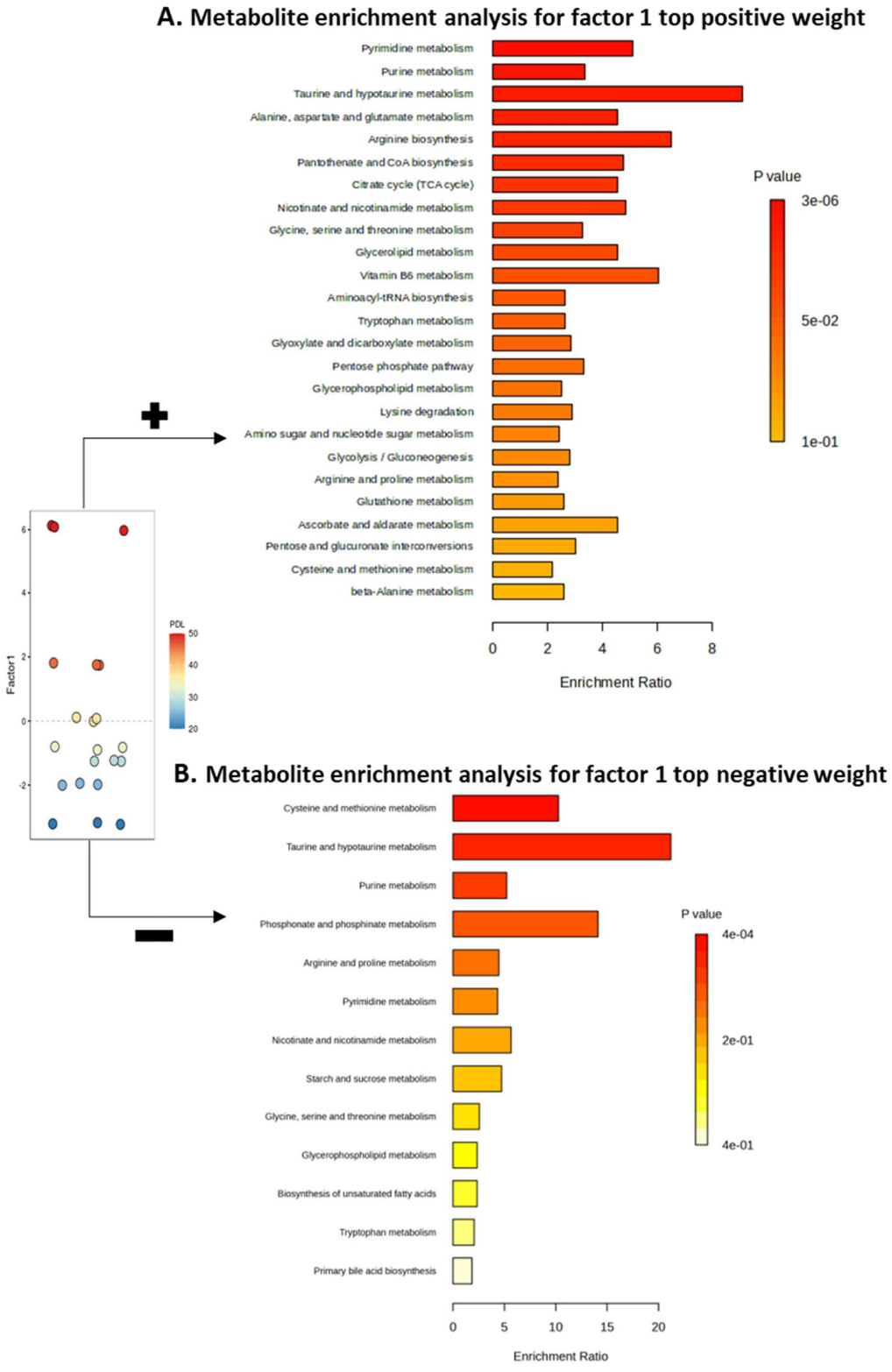

Figure 4.8 **MSEA for the top KEGG metabolite sets in the metabolomic data with the largest weights from factor 1.** Most significant KEGG pathways (adjusted p-value < 0.05) in the top weighted metabolomic data from factor 1 are shown for positive factor 1 values (**A**) and negative

factor 1 values (**B**) individually. Top KEGG pathways are shown along the vertical axis and enrichment ratios are shown along the horizontal axis, with the bar colours representing p-values, as shown in the legend. Positive and negative factor 1 values represent the last two time points (PDL46 and PDL50) and first two time points (PDL20 and PDL25) respectively, as shown in the colour bar next to the scatterplot of factor 1 values.

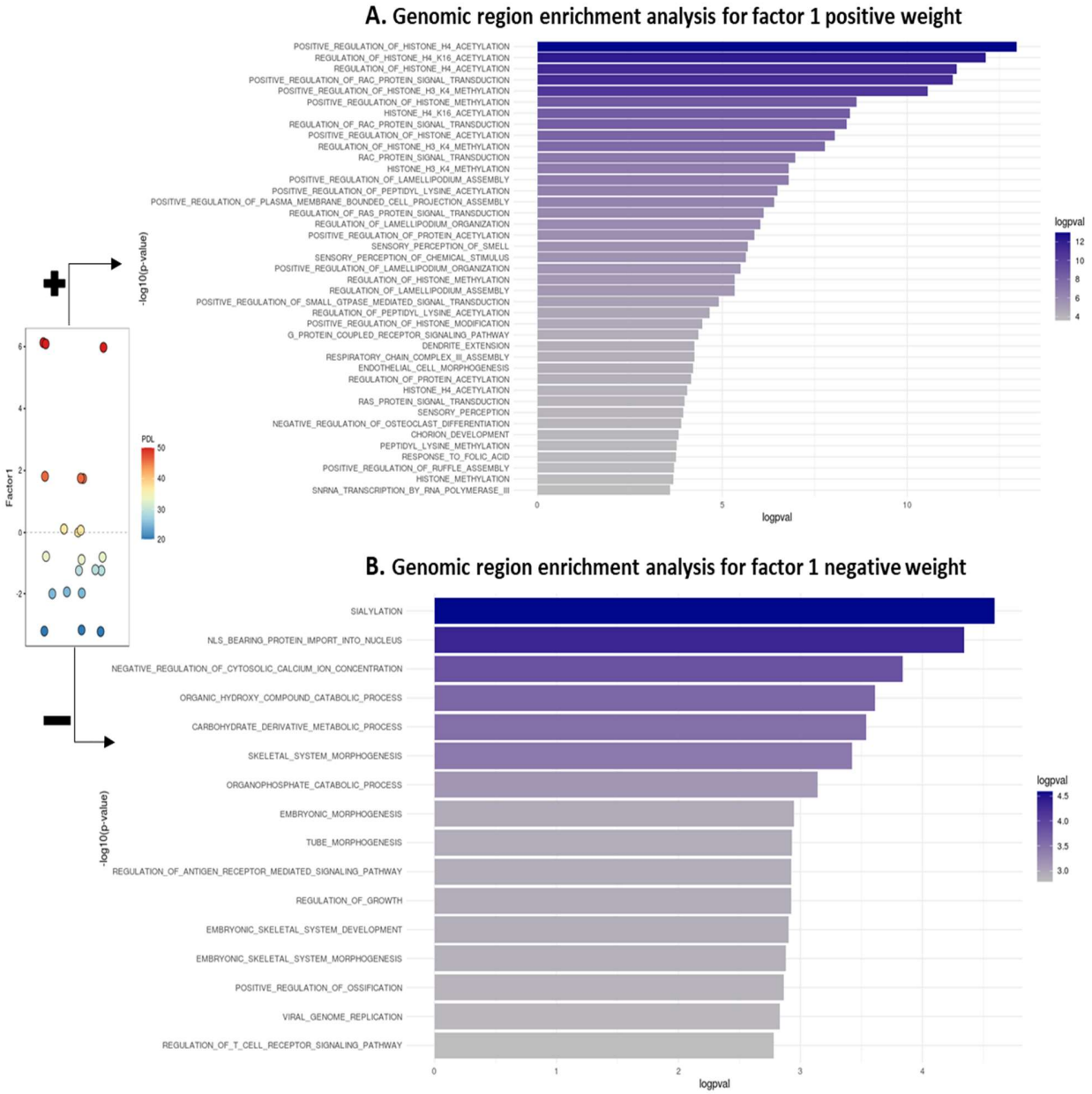

Figure 4.9 **GREA for the top MSigDB GOBP gene sets in the ATAC-seq data with the largest weights from factor 1.** Most significant GOBP gene sets (adjusted p-value < 0.05) in the top weighted ATAC-seq data from factor 1 are shown for positive factor 1 values (**A**) and negative factor 1 values (**B**) individually. Top GOBP gene sets are shown along the vertical axis and log p-values are shown along the horizontal axis, with the colour of the bars representing the log p-values, as shown in the legend. Positive and negative factor 1 values represent the last two time points (PDL46 and PDL50) and first two time points (PDL20 and PDL25) respectively, as shown in the colour bar next to the scatterplot of factor 1 values.

In contrast, GSEA using the gene members of the positive factor 4 values (representing PDL46) revealed significant enrichment for EMT, UV response, apical junction, and interferon alpha response hallmark gene sets (Figure 4.10A). Gene members of the negative factor 1 values (representing PDL50) were enriched for KRAS signalling, hedgehog signalling, TGF beta signalling and TNF signalling via NFKB hallmark gene sets (Figure 4.10B). As noted previously in section 4.2.3.2, the intermediate time point PDL46 is associated with gene sets involved in establishing and enforcing senescence (EMT, UV response down-regulated and interferon alpha response), whereas the late senescence time point PDL50 is additionally associated with gene sets involved in SASP production (hedgehog signalling, TGF beta signalling and TNF signalling via NFKB) (Smit and Peeper, 2010; Ohanna *et al.*, 2011; Tominaga and Suzuki, 2019; Frisch and MacFawn, 2020).

Next, MSEA using the metabolite members of the positive factor 4 values revealed significant enrichment for arginine biosynthesis, vitamin B6 metabolism and pyrimidine metabolism KEGG pathways (Figure 4.11A). On the other hand, negative factor 4 values were enriched for taurine and hypotaurine metabolism KEGG pathways (Figure 4.11B).

Lastly, GREA using the chromosome region members of the positive factor 4 values revealed enrichment for regulation of G protein coupled receptor signalling pathway GOBP gene set (Figure 4.12A), whereas members of the negative factor 4 values were enriched for positive regulation of apoptotic cell clearance and eosinophil chemotaxis GOBP gene sets (Figure 4.12B). Senescent cells can attract immune cells through cytokine- and chemokine-mediated immunosurveillance mechanisms, leading to their own removal (Prata *et al.*, 2018). The gene sets enriched in PDL50, positive regulation of apoptotic cell clearance and eosinophil chemotaxis, could indicate mechanisms underlying senescent cell-mediated activation of immune cell surveillance. This again indicates the prevalence of inflammatory SASP regulation at PDL50.

In summary, the results above give an overview of the gradual nature of the progression of senescence over multiple omic platforms. The next sections will describe the results from integrating the omic data to produce mechanistic networks driving the changes across the time series.

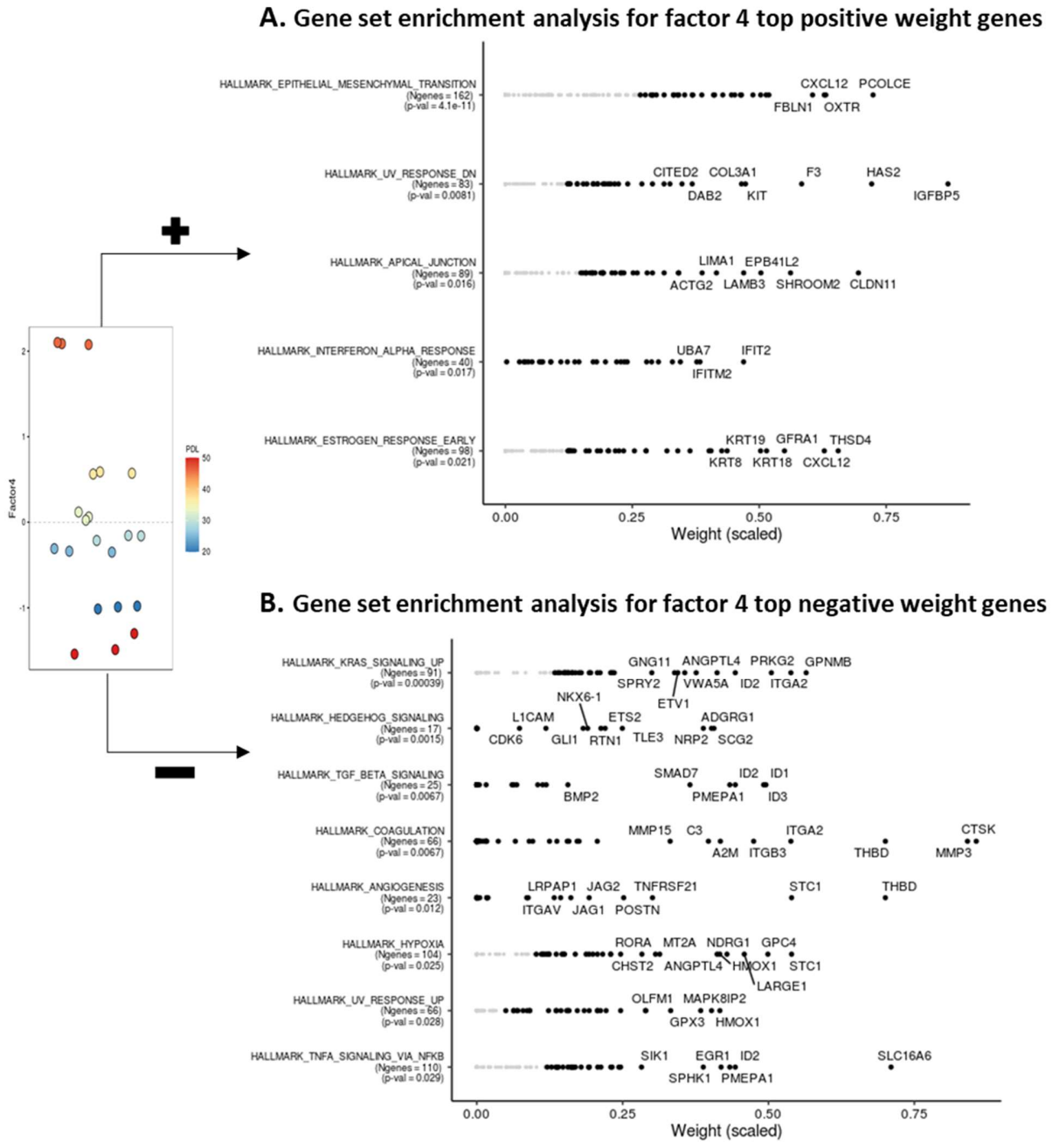

Figure 4.10 **GSEA for the top MSigDB hallmark pathways in the RNA-seq data with the largest weights from factor 4.** Most significant hallmark pathways (p-value < 0.05) in the top weighted RNA-seq data from factor 4 are shown for positive factor 4 values (**A**) and negative factor 4 values (**B**) separately. Top pathways are shown along the vertical axis and constituent gene weights are shown along the horizontal axis. Each row corresponds to a significant hallmark pathway, arranged by their p-value (shown in the brackets). Each dot corresponds to a constituent gene of the significant pathway. For each pathway, top constituent genes are sorted by the corresponding absolute weight value of the gene. The top genes with the highest absolute weight value are named/displayed and labelled in black, and the remaining genes are displayed as grey dots.

Positive and negative factor 4 values represent the last (PDL50) and second last (PDL46) time points respectively, as shown in the colour bar next to the scatterplot of factor 4 values.

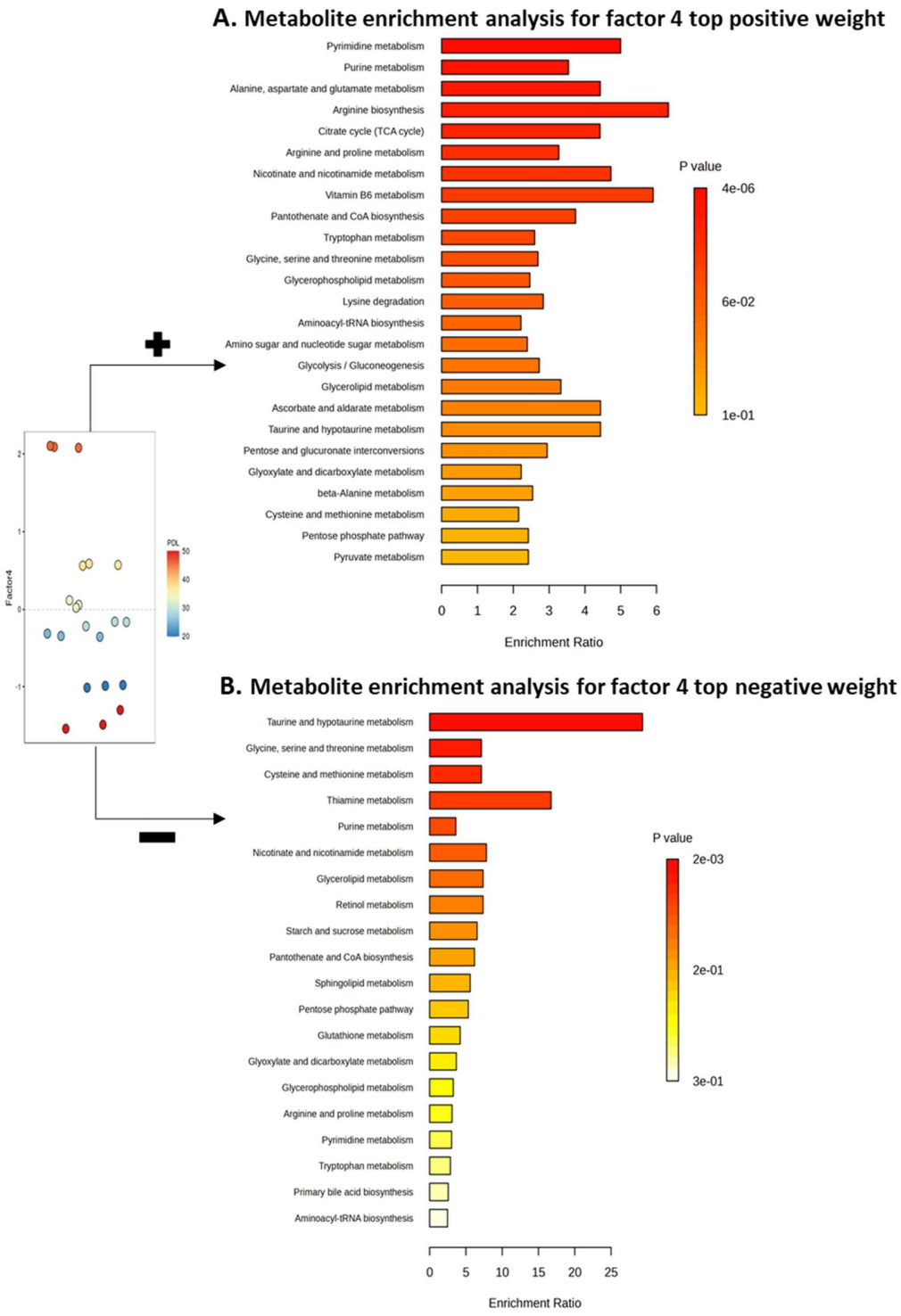

Figure 4.11 **MSEA for the top KEGG metabolite sets in the metabolomic data with the largest weights from factor 4.** Most significant KEGG pathways (adjusted p-value < 0.05) in the top weighted metabolomic data from factor 4 are shown for positive factor 4 values (**A**) and negative factor 4 values (**B**) individually. Top KEGG pathways are shown along the vertical axis and enrichment ratios are shown along the horizontal axis, with the bar colours representing p-values,

as shown in the legend. Positive and negative factor 4 values represent the last two time points (PDL46 and PDL50) and first two time points (PDL20 and PDL25) respectively, as shown in the colour bar next to the scatterplot of factor 4 values.

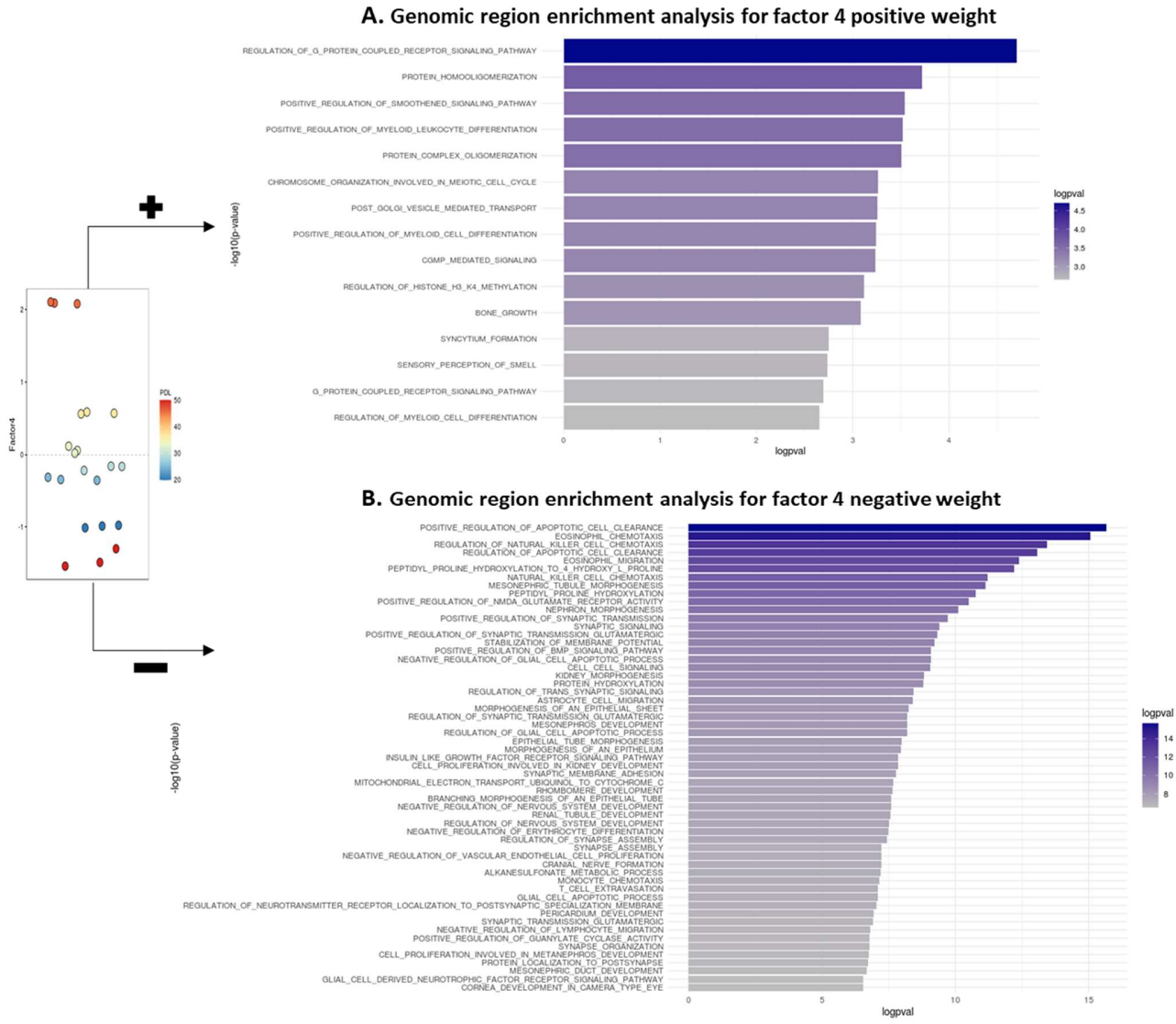

Figure 4.12 **GREA for the top MSigDB GOBP gene sets in the ATAC-seq data with the largest weights from factor 4.** Most significant GOBP gene sets (adjusted p-value < 0.05) in the top weighted ATAC-seq data from factor 4 are shown for positive factor 4 values (**A**) and negative factor 4 values (**B**) individually. Top GOBP gene sets are shown along the vertical axis and log p-values are shown along the horizontal axis, with the colour of the bars representing the log p-values, as shown in the legend. Positive and negative factor 4 values represent the last two time points (PDL46 and PDL50) and first two time points (PDL20 and PDL25) respectively, as shown in the colour bar next to the scatterplot of factor 4 values.

4.3.3 Transcriptional regulatory networks

RNA-seq and ATAC-seq data were integrated to produce TRNs, which refers to a collection of TFs and their target genes. TRNs were generated for each time point from differentially expressed genes and differentially accessible peak regions. Differential analysis was performed in a pair-wise manner to identify differentially expressed genes and accessible peak regions at every time point. The results of differential analysis for RNA-seq, ATAC-seq and metabolomic data are summarised in Table 3. Differential analysis results will not be discussed further as to not take the focus away from this project. Furthermore, this has already been done in great detail in the original publication (Chan *et al.*, 2022).

Results from differential analysis of RNA-seq and ATAC-seq data (significance at adjusted p-value < 0.05) were used to identify TRNs. Methods for this are detailed in sections 4.2.4.1 and 4.2.4.2. Normalised enrichment scores, which indicate TF regulatory activity based on the expression data of the TF target genes, and a correlation coefficient, for the top 50 TFs were visualised for each PDL time point as shown in Figure 4.13. As expected, and in agreement with results from MEFISTO in sections 4.3.1 and 4.3.2, the earlier time points PDL25 and PDL33 are prevalent in TF activity that promotes cell proliferation and suppresses senescence including NFATC4, KLF4, CEBPG (Huggins *et al.*, 2013; Mognol *et al.*, 2016; Yu *et al.*, 2023). On the other hand, the later time points PDL46 and PDL50 are prevalent in TF activity associated with cell senescence including TP53 and FOXO (Bourgeois and Madl, 2018). It is important to stress here that TF activity on their target genes, and the gene or protein levels of the specific TF are different measures. The TRNs identified were used in conjunction with differentially expressed metabolites to produce mechanistic networks described in the following section.

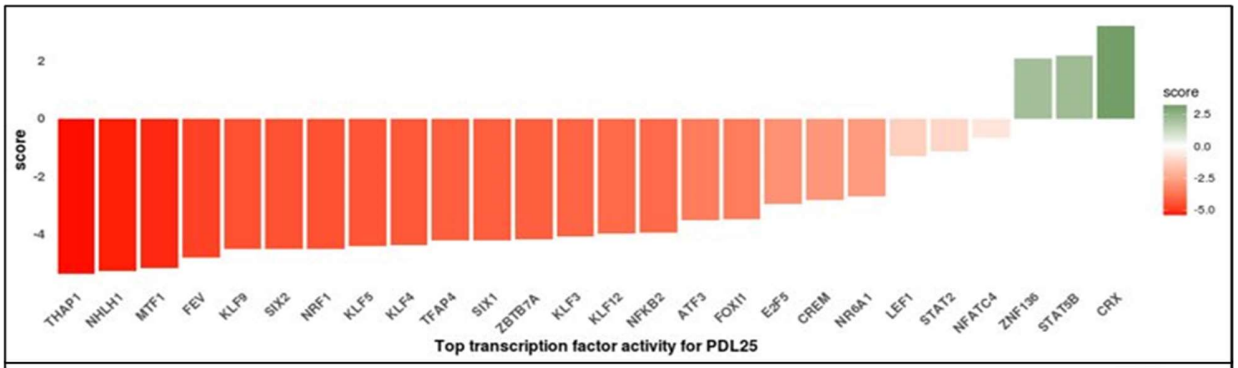

Top transcription factor activity for PDL25

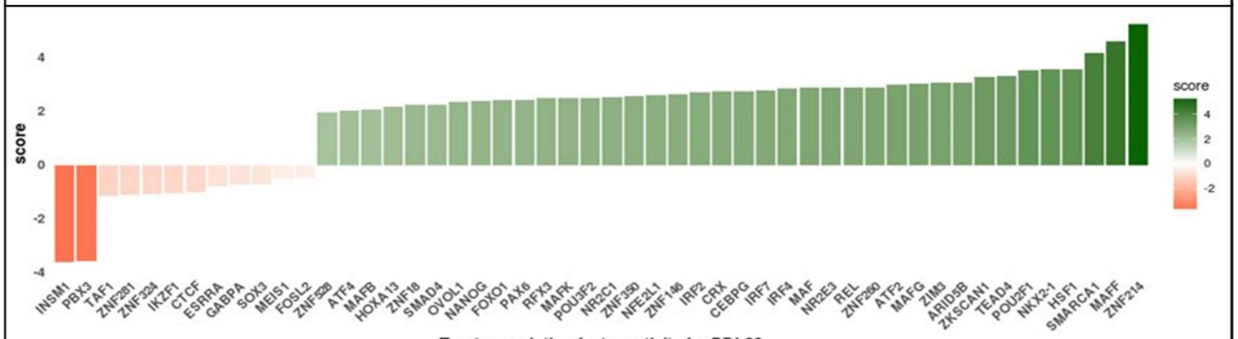

Top transcription factor activity for PDL33

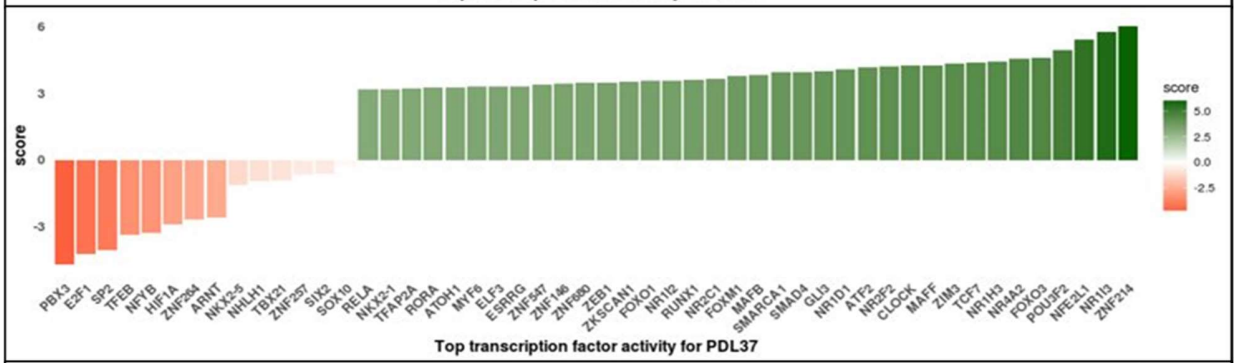

Top transcription factor activity for PDL37

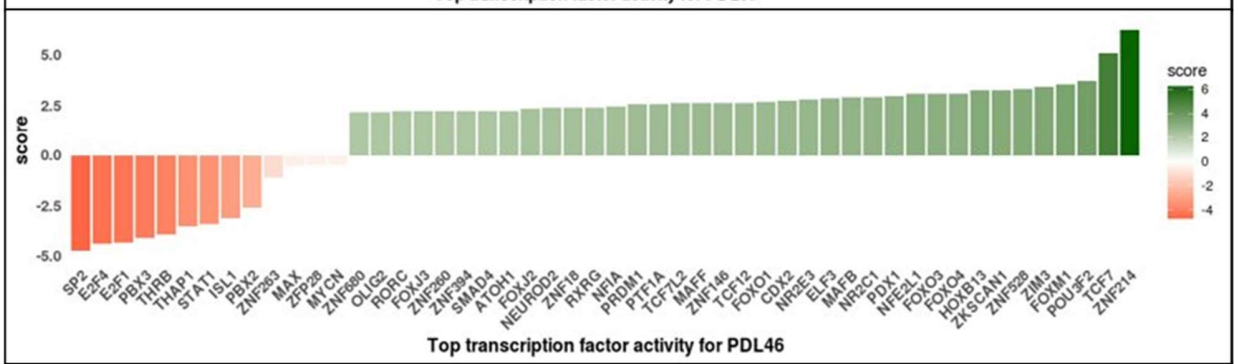

Top transcription factor activity for PDL46

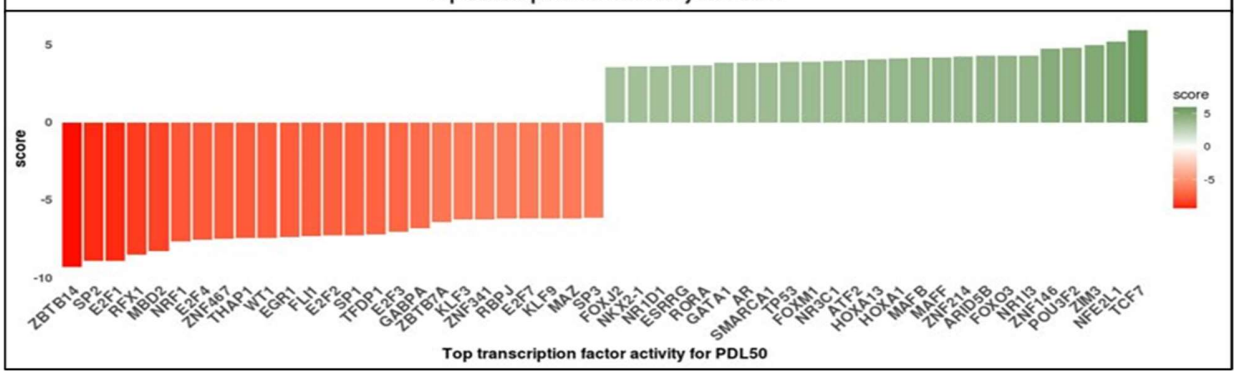

Top transcription factor activity for PDL50

Figure 4.13 **Differentially regulated TF activity for each PDL time point.** The bar plots display TF regulatory activity measured using a normalised enrichment score. Each panel shows the top 50 differentially regulated TF activity for every PDL time point (top to bottom: PDL25, PDL33, PDL37, PDL46 and PDL50, all compared to PDL20) (absolute Pearson correlation estimate > 0.9 and p-value < 0.05).

Table 3 **Summary of results from differential analysis for RNA-seq, ATAC-seq and metabolomics.** (Adjusted p-value < 0.05)

Time point	**Differentially expressed genes**	**Differentially accessible peak regions**	**Differentially expressed metabolites**
PDL25	2133	12111	NA
PDL33	2529	33618	59
PDL37	4205	38874	14
PDL46	3685	63073	153
PDL50	7768	105640	179

4.3.4 Omic data integration to produce mechanistic signalling networks across the senescence time series

Next, the TRNs, and differential genes and metabolites were used to infer downstream causal networks to explain dysregulation in the upstream expression data leading to cellular senescence, for each time point across the progression of senescence. This was done using CARNIVAL and COSMOS, and the resulting networks were studied and visualised using igraph and visNetwork. The output from CARNIVAL and COSMOS were analysed by performing an ORA on the filtered network nodes to identify which hallmark and GOBP gene sets were most represented at each time point. All these results were obtained using methods detailed in section 4.2.4.3.

Since metabolomic data was not available for the first time point PDL25, CARNIVAL was used with the TRNs, pathway enrichment scores and differentially expressed genes. ORA was performed to identify which pathways were over-represented in the CARNIVAL network nodes for PDL25. For the time point PDL25, ORA resulted in no significantly over-represented hallmark gene sets. However, ORA based on GOBP resulted in gene sets including phosphorylation, regulation of catalytic activity and cellular response to stress being significantly over-represented ($p < 0.05$)

(Figure 4.14). Hence, the network nodes belonging of these pathways were used to investigate the relevant mechanisms (Figure 4.15). STAT and IRF TFs are important for immune response mediation, cell proliferation, apoptosis and many other vital biological functions (Mogensen, 2019). The lack of a well characterised network at this time point is expected due to the small number of differential features (Table 3). Overall, the processes at this point mostly appear to be involved in normal cell function.

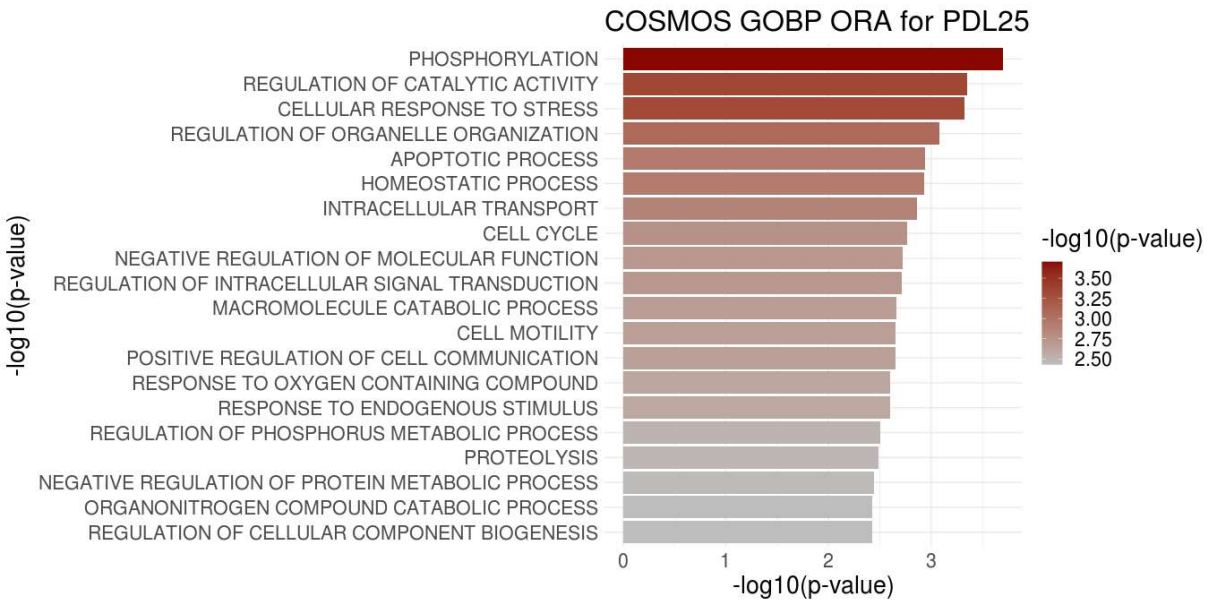

Figure 4.14 **Ranked over-represented pathways in the CARNIVAL solution networks for PDL25.** Bar plot showing results from ORA performed with MSigDB GOBP gene sets (vertical axis), ranked by p-value, as shown by the colour bars (horizontal axis) and the legend.

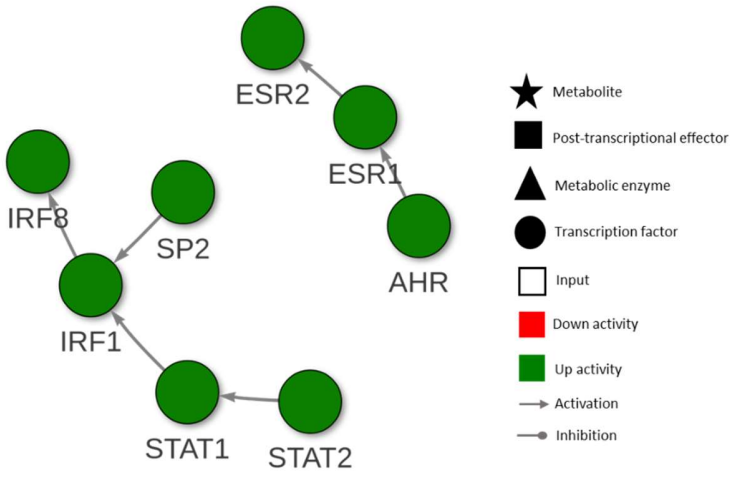

Figure 4.15 **CARNIVAL subnetwork for PDL25 centred on the phosphorylation, regulation of catalytic activity and cellular response to stress MSigDB GOBP gene sets.** This figure includes the main members of the phosphorylation, regulation of catalytic activity and cellular response to stress MSigDB GOBP pathways, which were the most enriched gene sets at the time point PDL25 (p-value < 0.05). Descriptions of the symbols used in this network are detailed in the legend provided.

COSMOS was used to identify mechanistic networks for the time points subsequent to PDL25 since metabolomic data was also available for these time points. ORA of the COSMOS network nodes for PDL33 revealed over-representation of the hallmark gene sets for UV response down-regulation and EMT (Figure 4.16A). Additionally, the GOBP gene sets for the response to endogenous stimulus, apoptotic process and phosphorylation were also over-represented (Figure 4.16B). COSMOS network nodes present in the response to endogenous stimulus and EMT pathway were investigated further since EMT was significantly enriched in the results from MEFISTO as well. This resulted in the network shown in Figure 4.17.

At this intermediate passage time point, some factors regulating cellular stress become prevalent, despite the downregulation of other factors including MAPK3, important for the regulation of senescence-associated proteins (Anerillas, Abdelmohsen and Gorospe, 2020). With regards to cellular stress, the network suggests hydrogen peroxide upregulation mediated by the mitochondrial enzyme monoamine oxidase A, an important source of ROS (Snezhkina *et al.*, 2020). Hydrogen peroxide, which is an important mediator of oxidative stress (Lenaz, 1998), leads to the activation of NFKB1 through its co-activator PARP1, both of which are important in

regulating SASP production (Ohanna *et al.*, 2011; Swindall, Stanley and Yang, 2013). Hydrogen peroxide also leads to STAT3 upregulation, which has been shown to regulate ROS-induced senescence (Waters *et al.*, 2019). The network suggests that STAT3 upregulation occurs through PRKCE. Conversely, PRKCE is known to mediate pro-proliferative processes (Black and Black, 2012). Additionally, within the network, PRKCE inhibits MAPK3 (an important effector in cell senescence) leading to the indirect activation of MYC, which depending on the context, can regulate senescence (Wu *et al.*, 2007; Van Riggelen and Felsher, 2010); alternatively, in this network, the inhibition of MAPK3 is followed by the activation of PPARG, an inducer of senescence (Gan *et al.*, 2008). The network suggests MYC co-operating with SP1, which has been shown to activate the transcription of the gene for hTERT (Kyo *et al.*, 2000). Conversely, the role of SP1 in the regulation of p21, which is a critical factor in senescence, has previously been established (Pardali *et al.*, 2000). These contradictory processes show the intermediate nature of the senescence program at this precise time point. Interestingly, the network also predicts hydrogen peroxide mediated activation of the EMT pathway, as previously reported in (Kim, Cui and Kim, 2013; Chen *et al.*, 2021). NFKB1 is known to play a role in EMT even though it is not considered to be a canonical EMT regulator (Cook and Vanderhyden, 2020). On the other hand, the network predicts that FN1, a canonical EMT factor itself, is also activated by hydrogen peroxide (Cook and Vanderhyden, 2020; I. H. Yang *et al.*, 2020). FN1 leads to the activation of PTK2 and STAT1, both of which have been reported to induce EMT (Cicchini *et al.*, 2008; Kaowinn *et al.*, 2018). To summarise, the processes at the time point PDL33 are involved in EMT and regulating the initial cell stress factors.

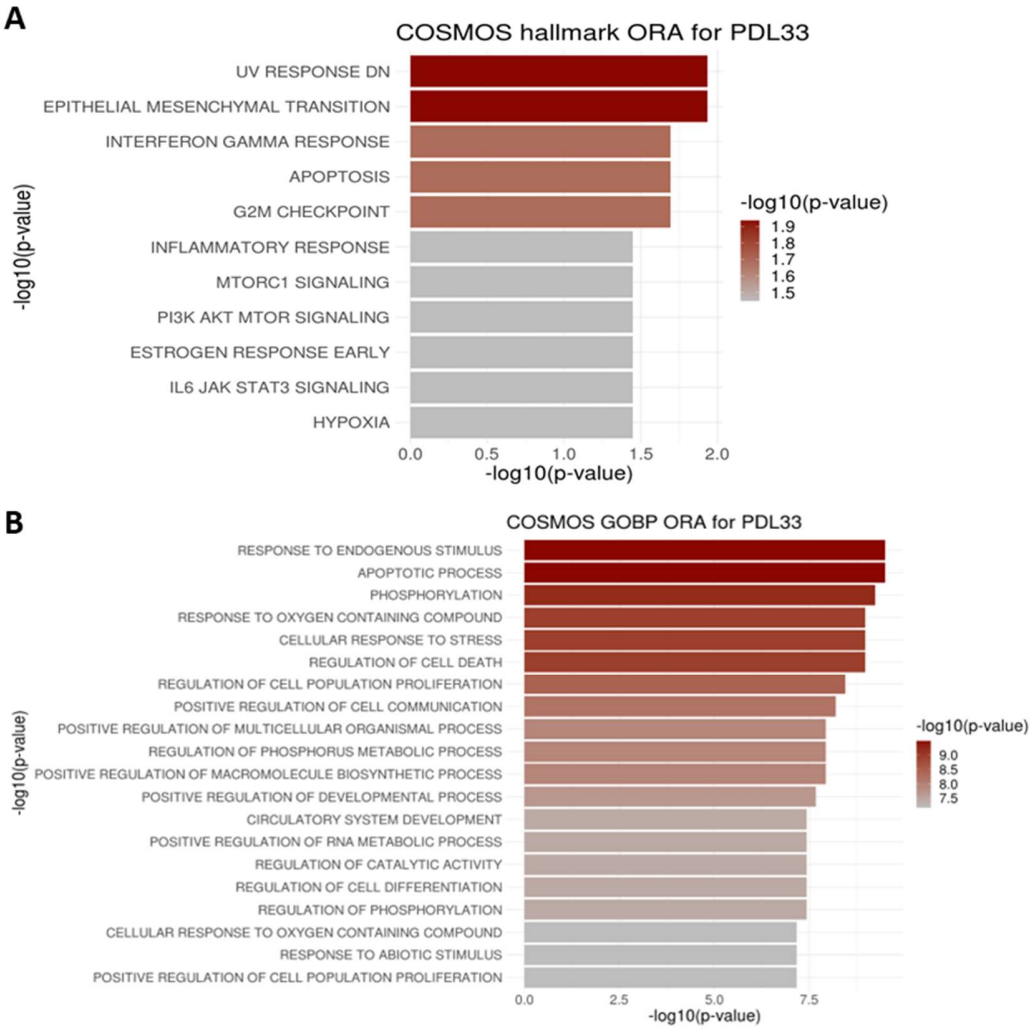

Figure 4.16 **Ranked over-represented pathways in the COSMOS solution networks for PDL33.** Bar plots showing results from ORA performed with MSigDB hallmark gene sets (**A**) and MSigDB GOBP gene sets (**B**), as shown on the vertical axis. Gene sets are ranked by p-values, as shown by the colour bars on the horizontal axis, and the legends.

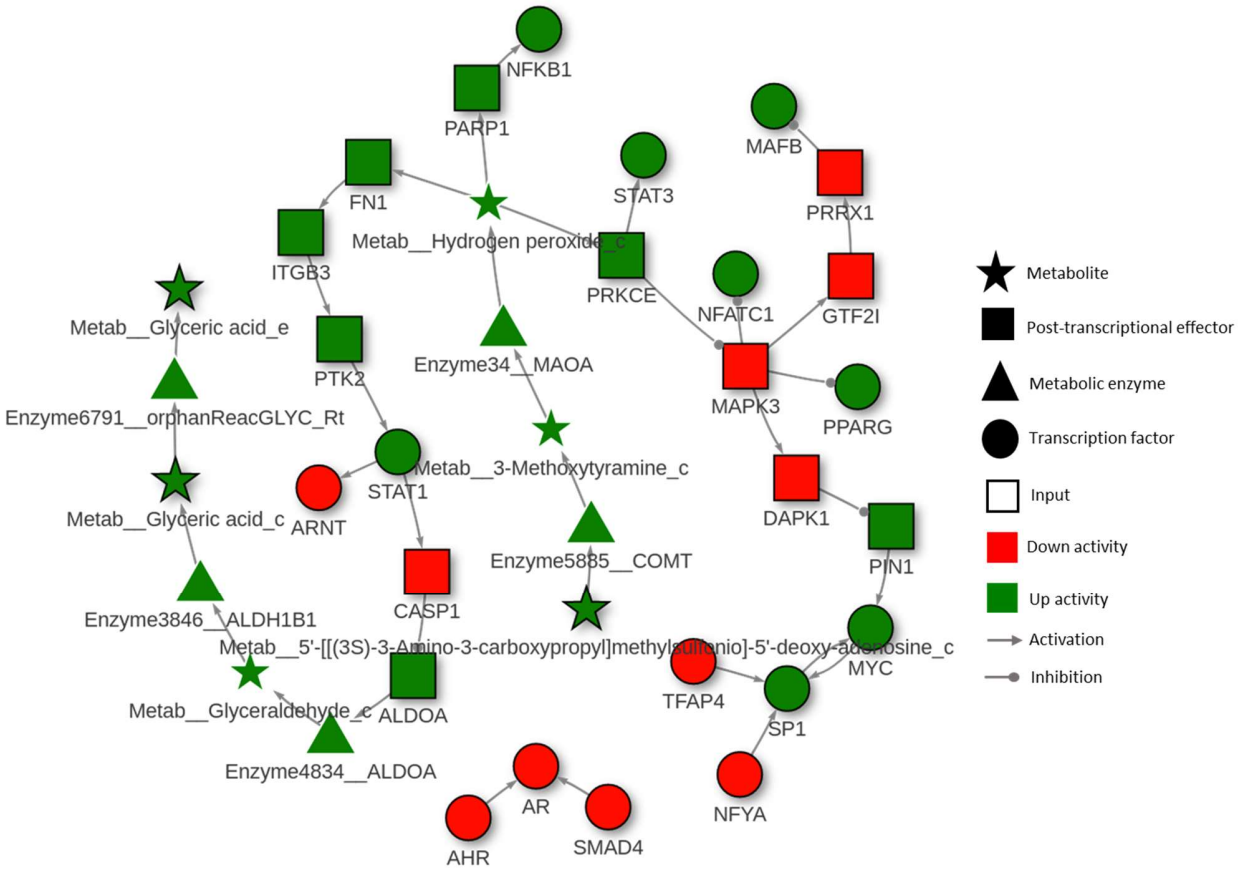

Figure 4.17 **COSMOS subnetwork for PDL33 centred on the response to endogenous stimulus GOBP gene set and epithelial mesenchymal transition hallmark gene set.** This figure includes the main members of the response to endogenous stimulus and epithelial mesenchymal transition gene sets, which were the most enriched gene sets at the time point PDL33 (p-value < 0.05). Descriptions of the symbols used in this network are detailed in the legend provided.

For the next time point PDL37, ORA of the COSMOS network nodes revealed the over-representation of both the G2M checkpoint and the E2F targets hallmark gene sets (Figure 4.18 A). ORA based on GOBP gene sets revealed apoptotic process and regulation of cell death gene sets to be significant (Figure 4.18B). The network nodes from all these gene sets were investigated further resulting in the network presented in Figure 4.19. The network suggests that at this time point, hydrogen peroxide-mediated stress results in the upregulation of several factors involved in regulating senescence and the cell cycle, such as MAPKs including MAPK3 (also known as ERK1) and MAPK8 (also known as JNK1) (Anerillas, Abdelmohsen and Gorospe, 2020), TP53 (Rufini *et al.*, 2013), SMAD3 (Tominaga and Suzuki, 2019) and RELA (Hwang *et al.*, 2013). This could progress the senescence process further compared to the previous time point where MAPK was downregulated. The network shows MAPKs (MAPK3 and MAPK8) activating SMAD proteins (SMAD3 and SMAD4). MAPK3 and MAPK8 have both been reported to facilitate SMAD3 phosphorylation allowing the formation of a complex with SMAD4, triggering transcriptional responses (Engel *et al.*, 1999; Hough, Radu and Doré, 2012). The MAPKs in the network are predicted to also activate other factors involved in regulating senescence, including STAT3, MYC, ATF2, SP3 and ETS1 (Van Riggelen and Felsher, 2010; Waters *et al.*, 2019; Anerillas, Abdelmohsen and Gorospe, 2020). The network also suggests oxidative stress-mediated FOXO4 activation through MAPK8, which is known to regulate senescence (Bourgeois and Madl, 2018). Lastly, BCL6, which can be activated by TP53, is downregulated at this time point (Margalit *et al.*, 2006). This could be a negative feedback mechanism, since BCL6 can inhibit p53-mediated senescence response (Shvarts *et al.*, 2002). Compared to the previous time point PDL33, where initial signs of cell stress were present, this time point, PDL37, is more associated with regulating both cell cycle and cell death pathways with the activation of key factors such as MAPKs and TP53.

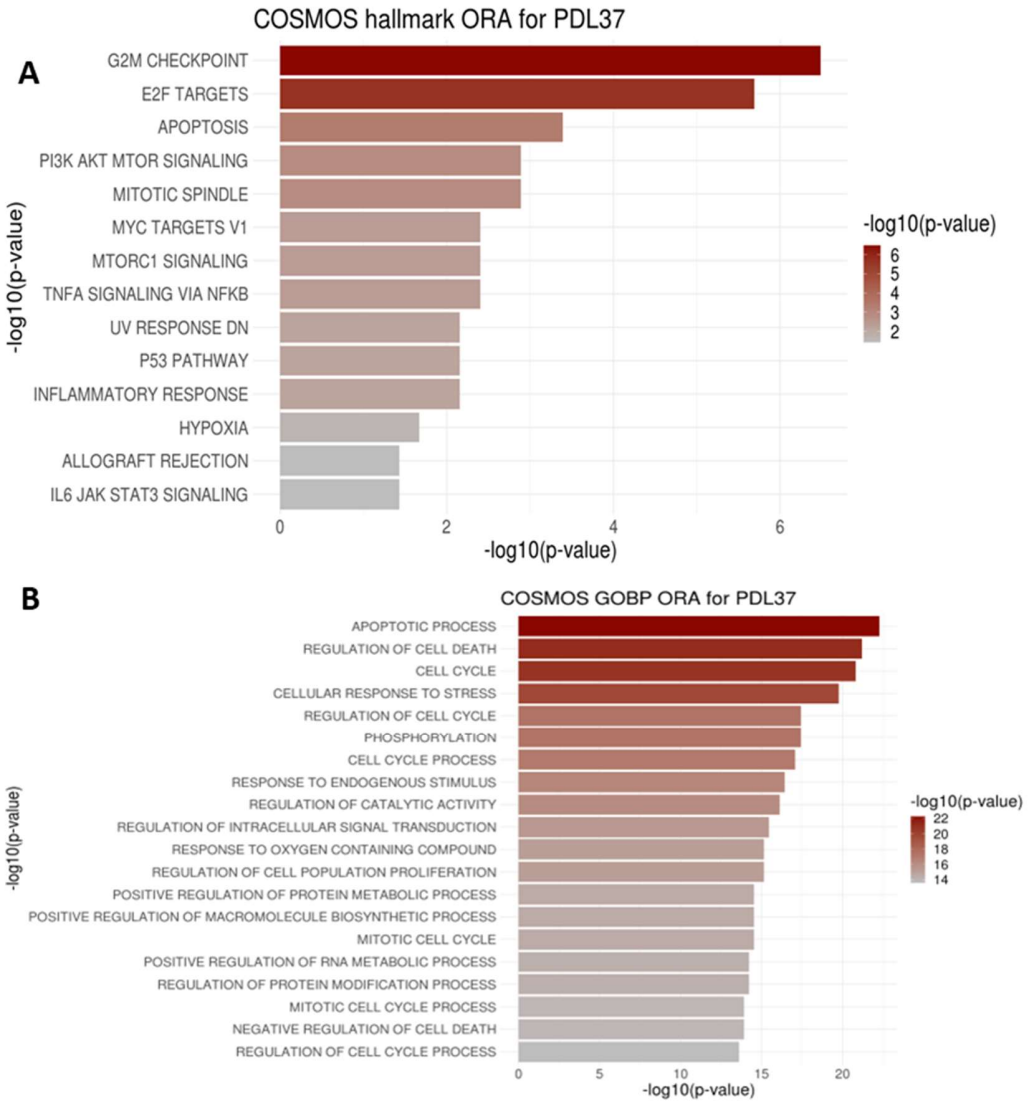

Figure 4.18 **Ranked over-represented pathways in the COSMOS solution networks for PDL37.** Bar plots showing results from ORA performed with MSigDB hallmark gene sets (**A**) and MSigDB GOBP gene sets (**B**), as shown on the vertical axis. Gene sets are ranked by p-values, as shown by the colour bars on the horizontal axis, and the legends.

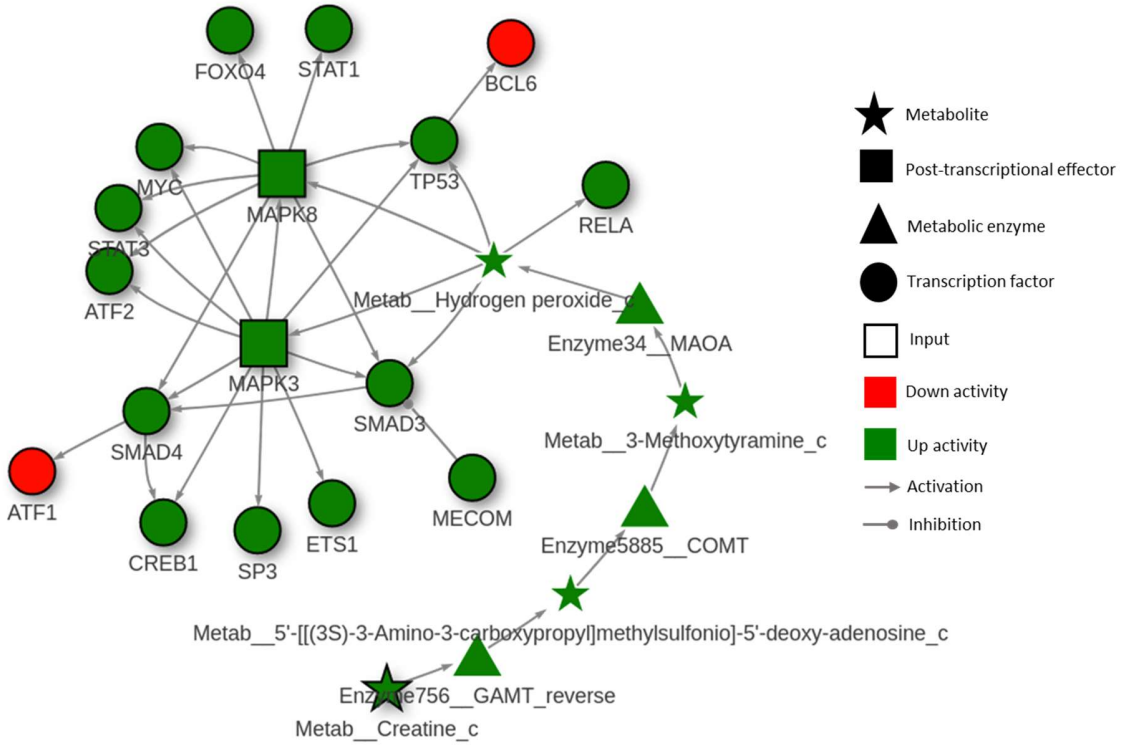

Figure 4.19 **COSMOS subnetwork for PDL37 centred on the apoptotic process and regulation of cell death GOBP gene sets and the G2M checkpoint and E2F targets hallmark gene sets.** This figure includes the main members of the apoptotic process and regulation of cell death GOBP gene sets and the G2M checkpoint and E2F targets hallmark gene sets, which were the most enriched gene sets at the time point PDL37 (p-value < 0.05). Descriptions of the symbols used in this network are detailed in the legend provided.

The time point PDL46 was investigated next. MEFISTO analysis identified this time point as the shift from intermediate to full senescence as detailed in sections 4.3.1 and 4.3.2. ORA of the COSMOS network nodes for this time point identified E2F targets, TNFA signalling via NFKB and G2M checkpoint hallmark gene sets to be over-represented (Figure 4.20A). Additionally, the GOBP gene sets apoptotic processes, regulation of cell death and cellular response to stress were also over-represented (Figure 4.20B). Nodes from the E2F targets and G2M checkpoint were investigated further since they contained common nodes, resulting in the network shown in Figure 4.21. The network predicts MAPK3 activation through the activity of metabolites adenosine triphosphate (ATP), uridine 5'-triphosphate (UTP) and N-acetyl L-cysteine (NAC) (Luke and Hexum, 2008a; Zhang, Lau and Monks, 2011a), resulting in BCL3 activation. BCL3 phosphorylation by ERKs, such as MAPK1 and MAPK3, has been shown to be important for its transcriptional activity (Buscà, Pouysségur and Lenormand, 2016; Wang *et al.*, 2017). BCL3, a key transcriptional coactivator for NFKB1 (Fujita *et al.*, 1993) , subsequently activates NFKB1, which is crucial for SASP production (Chien *et al.*, 2011). However, at this time point, NFKB1 is suggested to activate FOS, which is known to play an important role in the cell cycle and to have an inhibitory effect on senescence (Brown *et al.*, 1998; Fujioka *et al.*, 2004). This highlights the multi-faceted nature of NFKB1. Additionally, BCL3 is suggested to activate HDAC1, previously reported to play an important role in positively regulating the senescence phenotype through chromatin remodelling (Willis-Martinez *et al.*, 2010). HDAC1 subsequently leads to CREBBP activation, which is in turn involved in the acetylation of SASP target genes (Yu *et al.*, 2017), as well as the activation of other pro-senescent factors such as PPARG (Gan *et al.*, 2008) and RELB, an NFKB subunit upregulated in senescence (Jing *et al.*, 2011).

Next, network nodes present in the hallmark gene set TNFA signalling via NFKB were investigated as shown in Figure 4.22. This network predicts the activation of several factors involved in SASP regulation including CREBBP (Yu *et al.*, 2017), NFKB1 (Chien *et al.*, 2011) and CEBPB (Salotti and Johnson, 2019), as well as senescence regulation through cell cycle mediation including SMAD4 (Tominaga and Suzuki, 2019), PPARG (Gan *et al.*, 2008) and STAT3 (Waters *et al.*, 2019). These factors regulating senescence and SASP production are activated by MAPK3, which is to be expected given the crucial role of MAPKs in senescence (Anerillas, Abdelmohsen and Gorospe, 2020). Notably, the network suggests MAPK3 activation by purinergic signalling mediators ATP

and UTP (Amstrup and Novak, 2003; Luke and Hexum, 2008b). Purinergic signalling involves nucleotides which play a role as extracellular signalling molecules and has been implicated in cell senescence, although the exact mechanism is unclear (Cho *et al.*, 2014; Zanoni *et al.*, 2022; Majeed *et al.*, 2023). Interestingly, the network also predicts MAPK3 activation by NAC, which is an antioxidant shown to attenuate cell senescence (Khan *et al.*, 2017; Anderson *et al.*, 2019). This could be a mechanism to counteract the other molecular players of senescence in an attempt to ease cellular stress. However, some reports suggest NAC inhibits MAPK3 (Wuyts *et al.*, 2003) whereas other have reported activation of MAPK3 by NAC (Li, Dehnade and Zafarullah, 2000; Zhang, Lau and Monks, 2011b). This is unsurprising given the role of MAPK3 in cell survival mechanisms, although this requires further investigation (Lavoie, Gagnon and Therrien, 2020).

Lastly, the nodes represented by the GOBP gene sets apoptotic process, regulation of cell death and cellular response to stress pathways were investigated (Figure 4.23). This network suggests the MAPK3 mediated activation of regulators of apoptosis and the cell cycle. For instance, the network predicts MAPK3 activating NFATC4, a protein that plays a role in cell cycle processes and regulates p53 activity in senescence (Yang *et al.*, 2002; Martin and Bernard, 2018). MAPK3 is also predicted to activate MYC, which regulates the transcription of several genes controlling cell proliferation and apoptosis, and also interacts with CDK2 to mediate cell cycle regulators (Van Riggelen and Felsher, 2010). Furthermore, MAPK3 also activates EMT inducing factors such as TWIST1, ATF4 and CEBPB (Cook and Vanderhyden, 2020; Qi *et al.*, 2023). PDGFRA activation is predicted by the network mediated by ascorbic acid. This is relevant as it has been observed before in CCN1-induced senescence (Feng *et al.*, 2019). Interestingly, the network also suggests activation of CASP3, a pro-apoptotic protein usually downregulated in senescent cells (Hu *et al.*, 2022). This could be interpreted as if some pathways are trying to counteract senescence, however further work will be required to validate this conclusion. In summary, the causal networks at this time point are mostly associated with cell cycle and apoptosis regulation, with factors involved in SASP production beginning to be activated.

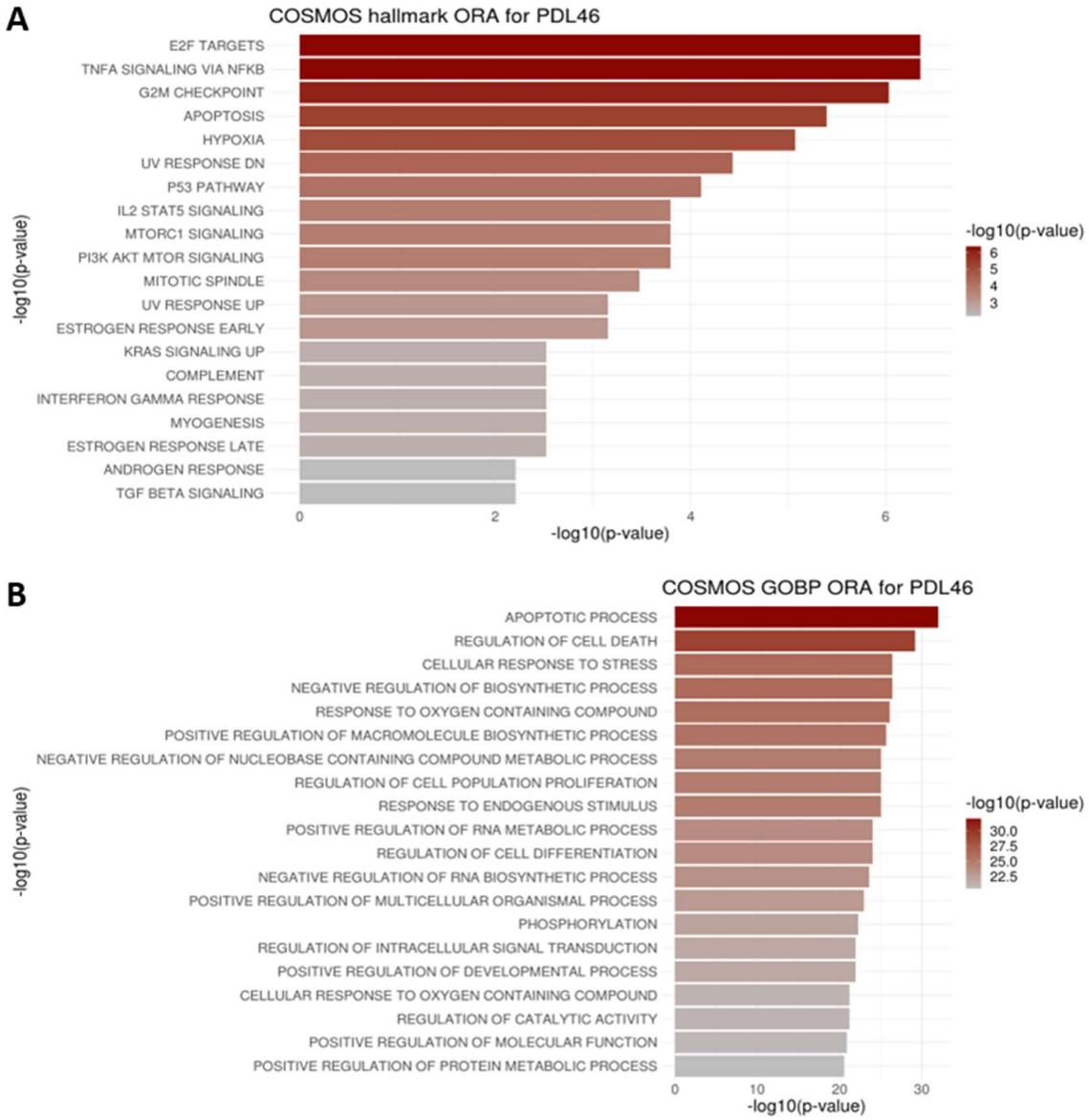

Figure 4.20 **Ranked over-represented pathways in the COSMOS solution networks for PDL46.** Bar plots showing results from ORA performed with MSigDB hallmark gene sets (**A**) and MSigDB GOBP gene sets (**B**), as shown on the vertical axis. Gene sets are ranked by p-values, as shown by the colour bars on the horizontal axis, and the legends.

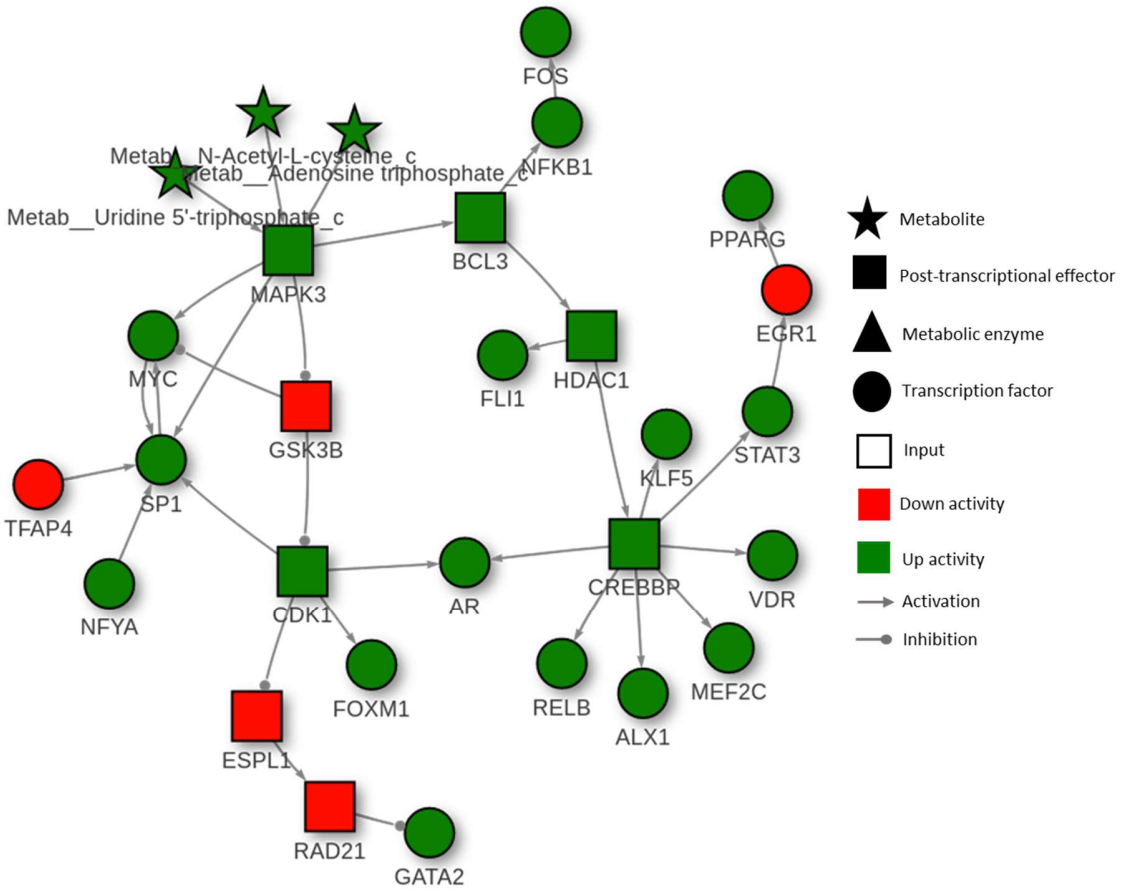

Figure 4.21 **COSMOS subnetwork for PDL46 centred on the G2M checkpoint and E2F targets hallmark gene sets.** This figure includes the main members of the G2M checkpoint and E2F targets hallmark gene sets, which were highly enriched at the time point PDL46 (p-value < 0.05). Descriptions of the symbols used in this network are detailed in the legend provided.

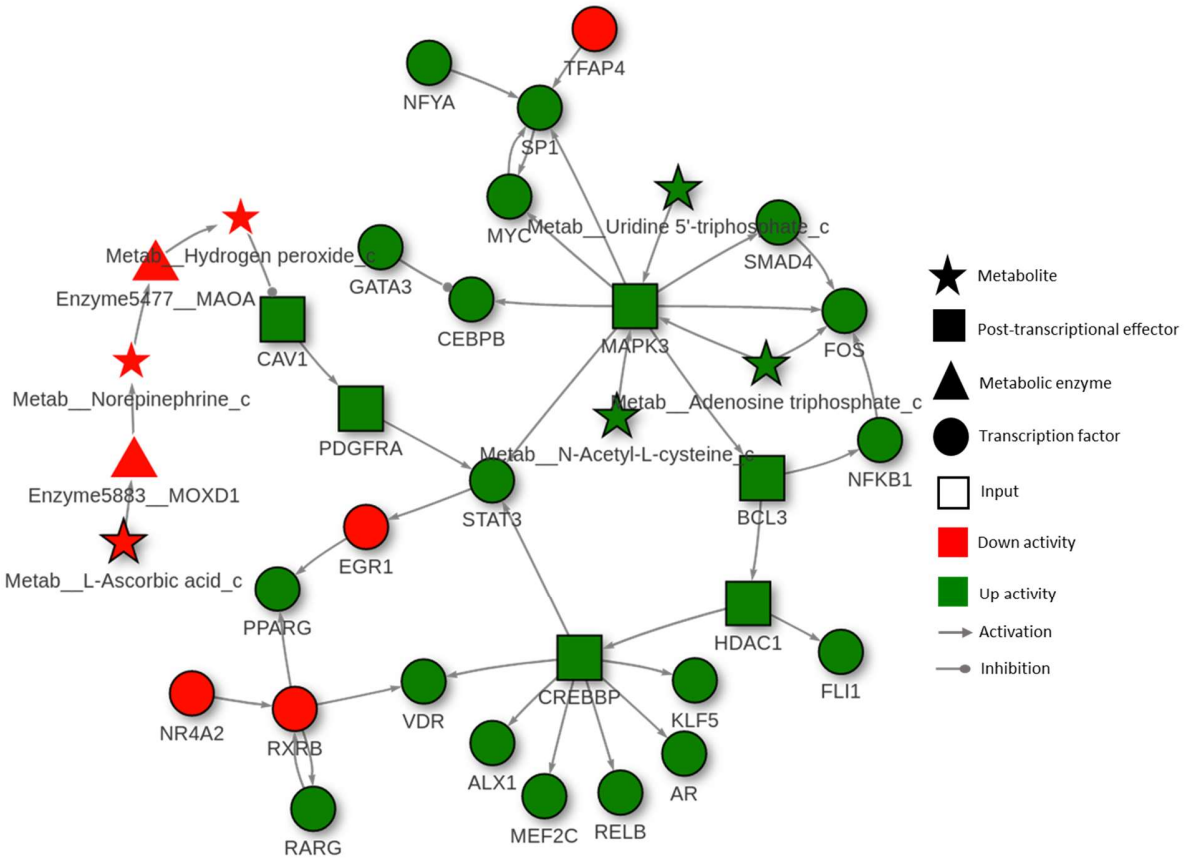

Figure 4.22 **COSMOS subnetwork for PDL46 centred on the TNFA signalling via NFKB hallmark gene set.** This figure includes the main members of the TNFA signalling via NFKB hallmark gene set, which was highly enriched at the time point PDL46 (p-value < 0.05). Descriptions of the symbols used in this network are detailed in the legend provided.

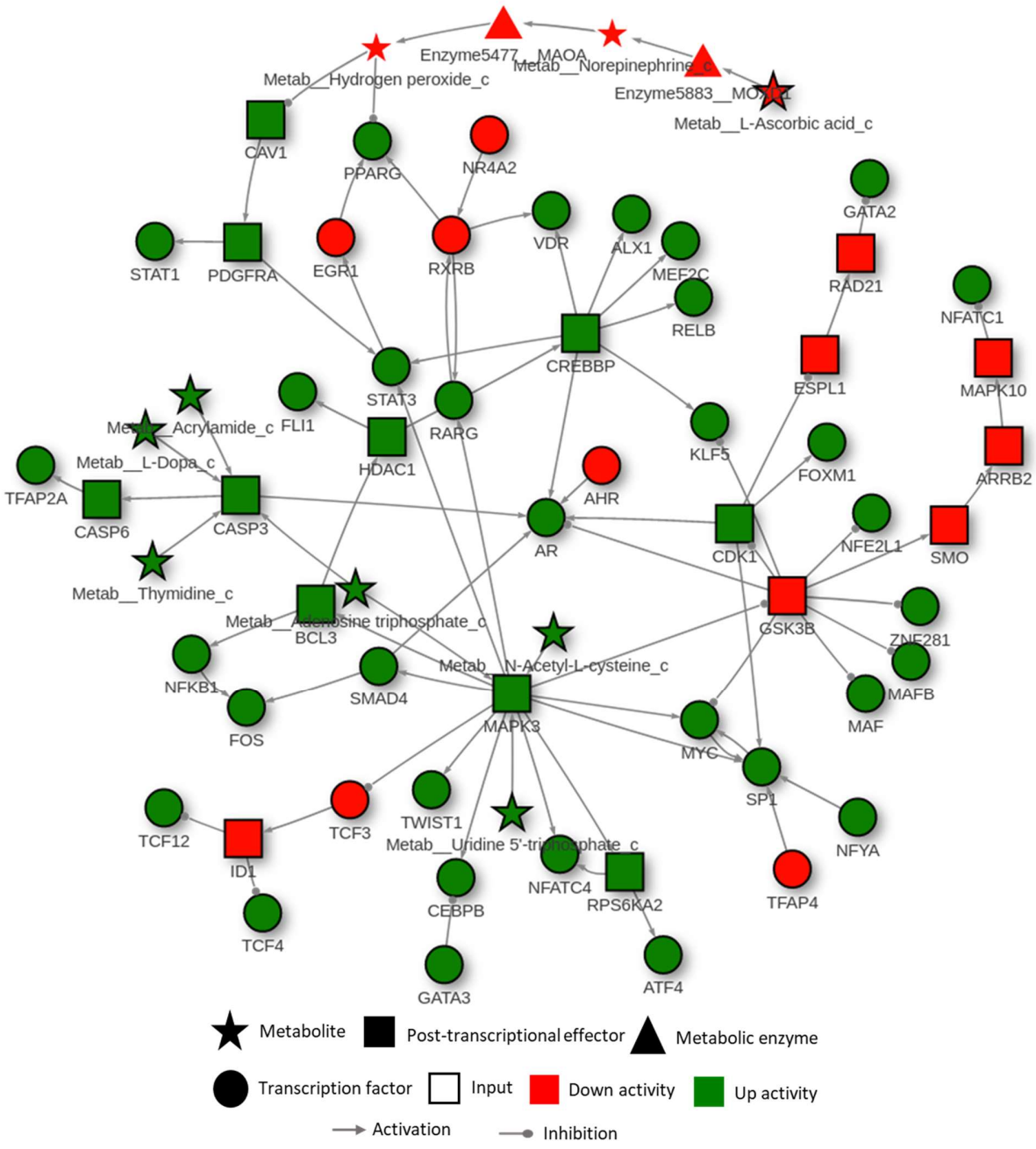

Figure 4.23 **COSMOS subnetwork for PDL46 centred on the apoptotic process, regulation of cell death and cellular response to stress GOBP gene sets.** This figure includes the main members of the apoptotic process, regulation of cell death and cellular response to stress GOBP gene sets, which were highly enriched at the time point PDL46 (p-value < 0.05). Descriptions of the symbols used in this network are detailed in the legend provided.

The last time point, PDL50, represents full late-stage senescence. ORA of the COSMOS network nodes for this time point identified several gene sets to be significantly over-represented. The hallmark gene sets G2M checkpoint, E2F targets and TNFA signalling via NFKB were significant, as well as, the GOBP gene sets apoptotic process, phosphorylation, cellular response to stress (Figure 4.24A and B). In addition to these GOBP gene sets, others potentially involved in SASP production were also significantly over-represented including regulation of catalytic activity, regulation of intracellular signal transduction, positive regulation of protein metabolic processes, regulation of protein modification processes and positive regulation of macromolecule biosynthetic process (Figure 4.24B).

Nodes from pathways of interest and the most statistical significance were investigated further. This resulted in networks for E2F targets hallmark gene set (Figure 4.25), TNFA signalling via NFKB hallmark gene set (Figure 4.26), apoptotic process GOBP gene set (Figure 4.27), regulation of catalytic activity GOBP gene set (Figure 4.28) and positive regulation of protein metabolic process GOBP gene set (Figure 4.29). The networks predict the increased prevalence of factors involved in SASP production including NFKB1, PPARG and TGFB2. Furthermore, p53 is predicted to be downregulated during this time point. Downregulation of p53 may be important for the induction of SASP during late-stage senescence since p53 has been shown to have antagonistic effects on SASP production through the suppression of MAPK activity, which is crucial for NFKB-mediated SASP production (Freund, Patil and Campisi, 2011b; Johmura and Nakanishi, 2016). Interestingly, the activation of several EMT factors is also suggested at this time point, including TWIST, TEAD and YAP, in agreement with the results from MEFISTO analysis. Furthermore, CCND3, a G1/S specific protein, seems also to be downregulated whereas anti-apoptotic proteins, such as XIAP, are predicted to be activated, indicating an established and durable cell cycle arrest at this time point (Peilin *et al.*, 2019).

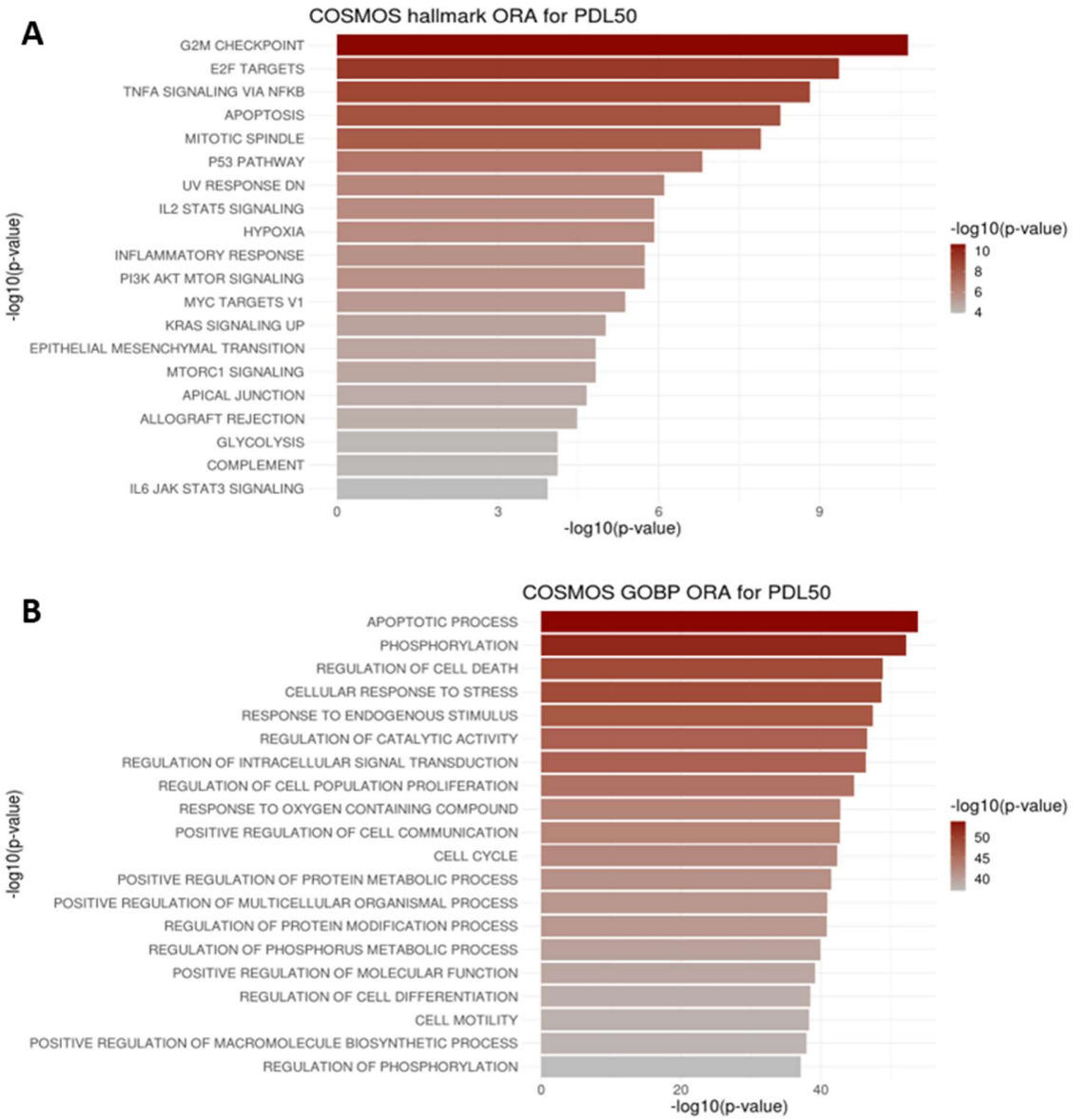

Figure 4.24 **Ranked over-represented pathways in the COSMOS solution networks for PDL50.** Bar plots showing results from ORA performed with MSigDB hallmark gene sets (**A**) and MSigDB GOBP gene sets (**B**), as shown on the vertical axis. Gene sets are ranked by p-values, as shown by the colour bars on the horizontal axis, and the legends.

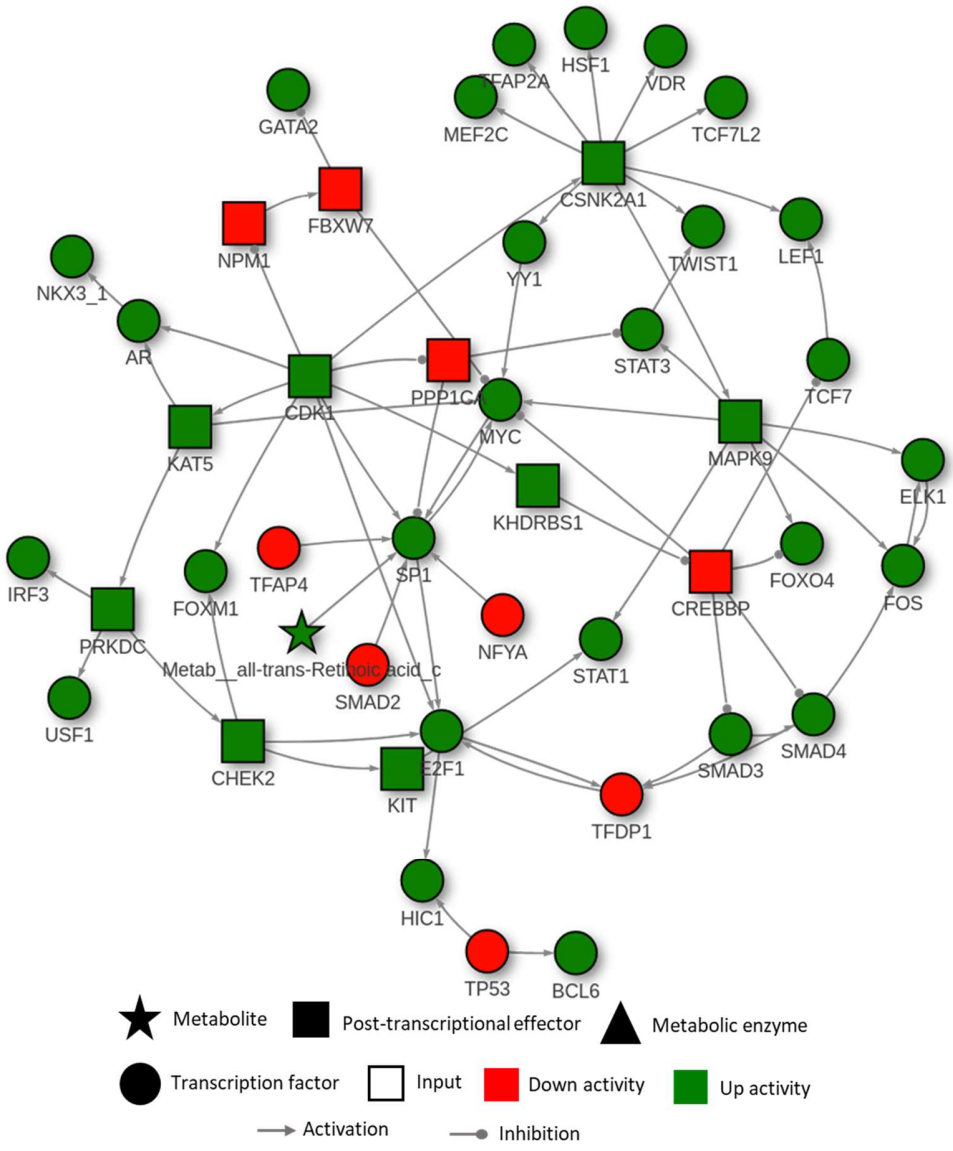

Figure 4.25 **COSMOS subnetwork for PDL50 centred on the E2F targets hallmark gene set.** This figure includes the main members of the E2F targets hallmark gene set, which was highly enriched at the time point PDL50 (p-value < 0.05). Descriptions of the symbols used in this network are detailed in the legend provided.

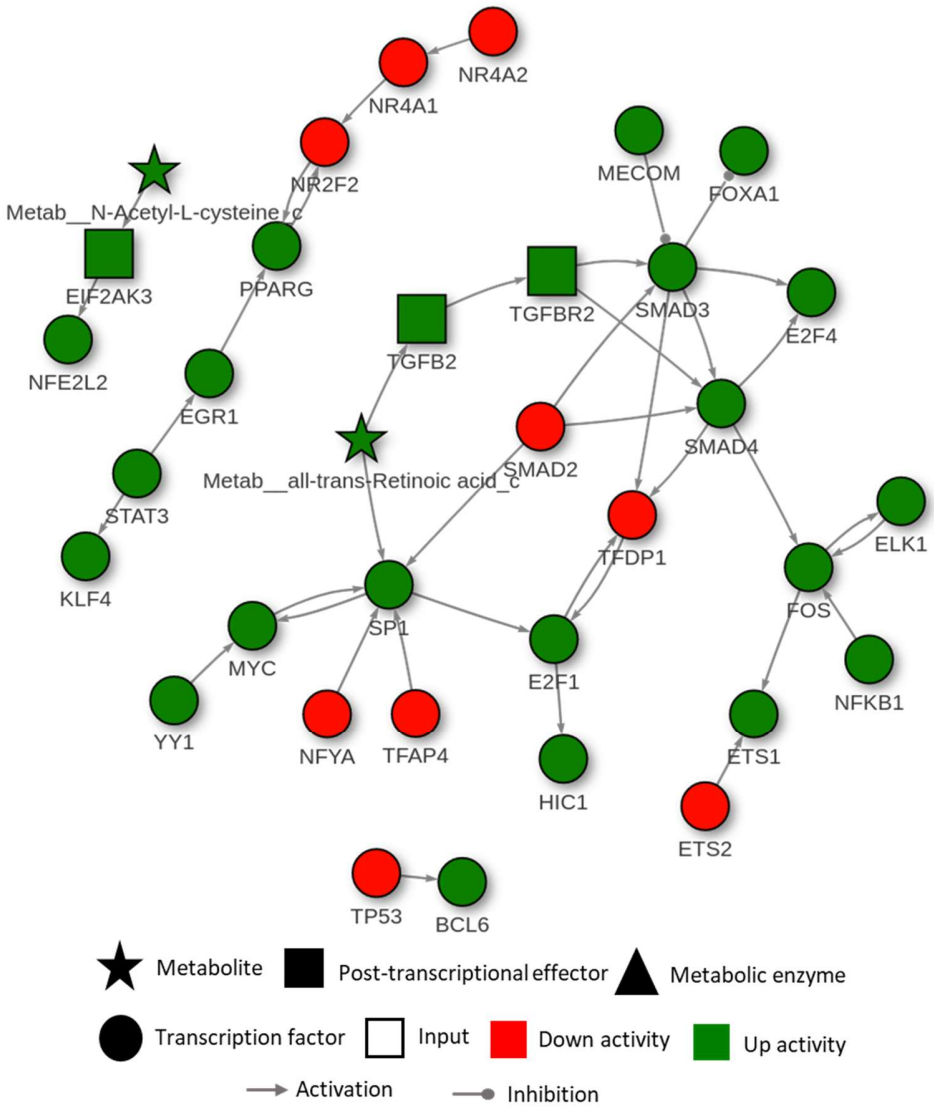

Figure 4.26 **COSMOS subnetwork for PDL50 centred on the TNFA signalling via NFKB hallmark gene set.** This figure includes the main members of the TNFA signalling via NFKB hallmark gene set, which was highly enriched at the time point PDL50 (p-value < 0.05). Descriptions of the symbols used in this network are detailed in the legend provided.

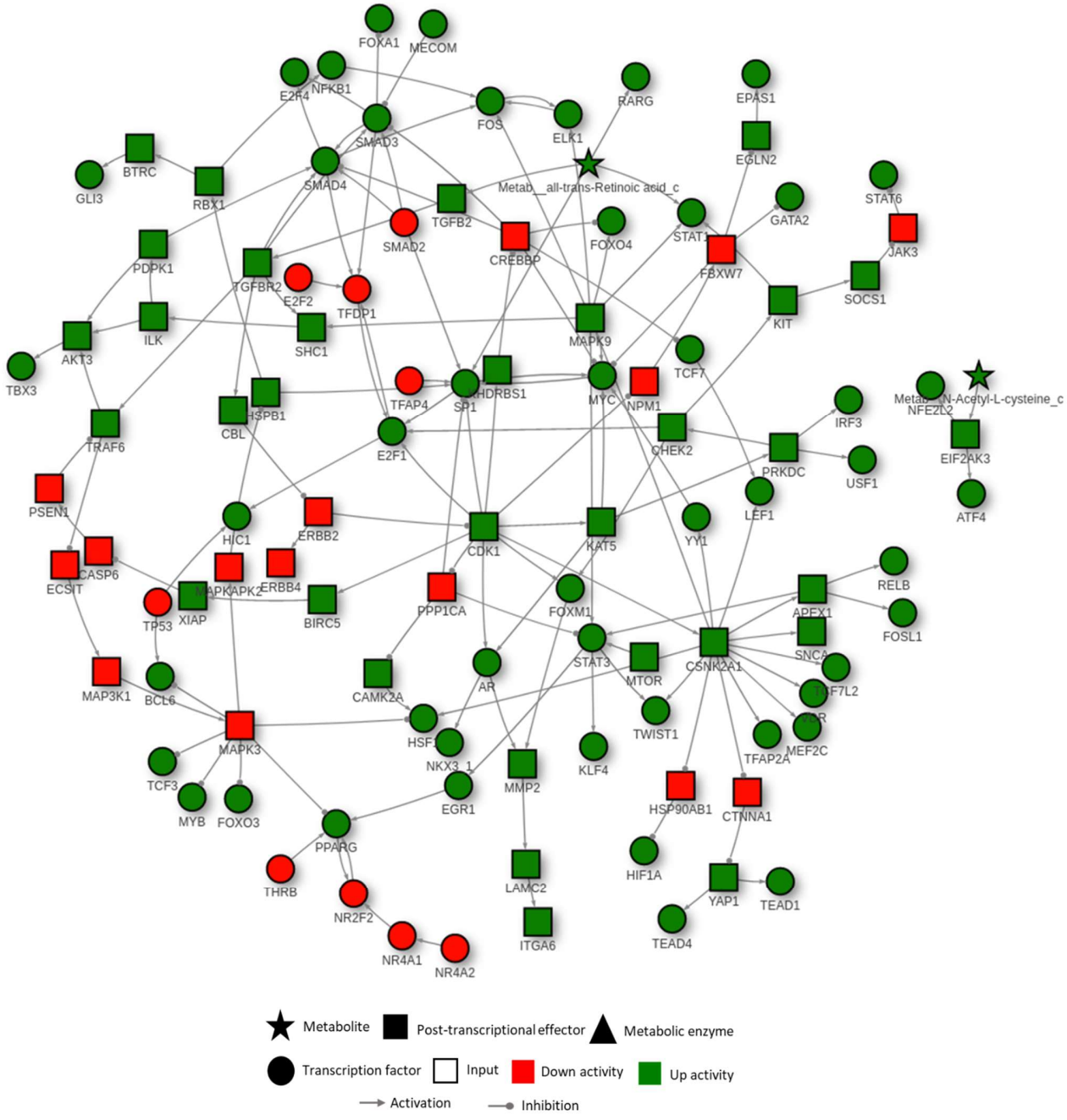

Figure 4.27 **COSMOS subnetwork for PDL50 centred on the apoptotic process GOBP gene set.** This figure includes the main members of the apoptotic process GOBP gene set, which was highly enriched at the time point PDL50 (p-value < 0.05). Descriptions of the symbols used in this network are detailed in the legend provided.

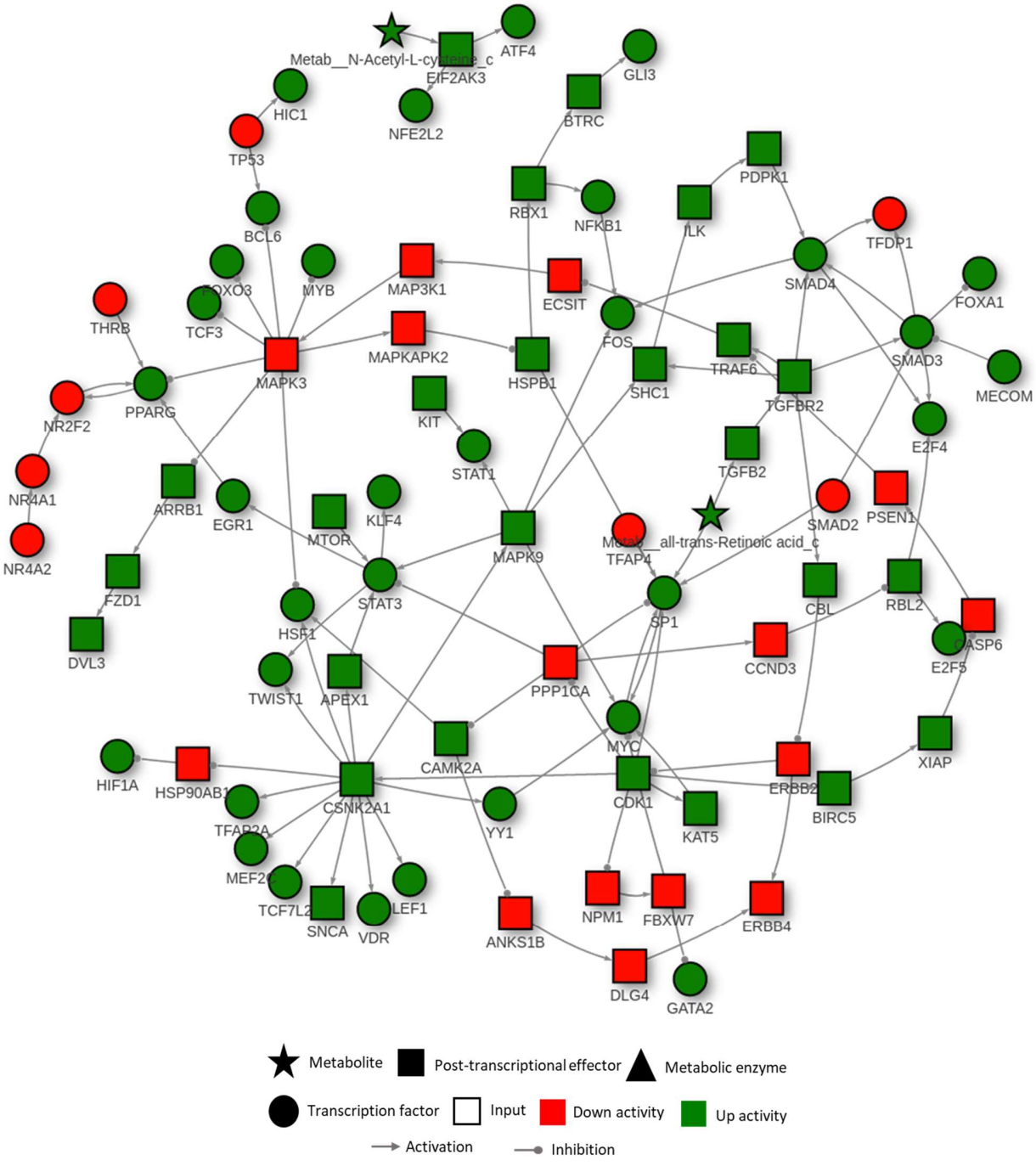

Figure 4.28 **COSMOS subnetwork for PDL50 centred on the regulation of catalytic activity GOBP gene set.** This figure includes the main members of the regulation of catalytic activity GOBP gene set, which was highly enriched at the time point PDL50 (p-value < 0.05). Descriptions of the symbols used in this network are detailed in the legend provided.

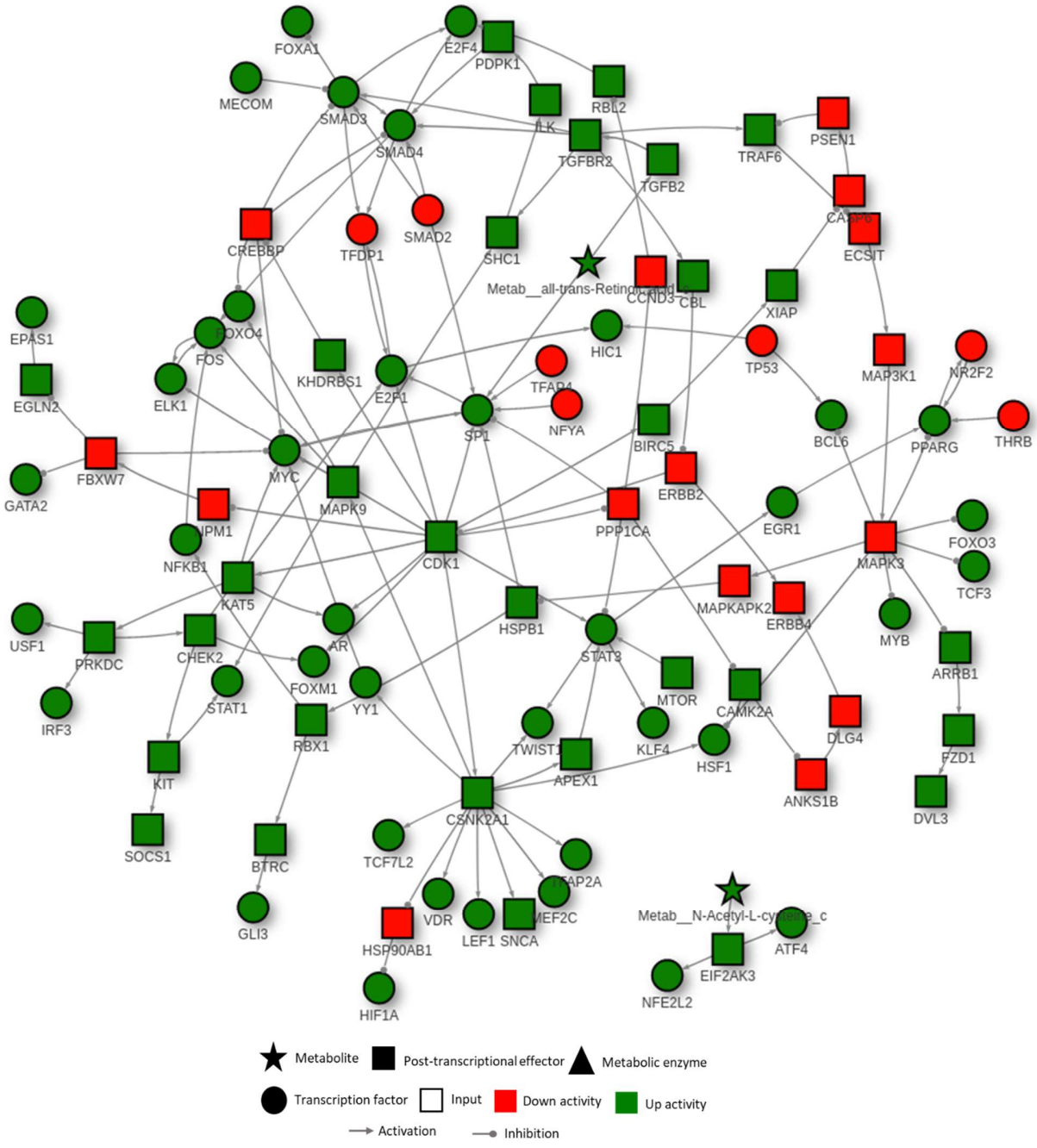

Figure 4.29 **COSMOS subnetwork for PDL50 centred on the positive regulation of protein metabolic process GOBP gene set.** This figure includes the main members of the positive regulation of protein metabolic process GOBP gene set, which was highly enriched at the time point PDL50 (p-value < 0.05). Descriptions of the symbols used in this network are detailed in the legend provided.

4.4 Conclusion

This project was focussed on an alternative strategy for integrating a previously published multi-omic time series dataset to uncover key sources of variation as well as novel mechanistic networks underlying cell senescence progression, with the results of the analysis highlighting the gradual multi-step nature of senescence. For the networks presented here, it is important to highlight that the relationship between gene expression and protein activity is not well characterised. With that said, while there might be an increase in the regulation of a gene, that does not necessarily mean that there is an increase in the activity of its corresponding protein. As such it is very possible to find discrepancies between protein activities inferred from CARNIVAL/COSMOS and changes in expression levels of its corresponding gene. The aim of inferring these networks was to identify proteins and their mode of action, which appear to be involved in the regulation of protein interaction networks that ultimately lead to changes in downstream expression activity. This was performed through CARNIVAL/COSMOS (Liu *et al.*, 2019; Dugourd *et al.*, 2021). Many of the network predictions made are in line with current thought about several systems within the literature as discussed, but also will require experimental validation. At this stage, the predictions can be used for hypothesis generation and in silico testing, and potentially to inform experimental work and mathematical computational models (such as those presented in Chapter 2). In addition to the omic data types included here, using phosphoproteomic data would provide a more accurate and complete picture. Lastly, the work presented here can be used to investigate networks for various processes involved in the senescence process depending on perturbations and research questions of interest.

Chapter 5. General discussion

Cellular senescence is a complex stress response that is accompanied by irreversible growth arrest, phenotypic changes, as well as secretory changes including the production of several cytokines, growth factors and MMPs, collectively known as SASP. Senescence is a dynamic multi-step process involving distinct but overlapping molecular mechanisms that play a role at different times from the cell cycle exit to late-stage senescence. Senescent cells accumulate in tissues and organs with age, and senescence is one of the hallmarks of ageing; They are involved in many age-related pathologies, but they also play many beneficial roles, primarily in the context of embryonic development, tumour suppression, and wound healing and tissue repair.

The focus of this PhD was to use computational systems biology methods to investigate cell senescence in physiology and disease at the tissue level, as well as the progression of cellular senescence at an intracellular mechanism level. To that end, tissue level modelling (Chapter 2 and Chapter 3) and bioinformatics (Chapter 4) approaches were adopted to address these areas, discussed in more detail in the next sections.

5.1 Chapter 2 and Chapter 3 – Modelling senescent cell dynamics in healthy wound healing, fibrosis and chronic wounds

The role of cellular senescence in ageing and age-related pathologies is established, as discussed in section 1.1.1. However, senescent cells also play important roles in physiological processes, mainly in embryonic development by mediating growth and tissue patterning, tumour suppression through the cell-cycle arrest and SASP-mediated immune surveillance, and wound healing and tissue repair with the attenuation of fibrosis. Senescent cells are highly dynamic and heterogenous, which makes them functionally versatile (Hernandez-Segura *et al.*, 2017; Kirschner *et al.*, 2020). This heterogeneity is partly derived from temporal and cell type-specific differences in SASP composition, as well as differences in mechanisms of secondary senescence (section 1.1). Such variability is especially prevalent in the dynamics of cell senescence in the context of wound healing or tissue repair, and its dysregulation, where senescent cells are known to play both favourable as well as detrimental roles (sections 2.1.2 and 3.1.2). However, research in the area of senescent cell heterogeneity, in the context of wound healing and related disorders, is lacking. Therefore in this work, wound healing was used as a biological context to investigate senescence

heterogeneity in physiology and disease, as senescent cells not only play an important role in the healthy tissue repair process (section 2.1.2) but are also associated with pathologies due to dysregulated repair mechanisms, such as fibrosis (section 3.1.2.1) and chronic wounds (section 3.1.2.2).

In Chapter 2, a computational model of wound healing including senescent cell dynamics was developed using the CPM framework, and the model was parametrised using existing data where possible, detailed in section 2.2. The model successfully demonstrated the mechanisms driving the beneficial effects of cell senescence in the wound healing process. This model was then used to demonstrate and investigate the range of senescent cell functional heterogeneity within the repair process in 0. The results from this chapter established that various spatiotemporal dynamics of senescent cells lead to different healing outcomes, including fibrosis and chronic wounds, and that deviation from the tightly controlled senescence program within wound healing leads to distinct pathological repair scenarios. To my knowledge, this is the first tissue-level computational modelling study that has investigated cell senescence functional heterogeneity in the context of wound healing, fibrosis and chronic wounds.

The model is a simplification of highly complex biological processes. Abstraction was necessary to keep the model computationally feasible, while at the same time exploring key processes of interest. The model can potentially be improved by including more immune cell types, different types of ECM components and more growth factors and cytokines that may be of interest. For the sake of model simplicity and computational feasibility, important cell types such as keratinocytes and vascular cells were not included in this model. Similarly, inflammation and ECM, both of which are highly complex, were modelled as single entities. However, given data availability, other cell types and dynamics, as well as inflammatory factors of interest and ECM components, such as fibronectin and Type III Collagen, can be easily implemented within the framework. TGF-β was not included in the model as it is involved in regulating a wide range of functions in multiple cell types and therefore lacked the signalling specificity as seen with PDGF, which previously has been shown to form a signalling circuit in tissue repair consisting of CSF1, PDGF, macrophages and fibroblasts (Zhou *et al.*, 2018; Adler *et al.*, 2020). In addition to this, the model can also be expanded to include the other stages of wound healing, such as the inflammatory phase, in more detail depending on research questions of interest and data

availability. The temporal aspect of senescent cell dynamics in wound healing can also be explored further using the wound healing model. In this project, the three-day delay used to simulate delayed senescence induction (detailed in section 3.2) was further extended to explore bigger delay durations with the sensitivity analysis as shown in section 3.3.2. However, advances in senescence induction could be explored by expanding the inflammatory phase which could provide further insights into chronic wound inflammation driven by senescent cells.

Furthermore, the model was parametrised to existing data to the best of my ability, as this work was independent, without experimental collaborators. Using existing data has its pitfalls: firstly, the amount of experimental work (appropriate and relevant for this model) on the dynamics of senescent cells and SASP in healthy and pathological wound healing is fairly limited, and secondly, the data was gathered from different sources and contexts, followed by calibration to the model (detailed in section 2.2.8.2). lastly, some of the data used was obtained from mouse model studies. While there are some important differences in mouse and human wound healing, this was taken into consideration when developing the wound healing model to the best of my ability. This was done mainly by including characteristics and processes that were common or general to both mouse and human. That being said, some of the important differences between human and mouse wound healing include; epidermis layer thickness, mechanism of wound closure, epidermal ridges, hair follicle sparsity, epidermal stem cell population and etc (Zomer and Trentin, 2018).

While this may not be ideal, this wound healing model can be used as a helpful base to inform experimental work on senescent cell dynamics in healthy and pathological wound healing. This could lead to the development of a more comprehensively parametrised and calibrated computational model, informed by experimental data specific to this context. Several sources of experimental data would be highly valuable to this work, including but not limited to, data on time series cell population changes, cell traction forces, chemical species (such as growth factors, cytokines, chemokines, and proteinases) concentrations, as well as chemical species rate of synthesis and degradation. This would ideally be followed by generating a dataset in order to validate the various model predictions regarding senescent cell dynamics in wound healing, fibrosis and chronic wounds, as well as corresponding SASP regulation and secondary senescence induction mechanisms. Such a model can be used to study potential treatment avenues, such as

senolytics for fibrosis and chronic wounds, and senescent cell manipulation for their beneficial effects. Furthermore, the effect of differences in the duration of the SASP phases (fibrogenic and fibrolytic) and SASP composition on the healing process can also be investigated. This highlights the strength of computational models, as they can easily be updated and improved based on new information and can then be used to inform experimental, and hopefully translational work in a reciprocal manner.

Further work

This work is being prepared for publication and will be uploaded onto GitHub. Further funding is being sought to develop the model further with experimental collaborators.

5.2 Chapter 4 – Time series multi-omic data integration to investigate cell senescence

As discussed, several times throughout this work, the progression of cell senescence is a dynamic multi-step process. It involves cell properties evolving gradually through the duration of senescence, in the form of distinct transcriptional, epigenetic, proteomic and metabolomic changes. Although multi-omic datasets have provided meaningful insights into senescence biology (section 1.2.2 and 4.1.1), an integrated multi-omic approach to investigate the temporal progression of senescence is lacking. Hence in Chapter 4, a time series multi-omic dataset, consisting of RNA-seq, ATAC-seq, metabolomic and proteomic data, was analysed to identify temporal patterns of variation and causal networks across the time series for mechanistic hypothesis generation.

The analysis was conducted with a workflow I developed using existing integration tools. The results from this analysis confirmed the multi-step and gradual nature of senescence progression, as well as the involvement of the EMT pathway in the senescence process. It was also revealed that senescence processes, especially involving cell cycle arrest and apoptosis evasion, begin early through to intermediate senescence, followed by effectors involved in inflammatory SASP production during late senescence. Most importantly, signaling networks were generated for each time point in the data, providing a mechanistic basis for these processes. A detailed explanation of the results from differential analysis and the comparison of the results from analysing each omic data type individually was not stressed on in this work as this was already discussed in detail in the original publication (Chan *et al.*, 2022), and this work was focused on an

alternative strategy to integrate the data. As described in Chapter 4, the proteomic data within this dataset did not contribute to much meaningful biological variance. This could be due to poor data quality; however, further investigation, such as exploring different factor analysis methods, would be helpful in confirming this.

This work can be strengthened with the inclusion of phosphoproteomic data, which provides insights to kinase and phosphatase activity. Furthermore, the PKN used for this work only contains currently known interactions between proteins (TFs, kinases, phosphatases and other effectors) and metabolites. Hence, it does not contain all possible interactions between these components. However, the PKN can be easily updated based on experimentally validated results for further analysis. It is important to keep in mind that not all the network interactions identified in this work are true mechanisms. They are only putative explanations that require experimental validation. Nonetheless, the networks from this work can be used to inform kinetic ODE modelling alongside appropriate experimental data, and the workflow applied can also be used for hypothesis generation for other datasets. An ODE model like this could be embedded into a tissue-level model, like the wound healing model, to dictate cell behaviour through intracellular signaling. Therefore, tools that enable an integrated multi-omic approach to identify upstream causative signaling networks from downstream expression data can be very valuable in providing a better mechanistic understanding of cellular changes, such as senescence.

Further work

This work is still in its initial stages and would benefit from further development. The results from this work have a broad scope and can be used for the mechanistic exploration of several factors involved in investigating cellular senescence. I intend to continue the work by investigating specific mechanisms and effectors that may be of interest to potential collaborators. The workflow can be readily used to generate a series of networks highlighting how mechanisms centred on a specific area of interest may contribute at different stages of development of the cellular senescent phenotype. I also intend to prepare this work for publication.

Computational approaches to studying cell senescence:

Computational approaches, such as the ones used in this thesis, are becoming increasingly useful to cellular senescence research. They provide a great depth of valuable information through

hypothesis generation, *in silico* experimentation, biomarker and drug discovery, and much more, all of it applicable and used for translational and precision medicine. The biological complexity of cell senescence can be extracted and represented using bioinformatics tools and mechanism-based dynamic computational models. On the other hand, ML and artificial intelligence (AI) are becoming increasingly prevalent in working over all this complexity to identify targets of intervention or perturbation. However, although ML and AI can suggest novel intervention targets, a lack of mechanistic understanding of the system will result in an inability to assess the potential effects and implications of those interventions. For all of the above, merging computational systems biology and ML/AI methods would be greatly beneficial for progress in this field, especially given the rapidly increasing body of knowledge and data on cellular senescence.

References

Abboud, S.L. and Pinzani, M. (1991) 'Peptide Growth Factors Stimulate Macrophage Colony-Stimulating Factor in Murine Stromal Cells', *Blood*, 78(1), pp. 103–109. Available at: https://doi.org/10.1182/BLOOD.V78.1.103.103.

Acosta, J.C. *et al.* (2008) 'Chemokine signaling via the CXCR2 receptor reinforces senescence', *Cell*, 133(6), pp. 1006–1018. Available at: https://doi.org/10.1016/J.CELL.2008.03.038.

Acosta, J.C. *et al.* (2013a) 'A complex secretory program orchestrated by the inflammasome controls paracrine senescence', *Nature cell biology*, 15(8), pp. 978–990. Available at: https://doi.org/10.1038/NCB2784.

Acosta, J.C. *et al.* (2013b) 'A complex secretory program orchestrated by the inflammasome controls paracrine senescence', *Nature cell biology*, 15(8), pp. 978–990. Available at: https://doi.org/10.1038/NCB2784.

Adams, T.S. *et al.* (2020) 'Single-cell RNA-seq reveals ectopic and aberrant lung-resident cell populations in idiopathic pulmonary fibrosis', *Science advances*, 6(28). Available at: https://doi.org/10.1126/SCIADV.ABA1983.

Adler, M. *et al.* (2020) 'Principles of Cell Circuits for Tissue Repair and Fibrosis', *iScience*, 23(2), p. 100841. Available at: https://doi.org/10.1016/j.isci.2020.100841.

Van Den Akker, E.B. *et al.* (2020) 'Metabolic Age Based on the BBMRI-NL 1 H-NMR Metabolomics Repository as Biomarker of Age-related Disease', *Circulation. Genomic and precision medicine*, 13(5), pp. 541–547. Available at: https://doi.org/10.1161/CIRCGEN.119.002610.

Alt, S., Ganguly, P. and Salbreux, G. (2017) 'Vertex models: from cell mechanics to tissue morphogenesis', *Philosophical Transactions of the Royal Society B: Biological Sciences*, 372(1720). Available at: https://doi.org/10.1098/RSTB.2015.0520.

Amstrup, J. and Novak, I. (2003) 'P2X7 receptor activates extracellular signal-regulated kinases ERK1 and ERK2 independently of Ca2+ influx', *The Biochemical journal*, 374(Pt 1), pp. 51–61. Available at: https://doi.org/10.1042/BJ20030585.

Andasari, V. *et al.* (2018) 'Computational model of wound healing: EGF secreted by fibroblasts promotes delayed re-epithelialization of epithelial keratinocytes', *Integrative Biology (United Kingdom)*, 10(10), pp. 605–634. Available at: https://doi.org/10.1039/c8ib00048d.

Anderson, R. *et al.* (2019) 'Length-independent telomere damage drives post-mitotic cardiomyocyte senescence', *The EMBO Journal*, 38(5). Available at: https://doi.org/10.15252/EMBJ.2018100492.

Andrews, S. (2010) 'FastQC: A Quality Control Tool for High Throughput Sequence Data'. Available at: http://www.bioinformatics.babraham.ac.uk/projects/fastqc/.

Anerillas, C., Abdelmohsen, K. and Gorospe, M. (2020) 'Regulation of senescence traits by MAPKs', *GeroScience*, 42(2), p. 397. Available at: https://doi.org/10.1007/S11357-020-00183-3.

Ankit Rohatgi (2022) 'WebPlotDigitizer'. Available at: https://automeris.io/WebPlotDigitizer.

Aran, D. *et al.* (2019) 'Reference-based analysis of lung single-cell sequencing reveals a transitional profibrotic macrophage', *Nature immunology*, 20(2), pp. 163–172. Available at: https://doi.org/10.1038/S41590-018-0276-Y.

Argelaguet, R. *et al.* (2018) 'Multi-Omics Factor Analysis—a framework for unsupervised integration of multi-omics data sets', *Molecular Systems Biology*, 14(6), p. e8124. Available at: https://doi.org/10.15252/MSB.20178124.

Atanelishvili, I. *et al.* (2019) 'Antifibrotic efficacy of nintedanib in a cellular model of systemic sclerosis-associated interstitial lung disease', *Clinical and experimental rheumatology*, 37(4), pp. 115–124.

Avelar, R.A. *et al.* (2020) 'A multidimensional systems biology analysis of cellular senescence in aging and disease', *Genome Biology 2020 21:1*, 21(1), pp. 1–22. Available at: https://doi.org/10.1186/S13059-020-01990-9.

Avivi-Green, C., Singal, M. and Vogel, W.F. (2006) 'Discoidin domain receptor 1-deficient mice are resistant to bleomycin-induced lung fibrosis', *American Journal of Respiratory and Critical Care Medicine*, 174(4), pp. 420–427. Available at: https://doi.org/10.1164/rccm.200603-333OC.

Babu, M.M. *et al.* (2004) 'Structure and evolution of transcriptional regulatory networks', *Current Opinion in Structural Biology*, 14(3), pp. 283–291. Available at: https://doi.org/10.1016/J.SBI.2004.05.004.

Badia-I-Mompel, P. *et al.* (2022) 'decoupleR: ensemble of computational methods to infer biological activities from omics data', *Bioinformatics Advances*, 2(1). Available at: https://doi.org/10.1093/BIOADV/VBAC016.

Bai, J. and Zeng, X. (2023) 'Computational modeling and simulation of epithelial wound closure', *Scientific Reports 2023 13:1*, 13(1), pp. 1–10. Available at: https://doi.org/10.1038/s41598-023-33111-4.

Bailey, T.L. *et al.* (2015) 'The MEME Suite', *Nucleic Acids Research*, 43(Web Server issue), p. W39. Available at: https://doi.org/10.1093/NAR/GKV416.

Bain, M.A. *et al.* (2019) 'Effect of Native Type I Collagen with Polyhexamethylene Biguanide Antimicrobial on Wounds: Interim Registry Results', *Plastic and Reconstructive Surgery Global Open*, 7(6), p. E2251. Available at: https://doi.org/10.1097/GOX.0000000000002251.

Baker, D.J. *et al.* (2011) 'Clearance of p16Ink4a-positive senescent cells delays ageing-associated disorders', *Nature*, 479(7372), pp. 232–236. Available at: https://doi.org/10.1038/NATURE10600.

Baker, D.J. *et al.* (2016) 'Naturally occurring p16(Ink4a)-positive cells shorten healthy lifespan', *Nature*, 530(7589), pp. 184–189. Available at: https://doi.org/10.1038/NATURE16932.

Bannon, P. *et al.* (2013) 'Diabetes induces stable intrinsic changes to myeloid cells that contribute to chronic inflammation during wound healing in mice', *Disease models & mechanisms*, 6(6), pp. 1434–1447. Available at: https://doi.org/10.1242/DMM.012237.

Bansal, R. *et al.* (2017) 'Integrin alpha 11 in the regulation of the myofibroblast phenotype: Implications for fibrotic diseases', *Experimental and Molecular Medicine*, 49(11), pp. e396–e396. Available at: https://doi.org/10.1038/emm.2017.213.

Basisty, N. *et al.* (2020) 'The power of proteomics to monitor senescence-associated secretory phenotypes and beyond: toward clinical applications',

https://doi.org/10.1080/14789450.2020.1766976, 17(4), pp. 297–308. Available at: https://doi.org/10.1080/14789450.2020.1766976.

Beauséjour, C.M. *et al.* (2003) 'Reversal of human cellular senescence: roles of the p53 and p16 pathways', *The EMBO journal*, 22(16), pp. 4212–4222. Available at: https://doi.org/10.1093/EMBOJ/CDG417.

Vande Berg, J.S. *et al.* (2005) 'Cultured pressure ulcer fibroblasts show replicative senescence with elevated production of plasmin, plasminogen activator inhibitor-1, and transforming growth factor-β1', *Wound Repair and Regeneration*, 13(1), pp. 76–83. Available at: https://doi.org/10.1111/j.1067-1927.2005.130110.x.

van den Berg, R.A. *et al.* (2006) 'Centering, scaling, and transformations: Improving the biological information content of metabolomics data', *BMC Genomics*, 7(1), pp. 1–15. Available at: https://doi.org/10.1186/1471-2164-7-142/FIGURES/9.

Berneburg, M. and Krutmann, J. (2000) 'Photoaging-associated large-scale deletions of mitochondrial DNA', *Methods in enzymology*, 319, pp. 366–376. Available at: https://doi.org/10.1016/S0076-6879(00)19036-6.

Beyer, C. *et al.* (2009) 'Hypoxia. Hypoxia in the pathogenesis of systemic sclerosis', *Arthritis Research & Therapy*, 11(2), p. 220. Available at: https://doi.org/10.1186/AR2598.

Bird, T.G. *et al.* (2018) 'TGFβ inhibition restores a regenerative response in acute liver injury by suppressing paracrine senescence', *Science translational medicine*, 10(454). Available at: https://doi.org/10.1126/SCITRANSLMED.AAN1230.

Bitter, E.E. *et al.* (2020) 'Thymidine kinase 1 through the ages: a comprehensive review', *Cell & Bioscience 2020 10:1*, 10(1), pp. 1–16. Available at: https://doi.org/10.1186/S13578-020-00493-1.

Black, A.R. and Black, J.D. (2012) 'Protein kinase C signaling and cell cycle regulation', *Frontiers in Immunology*, 3(JAN), p. 34014. Available at: https://doi.org/10.3389/FIMMU.2012.00423/BIBTEX.

Bonner, J.C. (2004) 'Regulation of PDGF and its receptors in fibrotic diseases', *Cytokine and Growth Factor Reviews*, 15(4), pp. 255–273. Available at: https://doi.org/10.1016/j.cytogfr.2004.03.006.

Bonyadi, M.R. and Michalewicz, Z. (2017) 'Particle swarm optimization for single objective continuous space problems: A review', *Evolutionary Computation*, 25(1), pp. 1–54. Available at: https://doi.org/10.1162/EVCO_R_00180.

Bossaert, M. *et al.* (2021) 'Transcription-associated topoisomerase 2α (Top2a) activity is a major effector of cytotoxicity induced by g-quadruplex ligands', *eLife*, 10. Available at: https://doi.org/10.7554/ELIFE.65184.

Boström, H. *et al.* (1996) 'PDGF-A signaling is a critical event in lung alveolar myofibroblast development and alveogenesis', *Cell*, 85(6), pp. 863–873. Available at: https://doi.org/10.1016/S0092-8674(00)81270-2.

Boulet, N. *et al.* (2023) 'Notch activation shifts the fate decision of senescent progenitors toward myofibrogenesis in human adipose tissue', *Aging Cell*, 22(3). Available at: https://doi.org/10.1111/ACEL.13776.

Bourgeois, B. and Madl, T. (2018) 'Regulation of cellular senescence via the FOXO4-p53 axis', *Febs Letters*, 592(12), p. 2083. Available at: https://doi.org/10.1002/1873-3468.13057.

Brown, J.R. *et al.* (1998) 'Fos Family Members Induce Cell Cycle Entry by Activating Cyclin D1', *Molecular and Cellular Biology*, 18(9), p. 5609. Available at: https://doi.org/10.1128/MCB.18.9.5609.

Buscà, R., Pouysségur, J. and Lenormand, P. (2016) 'ERK1 and ERK2 map kinases: Specific roles or functional redundancy?', *Frontiers in Cell and Developmental Biology*, 4(JUN), p. 195428. Available at: https://doi.org/10.3389/FCELL.2016.00053/BIBTEX.

Busuttil, R.A. *et al.* (2003) 'Oxygen accelerates the accumulation of mutations during the senescence and immortalization of murine cells in culture', *Aging cell*, 2(6), pp. 287–294. Available at: https://doi.org/10.1046/J.1474-9728.2003.00066.X.

Campisi, J. (2005) 'Senescent cells, tumor suppression, and organismal aging: good citizens, bad neighbors', *Cell*, 120(4), pp. 513–522. Available at: https://doi.org/10.1016/J.CELL.2005.02.003.

Chan, M. *et al.* (2022) 'Novel Insights from a Multiomics Dissection of the Hayflick Limit', *eLife*, 11. Available at: https://doi.org/10.7554/ELIFE.70283.

Chandrasegaran, S. *et al.* (2023) 'Systems Biology of Ageing', *Sub-cellular biochemistry*, 102, pp. 415–424. Available at: https://doi.org/10.1007/978-3-031-21410-3_16.

Charlebois, D.A. and Balázsi, G. (2019) 'Modeling cell population dynamics', *In Silico Biology*, 13(1–2), p. 21. Available at: https://doi.org/10.3233/ISB-180470.

Chen, X. *et al.* (2021) 'Moderate oxidative stress promotes epithelial–mesenchymal transition in the lens epithelial cells via the TGF-β/Smad and Wnt/β-catenin pathways', *Molecular and Cellular Biochemistry*, 476(3), pp. 1631–1642. Available at: https://doi.org/10.1007/S11010-020-04034-9/METRICS.

Chien, Y. *et al.* (2011) 'Control of the senescence-associated secretory phenotype by NF-κB promotes senescence and enhances chemosensitivity', *Genes & Development*, 25(20), p. 2125. Available at: https://doi.org/10.1101/GAD.17276711.

Childs, B.G. *et al.* (2016) 'Senescent intimal foam cells are deleterious at all stages of atherosclerosis', *Science (New York, N.Y.)*, 354(6311), pp. 472–477. Available at: https://doi.org/10.1126/SCIENCE.AAF6659.

Chinta, S.J. *et al.* (2018) 'Cellular Senescence Is Induced by the Environmental Neurotoxin Paraquat and Contributes to Neuropathology Linked to Parkinson's Disease', *Cell reports*, 22(4), pp. 930–940. Available at: https://doi.org/10.1016/J.CELREP.2017.12.092.

Cho, J. *et al.* (2014) 'Purinergic P2Y14 receptor modulates stress-induced hematopoietic stem/progenitor cell senescence', *The Journal of Clinical Investigation*, 124(7), p. 3159. Available at: https://doi.org/10.1172/JCI61636.

Choi, E.-H. and Park, S.-J. (2023) 'TXNIP: A key protein in the cellular stress response pathway and a potential therapeutic target', *Experimental & Molecular Medicine 2023 55:7*, 55(7), pp. 1348–1356. Available at: https://doi.org/10.1038/s12276-023-01019-8.

Cicchini, C. *et al.* (2008) 'TGFβ-induced EMT requires focal adhesion kinase (FAK) signaling', *Experimental Cell Research*, 314(1), pp. 143–152. Available at: https://doi.org/10.1016/J.YEXCR.2007.09.005.

Cipra, B.A. (2018) 'An Introduction to the Ising Model', *https://doi.org/10.1080/00029890.1987.12000742*, 94(10), pp. 937–959. Available at: https://doi.org/10.1080/00029890.1987.12000742.

Cochran, B.H. (1985) 'The Molecular Action of Platelet-Derived Growth Factor', *Advances in Cancer Research*, 45(C), pp. 183–216. Available at: https://doi.org/10.1016/S0065-230X(08)60269-9.

Collier, I.E. *et al.* (2011) 'Diffusion of MMPs on the surface of collagen fibrils: The mobile cell surface - collagen substratum interface', *PLoS ONE*, 6(9). Available at: https://doi.org/10.1371/journal.pone.0024029.

Conte, E. *et al.* (2011) 'Inhibition of PI3K prevents the proliferation and differentiation of human lung fibroblasts into myofibroblasts: The role of class I P110 isoforms', *PLoS ONE*, 6(10). Available at: https://doi.org/10.1371/journal.pone.0024663.

Cook, D.P. and Vanderhyden, B.C. (2020) 'Context specificity of the EMT transcriptional response', *Nature Communications 2020 11:1*, 11(1), pp. 1–9. Available at: https://doi.org/10.1038/s41467-020-16066-2.

Coppé, J.P. *et al.* (2008) 'Senescence-associated secretory phenotypes reveal cell-nonautonomous functions of oncogenic RAS and the p53 tumor suppressor', *PLoS biology*, 6(12). Available at: https://doi.org/10.1371/JOURNAL.PBIO.0060301.

Coppé, J.-P. *et al.* (2010) 'The Senescence-Associated Secretory Phenotype: The Dark Side of Tumor Suppression', *Annual Review of Pathology: Mechanisms of Disease*, 5(1), pp. 99–118. Available at: https://doi.org/10.1146/annurev-pathol-121808-102144.

Cui, S. *et al.* (2018) 'Postinfarction Hearts Are Protected by Premature Senescent Cardiomyocytes Via GATA4-Dependent CCN1 Secretion', *Journal of the American Heart Association:*

Cardiovascular and Cerebrovascular Disease, 7(18). Available at: https://doi.org/10.1161/JAHA.118.009111.

Cumming, B.D., McElwain, D.L.S. and Upton, Z. (2010) 'A mathematical model of wound healing and subsequent scarring', *Journal of the Royal Society, Interface*, 7(42), pp. 19–34. Available at: https://doi.org/10.1098/RSIF.2008.0536.

Cunningham, F. *et al.* (2022) 'Ensembl 2022', *Nucleic Acids Research*, 50(D1), pp. D988–D995. Available at: https://doi.org/10.1093/NAR/GKAB1049.

Curley, D.E. *et al.* (2021) 'Corticotropin Releasing Factor Binding Protein as a Novel Target to Restore Brain Homeostasis: Lessons Learned From Alcohol Use Disorder Research', *Frontiers in Behavioral Neuroscience*, 15. Available at: https://doi.org/10.3389/FNBEH.2021.786855.

Dalle Pezze, P. *et al.* (2014) 'Dynamic Modelling of Pathways to Cellular Senescence Reveals Strategies for Targeted Interventions', *PLoS Computational Biology*. Edited by A. Rzhetsky, 10(8), p. e1003728. Available at: https://doi.org/10.1371/journal.pcbi.1003728.

Dang, W. *et al.* (2009) 'Histone H4 lysine-16 acetylation regulates cellular lifespan', *Nature*, 459(7248), p. 802. Available at: https://doi.org/10.1038/NATURE08085.

Das, A. *et al.* (2015) 'Monocyte and macrophage plasticity in tissue repair and regeneration', *The American journal of pathology*, 185(10), pp. 2596–2606. Available at: https://doi.org/10.1016/J.AJPATH.2015.06.001.

De-Carvalho, D.P., Jacinto, A. and Saúde, L. (2021) 'The right time for senescence', *eLife*, 10. Available at: https://doi.org/10.7554/ELIFE.72449.

Demaria, M. *et al.* (2014) 'An essential role for senescent cells in optimal wound healing through secretion of PDGF-AA', *Developmental Cell*, 31(6), pp. 722–733. Available at: https://doi.org/10.1016/j.devcel.2014.11.012.

Demaria, M. *et al.* (2017) 'Cellular Senescence Promotes Adverse Effects of Chemotherapy and Cancer Relapse', *Cancer discovery*, 7(2), pp. 165–176. Available at: https://doi.org/10.1158/2159-8290.CD-16-0241.

Desmoulière, A. *et al.* (1997) 'Apoptosis during wound healing, fibrocontractive diseases and vascular wall injury', *International Journal of Biochemistry and Cell Biology*, pp. 19–30. Available at: https://doi.org/10.1016/S1357-2725(96)00117-3.

van Deursen, J.M. (2014) 'The role of senescent cells in ageing', *Nature*, 509(7501), pp. 439–446. Available at: https://doi.org/10.1038/nature13193.

van Deursen, J.M. (2019) 'Senolytic therapies for healthy longevity', *Science (New York, N.Y.)*, 364(6441), pp. 636–637. Available at: https://doi.org/10.1126/SCIENCE.AAW1299.

Diegelmann, R.F. (2003) 'Excessive neutrophils characterize chronic pressure ulcers', *Wound repair and regeneration : official publication of the Wound Healing Society [and] the European Tissue Repair Society*, 11(6), pp. 490–495. Available at: https://doi.org/10.1046/J.1524-475X.2003.11617.X.

Dirocco, D.P. *et al.* (2014) 'CDK4/6 inhibition induces epithelial cell cycle arrest and ameliorates acute kidney injury', *American journal of physiology. Renal physiology*, 306(4). Available at: https://doi.org/10.1152/AJPRENAL.00475.2013.

Distler, J.H.W. *et al.* (2019) 'Shared and distinct mechanisms of fibrosis', *Nature Reviews Rheumatology 2019 15:12*, 15(12), pp. 705–730. Available at: https://doi.org/10.1038/s41584-019-0322-7.

Dobaczewski, M. *et al.* (2010) 'Smad3 signaling critically regulates fibroblast phenotype and function in healing myocardial infarction', *Circulation Research*, 107(3), pp. 418–428. Available at: https://doi.org/10.1161/CIRCRESAHA.109.216101.

Dolivo, D.M., Larson, S.A. and Dominko, T. (2019) 'Crosstalk between mitogen-activated protein kinase inhibitors and transforming growth factor-β signaling results in variable activation of human dermal fibroblasts', *International Journal of Molecular Medicine*, 43(1), pp. 325–335. Available at: https://doi.org/10.3892/ijmm.2018.3949.

Driskell, I. *et al.* (2015) 'Genetically induced cell death in bulge stem cells reveals their redundancy for hair and epidermal regeneration', *Stem cells (Dayton, Ohio)*, 33(3), pp. 988–998. Available at: https://doi.org/10.1002/STEM.1910.

Dugourd, A. *et al.* (2021) 'Causal integration of multi-omics data with prior knowledge to generate mechanistic hypotheses', *Molecular Systems Biology*, 17(1), p. e9730. Available at: https://doi.org/10.15252/MSB.20209730.

Dulić, V. *et al.* (2000) 'Uncoupling between phenotypic senescence and cell cycle arrest in aging p21-deficient fibroblasts', *Molecular and cellular biology*, 20(18), pp. 6741–6754. Available at: https://doi.org/10.1128/MCB.20.18.6741-6754.2000.

Dupont, S. *et al.* (2011) 'Role of YAP/TAZ in mechanotransduction', *Nature*, 474(7350), pp. 179–184. Available at: https://doi.org/10.1038/nature10137.

Durinck, S. *et al.* (2005) 'BioMart and Bioconductor: a powerful link between biological databases and microarray data analysis', *Bioinformatics (Oxford, England)*, 21(16), pp. 3439–3440. Available at: https://doi.org/10.1093/BIOINFORMATICS/BTI525.

D'Urso, M. and Kurniawan, N.A. (2020) 'Mechanical and Physical Regulation of Fibroblast–Myofibroblast Transition: From Cellular Mechanoresponse to Tissue Pathology', *Frontiers in Bioengineering and Biotechnology*, 8, p. 609653. Available at: https://doi.org/10.3389/FBIOE.2020.609653.

Engel, M.E. *et al.* (1999) 'Interdependent SMAD and JNK Signaling in Transforming Growth Factor-β-mediated Transcription', *Journal of Biological Chemistry*, 274(52), pp. 37413–37420. Available at: https://doi.org/10.1074/JBC.274.52.37413.

Ermentrout, G.B. and Edelstein-Keshet, L. (1993) 'Cellular automata approaches to biological modeling', *Journal of theoretical biology*, 160(1), pp. 97–133. Available at: https://doi.org/10.1006/JTBI.1993.1007.

Ewels, P. *et al.* (2016) 'MultiQC: summarize analysis results for multiple tools and samples in a single report', *Bioinformatics*, 32(19), pp. 3047–3048. Available at: https://doi.org/10.1093/BIOINFORMATICS/BTW354.

Fabbri, E. *et al.* (2015) 'Aging and the burden of multimorbidity: associations with inflammatory and anabolic hormonal biomarkers', *The journals of gerontology. Series A, Biological sciences and medical sciences*, 70(1), pp. 63–70. Available at: https://doi.org/10.1093/GERONA/GLU127.

Falkenburg, J.H. *et al.* (1990) 'Gene-expression and release of macrophage-colony stimulating factor in quiescent and proliferating fibroblasts. Effects of serum, fibroblast growth-promoting factors, and IL-1.', *The Journal of Immunology*, 144(12), pp. 4657–4662. Available at: https://doi.org/10.4049/JIMMUNOL.144.12.4657.

Farbehi, N. *et al.* (2019) 'Single-cell expression profiling reveals dynamic flux of cardiac stromal, vascular and immune cells in health and injury', *eLife*, 8. Available at: https://doi.org/10.7554/ELIFE.43882.

Farr, J.N. *et al.* (2017) 'Targeting cellular senescence prevents age-related bone loss in mice', *Nature Medicine 2017 23:9*, 23(9), pp. 1072–1079. Available at: https://doi.org/10.1038/nm.4385.

Feng, T. *et al.* (2019) 'CCN1-Induced Cellular Senescence Promotes Heart Regeneration', *Circulation*, 139(21), pp. 2495–2498. Available at: https://doi.org/10.1161/CIRCULATIONAHA.119.039530.

Ferreira-Gonzalez, S. *et al.* (2018) 'Paracrine cellular senescence exacerbates biliary injury and impairs regeneration', *Nature communications*, 9(1). Available at: https://doi.org/10.1038/S41467-018-03299-5.

Filardy, A.A. *et al.* (2010) 'Proinflammatory clearance of apoptotic neutrophils induces an IL-12(low)IL-10(high) regulatory phenotype in macrophages', *Journal of immunology (Baltimore, Md. : 1950)*, 185(4), pp. 2044–2050. Available at: https://doi.org/10.4049/JIMMUNOL.1000017.

Fitzner, B. *et al.* (2012) 'Senescence determines the fate of activated rat pancreatic stellate cells', *Journal of Cellular and Molecular Medicine*, 16(11), pp. 2620–2630. Available at: https://doi.org/10.1111/J.1582-4934.2012.01573.X.

Fletcher, A.G. *et al.* (2013) 'Implementing vertex dynamics models of cell populations in biology within a consistent computational framework', *Progress in Biophysics and Molecular Biology*, 113(2), pp. 299–326. Available at: https://doi.org/10.1016/J.PBIOMOLBIO.2013.09.003.

Forrest, J. *et al.* (2023) 'coin-or/Cbc: Release releases/2.10.10'. Available at: https://doi.org/10.5281/ZENODO.7843975.

Fortuna, I. *et al.* (2020) 'CompuCell3D Simulations Reproduce Mesenchymal Cell Migration on Flat Substrates', *Biophysical Journal*, 118(11), pp. 2801–2815. Available at: https://doi.org/10.1016/j.bpj.2020.04.024.

Franceschi, C. *et al.* (2000) 'Inflamm-aging. An evolutionary perspective on immunosenescence', *Annals of the New York Academy of Sciences*, 908, pp. 244–254. Available at: https://doi.org/10.1111/J.1749-6632.2000.TB06651.X.

Freitas Robert A (1999) *Nanomedicine Volume I: Basic Capabilities*. Landes Bioscience.

Freund, A., Patil, C.K. and Campisi, J. (2011a) 'p38MAPK is a novel DNA damage response-independent regulator of the senescence-associated secretory phenotype', *The EMBO journal*, 30(8), pp. 1536–1548. Available at: https://doi.org/10.1038/EMBOJ.2011.69.

Freund, A., Patil, C.K. and Campisi, J. (2011b) 'p38MAPK is a novel DNA damage response-independent regulator of the senescence-associated secretory phenotype', *The EMBO journal*, 30(8), pp. 1536–1548. Available at: https://doi.org/10.1038/EMBOJ.2011.69.

Frisch, S.M. and MacFawn, I.P. (2020) 'Type I interferons and related pathways in cell senescence', *Aging Cell*, 19(10), p. 1957. Available at: https://doi.org/10.1111/ACEL.13234.

Frost, J. *et al.* (2012) 'Differential gene expression of MMP-1, TIMP-1 and HGF in clinically involved and uninvolved skin in South Africans with SSc', *Rheumatology*, 51(6), pp. 1049–1052. Available at: https://doi.org/10.1093/RHEUMATOLOGY/KER367.

Fujioka, S. *et al.* (2004) 'NF-kappaB and AP-1 connection: mechanism of NF-kappaB-dependent regulation of AP-1 activity', *Molecular and cellular biology*, 24(17), pp. 7806–7819. Available at: https://doi.org/10.1128/MCB.24.17.7806-7819.2004.

Fujita, T. *et al.* (1993) 'The candidate proto-oncogene bcl-3 encodes a transcriptional coactivator that activates through NF-kappa B p50 homodimers', *Genes & development*, 7(7B), pp. 1354–1363. Available at: https://doi.org/10.1101/GAD.7.7B.1354.

Gal, H. *et al.* (2020) 'Molecular pathways of senescence regulate placental structure and function.', *The EMBO journal*, 39(15), p. e105972. Available at: https://doi.org/10.15252/embj.2020105972.

Gan, Q. *et al.* (2008) 'PPAR{gamma} accelerates cellular senescence by inducing p16INK4{alpha} expression in human diploid fibroblasts', *Journal of cell science*, 121(Pt 13), pp. 2235–2245. Available at: https://doi.org/10.1242/JCS.026633.

Gao, Y. *et al.* (2023) 'Multi-omics analysis of human mesenchymal stem cells shows cell aging that alters immunomodulatory activity through the downregulation of PD-L1', *Nature Communications 2023 14:1*, 14(1), pp. 1–21. Available at: https://doi.org/10.1038/s41467-023-39958-5.

Giannandrea, M. and Parks, W.C. (2014) 'Diverse functions of matrix metalloproteinases during fibrosis', *Disease Models & Mechanisms*, 7(2), p. 193. Available at: https://doi.org/10.1242/DMM.012062.

Gibellini, F. and Smith, T.K. (2010) 'The Kennedy pathway—De novo synthesis of phosphatidylethanolamine and phosphatidylcholine', *IUBMB Life*, 62(6), pp. 414–428. Available at: https://doi.org/10.1002/IUB.337.

Ginhoux, F. *et al.* (2015) 'New insights into the multidimensional concept of macrophage ontogeny, activation and function', *Nature Immunology 2015 17:1*, 17(1), pp. 34–40. Available at: https://doi.org/10.1038/ni.3324.

Gire, V. and Dulic, V. (2015) 'Senescence from G2 arrest, revisited', *Cell cycle (Georgetown, Tex.)*, 14(3), pp. 297–304. Available at: https://doi.org/10.1080/15384101.2014.1000134.

Gkogkolou, P. and Böhm, M. (2012) 'Advanced glycation end products', *http://www.tandfonline.com/action/authorSubmission?journalCode=kder20&page=instructions*, 4(3), pp. 259–270. Available at: https://doi.org/10.4161/DERM.22028.

Glazier, J.A. and Graner, F. (1993) 'Simulation of the differential adhesion driven rearrangement of biological cells', *Physical review. E, Statistical physics, plasmas, fluids, and related interdisciplinary topics*, 47(3), pp. 2128–2154. Available at: https://doi.org/10.1103/PHYSREVE.47.2128.

Glont, M. *et al.* (2018) 'BioModels: expanding horizons to include more modelling approaches and formats', *Nucleic Acids Research*, 46(D1), pp. D1248–D1253. Available at: https://doi.org/10.1093/NAR/GKX1023.

Goldsby, H.J. *et al.* (2014) 'The Evolutionary Origin of Somatic Cells under the Dirty Work Hypothesis', *PLOS Biology*, 12(5), p. e1001858. Available at: https://doi.org/10.1371/JOURNAL.PBIO.1001858.

Golebiewska, E.M. and Poole, A.W. (2015) 'Platelet secretion: From haemostasis to wound healing and beyond', *Blood reviews*, 29(3), pp. 153–162. Available at: https://doi.org/10.1016/J.BLRE.2014.10.003.

Gonzalez-Meljem, J.M. *et al.* (2018) 'Paracrine roles of cellular senescence in promoting tumourigenesis', *British journal of cancer*, 118(10), pp. 1283–1288. Available at: https://doi.org/10.1038/S41416-018-0066-1.

Gorgoulis, V. *et al.* (2019) 'Cellular Senescence: Defining a Path Forward', *Joã o F. Passos*, 15, p. 14. Available at: https://doi.org/10.1016/j.cell.2019.10.005.

Graner, F. and Glazier, J.A. (1992) 'Simulation of biological cell sorting using a two-dimensional extended Potts model', *Physical Review Letters*, 69(13), p. 2013. Available at: https://doi.org/10.1103/PhysRevLett.69.2013.

Grinnell, F. *et al.* (1999) 'Release of mechanical tension triggers apoptosis of human fibroblasts in a model of regressing granulation tissue', *Experimental Cell Research*, 248(2), pp. 608–619. Available at: https://doi.org/10.1006/EXCR.1999.4440.

Grotendorst, G.R., Rahmanie, H. and Duncan, M.R. (2004) 'Combinatorial signaling pathways determine fibroblast proliferation and myofibroblast differentiation', *FASEB Journal*, 18(3), pp. 469–479. Available at: https://doi.org/10.1096/fj.03-0699com.

Gu, Z. and Hübschmann, D. (2023) 'rGREAT: an R/bioconductor package for functional enrichment on genomic regions', *Bioinformatics*, 39(1). Available at: https://doi.org/10.1093/BIOINFORMATICS/BTAC745.

Guerra, A., Belinha, J. and Jorge, R.N. (2018) 'Modelling skin wound healing angiogenesis: A review', *Journal of Theoretical Biology*, 459, pp. 1–17. Available at: https://doi.org/10.1016/J.JTBI.2018.09.020.

Guimera, A.M. *et al.* (2017) 'Systems modelling ageing: From single senescent cells to simple multi-cellular models', *Essays in Biochemistry*. Portland Press Ltd, pp. 369–377. Available at: https://doi.org/10.1042/EBC20160087.

Gumbiner, B.M. and Kim, N.G. (2014) 'The Hippo-YAP signaling pathway and contact inhibition of growth', *Journal of Cell Science*, 127(4), pp. 709–717. Available at: https://doi.org/10.1242/JCS.140103.

Guo, L., Degenstein, L. and Fuchs, E. (1996) 'Keratinocyte growth factor is required for hair development but not for wound healing', *Genes & development*, 10(2), pp. 165–175. Available at: https://doi.org/10.1101/GAD.10.2.165.

Gureghian, V. *et al.* (2023) 'A multi-omics integrative approach unravels novel genes and pathways associated with senescence escape after targeted therapy in NRAS mutant melanoma', *Cancer Gene Therapy 2023*, pp. 1–16. Available at: https://doi.org/10.1038/s41417-023-00640-z.

Hamburg-Shields, E. *et al.* (2015) 'Sustained β-catenin activity in dermal fibroblasts promotes fibrosis by up-regulating expression of extracellular matrix protein-coding genes', *Journal of Pathology*, 235(5), pp. 686–697. Available at: https://doi.org/10.1002/path.4481.

Hamsanathan, S. and Gurkar, A.U. (2022) 'Lipids as Regulators of Cellular Senescence', *Frontiers in Physiology*, 13, p. 796850. Available at: https://doi.org/10.3389/FPHYS.2022.796850.

Harding, K.G., Moore, K. and Phillips, T.J. (2005) 'Wound chronicity and fibroblast senescence – implications for treatment', *International Wound Journal*, 2(4), p. 364. Available at: https://doi.org/10.1111/J.1742-4801.2005.00149.X.

Hartenstein, B. *et al.* (2006) 'Epidermal development and wound healing in matrix metalloproteinase 13-deficient mice', *The Journal of investigative dermatology*, 126(2), pp. 486–496. Available at: https://doi.org/10.1038/SJ.JID.5700084.

Haugh, J.M. (2006) 'Deterministic model of dermal wound invasion incorporating receptor-mediated signal transduction and spatial gradient sensing', *Biophysical Journal*, 90(7), pp. 2297–2308. Available at: https://doi.org/10.1529/biophysj.105.077610.

Hayflick, L. and Moorhead, P.S. (1961) 'The serial cultivation of human diploid cell strains', *Experimental cell research*, 25(3), pp. 585–621. Available at: https://doi.org/10.1016/0014-4827(61)90192-6.

Heit, I. *et al.* (2001) 'Involvement of protein kinase Cδ in contact-dependent inhibition of growth in human and murine fibroblasts', *Oncogene 2001 20:37*, 20(37), pp. 5143–5154. Available at: https://doi.org/10.1038/sj.onc.1204657.

Helman, A. *et al.* (2016) 'p16(Ink4a)-induced senescence of pancreatic beta cells enhances insulin secretion', *Nature medicine*, 22(4), pp. 412–420. Available at: https://doi.org/10.1038/NM.4054.

Hernandez-Segura, A. *et al.* (2017) 'Unmasking Transcriptional Heterogeneity in Senescent Cells', *Current biology : CB*, 27(17), p. 2652. Available at: https://doi.org/10.1016/J.CUB.2017.07.033.

Hernandez-Segura, A., Nehme, J. and Demaria, M. (2018) 'Hallmarks of Cellular Senescence', *Trends in Cell Biology*, 28(6), pp. 436–453. Available at: https://doi.org/10.1016/J.TCB.2018.02.001.

Hiebert, P. *et al.* (2018) 'Nrf2-Mediated Fibroblast Reprogramming Drives Cellular Senescence by Targeting the Matrisome', *Developmental cell*, 46(2), pp. 145-161.e10. Available at: https://doi.org/10.1016/J.DEVCEL.2018.06.012.

Hinz, B. *et al.* (2001) 'Mechanical tension controls granulation tissue contractile activity and myofibroblast differentiation', *American Journal of Pathology*, 159(3), pp. 1009–1020. Available at: https://doi.org/10.1016/S0002-9440(10)61776-2.

Hinz, Boris (2016) 'Myofibroblasts', *Experimental Eye Research*. Academic Press, pp. 56–70. Available at: https://doi.org/10.1016/j.exer.2015.07.009.

Hinz, B. (2016) 'The role of myofibroblasts in wound healing', *Current Research in Translational Medicine*, 64(4), pp. 171–177. Available at: https://doi.org/10.1016/J.RETRAM.2016.09.003.

Hinz, B. and Lagares, D. (2019) 'Evasion of apoptosis by myofibroblasts: a hallmark of fibrotic diseases', *Nature Reviews Rheumatology*. Nature Research, pp. 11–31. Available at: https://doi.org/10.1038/s41584-019-0324-5.

Hirashima, T., Rens, E.G. and Merks, R.M.H. (2017) 'Cellular Potts modeling of complex multicellular behaviors in tissue morphogenesis', *Development, Growth & Differentiation*, 59(5), pp. 329–339. Available at: https://doi.org/10.1111/DGD.12358.

Hoare, M. *et al.* (2016) 'NOTCH1 mediates a switch between two distinct secretomes during senescence', *Nature cell biology*, 18(9), pp. 979–992. Available at: https://doi.org/10.1038/NCB3397.

Hoare, M. and Narita, M. (2017) 'NOTCH and the 2 SASPs of senescence', *Cell Cycle*. Taylor and Francis Inc., pp. 239–240. Available at: https://doi.org/10.1080/15384101.2016.1248730.

Honda, H. (1978) 'Description of cellular patterns by Dirichlet domains: The two-dimensional case', *Journal of Theoretical Biology*, 72(3), pp. 523–543. Available at: https://doi.org/10.1016/0022-5193(78)90315-6.

Honda, H., Tanemura, M. and Nagai, T. (2004) 'A three-dimensional vertex dynamics cell model of space-filling polyhedra simulating cell behavior in a cell aggregate', *Journal of Theoretical Biology*, 226(4), pp. 439–453. Available at: https://doi.org/10.1016/J.JTBI.2003.10.001.

Hornbeck, P. V. *et al.* (2015) 'PhosphoSitePlus, 2014: mutations, PTMs and recalibrations', *Nucleic acids research*, 43(Database issue), pp. D512–D520. Available at: https://doi.org/10.1093/NAR/GKU1267.

Horowitz, J.C. *et al.* (2007) 'Combinatorial activation of FAK and AKT by transforming growth factor-β1 confers an anoikis-resistant phenotype to myofibroblasts', *Cellular Signalling*, 19(4), pp. 761–771. Available at: https://doi.org/10.1016/j.cellsig.2006.10.001.

Horvath, S. (2013) 'DNA methylation age of human tissues and cell types', *Genome Biology*, 14(10), pp. 1–20. Available at: https://doi.org/10.1186/GB-2013-14-10-R115/COMMENTS.

Hough, C., Radu, M. and Doré, J.J.E. (2012) 'TGF-Beta Induced Erk Phosphorylation of Smad Linker Region Regulates Smad Signaling', *PLoS ONE*, 7(8), p. 42513. Available at: https://doi.org/10.1371/JOURNAL.PONE.0042513.

Hu, B., Wu, Z. and Phan, S.H. (2003) 'Smad3 Mediates Transforming Growth Factor-β–Induced α-Smooth Muscle Actin Expression', *American Journal of Respiratory Cell and Molecular Biology*, 29(3), pp. 397–404. Available at: https://doi.org/10.1165/rcmb.2003-0063OC.

Hu, L. *et al.* (2022) 'Why Senescent Cells Are Resistant to Apoptosis: An Insight for Senolytic Development', *Frontiers in Cell and Developmental Biology*, 10, p. 822816. Available at: https://doi.org/10.3389/FCELL.2022.822816/BIBTEX.

Huang, W. *et al.* (2022) 'Cellular senescence: the good, the bad and the unknown', *Nature Reviews Nephrology 2022 18:10*, 18(10), pp. 611–627. Available at: https://doi.org/10.1038/s41581-022-00601-z.

Huang, W.C. *et al.* (2012) 'Classical Macrophage Activation Up-Regulates Several Matrix Metalloproteinases through Mitogen Activated Protein Kinases and Nuclear Factor-κB', *PLOS ONE*, 7(8), p. e42507. Available at: https://doi.org/10.1371/JOURNAL.PONE.0042507.

Huang, X. *et al.* (2012) 'Matrix Stiffness–Induced Myofibroblast Differentiation Is Mediated by Intrinsic Mechanotransduction', *American Journal of Respiratory Cell and Molecular Biology*, 47(3), pp. 340–348. Available at: https://doi.org/10.1165/rcmb.2012-0050OC.

Huggins, C.J. *et al.* (2013) 'C/EBPγ suppresses senescence and inflammatory gene expression by heterodimerizing with C/EBPβ', *Molecular and cellular biology*, 33(16), pp. 3242–3258. Available at: https://doi.org/10.1128/MCB.01674-12.

Hughes, C.E. *et al.* (2020) 'Cysteine Toxicity Drives Age-Related Mitochondrial Decline by Altering Iron Homeostasis', *Cell*, 180(2), pp. 296-310.e18. Available at: https://doi.org/10.1016/J.CELL.2019.12.035/ATTACHMENT/42F19D6F-B6D2-4489-A657-4445A62FF39A/MMC2.XLSX.

Hundal, R.S. *et al.* (2003) 'Oxidized Low Density Lipoprotein Inhibits Macrophage Apoptosis by Blocking Ceramide Generation, Thereby Maintaining Protein Kinase B Activation, Bcl-X L Levels',

Journal of Biological Chemistry, 278(27), pp. 24399–24408. Available at: https://doi.org/10.1074/jbc.M209179200.

Hunt, M. *et al.* (2023) 'Multifaceted roles of mitochondria in wound healing and chronic wound pathogenesis', *Frontiers in Cell and Developmental Biology*, 11. Available at: https://doi.org/10.3389/FCELL.2023.1252318.

Huy, H. *et al.* (2018) 'TXNIP regulates AKT-mediated cellular senescence by direct interaction under glucose-mediated metabolic stress', *Aging cell*, 17(6). Available at: https://doi.org/10.1111/ACEL.12836.

Hwang, J.W. *et al.* (2013) 'Redox regulation of SIRT1 in inflammation and cellular senescence', *Free Radical Biology and Medicine*, 61, pp. 95–110. Available at: https://doi.org/10.1016/J.FREERADBIOMED.2013.03.015.

Iredale, J.P. *et al.* (1996) 'Tissue inhibitor of metalloproteinase-1 messenger RNA expression is enhanced relative to interstitial collagenase messenger RNA in experimental liver injury and fibrosis', *Hepatology*, 24(1), pp. 176–184. Available at: https://doi.org/10.1053/jhep.1996.v24.pm0008707259.

Ishiguro, S. *et al.* (2009) 'Basic fibroblast growth factor induces down-regulation of α-smooth muscle actin and reduction of myofibroblast areas in open skin wounds', *Wound Repair and Regeneration*, 17(4), pp. 617–625. Available at: https://doi.org/10.1111/j.1524-475X.2009.00511.x.

Itano, N. *et al.* (2002) 'Abnormal accumulation of hyaluronan matrix diminishes contact inhibition of cell growth and promotes cell migration', *Proceedings of the National Academy of Sciences of the United States of America*, 99(6), pp. 3609–3614. Available at: https://doi.org/10.1073/PNAS.052026799/ASSET/BA839DAB-B4B2-4943-B280-3C4A91CEE640/ASSETS/GRAPHIC/PQ0520267004.JPEG.

Ito, Y., Hoare, M. and Narita, M. (2017) 'Spatial and Temporal Control of Senescence', *Trends in Cell Biology*. Elsevier Ltd, pp. 820–832. Available at: https://doi.org/10.1016/j.tcb.2017.07.004.

Jackson, S.P. and Bartek, J. (2009) 'The DNA-damage response in human biology and disease', *Nature*, 461(7267), pp. 1071–1078. Available at: https://doi.org/10.1038/NATURE08467.

Jansen, R. *et al.* (2021) 'An integrative study of five biological clocks in somatic and mental health', *eLife*, 10, pp. 1–20. Available at: https://doi.org/10.7554/ELIFE.59479.

Januszyk, M. *et al.* (2014) 'Diabetes irreversibly depletes bone marrow-derived mesenchymal progenitor cell subpopulations', *Diabetes*, 63(9), pp. 3047–3056. Available at: https://doi.org/10.2337/DB13-1366/-/DC1.

Jeck, W.R., Siebold, A.P. and Sharpless, N.E. (2012) 'Review: a meta-analysis of GWAS and age-associated diseases', *Aging cell*, 11(5), pp. 727–731. Available at: https://doi.org/10.1111/J.1474-9726.2012.00871.X.

Jeon, O.H. *et al.* (2017) 'Local clearance of senescent cells attenuates the development of post-traumatic osteoarthritis and creates a pro-regenerative environment', *Nature medicine*, 23(6), pp. 775–781. Available at: https://doi.org/10.1038/NM.4324.

Ji, H. *et al.* (2014) 'Rho/Rock cross-talks with transforming growth factor-β/Smad pathway participates in lung fibroblast-myofibroblast differentiation', *Biomedical Reports*, 2(6), pp. 787–792. Available at: https://doi.org/10.3892/br.2014.323.

Jin, H. *et al.* (2019) 'Epithelial innate immunity mediates tubular cell senescence after kidney injury', *JCI insight*, 4(2). Available at: https://doi.org/10.1172/JCI.INSIGHT.125490.

Jing, H. *et al.* (2011) 'Opposing roles of NF-κB in anti-cancer treatment outcome unveiled by cross-species investigations', *Genes & development*, 25(20), pp. 2137–2146. Available at: https://doi.org/10.1101/GAD.17620611.

Jirouskova, M. *et al.* (2012) 'Hepatoprotective effect of MMP-19 deficiency in a mouse model of chronic liver fibrosis', *PloS one*, 7(10). Available at: https://doi.org/10.1371/JOURNAL.PONE.0046271.

Johmura, Y. and Nakanishi, M. (2016) 'Multiple facets of p53 in senescence induction and maintenance', *Cancer Science*, 107(11), p. 1550. Available at: https://doi.org/10.1111/CAS.13060.

Juhl, P. *et al.* (2020) 'Dermal fibroblasts have different extracellular matrix profiles induced by TGF-β, PDGF and IL-6 in a model for skin fibrosis', *Scientific Reports 2020 10:1*, 10(1), pp. 1–10. Available at: https://doi.org/10.1038/s41598-020-74179-6.

Jun, J. Il and Lau, L.F. (2010) 'The matricellular protein CCN1 induces fibroblast senescence and restricts fibrosis in cutaneous wound healing', *Nature Cell Biology*, 12(7), pp. 676–685. Available at: https://doi.org/10.1038/ncb2070.

Jun, J.I.I. and Lau, L.F. (2017) 'CCN2 induces cellular senescence in fibroblasts', *Journal of Cell Communication and Signaling*, 11(1), p. 15. Available at: https://doi.org/10.1007/S12079-016-0359-1.

Kadler, K.E., Hill, A. and Canty-Laird, E.G. (2008) 'Collagen fibrillogenesis: fibronectin, integrins, and minor collagens as organizers and nucleators.', *Current opinion in cell biology*, 20(5), pp. 495–501. Available at: https://doi.org/10.1016/j.ceb.2008.06.008.

Kale, A. *et al.* (2020) 'Role of immune cells in the removal of deleterious senescent cells', *Immunity & Ageing 2020 17:1*, 17(1), pp. 1–9. Available at: https://doi.org/10.1186/S12979-020-00187-9.

Kang, C. *et al.* (2015) 'The DNA damage response induces inflammation and senescence by inhibiting autophagy of GATA4', *Science (New York, N.Y.)*, 349(6255). Available at: https://doi.org/10.1126/SCIENCE.AAA5612.

Kang, C. (2019) 'Senolytics and Senostatics: A Two-Pronged Approach to Target Cellular Senescence for Delaying Aging and Age-Related Diseases', *Molecules and Cells*, 42(12), p. 821. Available at: https://doi.org/10.14348/MOLCELLS.2019.0298.

Kang, T.W. *et al.* (2011) 'Senescence surveillance of pre-malignant hepatocytes limits liver cancer development', *Nature*, 479(7374), pp. 547–551. Available at: https://doi.org/10.1038/NATURE10599.

Kaowinn, S. *et al.* (2018) 'STAT1-HDAC4 signaling induces epithelial-mesenchymal transition and sphere formation of cancer cells overexpressing the oncogene, CUG2', *Oncology Reports*, 40(5), p. 2619. Available at: https://doi.org/10.3892/OR.2018.6701.

Kapetanaki, M.G., Mora, A.L. and Rojas, M. (2013) 'Influence of age on wound healing and fibrosis', *The Journal of Pathology*, 229(2), pp. 310–322. Available at: https://doi.org/10.1002/path.4122.

Kato, K. *et al.* (2020) 'Impaired myofibroblast dedifferentiation contributes to nonresolving fibrosis in aging', *American Journal of Respiratory Cell and Molecular Biology*, 62(5), pp. 633–644. Available at: https://doi.org/10.1165/RCMB.2019-0092OC/SUPPL_FILE/DISCLOSURES.PDF.

Khan, S.Y. *et al.* (2017) 'Premature senescence of endothelial cells upon chronic exposure to TNFα can be prevented by N-acetyl cysteine and plumericin', *Scientific Reports 2017 7:1*, 7(1), pp. 1–13. Available at: https://doi.org/10.1038/srep39501.

Khanna, S. *et al.* (2010) 'Macrophage dysfunction impairs resolution of inflammation in the wounds of diabetic mice', *PloS one*, 5(3). Available at: https://doi.org/10.1371/JOURNAL.PONE.0009539.

Kihara, T., Ito, J. and Miyake, J. (2013) 'Measurement of Biomolecular Diffusion in Extracellular Matrix Condensed by Fibroblasts Using Fluorescence Correlation Spectroscopy', *PLoS ONE*, 8(11), p. 82382. Available at: https://doi.org/10.1371/JOURNAL.PONE.0082382.

Kim, M.C., Cui, F.J. and Kim, Y. (2013) 'Hydrogen peroxide promotes epithelial to mesenchymal transition and stemness in human malignant mesothelioma cells', *Asian Pacific journal of cancer prevention : APJCP*, 14(6), pp. 3625–3630. Available at: https://doi.org/10.7314/APJCP.2013.14.6.3625.

Kim, M.G. *et al.* (2019) 'Impact of aging on transition of acute kidney injury to chronic kidney disease', *Scientific reports*, 9(1). Available at: https://doi.org/10.1038/S41598-019-54585-1.

Kim, M.H. *et al.* (2008) 'Dynamics of Neutrophil Infiltration during Cutaneous Wound Healing and Infection Using Fluorescence Imaging', *The Journal of investigative dermatology*, 128(7), p. 1812. Available at: https://doi.org/10.1038/SJ.JID.5701223.

King, L.E. *et al.* (2022) 'Apoptotic priming is defined by the dynamic exchange of Bcl-2 proteins between mitochondria and cytosol', *Cell Death & Differentiation 2022 29:11*, 29(11), pp. 2262–2274. Available at: https://doi.org/10.1038/s41418-022-01013-z.

Kirkwood, T.B.L. (2005) 'Understanding the Odd Science of Aging', *Cell*, 120(4), pp. 437–447. Available at: https://doi.org/10.1016/J.CELL.2005.01.027.

Kirkwood, T.B.L. (2011) 'Systems biology of ageing and longevity', *Philosophical transactions of the Royal Society of London. Series B, Biological sciences*, 366(1561), pp. 64–70. Available at: https://doi.org/10.1098/rstb.2010.0275.

Kirschner, K. *et al.* (2020) 'Functional heterogeneity in senescence', *Biochemical Society Transactions*, 48(3), pp. 765–773. Available at: https://doi.org/10.1042/BST20190109.

Kitano, H. (2002) 'Computational systems biology', *Nature 2002 420:6912*, 420(6912), pp. 206–210. Available at: https://doi.org/10.1038/nature01254.

Kizilay Mancini, O. *et al.* (2022) 'Oxidative stress-induced senescence mediates inflammatory and fibrotic phenotypes in fibroblasts from systemic sclerosis patients', *Rheumatology*, 61(3), pp. 1265–1275. Available at: https://doi.org/10.1093/RHEUMATOLOGY/KEAB477.

Kolaczkowska, E. and Kubes, P. (2013) 'Neutrophil recruitment and function in health and inflammation', *Nature Reviews Immunology 2013 13:3*, 13(3), pp. 159–175. Available at: https://doi.org/10.1038/nri3399.

Krishnamurthy, J. *et al.* (2004) 'Ink4a/Arf expression is a biomarker of aging', *The Journal of clinical investigation*, 114(9), pp. 1299–1307. Available at: https://doi.org/10.1172/JCI22475.

Krizhanovsky, V. *et al.* (2008) 'Senescence of Activated Stellate Cells Limits Liver Fibrosis', *Cell*, 134(4), pp. 657–667. Available at: https://doi.org/10.1016/j.cell.2008.06.049.

Krzyszczyk, P. *et al.* (2018) 'The Role of Macrophages in Acute and Chronic Wound Healing and Interventions to Promote Pro-wound Healing Phenotypes', *Frontiers in Physiology*, 9(MAY), p. 419. Available at: https://doi.org/10.3389/FPHYS.2018.00419.

Kuehlmann, B. *et al.* (2020) 'Mechanotransduction in Wound Healing and Fibrosis', *Journal of Clinical Medicine*, 9(5), p. 1423. Available at: https://doi.org/10.3390/jcm9051423.

Kuilman, T. *et al.* (2008) 'Oncogene-induced senescence relayed by an interleukin-dependent inflammatory network', *Cell*, 133(6), pp. 1019–1031. Available at: https://doi.org/10.1016/J.CELL.2008.03.039.

Kulakovskiy, I. V. *et al.* (2018) 'HOCOMOCO: towards a complete collection of transcription factor binding models for human and mouse via large-scale ChIP-Seq analysis', *Nucleic Acids Research*, 46(D1), pp. D252–D259. Available at: https://doi.org/10.1093/NAR/GKX1106.

Kulkarni, A.A. *et al.* (2011) 'PPAR-γ Ligands Repress TGFβ-Induced Myofibroblast Differentiation by Targeting the PI3K/Akt Pathway: Implications for Therapy of Fibrosis', *PLoS ONE*. Edited by R.K. Aziz, 6(1), p. e15909. Available at: https://doi.org/10.1371/journal.pone.0015909.

Kumari, R. and Jat, P. (2021) 'Mechanisms of Cellular Senescence: Cell Cycle Arrest and Senescence Associated Secretory Phenotype', *Frontiers in Cell and Developmental Biology*, 9, p. 645593. Available at: https://doi.org/10.3389/FCELL.2021.645593/BIBTEX.

Kwang, S.K. *et al.* (2007) 'Induction of cellular senescence by insulin-like growth factor binding protein-5 through a p53-dependent mechanism', *Molecular biology of the cell*, 18(11), pp. 4543–4552. Available at: https://doi.org/10.1091/MBC.E07-03-0280.

Kyo, S. *et al.* (2000) 'Sp1 cooperates with c-Myc to activate transcription of the human telomerase reverse transcriptase gene (hTERT)', *Nucleic acids research*, 28(3), pp. 669–677. Available at: https://doi.org/10.1093/NAR/28.3.669.

Lacey, D.C. *et al.* (2012) 'Defining GM-CSF– and Macrophage-CSF–Dependent Macrophage Responses by In Vitro Models', *The Journal of Immunology*, 188(11), pp. 5752–5765. Available at: https://doi.org/10.4049/JIMMUNOL.1103426.

Lachowski, D. *et al.* (2019) 'Matrix stiffness modulates the activity of MMP-9 and TIMP-1 in hepatic stellate cells to perpetuate fibrosis', *Scientific Reports 2019 9:1*, 9(1), pp. 1–9. Available at: https://doi.org/10.1038/s41598-019-43759-6.

Lagnado, A. *et al.* (2021) 'Neutrophils induce paracrine telomere dysfunction and senescence in ROS-dependent manner', *The EMBO journal*, 40(9). Available at: https://doi.org/10.15252/EMBJ.2020106048.

Lau, L. *et al.* (2019) 'Uncoupling the Senescence-Associated Secretory Phenotype from Cell Cycle Exit via Interleukin-1 Inactivation Unveils Its Protumorigenic Role', *Molecular and cellular biology*, 39(12). Available at: https://doi.org/10.1128/MCB.00586-18.

Lauer, G. *et al.* (2000) 'Expression and proteolysis of vascular endothelial growth factor is increased in chronic wounds', *The Journal of investigative dermatology*, 115(1), pp. 12–18. Available at: https://doi.org/10.1046/J.1523-1747.2000.00036.X.

Lavoie, H., Gagnon, J. and Therrien, M. (2020) 'ERK signalling: a master regulator of cell behaviour, life and fate', *Nature reviews. Molecular cell biology*, 21(10), pp. 607–632. Available at: https://doi.org/10.1038/S41580-020-0255-7.

Lawrence, M. *et al.* (2013) 'Software for Computing and Annotating Genomic Ranges', *PLOS Computational Biology*, 9(8), p. e1003118. Available at: https://doi.org/10.1371/JOURNAL.PCBI.1003118.

Lawrence, M., Gentleman, R. and Carey, V. (2009) 'rtracklayer: an R package for interfacing with genome browsers', *Bioinformatics*, 25(14), pp. 1841–1842. Available at: https://doi.org/10.1093/BIOINFORMATICS/BTP328.

Lebleu, V.S. and Kalluri, R. (2011) 'Blockade of PDGF receptor signaling reduces myofibroblast number and attenuates renal fibrosis', *Kidney international*, 80(11), p. 1119. Available at: https://doi.org/10.1038/KI.2011.300.

Lee, S. and Schmitt, C.A. (2019) 'The dynamic nature of senescence in cancer', *Nature Cell Biology 2019 21:1*, 21(1), pp. 94–101. Available at: https://doi.org/10.1038/s41556-018-0249-2.

Lehallier, B. *et al.* (2019) 'Undulating changes in human plasma proteome profiles across the lifespan', *Nature medicine*, 25(12), pp. 1843–1850. Available at: https://doi.org/10.1038/S41591-019-0673-2.

Leinonen, R. *et al.* (2010) 'The Sequence Read Archive', *Nucleic Acids Research*, 39(suppl_1), pp. D19–D21. Available at: https://doi.org/10.1093/NAR/GKQ1019.

Lenaz, G. (1998) 'Role of mitochondria in oxidative stress and ageing', *Biochimica et Biophysica Acta (BBA) - Bioenergetics*, 1366(1–2), pp. 53–67. Available at: https://doi.org/10.1016/S0005-2728(98)00120-0.

Di Leonardo, A. *et al.* (1994) 'DNA damage triggers a prolonged p53-dependent G1 arrest and long-term induction of Cip1 in normal human fibroblasts', *Genes & development*, 8(21), pp. 2540–2551. Available at: https://doi.org/10.1101/GAD.8.21.2540.

Li, C. *et al.* (2021) 'Senolytic therapy ameliorates renal fibrosis postacute kidney injury by alleviating renal senescence', *FASEB journal : official publication of the Federation of American Societies for Experimental Biology*, 35(1). Available at: https://doi.org/10.1096/FJ.202001855RR.

Li, J. *et al.* (2018) 'Suppression of RRM2 inhibits cell proliferation, causes cell cycle arrest and promotes the apoptosis of human neuroblastoma cells and in human neuroblastoma RRM2 is suppressed following chemotherapy', *Oncology reports*, 40(1), pp. 355–360. Available at: https://doi.org/10.3892/OR.2018.6420.

Li, J., Chen, J. and Kirsner, R. (2007) 'Pathophysiology of acute wound healing', *Clinics in Dermatology*, 25(1), pp. 9–18. Available at: https://doi.org/10.1016/J.CLINDERMATOL.2006.09.007.

Li, J.F. and Lowengrub, J. (2014) 'The effects of cell compressibility, motility and contact inhibition on the growth of tumor cell clusters using the Cellular Potts Model', *Journal of Theoretical Biology*, 343, pp. 79–91. Available at: https://doi.org/10.1016/j.jtbi.2013.10.008.

Li, W. *et al.* (2009) 'The dependency of solute diffusion on molecular weight and shape in intact bone', *Bone*, 45(5), p. 1017. Available at: https://doi.org/10.1016/J.BONE.2009.07.076.

Li, W.Q., Dehnade, F. and Zafarullah, M. (2000) 'Thiol antioxidant, N-acetylcysteine, activates extracellular signal-regulated kinase signaling pathway in articular chondrocytes', *Biochemical and biophysical research communications*, 275(3), pp. 789–794. Available at: https://doi.org/10.1006/BBRC.2000.3385.

Limbad, C. *et al.* (2020) 'Astrocyte senescence promotes glutamate toxicity in cortical neurons', *PLoS ONE*, 15(1). Available at: https://doi.org/10.1371/JOURNAL.PONE.0227887.

Lindahl, P. *et al.* (1997) 'Pericyte loss and microaneurysm formation in PDGF-B-deficient mice', *Science (New York, N.Y.)*, 277(5323), pp. 242–245. Available at: https://doi.org/10.1126/SCIENCE.277.5323.242.

Lindahl, P. and Betsholtz, C. (1998) 'Not all myofibroblasts are alike: revisiting the role of PDGF-A and PDGF-B using PDGF-targeted mice', *Current opinion in nephrology and hypertension*, 7(1), pp. 21–26. Available at: https://doi.org/10.1097/00041552-199801000-00004.

Liu, A. *et al.* (2019) 'From expression footprints to causal pathways: contextualizing large signaling networks with CARNIVAL', *npj Systems Biology and Applications 2019 5:1*, 5(1), pp. 1–10. Available at: https://doi.org/10.1038/s41540-019-0118-z.

Liu, F. *et al.* (2015) 'Mechanosignaling through YAP and TAZ drives fibroblast activation and fibrosis', *American Journal of Physiology - Lung Cellular and Molecular Physiology*, 308(4), pp. L344–L357. Available at: https://doi.org/10.1152/ajplung.00300.2014.

Liu, G.H. *et al.* (2021) 'Aging Atlas: a multi-omics database for aging biology', *Nucleic Acids Research*, 49(D1), pp. D825–D830. Available at: https://doi.org/10.1093/NAR/GKAA894.

Liu, T. *et al.* (2022) 'PaintOmics 4: new tools for the integrative analysis of multi-omics datasets supported by multiple pathway databases', *Nucleic Acids Research*, 50(W1), pp. W551–W559. Available at: https://doi.org/10.1093/NAR/GKAC352.

Liu, Y. *et al.* (2013) 'Transforming growth factor-β (TGF-β)-mediated connective tissue growth factor (CTGF) expression in hepatic stellate cells requires Stat3 signaling activation', *Journal of Biological Chemistry*, 288(42), pp. 30708–30719. Available at: https://doi.org/10.1074/jbc.M113.478685.

Loots, M.A.M. *et al.* (1998) 'Differences in cellular infiltrate and extracellular matrix of chronic diabetic and venous ulcers versus acute wounds', *The Journal of investigative dermatology*, 111(5), pp. 850–857. Available at: https://doi.org/10.1046/J.1523-1747.1998.00381.X.

López-Otín, C. *et al.* (2013) 'The Hallmarks of Aging', *Cell*, 153(6), pp. 1194–1217. Available at: https://doi.org/10.1016/J.CELL.2013.05.039.

Love, M.I., Huber, W. and Anders, S. (2014) 'Moderated estimation of fold change and dispersion for RNA-seq data with DESeq2', *Genome Biology*, 15(12), p. 550. Available at: https://doi.org/10.1186/s13059-014-0550-8.

Lucas, T. *et al.* (2010) 'Differential Roles of Macrophages in Diverse Phases of Skin Repair', *The Journal of Immunology*, 184(7), pp. 3964–3977. Available at: https://doi.org/10.4049/JIMMUNOL.0903356.

Luetteke, N.C. *et al.* (1993) 'TGF alpha deficiency results in hair follicle and eye abnormalities in targeted and waved-1 mice', *Cell*, 73(2), pp. 263–278. Available at: https://doi.org/10.1016/0092-8674(93)90228-I.

Lujambio, A. *et al.* (2013) 'Non-cell-autonomous tumor suppression by p53', *Cell*, 153(2), pp. 449–460. Available at: https://doi.org/10.1016/j.cell.2013.03.020.

Luke, T.M. and Hexum, T.D. (2008a) 'UTP and ATP increase extracellular signal-regulated kinase 1/2 phosphorylation in bovine chromaffin cells through epidermal growth factor receptor transactivation', *Purinergic Signalling*, 4(4), p. 323. Available at: https://doi.org/10.1007/S11302-008-9098-Y.

Luke, T.M. and Hexum, T.D. (2008b) 'UTP and ATP increase extracellular signal-regulated kinase 1/2 phosphorylation in bovine chromaffin cells through epidermal growth factor receptor transactivation', *Purinergic Signalling*, 4(4), p. 323. Available at: https://doi.org/10.1007/S11302-008-9098-Y.

Maher, T.M. *et al.* (2010) 'Diminished prostaglandin E2 contributes to the apoptosis paradox in idiopathic pulmonary fibrosis', *American Journal of Respiratory and Critical Care Medicine*, 182(1), pp. 73–82. Available at: https://doi.org/10.1164/rccm.200905-0674OC.

Maini, P.K., Olsen, L. and Sherratt, J.A. (2002) 'MATHEMATICAL MODELS FOR CELL-MATRIX INTERACTIONS DURING DERMAL WOUND HEALING', *https://doi.org/10.1142/S0218127402005674*, 12(9), pp. 2021–2029. Available at: https://doi.org/10.1142/S0218127402005674.

Majeed, Y. *et al.* (2023) 'STAT1- and NFAT-independent amplification of purinoceptor function integrates cellular senescence with interleukin-6 production in preadipocytes', *British Journal of Pharmacology*, 180(5), pp. 609–627. Available at: https://doi.org/10.1111/BPH.15978.

Margalit, O. *et al.* (2006) 'BCL6 is regulated by p53 through a response element frequently disrupted in B-cell non-Hodgkin lymphoma', *Blood*, 107(4), pp. 1599–1607. Available at: https://doi.org/10.1182/BLOOD-2005-04-1629.

Mario Gonzalez-Meljem, J. *et al.* (2017) 'Stem cell senescence drives age-attenuated induction of pituitary tumours in mouse models of paediatric craniopharyngioma', *Nature communications*, 8(1). Available at: https://doi.org/10.1038/S41467-017-01992-5.

Martin, L., Schumacher, L. and Chandra, T. (2023) 'Modelling the dynamics of senescence spread', *Aging cell*, 22(8). Available at: https://doi.org/10.1111/ACEL.13892.

Martin, M. (2011) 'Cutadapt removes adapter sequences from high-throughput sequencing reads', *EMBnet.journal*, 17(1), p. 10. Available at: https://doi.org/10.14806/ej.17.1.200.

Martin, N. and Bernard, D. (2018) 'Calcium signaling and cellular senescence', *Cell Calcium*, 70, pp. 16–23. Available at: https://doi.org/10.1016/J.CECA.2017.04.001.

Masid, M., Ataman, M. and Hatzimanikatis, V. (2020) 'Analysis of human metabolism by reducing the complexity of the genome-scale models using redHUMAN', *Nature Communications 2020 11:1*, 11(1), pp. 1–12. Available at: https://doi.org/10.1038/s41467-020-16549-2.

Mastrantonio, R., You, H. and Tamagnone, L. (2021) 'Semaphorins as emerging clinical biomarkers and therapeutic targets in cancer', *Theranostics*, 11(7), p. 3262. Available at: https://doi.org/10.7150/THNO.54023.

Matsuda, S. *et al.* (2023) 'TGF-β in the microenvironment induces a physiologically occurring immune-suppressive senescent state', *Cell Reports*, 42(3). Available at: https://doi.org/10.1016/j.celrep.2023.112129.

Matsuya, K. *et al.* (2016) 'A Discrete Mathematical Model for Angiogenesis', *https://doi.org/10.1137/15M1038773*, 76(6), pp. 2243–2259. Available at: https://doi.org/10.1137/15M1038773.

Mavromatis, L.A. *et al.* (2023) 'Multi-omic underpinnings of epigenetic aging and human longevity', *Nature Communications 2023 14:1*, 14(1), pp. 1–15. Available at: https://doi.org/10.1038/s41467-023-37729-w.

Mc Auley, M.T. *et al.* (2012) 'A whole-body mathematical model of cholesterol metabolism and its age-associated dysregulation', *BMC Systems Biology*, 6, p. 130. Available at: https://doi.org/10.1186/1752-0509-6-130.

McAndrews, K.M. *et al.* (2022) 'Dermal αSMA+ myofibroblasts orchestrate skin wound repair via β1 integrin and independent of type I collagen production', *The EMBO Journal*, 41(7), p. e109470. Available at: https://doi.org/10.15252/EMBJ.2021109470.

McDougall, S. *et al.* (2006) 'Fibroblast migration and collagen deposition during dermal wound healing: Mathematical modelling and clinical implications', in *Philosophical Transactions of the Royal Society A: Mathematical, Physical and Engineering Sciences*. Royal Society, pp. 1385–1405. Available at: https://doi.org/10.1098/rsta.2006.1773.

McHugh, D. and Gil, J. (2018) 'Senescence and aging: Causes, consequences, and therapeutic avenues', *The Journal of Cell Biology*, 217(1), p. 65. Available at: https://doi.org/10.1083/JCB.201708092.

Medeiros Tavares Marques, J.C. *et al.* (2017) 'Identification of new genes associated to senescent and tumorigenic phenotypes in mesenchymal stem cells', *Scientific Reports 2017 7:1*, 7(1), pp. 1–13. Available at: https://doi.org/10.1038/s41598-017-16224-5.

Melk, A. *et al.* (2004) 'Expression of p16INK4a and other cell cycle regulator and senescence associated genes in aging human kidney', *Kidney international*, 65(2), pp. 510–520. Available at: https://doi.org/10.1111/J.1523-1755.2004.00438.X.

Melzer, D. *et al.* (2007) 'A common variant of the p16(INK4a) genetic region is associated with physical function in older people', *Mechanisms of ageing and development*, 128(5–6), pp. 370–377. Available at: https://doi.org/10.1016/J.MAD.2007.03.005.

Mendez, M. V. *et al.* (1998) 'Fibroblasts cultured from venous ulcers display cellular characteristics of senescence', *Journal of Vascular Surgery*, 28(5), pp. 876–883. Available at: https://doi.org/10.1016/S0741-5214(98)70064-3.

Mendez, M. V. *et al.* (1999) 'The proliferative capacity of neonatal skin fibroblasts is reduced after exposure to venous ulcer wound fluid: A potential mechanism for senescence in venous ulcers',

Journal of Vascular Surgery, 30(4), pp. 734–743. Available at: https://doi.org/10.1016/S0741-5214(99)70113-8.

Merks, R.M.H., Newman, S.A. and Glazier, J.A. (2004) 'Cell-oriented modeling of in vitro capillary development', *Lecture Notes in Computer Science (including subseries Lecture Notes in Artificial Intelligence and Lecture Notes in Bioinformatics)*, 3305, pp. 425–434. Available at: https://doi.org/10.1007/978-3-540-30479-1_44/COVER.

Meyer, D.H. and Schumacher, B. (2021) 'BiT age: A transcriptome-based aging clock near the theoretical limit of accuracy', *Aging cell*, 20(3). Available at: https://doi.org/10.1111/ACEL.13320.

Meyer, K. *et al.* (2016) 'Essential Role for Premature Senescence of Myofibroblasts in Myocardial Fibrosis', *Journal of the American College of Cardiology*, 67(17), pp. 2018–2028. Available at: https://doi.org/10.1016/j.jacc.2016.02.047.

Di Micco, R. *et al.* (2021) 'Cellular senescence in ageing: from mechanisms to therapeutic opportunities', *Nature reviews. Molecular cell biology*, 22(2), pp. 75–95. Available at: https://doi.org/10.1038/S41580-020-00314-W.

Midgley, A.C. *et al.* (2013) 'Transforming growth factor-β1 (TGF-β1)-stimulated fibroblast to myofibroblast differentiation is mediated by hyaluronan (HA)-facilitated epidermal growth factor receptor (EGFR) and CD44 co-localization in lipid rafts', *Journal of Biological Chemistry*, 288(21), pp. 14824–14838. Available at: https://doi.org/10.1074/jbc.M113.451336.

Mirza, R., DiPietro, L.A. and Koh, T.J. (2009) 'Selective and specific macrophage ablation is detrimental to wound healing in mice', *American Journal of Pathology*, 175(6), pp. 2454–2462. Available at: https://doi.org/10.2353/ajpath.2009.090248.

Miwa, S. *et al.* (2022) 'Mitochondrial dysfunction in cell senescence and aging', *The Journal of Clinical Investigation*, 132(13). Available at: https://doi.org/10.1172/JCI158447.

Mogensen, T.H. (2019) 'IRF and STAT transcription factors - From basic biology to roles in infection, protective immunity, and primary immunodeficiencies', *Frontiers in Immunology*, 10(JAN), p. 426889. Available at: https://doi.org/10.3389/FIMMU.2018.03047/BIBTEX.

Mognol, G.P. *et al.* (2016) 'Cell cycle and apoptosis regulation by NFAT transcription factors: new roles for an old player', *Cell Death & Disease*, 7(4), p. e2199. Available at: https://doi.org/10.1038/CDDIS.2016.97.

Moura, J. *et al.* (2017) 'Impaired T-cell differentiation in diabetic foot ulceration', *Cellular & molecular immunology*, 14(9), pp. 758–769. Available at: https://doi.org/10.1038/CMI.2015.116.

Moura, J. *et al.* (2019) 'Immune aging in diabetes and its implications in wound healing', *Clinical immunology (Orlando, Fla.)*, 200, p. 43. Available at: https://doi.org/10.1016/J.CLIM.2019.02.002.

Muñoz-Espín, D. *et al.* (2013) 'Programmed cell senescence during mammalian embryonic development', *Cell*, 155(5), p. 1104. Available at: https://doi.org/10.1016/J.CELL.2013.10.019.

Muñoz-Espín, D. and Serrano, M. (2014) 'Cellular senescence: from physiology to pathology', *Nature Reviews Molecular Cell Biology 2014 15:7*, 15(7), pp. 482–496. Available at: https://doi.org/10.1038/nrm3823.

Muppala, S. *et al.* (2019) 'YAP and TAZ are distinct effectors of corneal myofibroblast transformation', *Experimental Eye Research*, 180, pp. 102–109. Available at: https://doi.org/10.1016/j.exer.2018.12.009.

Murray, P.J. and Wynn, T.A. (2011) 'Protective and pathogenic functions of macrophage subsets', *Nature Reviews Immunology 2011 11:11*, 11(11), pp. 723–737. Available at: https://doi.org/10.1038/nri3073.

Mylonas, K.J. *et al.* (2021) 'Cellular senescence inhibits renal regeneration after injury in mice, with senolytic treatment promoting repair', *Science translational medicine*, 13(594). Available at: https://doi.org/10.1126/SCITRANSLMED.ABB0203.

Naesens, M. (2011) 'Replicative Senescence in Kidney Aging, Renal Disease, and Renal Transplantation', *Discovery Medicine*, 11(56), pp. 65–75.

Narzt, M.S. *et al.* (2021) 'Epilipidomics of Senescent Dermal Fibroblasts Identify Lysophosphatidylcholines as Pleiotropic Senescence-Associated Secretory Phenotype (SASP) Factors', *The Journal of investigative dermatology*, 141(4S), pp. 993-1006.e15. Available at: https://doi.org/10.1016/J.JID.2020.11.020.

Nelson, P. and Masel, J. (2017) 'Intercellular competition and the inevitability of multicellular aging', *Proceedings of the National Academy of Sciences of the United States of America*, 114(49), pp. 12982–12987. Available at: https://doi.org/10.1073/PNAS.1618854114/SUPPL_FILE/PNAS.201618854SI.PDF.

Ogrodnik, M. *et al.* (2017) 'Cellular senescence drives age-dependent hepatic steatosis', *Nature Communications 2017 8:1*, 8(1), pp. 1–12. Available at: https://doi.org/10.1038/ncomms15691.

Ogrodnik, M. *et al.* (2019) 'Obesity-Induced Cellular Senescence Drives Anxiety and Impairs Neurogenesis.', *Cell metabolism*, 29(5), p. 1233. Available at: https://doi.org/10.1016/j.cmet.2019.01.013.

Ohanna, M. *et al.* (2011) 'Senescent cells develop a PARP-1 and nuclear factor-κB-associated secretome (PNAS)', *Genes & Development*, 25(12), pp. 1245–1261. Available at: https://doi.org/10.1101/GAD.625811.

De Oliveira, S., Rosowski, E.E. and Huttenlocher, A. (2016) 'Neutrophil migration in infection and wound repair: going forward in reverse', *Nature reviews. Immunology*, 16(6), p. 378. Available at: https://doi.org/10.1038/NRI.2016.49.

Olsen, L., Sherratt, J.A. and Maini, P.K. (1995) 'A Mechanochemical Model for Adult Dermal Wound Contraction and the Permanence of the Contracted Tissue Displacement Profile', *Journal of Theoretical Biology*, 177(2), pp. 113–128. Available at: https://doi.org/10.1006/JTBI.1995.0230.

Onozuka, I. *et al.* (2011) 'Cholestatic liver fibrosis and toxin-induced fibrosis are exacerbated in matrix metalloproteinase-2 deficient mice', *Biochemical and biophysical research communications*, 406(1), pp. 134–140. Available at: https://doi.org/10.1016/J.BBRC.2011.02.012.

Ovadya, Y. *et al.* (2018) 'Impaired immune surveillance accelerates accumulation of senescent cells and aging', *Nature communications*, 9(1). Available at: https://doi.org/10.1038/S41467-018-07825-3.

Oyewole, A.O. *et al.* (2014) 'Comparing the effects of mitochondrial targeted and localized antioxidants with cellular antioxidants in human skin cells exposed to UVA and hydrogen

peroxide', *FASEB journal : official publication of the Federation of American Societies for Experimental Biology*, 28(1), pp. 485–494. Available at: https://doi.org/10.1096/FJ.13-237008.

Özcan, S. *et al.* (2016) 'Unbiased analysis of senescence associated secretory phenotype (SASP) to identify common components following different genotoxic stresses', *Aging*, 8(7), pp. 1316–1329. Available at: https://doi.org/10.18632/AGING.100971.

Palmer, A.K. *et al.* (2019) 'Cellular senescence: at the nexus between ageing and diabetes', *Diabetologia*, 62(10), p. 1835. Available at: https://doi.org/10.1007/S00125-019-4934-X.

Paluvai, H., Di Giorgio, E. and Brancolini, C. (2020) 'The Histone Code of Senescence', *Cells*, 9(2). Available at: https://doi.org/10.3390/CELLS9020466.

Pan, C.C. *et al.* (2023) 'Antagonizing the irreversible thrombomodulin-initiated proteolytic signaling alleviates age-related liver fibrosis via senescent cell killing', *Cell Research 2023 33:7*, 33(7), pp. 516–532. Available at: https://doi.org/10.1038/s41422-023-00820-4.

Pang, Z. *et al.* (2021) 'MetaboAnalyst 5.0: narrowing the gap between raw spectra and functional insights', *Nucleic Acids Research*, 49(W1), pp. W388–W396. Available at: https://doi.org/10.1093/NAR/GKAB382.

Pardali, K. *et al.* (2000) 'Role of Smad proteins and transcription factor Sp1 in p21Waf1/Cip1 regulation by transforming growth factor-β', *Journal of Biological Chemistry*, 275(38), pp. 29244–29256. Available at: https://doi.org/10.1074/jbc.M909467199.

Parimon, T. *et al.* (2020) 'Alveolar Epithelial Type II Cells as Drivers of Lung Fibrosis in Idiopathic Pulmonary Fibrosis', *International journal of molecular sciences*, 21(7). Available at: https://doi.org/10.3390/IJMS21072269.

Park, S.Y. *et al.* (2019) 'Epsilon-Globin HBE1 Enhances Radiotherapy Resistance by Down-Regulating BCL11A in Colorectal Cancer Cells', *Cancers*, 11(4). Available at: https://doi.org/10.3390/CANCERS11040498.

Parry, A.J. *et al.* (2018) 'NOTCH-mediated non-cell autonomous regulation of chromatin structure during senescence', *Nature Communications 2018 9:1*, 9(1), pp. 1–15. Available at: https://doi.org/10.1038/s41467-018-04283-9.

Pastar, I. *et al.* (2010) 'Attenuation of the transforming growth factor beta-signaling pathway in chronic venous ulcers', *Molecular medicine (Cambridge, Mass.)*, 16(3–4), pp. 92–101. Available at: https://doi.org/10.2119/MOLMED.2009.00149.

Patel, K. *et al.* (2021) 'TimiRGeN: R/Bioconductor package for time series microRNA-mRNA integration and analysis', *Bioinformatics (Oxford, England)*, 37(20), pp. 3604–3609. Available at: https://doi.org/10.1093/BIOINFORMATICS/BTAB377.

Patro, R. *et al.* (2017) 'Salmon provides fast and bias-aware quantification of transcript expression', *Nature Methods*, 14(4), pp. 417–419. Available at: https://doi.org/10.1038/nmeth.4197.

Peilin, W. *et al.* (2019) 'Directed elimination of senescent cells attenuates development of osteoarthritis by inhibition of c-IAP and XIAP', *Biochimica et biophysica acta. Molecular basis of disease*, 1865(10), pp. 2618–2632. Available at: https://doi.org/10.1016/J.BBADIS.2019.05.017.

Peirce, S.M., Van Gieson, E.J. and Skalak, T.C. (2004) 'Multicellular simulation predicts microvascular patterning and in silico tissue assembly', *The FASEB Journal*, 18(6), pp. 731–733. Available at: https://doi.org/10.1096/FJ.03-0933FJE.

Pen, I. and Flatt, T. (2021) 'Asymmetry, division of labour and the evolution of ageing in multicellular organisms', *Philosophical Transactions of the Royal Society B*, 376(1823). Available at: https://doi.org/10.1098/RSTB.2019.0729.

Pierce, G.F. *et al.* (1995) 'Detection of platelet-derived growth factor (PDGF)-AA in actively healing human wounds treated with recombinant PDGF-BB and absence of PDGF in chronic nonhealing wounds', *The Journal of clinical investigation*, 96(3), pp. 1336–1350. Available at: https://doi.org/10.1172/JCI118169.

Pinu, F.R. *et al.* (2019) 'Systems Biology and Multi-Omics Integration: Viewpoints from the Metabolomics Research Community', *Metabolites*, 9(4). Available at: https://doi.org/10.3390/METABO9040076.

Pleyer, J. and Fleck, C. (2023) 'Agent-based models in cellular systems', *Frontiers in Physics*, 10, p. 968409. Available at: https://doi.org/10.3389/FPHY.2022.968409/BIBTEX.

Prata, L.G.P.L. *et al.* (2018) 'Senescent cell clearance by the immune system: Emerging therapeutic opportunities', *Seminars in immunology*, 40. Available at: https://doi.org/10.1016/J.SMIM.2019.04.003.

Prattichizzo, F. *et al.* (2018) 'Short-term sustained hyperglycaemia fosters an archetypal senescence-associated secretory phenotype in endothelial cells and macrophages', *Redox biology*, 15, pp. 170–181. Available at: https://doi.org/10.1016/J.REDOX.2017.12.001.

Psaroudis, R.T. *et al.* (2022) 'CD26 is a senescence marker associated with reduced immunopotency of human adipose tissue-derived multipotent mesenchymal stromal cells', *Stem Cell Research and Therapy*, 13(1), pp. 1–10. Available at: https://doi.org/10.1186/S13287-022-03026-4/FIGURES/5.

Pulido, T., Velarde, M.C. and Alimirah, F. (2021) 'The senescence-associated secretory phenotype: Fueling a wound that never heals', *Mechanisms of Ageing and Development*, 199, p. 111561. Available at: https://doi.org/10.1016/J.MAD.2021.111561.

Qi, L. *et al.* (2023) 'CEBPB regulates the migration, invasion and EMT of breast cancer cells by inhibiting THBS2 expression and O-fucosylation', *Human molecular genetics*, 32(11), pp. 1850–1863. Available at: https://doi.org/10.1093/HMG/DDAD022.

Radzvilavicius, A.L. *et al.* (2016) 'Selection for Mitochondrial Quality Drives Evolution of the Germline', *PLOS Biology*, 14(12), p. e2000410. Available at: https://doi.org/10.1371/JOURNAL.PBIO.2000410.

Ramachandran, P. *et al.* (2019) 'Resolving the fibrotic niche of human liver cirrhosis at single cell level', *Nature*, 575(7783), p. 512. Available at: https://doi.org/10.1038/S41586-019-1631-3.

Rattanavirotkul, N., Kirschner, K. and Chandra, T. (2021) 'Induction and transmission of oncogene-induced senescence', *Cellular and Molecular Life Sciences*, 78(3), pp. 843–852. Available at: https://doi.org/10.1007/S00018-020-03638-0/FIGURES/3.

Rawlings, T.M. *et al.* (2021) 'Modelling the impact of decidual senescence on embryo implantation in human endometrial assembloids', *eLife*, 10. Available at: https://doi.org/10.7554/ELIFE.69603.

Razdan, N., Vasilopoulos, T. and Herbig, U. (2018) 'Telomere dysfunction promotes transdifferentiation of human fibroblasts into myofibroblasts', *Aging cell*, 17(6). Available at: https://doi.org/10.1111/ACEL.12838.

Van Riggelen, J. and Felsher, D.W. (2010) 'Myc and a Cdk2 senescence switch', *Nature Cell Biology 2010 12:1*, 12(1), pp. 7–9. Available at: https://doi.org/10.1038/ncb0110-7.

Ritchie, M.E. *et al.* (2015) 'limma powers differential expression analyses for RNA-sequencing and microarray studies', *Nucleic acids research* [Preprint]. Available at: https://doi.org/10.1093/nar/gkv007.

Ritschka, B. *et al.* (2017) 'The senescence-associated secretory phenotype induces cellular plasticity and tissue regeneration', *Genes and Development*, 31(2), pp. 172–183. Available at: https://doi.org/10.1101/GAD.290635.116/-/DC1.

Ritschka, B. *et al.* (2020) 'The senotherapeutic drug ABT-737 disrupts aberrant p21 expression to restore liver regeneration in adult mice', *Genes & development*, 34(7–8), pp. 489–494. Available at: https://doi.org/10.1101/GAD.332643.119.

Rodier, F. *et al.* (2009) 'Persistent DNA damage signalling triggers senescence-associated inflammatory cytokine secretion', *Nature cell biology*, 11(8), pp. 973–979. Available at: https://doi.org/10.1038/NCB1909.

Rodrigues, M. *et al.* (2019) 'Wound healing: A cellular perspective', *Physiological Reviews*, 99(1), pp. 665–706. Available at: https://doi.org/10.1152/physrev.00067.2017.

Rognoni, E. *et al.* (2018) 'Fibroblast state switching orchestrates dermal maturation and wound healing', *Molecular Systems Biology*, 14(8). Available at: https://doi.org/10.15252/msb.20178174.

Rufini, A. *et al.* (2013) 'Senescence and aging: the critical roles of p53', *Oncogene 2013 32:43*, 32(43), pp. 5129–5143. Available at: https://doi.org/10.1038/onc.2012.640.

Ruscetti, M. *et al.* (2018) 'NK cell-mediated cytotoxicity contributes to tumor control by a cytostatic drug combination', *Science (New York, N.Y.)*, 362(6421), pp. 1416–1422. Available at: https://doi.org/10.1126/SCIENCE.AAS9090.

Rutledge, J., Oh, H. and Wyss-Coray, T. (2022) 'Measuring biological age using omics data', *Nature Reviews Genetics 2022*, pp. 1–13. Available at: https://doi.org/10.1038/s41576-022-00511-7.

Saitou, T. *et al.* (2012) 'Mathematical modeling of invadopodia formation', *Journal of Theoretical Biology*, 298, pp. 138–146. Available at: https://doi.org/10.1016/j.jtbi.2011.12.018.

Salotti, J. and Johnson, P.F. (2019) 'Regulation of senescence and the SASP by the transcription factor C/EBPβ', *Experimental Gerontology*, 128, p. 110752. Available at: https://doi.org/10.1016/J.EXGER.2019.110752.

Samdavid Thanapaul, R.J.R. *et al.* (2022) 'Elevated skin senescence in young mice causes delayed wound healing', *GeroScience*, 44(3), pp. 1871–1878. Available at: https://doi.org/10.1007/S11357-022-00551-1.

Sanada, F. *et al.* (2018) 'IGF Binding Protein-5 Induces Cell Senescence', *Frontiers in Endocrinology*, 9(FEB), p. 1. Available at: https://doi.org/10.3389/FENDO.2018.00053.

Sanders, Y.Y. *et al.* (2013) 'Histone Modifications in Senescence-Associated Resistance to Apoptosis by Oxidative Stress', *Redox Biology*, 1(1), pp. 8–16. Available at: https://doi.org/10.1016/J.REDOX.2012.11.004.

Sanghi, A. *et al.* (2021) 'Chromatin accessibility associates with protein-RNA correlation in human cancer', *Nature Communications 2021 12:1*, 12(1), pp. 1–14. Available at: https://doi.org/10.1038/s41467-021-25872-1.

Savill, N.J. and Sherratt, J.A. (2003) 'Control of epidermal stem cell clusters by Notch-mediated lateral induction', *Developmental Biology*, 258(1), pp. 141–153. Available at: https://doi.org/10.1016/S0012-1606(03)00107-6.

Schafer, M.J. *et al.* (2017) 'Cellular senescence mediates fibrotic pulmonary disease', *Nature Communications*, 8. Available at: https://doi.org/10.1038/ncomms14532.

Schnabl, B. *et al.* (2001) 'The role of Smad3 in mediating mouse hepatic stellate cell activation', *Hepatology*, 34(1), pp. 89–100. Available at: https://doi.org/10.1053/jhep.2001.25349.

Schubert, M. *et al.* (2018) 'Perturbation-response genes reveal signaling footprints in cancer gene expression', *Nature Communications 2017 9:1*, 9(1), pp. 1–11. Available at: https://doi.org/10.1038/s41467-017-02391-6.

Scianna, M. (2015) 'An extended Cellular Potts Model analyzing a wound healing assay', *Computers in Biology and Medicine*, 62, pp. 33–54. Available at: https://doi.org/10.1016/j.compbiomed.2015.04.009.

Scianna, M., Bassino, E. and Munaron, L. (2015) 'A cellular Potts model analyzing differentiated cell behavior during in vivo vascularization of a hypoxic tissue', *Computers in Biology and Medicine*, 63, pp. 143–156. Available at: https://doi.org/10.1016/J.COMPBIOMED.2015.05.020.

Seppa, H. *et al.* (1982) 'Platelet-derived growth factor in chemotactic for fibroblasts', *The Journal of cell biology*, 92(2), pp. 584–588. Available at: https://doi.org/10.1083/JCB.92.2.584.

Serezani, A.P.M. *et al.* (2022) 'Multiplatform Single-Cell Analysis Identifies Immune Cell Types Enhanced in Pulmonary Fibrosis', *American journal of respiratory cell and molecular biology*, 67(1), pp. 50–60. Available at: https://doi.org/10.1165/RCMB.2021-0418OC.

Severino, V. *et al.* (2013) 'Insulin-like growth factor binding proteins 4 and 7 released by senescent cells promote premature senescence in mesenchymal stem cells', *Cell Death & Disease 2013 4:11*, 4(11), pp. e911–e911. Available at: https://doi.org/10.1038/cddis.2013.445.

Shabestani Monfared, G., Ertl, P. and Rothbauer, M. (2020) 'An on-chip wound healing assay fabricated by xurography for evaluation of dermal fibroblast cell migration and wound closure', *Scientific Reports*, 10(1), p. 16192. Available at: https://doi.org/10.1038/s41598-020-73055-7.

Shapiro, S.D., Kobayashi, D.K. and Ley, T.J. (1993) 'Cloning and characterization of a unique elastolytic metalloproteinase produced by human alveolar macrophages.', *Journal of Biological Chemistry*, 268(32), pp. 23824–23829. Available at: https://doi.org/10.1016/S0021-9258(20)80459-1.

Sherratt, J.A. and Murray, J.D. (1990) 'Models of epidermal wound healing', *Proceedings of the Royal Society of London. Series B: Biological Sciences*, 241(1300), pp. 29–36. Available at: https://doi.org/10.1098/RSPB.1990.0061.

Shi, Y. *et al.* (2015) 'Wnt and Notch signaling pathway involved in wound healing by targeting c-Myc and Hes1 separately', *Stem Cell Research & Therapy*, 6(1). Available at: https://doi.org/10.1186/S13287-015-0103-4.

Shibamoto, M. *et al.* (2019) 'Activation of DNA Damage Response and Cellular Senescence in Cardiac Fibroblasts Limit Cardiac Fibrosis After Myocardial Infarction', *International heart journal*, 60(4), pp. 944–957. Available at: https://doi.org/10.1536/IHJ.18-701.

Shvarts, A. *et al.* (2002) 'A senescence rescue screen identifies BCL6 as an inhibitor of anti-proliferative p19(ARF)-p53 signaling', *Genes & development*, 16(6), pp. 681–686. Available at: https://doi.org/10.1101/GAD.929302.

da Silva, P.F.L. *et al.* (2019) 'The bystander effect contributes to the accumulation of senescent cells in vivo', *Aging Cell*, 18(1), p. e12848. Available at: https://doi.org/10.1111/ACEL.12848.

Sindrilaru, A. *et al.* (2011) 'An unrestrained proinflammatory M1 macrophage population induced by iron impairs wound healing in humans and mice', *The Journal of clinical investigation*, 121(3), pp. 985–997. Available at: https://doi.org/10.1172/JCI44490.

Singer, A.J. and Clark, R.A.F. (1999) 'Cutaneous wound healing', *The New England journal of medicine*. Edited by F.H. Epstein, 341(10), pp. 738–746. Available at: https://doi.org/10.1056/NEJM199909023411006.

Singh, P. *et al.* (2023) 'Taurine deficiency as a driver of aging', *Science*, 380(6649). Available at: https://doi.org/10.1126/SCIENCE.ABN9257/SUPPL_FILE/SCIENCE.ABN9257_MDAR_REPRODUCIBILITY_CHECKLIST.PDF.

Singh, V. *et al.* (2011) 'Effect of TGFβ and PDGF-B blockade on corneal myofibroblast development in mice', *Experimental Eye Research*, 93(6), pp. 810–817. Available at: https://doi.org/10.1016/J.EXER.2011.09.012.

Skalli, O. *et al.* (1986) 'A monoclonal antibody against α-smooth muscle actin: A new probe for smooth muscle differentiation', *Journal of Cell Biology*, 103(6), pp. 2787–2796. Available at: https://doi.org/10.1083/jcb.103.6.2787.

Smit, M.A. and Peeper, D.S. (2010) 'Epithelial-mesenchymal transition and senescence: two cancer-related processes are crossing paths', *Aging (Albany NY)*, 2(10), p. 735. Available at: https://doi.org/10.18632/AGING.100209.

Snezhkina, A. V. *et al.* (2020) 'ROS generation and antioxidant defense systems in normal and malignant cells', *Oxidative Medicine and Cellular Longevity*, 2019. Available at: https://doi.org/10.1155/2019/6175804.

Socci, L. *et al.* (2007) 'An axisymmetric computational model of skin expansion and growth', *Biomechanics and modeling in mechanobiology*, 6(3), pp. 177–188. Available at: https://doi.org/10.1007/S10237-006-0047-9.

Soneson, C., Love, M.I. and Robinson, M.D. (2016) 'Differential analyses for RNA-seq: transcript-level estimates improve gene-level inferences', *F1000Research 2016 4:1521*, 4, p. 1521. Available at: https://doi.org/10.12688/f1000research.7563.2.

Song, Q. *et al.* (2022) 'Integrated multi-omics approach revealed cellular senescence landscape', *Nucleic Acids Research*, 50(19), pp. 10947–10963. Available at: https://doi.org/10.1093/NAR/GKAC885.

Sprenger, H.G. *et al.* (2021) 'Cellular pyrimidine imbalance triggers mitochondrial DNA–dependent innate immunity', *Nature Metabolism 2021 3:5*, 3(5), pp. 636–650. Available at: https://doi.org/10.1038/s42255-021-00385-9.

Sreedhar, A., Aguilera-Aguirre, L. and Singh, K.K. (2020) 'Mitochondria in skin health, aging, and disease', *Cell Death & Disease*, 11(6). Available at: https://doi.org/10.1038/S41419-020-2649-Z.

Stacey, M.C. *et al.* (2019) 'Evaluation of wound fluid biomarkers to determine healing in adults with venous leg ulcers: A prospective study', *Wound Repair and Regeneration*, 27(5), pp. 509–518. Available at: https://doi.org/10.1111/WRR.12723.

Stanley, A. and Osler, T. (2001) 'Senescence and the healing rates of venous ulcers', *Journal of Vascular Surgery*, 33(6), pp. 1206–1211. Available at: https://doi.org/10.1067/MVA.2001.115379.

Stegenga, M.E. *et al.* (2008) 'Effect of acute hyperglycaemia and/or hyperinsulinaemia on proinflammatory gene expression, cytokine production and neutrophil function in humans', *Diabetic medicine : a journal of the British Diabetic Association*, 25(2), pp. 157–164. Available at: https://doi.org/10.1111/J.1464-5491.2007.02348.X.

Stojadinovic, O. *et al.* (2005) 'Molecular Pathogenesis of Chronic Wounds : The Role of β-Catenin and c-myc in the Inhibition of Epithelialization and Wound Healing', *The American Journal of Pathology*, 167(1), p. 59. Available at: https://doi.org/10.1016/S0002-9440(10)62953-7.

Stojadinovic, O. *et al.* (2008) 'Deregulation of keratinocyte differentiation and activation: a hallmark of venous ulcers', *Journal of cellular and molecular medicine*, 12(6B), pp. 2675–2690. Available at: https://doi.org/10.1111/J.1582-4934.2008.00321.X.

Stojadinovic, O. *et al.* (2014) 'Deregulation of epidermal stem cell niche contributes to pathogenesis of nonhealing venous ulcers', *Wound repair and regeneration : official publication of the Wound Healing Society [and] the European Tissue Repair Society*, 22(2), pp. 220–227. Available at: https://doi.org/10.1111/WRR.12142.

Storer, M. *et al.* (2013) 'Senescence is a developmental mechanism that contributes to embryonic growth and patterning', *Cell*, 155(5), p. 1119. Available at: https://doi.org/10.1016/J.CELL.2013.10.041.

Stout, R. and Birch-Machin, M. (2019) 'Mitochondria's Role in Skin Ageing', *Biology*, 8(2). Available at: https://doi.org/10.3390/BIOLOGY8020029.

Subramanian, A. *et al.* (2005) 'Gene set enrichment analysis: A knowledge-based approach for interpreting genome-wide expression profiles', *Proceedings of the National Academy of Sciences of the United States of America*, 102(43), pp. 15545–15550. Available at: https://doi.org/10.1073/PNAS.0506580102/SUPPL_FILE/06580FIG7.JPG.

Subramanian, I. *et al.* (2020) 'Multi-omics Data Integration, Interpretation, and Its Application', *Bioinformatics and Biology Insights*, 14. Available at: https://doi.org/10.1177/1177932219899051.

Sun, D. and Buttitta, L. (2017) 'States of G0 and the proliferation-quiescence decision in cells, tissues and during development', *The International journal of developmental biology*, 61(6–7), pp. 357–366. Available at: https://doi.org/10.1387/IJDB.160343LB.

Sun, T. *et al.* (2009) 'Exploring hypotheses of the actions of TGF-beta1 in epidermal wound healing using a 3D computational multiscale model of the human epidermis', *PloS one*, 4(12). Available at: https://doi.org/10.1371/JOURNAL.PONE.0008515.

Swat, M.H. *et al.* (2012) 'Multi-Scale Modeling of Tissues Using CompuCell3D', in *Methods in Cell Biology*. Academic Press Inc., pp. 325–366. Available at: https://doi.org/10.1016/B978-0-12-388403-9.00013-8.

Swat, M.H. *et al.* (2015) 'Emergent stratification in solid tumors selects for reduced cohesion of tumor cells: A multi-cell, virtual-tissue model of tumor evolution using CompuCell3D', *PLoS ONE*, 10(6), p. e0127972. Available at: https://doi.org/10.1371/journal.pone.0127972.

Swift, M.E. *et al.* (2001) 'Age-related alterations in the inflammatory response to dermal injury', *The Journal of investigative dermatology*, 117(5), pp. 1027–1035. Available at: https://doi.org/10.1046/J.0022-202X.2001.01539.X.

Swindall, A.F., Stanley, J.A. and Yang, E.S. (2013) 'PARP-1: Friend or Foe of DNA Damage and Repair in Tumorigenesis?', *Cancers 2013, Vol. 5, Pages 943-958*, 5(3), pp. 943–958. Available at: https://doi.org/10.3390/CANCERS5030943.

Szathmáry, E. and Smith, J.M. (1995) 'The major evolutionary transitions', *Nature 1995 374:6519*, 374(6519), pp. 227–232. Available at: https://doi.org/10.1038/374227a0.

Szklarczyk, D. *et al.* (2016) 'STITCH 5: augmenting protein-chemical interaction networks with tissue and affinity data', *Nucleic acids research*, 44(D1), pp. D380–D384. Available at: https://doi.org/10.1093/NAR/GKV1277.

Takeda, K. *et al.* (1994) 'Decreased Collagenase Expression in Cultured Systemic Sclerosis Fibroblasts', *Journal of Investigative Dermatology*, 103(3), pp. 359–363. Available at: https://doi.org/10.1111/1523-1747.EP12394936.

Tasdemir, N. *et al.* (2016) 'BRD4 Connects Enhancer Remodeling to Senescence Immune Surveillance', *Cancer discovery*, 6(6), pp. 613–629. Available at: https://doi.org/10.1158/2159-8290.CD-16-0217.

Teo, Y.V. *et al.* (2019) 'Notch Signaling Mediates Secondary Senescence', *Cell Reports*, 27(4), pp. 997-1007.e5. Available at: https://doi.org/10.1016/j.celrep.2019.03.104.

Tomasek, J.J. *et al.* (2002) 'Myofibroblasts and mechano: Regulation of connective tissue remodelling', *Nature Reviews Molecular Cell Biology*, pp. 349–363. Available at: https://doi.org/10.1038/nrm809.

Tominaga, K. and Suzuki, H.I. (2019) 'TGF-β Signaling in Cellular Senescence and Aging-Related Pathology', *International Journal of Molecular Sciences 2019, Vol. 20, Page 5002*, 20(20), p. 5002. Available at: https://doi.org/10.3390/IJMS20205002.

Tranquillo, R.T. and Murray, J.D. (1992) 'Continuum model of fibroblast-driven wound contraction: Inflammation-mediation', *Journal of Theoretical Biology*, 158(2), pp. 135–172. Available at: https://doi.org/10.1016/S0022-5193(05)80715-5.

Trojanowska, M. (2008) 'Role of PDGF in fibrotic diseases and systemic sclerosis', *Rheumatology*, 47(suppl_5), pp. v2–v4. Available at: https://doi.org/10.1093/RHEUMATOLOGY/KEN265.

Türei, D., Korcsmáros, T. and Saez-Rodriguez, J. (2016) 'OmniPath: guidelines and gateway for literature-curated signaling pathway resources', *Nature Methods 2016 13:12*, 13(12), pp. 966–967. Available at: https://doi.org/10.1038/nmeth.4077.

Uekita, T. *et al.* (2001) 'Cytoplasmic tail–dependent internalization of membrane-type 1 matrix metalloproteinase is important for its invasion-promoting activity', *The Journal of Cell Biology*, 155(7), p. 1345. Available at: https://doi.org/10.1083/JCB.200108112.

Uemura, M. *et al.* (2005) 'Smad2 and Smad3 play different roles in rat hepatic stellate cell function and α-smooth muscle actin organization', *Molecular Biology of the Cell*, 16(9), pp. 4214–4224. Available at: https://doi.org/10.1091/mbc.E05-02-0149.

Urciuolo, F. *et al.* (2022) 'Bioengineered Wound Healing Skin Models: The Role of Immune Response and Endogenous ECM to Fully Replicate the Dynamic of Scar Tissue Formation In Vitro',

Bioengineering 2022, Vol. 9, Page 233, 9(6), p. 233. Available at: https://doi.org/10.3390/BIOENGINEERING9060233.

Uxa, S. *et al.* (2021) 'Ki-67 gene expression', *Cell Death & Differentiation 2021 28:12*, 28(12), pp. 3357–3370. Available at: https://doi.org/10.1038/s41418-021-00823-x.

Uyar, B. *et al.* (2020) 'Single-cell analyses of aging, inflammation and senescence', *Ageing research reviews*, 64. Available at: https://doi.org/10.1016/J.ARR.2020.101156.

Valentijn, F.A. *et al.* (2018) 'Cellular senescence in the aging and diseased kidney', *Journal of cell communication and signaling*, 12(1), pp. 69–82. Available at: https://doi.org/10.1007/S12079-017-0434-2.

Vannella, K.M. and Wynn, T.A. (2017) 'Mechanisms of Organ Injury and Repair by Macrophages', *Annual review of physiology*, 79, pp. 593–617. Available at: https://doi.org/10.1146/ANNUREV-PHYSIOL-022516-034356.

Väremo, L., Nielsen, J. and Nookaew, I. (2013) 'Enriching the gene set analysis of genome-wide data by incorporating directionality of gene expression and combining statistical hypotheses and methods', *Nucleic Acids Research*, 41(8), pp. 4378–4391. Available at: https://doi.org/10.1093/NAR/GKT111.

Varney, S.D. *et al.* (2016) 'Hic-5 is required for myofibroblast differentiation by regulating mechanically dependent MRTF-A nuclear accumulation', *Journal of Cell Science*, 129(4), pp. 774–787. Available at: https://doi.org/10.1242/jcs.170589.

Velten, B. *et al.* (2022) 'Identifying temporal and spatial patterns of variation from multimodal data using MEFISTO', *Nature Methods 2022 19:2*, 19(2), pp. 179–186. Available at: https://doi.org/10.1038/s41592-021-01343-9.

Volk, S.W. *et al.* (2011) 'Diminished Type III Collagen Promotes Myofibroblast Differentiation and Increases Scar Deposition in Cutaneous Wound Healing', *Cells Tissues Organs*, 194(1), pp. 25–37. Available at: https://doi.org/10.1159/000322399.

Wagner, W. *et al.* (2008) 'Replicative Senescence of Mesenchymal Stem Cells: A Continuous and Organized Process', *PLoS ONE*, 3(5). Available at: https://doi.org/10.1371/JOURNAL.PONE.0002213.

Wajapeyee, N. *et al.* (2008) 'Oncogenic BRAF Induces Senescence and Apoptosis through Pathways Mediated by the Secreted Protein IGFBP7', *Cell*, 132(3), pp. 363–374. Available at: https://doi.org/10.1016/j.cell.2007.12.032.

Walaszczyk, A. *et al.* (2019) 'Pharmacological clearance of senescent cells improves survival and recovery in aged mice following acute myocardial infarction', *Aging cell*, 18(3). Available at: https://doi.org/10.1111/ACEL.12945.

Wallace, H.J. and Stacey, M.C. (1998) 'Levels of tumor necrosis factor-alpha (TNF-alpha) and soluble TNF receptors in chronic venous leg ulcers--correlations to healing status', *The Journal of investigative dermatology*, 110(3), pp. 292–296. Available at: https://doi.org/10.1046/J.1523-1747.1998.00113.X.

Wang, Q. *et al.* (2022) 'Exploring Epigenomic Datasets by ChIPseeker', *Current Protocols*, 2(10), p. e585. Available at: https://doi.org/10.1002/CPZ1.585.

Wang, V.Y.F. *et al.* (2017) 'Bcl3 phosphorylation by Akt, Erk2 and IKK is required for its transcriptional activity', *Molecular cell*, 67(3), p. 484. Available at: https://doi.org/10.1016/J.MOLCEL.2017.06.011.

Wang, X. *et al.* (2019) 'Induction of Fibroblast Senescence During Mouse Corneal Wound Healing', *Investigative ophthalmology & visual science*, 60(10), pp. 3669–3679. Available at: https://doi.org/10.1167/IOVS.19-26983.

Wang, Z. and Shi, C. (2020) 'Cellular senescence is a promising target for chronic wounds: a comprehensive review', *Burns & Trauma*, 8. Available at: https://doi.org/10.1093/burnst/tkaa021.

Waters, D.W. *et al.* (2019) 'STAT3 regulates the onset of oxidant-induced senescence in lung fibroblasts', *American Journal of Respiratory Cell and Molecular Biology*, 61(1), pp. 61–73. Available at: https://doi.org/10.1165/RCMB.2018-0328OC/SUPPL_FILE/DISCLOSURES.PDF.

Wiley, C.D. *et al.* (2017) 'Analysis of individual cells identifies cell-to-cell variability following induction of cellular senescence', *Aging Cell*, 16(5), pp. 1043–1050. Available at: https://doi.org/10.1111/ACEL.12632.

Wilkinson, H.N. and Hardman, M.J. (2020) 'Wound healing: cellular mechanisms and pathological outcomes: Cellular Mechanisms of Wound Repair', *Open Biology*, 10(9). Available at: https://doi.org/10.1098/RSOB.200223/.

Willforss, J., Chawade, A. and Levander, F. (2019) 'NormalyzerDE: Online Tool for Improved Normalization of Omics Expression Data and High-Sensitivity Differential Expression Analysis', *Journal of Proteome Research*, 18(2), pp. 732–740. Available at: https://doi.org/10.1021/ACS.JPROTEOME.8B00523/SUPPL_FILE/PR8B00523_SI_010.ZIP.

Willis-Martinez, D. *et al.* (2010) 'Role of HDAC1 in senescence, aging, and cancer', *Experimental gerontology*, 45(4), p. 279. Available at: https://doi.org/10.1016/J.EXGER.2009.10.001.

Witte, M.B. and Barbul, A. (1997) 'General principles of wound healing', *Surgical Clinics of North America*, 77(3), pp. 509–528. Available at: https://doi.org/10.1016/S0039-6109(05)70566-1.

Wolstein, J.M. *et al.* (2010a) 'INK4a knockout mice exhibit increased fibrosis under normal conditions and in response to unilateral ureteral obstruction', *American Journal of Physiology - Renal Physiology*, 299(6), pp. 1486–1495. Available at: https://doi.org/10.1152/AJPRENAL.00378.2010/ASSET/IMAGES/LARGE/ZH20121060830009.JPEG.

Wolstein, J.M. *et al.* (2010b) 'INK4a knockout mice exhibit increased fibrosis under normal conditions and in response to unilateral ureteral obstruction', *American journal of physiology. Renal physiology*, 299(6). Available at: https://doi.org/10.1152/AJPRENAL.00378.2010.

Woodcock, H. V. *et al.* (2019) 'The mTORC1/4E-BP1 axis represents a critical signaling node during fibrogenesis', *Nature Communications*, 10(1). Available at: https://doi.org/10.1038/s41467-018-07858-8.

Wu, C.H. *et al.* (2007) 'Cellular senescence is an important mechanism of tumor regression upon c-Myc inactivation', *Proceedings of the National Academy of Sciences of the United States of*

America, 104(32), pp. 13028–13033. Available at: https://doi.org/10.1073/PNAS.0701953104/SUPPL_FILE/01953FIG11.PDF.

Wu, L. *et al.* (2022) 'Integrated Multi-Omics for Novel Aging Biomarkers and Antiaging Targets', *Biomolecules*, 12(1). Available at: https://doi.org/10.3390/BIOM12010039.

Wuyts, W.A. *et al.* (2003) 'N-acetylcysteine reduces chemokine release via inhibition of p38 MAPK in human airway smooth muscle cells', *European Respiratory Journal*, 22(1), pp. 43–49. Available at: https://doi.org/10.1183/09031936.03.00064803.

Wyles, S.P. *et al.* (2023) 'A chronic wound model to investigate skin cellular senescence', *Aging*, 15(8), pp. 2852–2862. Available at: https://doi.org/10.18632/AGING.204667.

Wynn, T.A. (2008) 'Cellular and molecular mechanisms of fibrosis', *Journal of Pathology*, pp. 199–210. Available at: https://doi.org/10.1002/path.2277.

Wysocki, A.B., Staiano-Coico, L. and Grinnell, F. (1993) 'Wound fluid from chronic leg ulcers contains elevated levels of metalloproteinases MMP-2 and MMP-9', *The Journal of investigative dermatology*, 101(1), pp. 64–68. Available at: https://doi.org/10.1111/1523-1747.EP12359590.

Xaus, J. *et al.* (2001) 'Molecular Mechanisms Involved in Macrophage Survival, Proliferation, Activation or Apoptosis', *Immunobiology*, 204(5), pp. 543–550. Available at: https://doi.org/https://doi.org/10.1078/0171-2985-00091.

Xie, J. *et al.* (2017) 'Premature senescence of cardiac fibroblasts and atrial fibrosis in patients with atrial fibrillation', *Oncotarget*, 8(35), pp. 57981–57990. Available at: https://doi.org/10.18632/ONCOTARGET.19853.

Xie, T. *et al.* (2018) 'Single-Cell Deconvolution of Fibroblast Heterogeneity in Mouse Pulmonary Fibrosis', *Cell reports*, 22(13), pp. 3625–3640. Available at: https://doi.org/10.1016/J.CELREP.2018.03.010.

Xiong, Y. *et al.* (2014) 'Long term exposure to L-arginine accelerates endothelial cell senescence through arginase-II and S6K1 signaling', *Aging*, 6(5), pp. 369–379. Available at: https://doi.org/10.18632/AGING.100663.

Xu, M. *et al.* (2015) 'Targeting senescent cells enhances adipogenesis and metabolic function in old age', *eLife*, 4(DECEMBER2015). Available at: https://doi.org/10.7554/ELIFE.12997.

Xu, M. *et al.* (2018) 'Senolytics improve physical function and increase lifespan in old age', *Nature medicine*, 24(8), pp. 1246–1256. Available at: https://doi.org/10.1038/S41591-018-0092-9.

Xue, D. *et al.* (2022) 'Expansion of Fcγ Receptor IIIa-Positive Macrophages, Ficolin 1-Positive Monocyte-Derived Dendritic Cells, and Plasmacytoid Dendritic Cells Associated With Severe Skin Disease in Systemic Sclerosis', *Arthritis & rheumatology (Hoboken, N.J.)*, 74(2), pp. 329–341. Available at: https://doi.org/10.1002/ART.41813.

Xue, J. *et al.* (2014) 'Transcriptome-Based Network Analysis Reveals a Spectrum Model of Human Macrophage Activation', *Immunity*, 40(2), pp. 274–288. Available at: https://doi.org/10.1016/j.immuni.2014.01.006.

Xue, W. *et al.* (2007) 'Senescence and tumour clearance is triggered by p53 restoration in murine liver carcinomas', *Nature*, 445(7128), pp. 656–660. Available at: https://doi.org/10.1038/NATURE05529.

Yager, D.R. *et al.* (1997) 'Ability of chronic wound fluids to degrade peptide growth factors is associated with increased levels of elastase activity and diminished levels of proteinase inhibitors', *Wound repair and regeneration : official publication of the Wound Healing Society [and] the European Tissue Repair Society*, 5(1), pp. 23–32. Available at: https://doi.org/10.1046/J.1524-475X.1997.50108.X.

Yamashita, C.M. *et al.* (2011) 'Matrix Metalloproteinase 3 Is a Mediator of Pulmonary Fibrosis', *The American Journal of Pathology*, 179(4), pp. 1733–1745. Available at: https://doi.org/10.1016/J.AJPATH.2011.06.041.

Yang, I.H. *et al.* (2020) 'Oxidative stress enhanced the transforming growth factor-β2-induced epithelial-mesenchymal transition through chemokine ligand 1 on ARPE-19 cell', *Scientific Reports*, 10(1). Available at: https://doi.org/10.1038/S41598-020-60785-X.

Yang, J. *et al.* (2020) 'Analysis of chromatin organization and gene expression in T cells identifies functional genes for rheumatoid arthritis', *Nature Communications 2020 11:1*, 11(1), pp. 1–13. Available at: https://doi.org/10.1038/s41467-020-18180-7.

Yang, T.T.C. *et al.* (2002) 'Phosphorylation of NFATc4 by p38 Mitogen-Activated Protein Kinases', *Molecular and Cellular Biology*, 22(11), p. 3892. Available at: https://doi.org/10.1128/MCB.22.11.3892-3904.2002.

Yao, L. *et al.* (2019) 'Paracrine signalling during ZEB1-mediated epithelial–mesenchymal transition augments local myofibroblast differentiation in lung fibrosis', *Cell Death and Differentiation*, 26(5), pp. 943–957. Available at: https://doi.org/10.1038/s41418-018-0175-7.

Yosef, R. *et al.* (2016) 'Directed elimination of senescent cells by inhibition of BCL-W and BCL-XL', *Nature communications*, 7. Available at: https://doi.org/10.1038/NCOMMS11190.

Yu, H. (2007) 'Cdc20: A WD40 Activator for a Cell Cycle Degradation Machine', *Molecular Cell*, 27(1), pp. 3–16. Available at: https://doi.org/10.1016/J.MOLCEL.2007.06.009.

Yu, P. *et al.* (2023) 'KLF9 inhibits the proliferation, invasion, and migration of renal cell carcinoma through the SDF-1/CXCR4 axis', *The Kaohsiung journal of medical sciences*, 39(6), pp. 587–595. Available at: https://doi.org/10.1002/KJM2.12671.

Yu, S. *et al.* (2017) 'Melatonin regulates PARP1 to control the senescence-associated secretory phenotype (SASP) in human fetal lung fibroblast cells', *Journal of Pineal Research*, 63(1), p. e12405. Available at: https://doi.org/10.1111/JPI.12405.

Yuan, Q., Tan, R.J. and Liu, Y. (2019) 'Myofibroblast in Kidney Fibrosis: Origin, Activation, and Regulation', *Advances in experimental medicine and biology*, 1165, pp. 253–283. Available at: https://doi.org/10.1007/978-981-13-8871-2_12.

Yue, Z. *et al.* (2022) 'Senescence-associated secretory phenotype and its impact on oral immune homeostasis', *Frontiers in Immunology*, 13. Available at: https://doi.org/10.3389/FIMMU.2022.1019313.

Zanoni, M. *et al.* (2022) 'Irradiation causes senescence, ATP release, and P2X7 receptor isoform switch in glioblastoma', *Cell Death & Disease 2022 13:1*, 13(1), pp. 1–14. Available at: https://doi.org/10.1038/s41419-022-04526-0.

Zhang, F., Lau, S.S. and Monks, T.J. (2011a) 'The Cytoprotective Effect of N-acetyl-L-cysteine against ROS-Induced Cytotoxicity Is Independent of Its Ability to Enhance Glutathione Synthesis', *Toxicological Sciences*, 120(1), p. 87. Available at: https://doi.org/10.1093/TOXSCI/KFQ364.

Zhang, F., Lau, S.S. and Monks, T.J. (2011b) 'The Cytoprotective Effect of N-acetyl-L-cysteine against ROS-Induced Cytotoxicity Is Independent of Its Ability to Enhance Glutathione Synthesis', *Toxicological Sciences*, 120(1), pp. 87–97. Available at: https://doi.org/10.1093/TOXSCI/KFQ364.

Zhang, H.-Y. and Phan, S.H. (1999) 'Inhibition of Myofibroblast Apoptosis by Transforming Growth Factor β1', *American Journal of Respiratory Cell and Molecular Biology*, 21(6), pp. 658–665. Available at: https://doi.org/10.1165/ajrcmb.21.6.3720.

Zhang, Y., Wang, S. and Ji, G. (2015) 'A Comprehensive Survey on Particle Swarm Optimization Algorithm and Its Applications', *Mathematical Problems in Engineering*, 2015. Available at: https://doi.org/10.1155/2015/931256.

Zhao, J., Feng, Q.P. and Wei, W.Q. (2022) 'Integration of Omics and Phenotypic Data for Precision Medicine', *Methods in Molecular Biology*, 2486, pp. 19–35. Available at: https://doi.org/10.1007/978-1-0716-2265-0_2/TABLES/1.

Zhao, M. *et al.* (2022) 'Targeting fibrosis: mechanisms and clinical trials', *Signal Transduction and Targeted Therapy 2022 7:1*, 7(1), pp. 1–21. Available at: https://doi.org/10.1038/s41392-022-01070-3.

Zhao, R. *et al.* (2016) 'Inflammation in Chronic Wounds', *International journal of molecular sciences*, 17(12). Available at: https://doi.org/10.3390/IJMS17122085.

Zhou, B. *et al.* (2017) 'MicroRNA-202-3p regulates scleroderma fibrosis by targeting matrix metalloproteinase 1', *Biomedicine & pharmacotherapy = Biomedecine & pharmacotherapie*, 87, pp. 412–418. Available at: https://doi.org/10.1016/J.BIOPHA.2016.12.080.

Zhou, X. *et al.* (2018) 'Circuit Design Features of a Stable Two-Cell System', *Cell*, 172(4), pp. 744-757.e17. Available at: https://doi.org/10.1016/j.cell.2018.01.015.

Zhu, F. *et al.* (2013) 'Senescent cardiac fibroblast is critical for cardiac fibrosis after myocardial infarction.', *PloS one*, 8(9). Available at: https://doi.org/10.1371/journal.pone.0074535.

Zomer, H.D. and Trentin, A.G. (2018) 'Skin wound healing in humans and mice: Challenges in translational research', *Journal of Dermatological Science*, 90(1), pp. 3–12. Available at: https://doi.org/10.1016/J.JDERMSCI.2017.12.009.

Zouboulis, C.C. *et al.* (2008) 'Human skin stem cells and the ageing process', *Experimental gerontology*, 43(11), pp. 986–997. Available at: https://doi.org/10.1016/J.EXGER.2008.09.001.

Appendix A

Table A.1: Summary of results from PSO. The best swarm results are highlighted.

No.	iter	swrm	prtcl	PDGFf	SNCthr	MMPthr	ECMthr	INFthr	CSFthr	Qual	Time	pBestE	sBestE	ggBestE
952	29	1	8	0.06279	4.739	0.021	8.783	2.526	2.27	35.11842	6122.5	--	--	--
953	29	1	9	0.06287	4.742	0.02316	8.658	2.865	3.62	32.841105	6120	--	--	--
954	29	1	10	0.05702	4.768	0.02108	8.754	2.8	3.381	27.922717	6127.5	1	1	1
955	29	1	11	0.1038	4.784	0.02766	7.513	2.822	4.787	30.535934	6137	--	--	--
956	29	1	12	0.104	3.419	0.02239	8.741	2.858	3.634	33.313709	6105	--	--	--
957	29	1	13	0.0525	4.303	0.02098	8.232	2.864	3.893	31.885332	6190.5	--	--	--
1436	44	1	12	0.05524	4.75	0.03017	8.629	2.829	3.231	34.09962	6088.5	--	--	--
1437	44	1	13	0.05742	4.499	0.02103	9.486	2.855	2.985	32.017855	6165	--	--	--
1438	44	1	14	0.06839	4.761	0.02528	8.816	2.823	3.514	32.181122	6137	--	--	--
1439	44	1	15	0.0525	4.764	0.02106	8.095	2.579	3.744	30.822759	6121	--	--	--
1440	45	0	0	0.0525	4.249	0.02103	8.293	2.412	3.428	32.361774	6105.5	--	--	--
1441	45	0	1	0.08877	4.327	0.02101	8.047	2.416	2.532	28.867892	6128.5	1	--	--
1442	45	0	2	0.08819	4.341	0.02128	8.095	2.441	2.324	37.455692	6093.5	--	--	--
1443	45	0	3	0.08976	4.329	0.02094	8.081	2.403	2.632	30.175298	6137	--	--	--
1444	45	0	4	0.08104	4.288	0.02093	8.021	2.373	3.285	27.84	6138.5	1	1	1
1445	45	0	5	0.1451	4.36	0.02066	8.107	2.419	3.909	30.716096	6142	--	--	--
1446	45	0	6	0.05104	4.084	0.02297	8.027	2.462	2.348	33.894945	6117.5	--	--	--
1447	45	0	7	0.2707	3.171	0.02093	7.892	2.542	4.75	34.041163	6086.5	--	--	--
1448	45	0	8	0.1361	2.96	0.0362	8.029	2.117	3.774	29.694693	6105	1	--	--
1449	45	0	9	0.08904	4.328	0.02088	8.751	2.483	3.353	31.630388	6119.5	--	--	--
1450	45	0	10	0.07838	4	0.02101	9.545	2.485	3.227	32.744422	6073.5	--	--	--
1451	45	0	11	0.09498	4.703	0.02126	8.081	2.726	2.09	33.811042	6052	--	--	--
1452	45	0	12	0.1525	3.399	0.021	8.298	2.668	3.306	30.508928	6128.5	--	--	--
1453	45	0	13	0.1002	4.636	0.02487	8.069	2.413	2.8	34.490858	6095	--	--	--
1454	45	0	14	0.2206	4.427	0.02062	9.157	2.409	4.75	33.429398	6109.5	--	--	--
1455	45	0	15	0.06029	4.306	0.02117	8.678	2.449	4.097	31.192841	6111	--	--	--
1456	45	1	0	0.0525	4.793	0.02088	8.856	2.865	3.407	30.622941	6156.5	--	--	--
1457	45	1	1	0.0525	4.773	0.02883	8.712	2.718	3.328	30.515908	6154.5	--	--	--
1458	45	1	2	0.05668	4.79	0.02115	8.758	2.808	3.263	31.313928	6186.5	--	--	--
1459	45	1	3	0.1736	3.788	0.02122	9.551	2.9	3.354	31.255046	6102.5	--	--	--
1460	45	1	4	0.06337	4.203	0.02074	8.213	2.807	3.828	32.901265	6118.5	--	--	--
1461	45	1	5	0.05693	4.673	0.02027	10.45	2.896	4.75	35.483672	6076	--	--	--
1462	45	1	6	0.05075	4.752	0.02126	8.794	2.905	3.906	29.504431	6103	--	--	--
1463	45	1	7	0.1414	4.707	0.02426	8.755	2.55	3.534	34.362713	6110	--	--	--
1464	45	1	8	0.05828	4.815	0.02093	8.807	2.792	3.364	32.858776	6161	--	--	--
1465	45	1	9	0.06137	4.765	0.02182	8.752	2.809	3.502	31.171999	6154.5	--	--	--
1466	45	1	10	0.05707	4.768	0.02079	8.771	2.801	3.314	29.773429	6171.5	--	--	--
1467	45	1	11	0.1039	4.83	0.02404	7.892	2.55	3.245	32.590974	6107.5	--	--	--
1906	59	1	2	0.05585	4.769	0.02116	8.757	2.807	3.372	31.462815	6123	--	--	--
1907	59	1	3	0.0525	3.643	0.02095	8.864	2.841	3.375	30.108388	6134	--	--	--
1908	59	1	4	0.07303	4.489	0.02104	8.342	2.77	3.497	34.264949	6135	--	--	--
1909	59	1	5	0.05702	4.737	0.02089	7.159	2.63	4.75	30.983947	6127	--	--	--
1910	59	1	6	0.05257	4.734	0.02038	8.64	2.774	4.025	30.033082	6129	--	--	--
1911	59	1	7	0.09387	4.861	0.021	8.738	2.787	3.388	32.237257	6139.5	--	--	--
1912	59	1	8	0.06028	4.775	0.02102	8.794	2.844	4.313	33.344807	6127	--	--	--
1913	59	1	9	0.06706	4.813	0.02044	8.737	2.84	3.561	35.647303	6136	--	--	--
1914	59	1	10	0.0569	4.768	0.02111	8.756	2.801	3.375	33.289851	6141.5	--	--	--
1915	59	1	11	0.07892	4.84	0.02085	8.617	2.67	3.423	35.947228	6124	--	--	--
1916	59	1	12	0.05444	3.766	0.02745	8.798	2.815	3.617	30.609554	6159.5	--	--	--
1917	59	1	13	0.05633	4.383	0.0211	7.134	2.808	3.405	31.630245	6134.5	--	--	--
1918	59	1	14	0.05731	4.749	0.02674	8.493	2.808	3.333	33.740952	6114.5	--	--	--
1919	59	1	15	0.08716	4.76	0.02101	8.755	2.421	3.307	31.534841	6146.5	--	--	--